MATHEMATICAL MODELING AND CONTROL OF POLLUTANT DYNAMICS IN INDOOR AIR

Thesis by
William W Nazaroff

In Partial Fulfillment of the Requirements
for the Degree of
Doctor of Philosophy

California Institute of Technology
Pasadena, California

1989

(Submitted September 27, 1988)

Dedicated to the memory of
Sonia Hamann-Nazaroff.
The influence of her short life upon mine
remains deep
and, sometimes, mysterious.

ACKNOWLEDGEMENTS

The completion of this thesis represents the realization of a closely held dream. I am grateful for the support and assistance freely given to me by so many people during the course of the research. This opportunity to publicly acknowledge their contributions is welcome.

First, I thank Professor Glen Cass, my thesis advisor. His enthusiasm for air pollution research and for Caltech was instrumental in my decision to come here to study. During my tenure, he has provided for me an excellent working environment, better than I thought possible for a graduate student. Moreover, he has created an atmosphere of expectation and support in which I felt both called to give and capable of giving my best effort. I have been privileged to work very closely with him on the research reported in this thesis. Many of the ideas expressed arose from discussions between us. His detailed comments have sharpened my thoughts and strengthened my expression of them.

Professor Cass and each of the other members of my thesis committee—Professors John Seinfeld, Richard Flagan, Norman Brooks, and Fredrick Shair—have made important contributions to my professional life. I have benefitted from their commitment to high quality teaching. I am particularly grateful for their enthusiastic support of my aspiration to join their profession.

The work described in this thesis was built on a solid foundation, constructed by many former Caltech graduate students. In this regard, I especially thank Ted Russell, Greg McRae and Fred Gelbard. Having access to their computer-based implementations of mathematical models of air pollutant dynamics permitted me to make rapid progress in the early stages of my research.

Much of the experimental work reported in this thesis, particularly that described in Chapter 6, could not have been completed without the capable support of many others. I thank the Caltech staff members—Theresa Fall, Lynn Salmon, and Mary Ligocki—and undergraduate students—Mike Jones, Harvey Liu, and Timothy Ma—who worked on the

museum aerosol study. Fellow graduate students, Rob Harley and Wolfgang Rogge, helped me with the round-the-clock monitoring shifts at the Scott Gallery and the Sepulveda House. Luiz Palma assisted me with the experiments to calibrate the optical particle counters. Also, I am grateful for the support we received in obtaining access to the five museums: the Getty Museum, the Norton Simon Museum, the Scott Gallery, the Sepulveda House, and the Southwest Museum. Special thanks go to John Coghlan, the artifacts curator at the Sepulveda House, and to John Sudolcan, the building manager at the Norton Simon Museum, who were extraordinarily accommodating and supportive of our activities. We received important support in sample analysis from the Air and Industrial Hygiene Laboratory of the California Department of Health and Human Services (Berkeley, California), NEA, Inc. (Beaverton, Oregon), and Sunset Laboratories (Forest Grove, Oregon). Rich Sextro arranged for me to borrow the portable gas chromatograph; both he and Bud Offermann supplied me with important information about the experiment results analyzed in Chapter 5.

Thank you: Rayma Harrison, for your excellent support in the library; Ken McCue, for developing and maintaining a superb computational environment; and Rich Eastvedt, for your wonderful carpentry work on the OPC calibration box.

As much as I appreciate the support I received in carrying out my research, I think that I am more grateful for the personal support and encouragement that I received from other graduate students and staff at Caltech. Thank you Luise Betterton, Christina Conti, Dixie Fiedler, Rob Harley, Lynn Hildemann, Sue Larson, Monica Mazurek, Hung Nguyen, Chris Pilinis, and Tony Wexler for helping me keep a smile on my face.

I offer special thanks to you: Steve Nazaroff, for great racquetball competition; Tony Nero, for challenging ideas; and Mary Doussette, for profound personal insights.

Throughout my stay at Caltech, I have been the recipient of generous financial support. The research described in this thesis was made possible by funds from a contract with the Getty Conservation Institute, from which I received support as a research

assistant. In addition, I am grateful for personal financial support provided by an Earle C. Anthony Graduate Fellowship, an ARCS Foundation Fellowship, and graduate scholarships from the Air Pollution Control Association and the Switzer Foundation.

This endeavor has been a struggle. To the detriment of all of my life other than my profession, I have been driven by some inexplicable inner motive to work at a pace that is near my limit. Throughout these four years, my wife, Ingrid, has been patiently and unwaveringly supportive. Thank you, Ingrid. I love you—and Rani and Alexis—more than I can express.

ABSTRACT

To assess the total human-health and material-damage risks associated with air-pollutant exposure, the concentrations and fates of pollutants in indoor atmospheres must be understood. Three observations reinforce this point: (1) concentrations of many pollutants are commonly higher in indoor air than in outdoor air; (2) in many countries, people spend more time indoors than outside; and (3) many of the most precious material possessions of society are kept indoors. In this thesis, mathematical models are developed as tools to improve the understanding of pollutant dynamics in indoor air. These tools are applied to the problem of protecting works of art from damage due to air pollutant exposure, particularly for the purpose of understanding how to control soiling due to airborne particle deposition.

A deterministic mathematical model first is formulated to describe the time-dependent concentrations of chemically reactive gases and airborne particles in indoor air, then implemented as a computer program. Using a flexible, multichamber description of a building, the model accounts for the effects of ventilation, filtration, deposition onto surfaces, and direct emission for all pollutants. In addition, the influence of homogeneous photolytic and thermal chemical reactions is computed for gases that are present in the photochemical smog system. The model is capable of determining the chemical composition and size distribution of indoor aerosols, accounting for the effect of coagulation in addition to the processes itemized above. The model computes the fate of pollutants in indoor air, determining the absolute strengths of the sources and sinks for each species.

To permit the simulation of soiling problems, modeling calculations for the deposition of particles and other pollutants onto surfaces are particularly detailed. Equations that predict the rate of pollutant deposition onto indoor surfaces are developed, accounting for the effects of advection, diffusion, and, for particles, gravitational settling

and thermophoresis. Three air flow regimes are analyzed: natural convection induced by a temperature difference between the surface and the nearby air, forced laminar flow parallel to a surface, and homogeneous turbulence in the core of the room. The analysis of a vertical isothermal flat plate in natural convection flow shows that, for this flow regime, thermophoresis is an important particle transport process within the boundary layer adjacent to the surface, effectively repelling particles larger than approximately 0.1 μm in diameter if the surface is even a few degrees K warmer than the nearby air.

To test model performance, and to investigate the dynamic behavior of indoor pollutants, the model is applied to several indoor air quality problems. In one case, modeling predictions are made of pollutant concentrations in a museum gallery in Southern California into which photochemical smog is introduced by the ventilation system. Good agreement is obtained between measured and modeled concentrations of NO, NO_2 and O_3. The model predicts substantial production of several species, including HNO_2, HNO_3, NO_3, and N_2O_5, due to chemical reaction within the museum atmosphere. The aerosol mechanics aspects are tested by applying the model to the problem of predicting the evolution of the aerosol size distribution following combustion of a cigarette in a single room having a low air-exchange rate, and good agreement is found between model predictions and measured values.

The completed indoor air quality model next is used to evaluate the soiling hazard to art objects in museums resulting from the deposition of particles containing elemental carbon (soot) or soil dust. Time-resolved measurements of the indoor and outdoor aerosol size distribution in three Southern California museums are reported. Model predictions of indoor aerosol characteristics based on measured outdoor aerosol characteristics and data on building dynamics agree well with measurements. The predictions also show that generally less than 1% of the fine particles (0.05-2 μm in diameter) entering the museums deposit onto the walls. Nevertheless, deposition calculations indicate that, at the rates determined for the study days, elemental carbon

(soot) particles would accumulate on vertical surfaces in the museums at a rate sufficient to yield perceptible soiling in characteristic times of 1-40 years, depending on the museum studied. These are very short periods, considering that many art objects are to be preserved indefinitely.

To test the accuracy of the particle deposition calculations, model predictions are made of the annual mean deposition velocity of particles onto the walls of five Southern California museums, using the results of short-term monitoring of near-wall air velocities and long-term monitoring of surface-air temperature differences. The predictions are compared against the results of measurements in these museums of the deposition velocities of sulfates and of fine particles. The modeling and measurement results generally concur, revealing that the deposition velocities for a given particle size vary by a factor of as much as 30 among the sites studied, with the lowest values associated with laminar forced flow adjacent to the building walls, and highest values found in museums where deposition is driven by turbulence in the core of the room.

Methods for reducing the soiling rate of objects displayed in museums are identified and include the following: (1) reducing the rate of supply of outdoor air into the building; (2) increasing the effectiveness of particle filtration; (3) altering the air flow conditions within the building to reduce the particle deposition velocity onto surfaces of concern; (4) placing objects within display cases or framing objects behind glass; (5) managing the building site to achieve low outdoor concentrations; and (6) eliminating indoor particle sources. The mathematical model of indoor aerosol dynamics is combined with experimental data collected at an historic museum in Southern California to determine the potential effectiveness of these control measures. According to model results, with careful design of control measures the soiling rate can be reduced by at least two orders of magnitude, thereby extending to periods of a century or more the time before noticeable soiling will occur.

TABLE OF CONTENTS

LIST OF FIGURES

LIST OF TABLES

CHAPTER 1

INTRODUCTION

1.1 Perspective on Indoor Air Quality

The importance of indoor air pollution was established a few decades ago, when several investigations addressed the impact of heating and cooking systems on indoor air quality (Biersteker et al., 1965; Yocum et al., 1974; Hollowell et al., 1976). Elevated concentrations of sulfur dioxide, carbon monoxide, and oxides of nitrogen were observed in some indoor environments, particularly where combustion byproducts were vented directly, whether by design or through equipment failure, into the indoor air. Subsequently, it was determined that, due to direct indoor emissions, the indoor concentrations of many air pollutants exceed the concentrations found outdoors. Some pollutants that are commonly found at elevated concentrations in indoor air are listed in Table 1.1. Taken in combination with the high proportion of time that people spend indoors and the fact that many vulnerable objects are stored indoors, the observation of elevated indoor pollutant concentrations implies that understanding indoor environments is an essential component of assessing the total human-health and material-damage risks associated with air pollutant exposure.

Even for pollutants that are not commonly emitted indoors, an understanding of the concentrations prevalent in indoor air is important. For example, ozone is a major constituent of photochemical smog. When outdoor ozone concentrations are excessive, it is recommended that people curtail activities and remain indoors. However, ozone in outdoor air may enter a building along with air that is provided, intentionally or otherwise, for ventilation. An important issue, addressed in several studies, is the degree of protection afforded by being indoors from pollutants that are of outdoor origin (Mueller et al., 1973; Sabersky et al., 1973; Thompson, et al., 1973; Shair and Heitner,

Table 1.1 Air pollutants commonly found at elevated concentrations indoors, and common indoor sources.

Species [a]	Common source	Reference
asbestos	insulation	Committee on Indoor Pollutants, 1981
biogenic agents *(Legionella pneumophila)*	air-conditioning systems	Solomon and Burge, 1984
formaldehyde	pressed-wood products, insulation	Hollowell and Miksch, 1981; Gammage and Gupta, 1984
nitrogen oxides	combustion appliances	Traynor et al, 1982; Leaderer, 1982
particles	combustion appliances, cigarette smoking	Repace and Lowrey, 1980; Tu and Knutson, 1988
pesticides (chlordane)	building substructures	Anderson and Hites, 1988
polychlorinated biphenyls	fluorescent light ballasts	MacLeod, 1981
radon	soil	Hopke, 1987; Nazaroff and Nero, 1988
volatile organic compounds (dichlorobenzene, tetrachloroethylene)	consumer products	Wallace et al., 1985; Pellizzarri et al., 1986

[a] Examples, where appropriate, are given in parentheses.

1974; Derham, et al., 1974; Cohen and Cohen, 1980).

In addition to constituting a human health risk, indoor air pollution has the potential to cause serious damage to important materials. Classes of buildings in which the materials damage potential of air pollutants is a particularly serious concern include archives (Committee on Preservation of Historical Records, 1986) and museums (Thomson, 1978; Baer and Banks, 1985). Some of the most stringent standards for indoor air quality are specified for these buildings (Mathey et al., 1983). Since the collections must be preserved indefinitely, even very slow rates of deterioration could lead to unacceptable accumulated damage. A related concern arises in certain manufacturing processes. For example, in the fabrication of microelectronic components, deposition of airborne particles onto wafer surfaces may cause the failure of an integrated circuit (Cooper, 1986). Electronics manufacturers have made large investments to establish particle-free clean rooms to minimize the effects of this problem (e.g., Schafer and Kotz, 1987).

Overall, then, indoor air quality is important in several contexts. The general problem may be considered in the following manner. Pollutants from indoor emission sources are combined with those introduced from outdoor air via the ventilation system to produce a complex mixture of contaminants. The resulting indoor concentrations depend not only on the characteristics of these sources, but also on transformation, transport, and removal processes, as indicated schematically in Figure 1.1. Depending on the circumstances, any one or any combination of these processes may be essential in governing the indoor concentration of a pollutant, which may itself vary significantly in space and time. In turn, the indoor pollutant concentrations represent the pivotal parameters in appraising indoor air quality. However, a comprehensive assessment of the indoor air pollution problem does not end with determining ambient concentrations. Other information must be integrated into the analysis to assess effects. For example, information on pollutant concentrations must be combined with human occupancy and

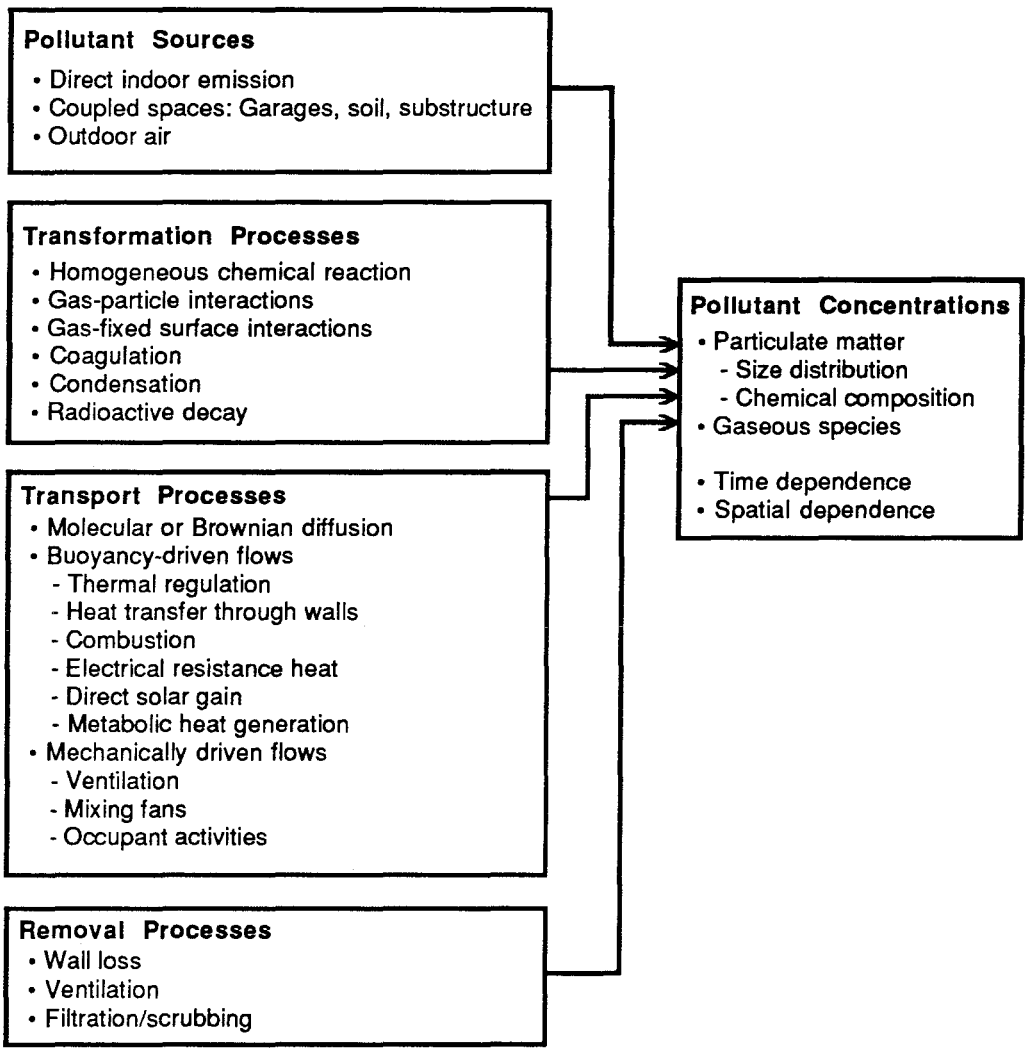

Figure 1.1 Chemical and physical processes affecting indoor air quality.

sensitivity data to assess human health effects. For appraising the risk of material damage, one must add an understanding of the transport of pollutants to surfaces and the reactivity of the pollutant species with the surface material. If an indoor air quality problem is serious enough to warrant corrective action, a variety of control techniques can effectively be employed, provided that the influence of the various factors governing the magnitude of the problem is sufficiently understood. Rigorous investigation of the spectrum of technical issues concerning indoor air pollution requires both the creative application of existing scientific and engineering methods and the development of new tools and techniques. In this sense, given the complexity of the subject and its practical importance, it may be appropriate to consider studies of the technical issues in indoor air quality as constituting a distinct applied-science discipline: indoor atmospheric science.*

In addition to the technical issues, it is important to note that the -issue of indoor air quality raises a number of new and important legal and public policy concerns (Spengler and Sexton, 1983; Sexton and Wesolowski, 1985; Nero, 1988).

1.2 Mathematical Modeling of Indoor Air Pollution

The importance of indoor air quality, the desire to deliberately control indoor pollutant levels, and the many factors that determine pollutant concentrations and effects, combine to establish the need for mathematical models that describe indoor atmospheres. A deterministic mathematical representation is sought for the physical and chemical processes that govern the dynamic behavior of indoor air pollutants. By translating this representation into a computer code, predictions may be made of the evolution of pollutant concentrations and of the fate of pollutants. These predictions can be used to assess the hazard associated with indoor air quality and to evaluate proposed control measures in advance of their use. A key aspect in the formulation of such a model is that all of the input variables should be accessible by means that are independent of measured

* This concept was first put forward by Dr. A. V. Nero, Lawrence Berkeley Laboratory, in 1983.

indoor concentrations. This requirement distinguishes deterministic models from statistical models (e.g., Sexton et al., 1983), in which one uses measured indoor concentrations from many sites along with other information to develop correlations among dependent and independent variables.

Deterministic mathematical models of indoor air quality that are well formulated and thoroughly tested could assist scientists, engineers, architects, building managers, policy makers, and others, with many goals:

- to assess the risk of human health impacts or material damage effects from exposure to indoor air pollutants;
- to develop effective and efficient control measures;
- to provide information on parameters that are not easily measured, such as the fate of indoor air pollutants;
- to extend measurement data from one or more sets of buildings to a broader class of structures; and
- to evaluate the indoor air quality of a proposed building in advance of construction.

In addition, mathematical models could play a central role in designing experiments and in interpreting the resulting data. Such models would thereby constitute an important tool for evaluating and appraising the current understanding of physical and chemical processes governing indoor pollutant behavior.

The early mathematical models of indoor air quality were based on a relatively simple mass-balance representation of the indoor atmosphere (Turk, 1963; Shair and Heitner, 1974; Esmen, 1978; Alzona et al., 1979; Ishizu, 1980). In these models, gaseous pollutants are treated as chemically independent. Aerosols are represented by the total suspended mass of particulate matter (Alzona et al., 1979); no information on aerosol size or chemical composition is incorporated into the model. These models have been successfully applied in some situations. However, they are inadequate for addressing

many important issues concerning indoor air pollutants. For example, data on indoor pollutant concentrations suggest that some chemical reactions may proceed at rates exceeding the ventilation rate (e.g., $NO_2 + O_3 \rightarrow NO_3 + O_2$). Particle size plays a major role in every aspect of aerosol behavior, such as the retention efficiency upon inhalation. Furthermore, one chemical constituent of airborne particles, elemental carbon (soot), may be responsible for a dominant portion of the soiling hazard associated with the particle deposition onto vertical indoor surfaces. Despite further development (e.g., Özkaynak et al., 1982; Schiller, 1984; Ryan et al., 1988), available indoor air quality models (apart from those described in this thesis) lack the capability of addressing generalized chemical reaction systems, aerosol mechanics, and related issues.

1.3 Objectives of this Research

The broad aim of this research is to advance the understanding of physical and chemical dynamic processes that govern the concentrations and fates of pollutants in indoor air. This goal is accomplished through the development and application of a deterministic mathematical model of indoor air quality. A mathematical description of indoor pollutant behavior is established. A numerical solution based on this description is then implemented in the form of a computer program. The performance of the model is tested by comparing model predictions with measurement results in several situations. The model is applied to a specific indoor air quality issue: protecting works of art from damage due to indoor air pollution exposure. Assessing the soiling hazard in museums due to particle deposition is emphasized, as is evaluating the effectiveness of control measures. By contributing to the solution of a problem with practical importance, the utility of the mathematical tools developed in this thesis is demonstrated.

1.4 Outline of Thesis Contents

The core elements of this thesis are contained in Chapters 2 and 5. In Chapter 2, a mathematical model of chemically reactive gaseous pollutants in indoor air is described.

The model is capable of treating an arbitrary chemical kinetic mechanism; the focus is on pollutants associated with the photochemical smog system. The model describes the time dependence of indoor air pollutant concentrations, accounting for the effects of direct emission, ventilation, filtration, deposition and chemical reaction. A flexible multichamber representation is used to describe a building. In Chapter 2, the model is tested against experimental data for a case in which outdoor air, containing photochemically reactive pollutants, is introduced into a museum gallery. Several perturbations from the base case conditions are considered, to study the likely effects of pollutant sources and altered building design on indoor air chemistry.

In Chapter 5, an indoor air quality modeling approach is developed for the case of airborne particles. A multicomponent sectional representation is used to describe the indoor aerosol. Using the multichamber representation of a building introduced in Chapter 2, the indoor aerosol model explicitly accounts for the effects of ventilation, filtration, deposition, direct indoor emission, and coagulation. The deposition calculations are especially detailed to permit the simulation of soiling problems. The aerosol model itself is coupled to the gas-phase model described in Chapter 2, permitting future calculations that account for gas-to-particle conversion processes. In Chapter 5, the model is applied to explain the results of an experiment in which cigarette smoke was emitted into a poorly ventilated room.

The development of the model's capability to make detailed predictions of pollutant deposition onto indoor surfaces is contained in Chapters 3 and 4. Chapter 3 describes a theoretical analysis of particle deposition onto a vertical isothermal flat plate from a laminar natural convection flow. Scaling arguments are used to simplify the governing transport equations, to determine conditions under which thermophoresis dominates Brownian motion in the concentration boundary layer, and to determine the magnitude of the particle deposition velocity onto the plate. By means of a similarity transformation, the system of partial differential equations is converted to a system of

ordinary differential equations, which are then solved numerically. The results suggest that particle deposition is much more rapid to a vertical surface that is cold, relative to the nearby air temperature, than to one that is warm.

The analysis in Chapter 3 addresses one specific set of deposition conditions. In general, deposition of both gases and particles is important; some indoor surfaces are horizontal rather than vertical; air flow along the surface may be driven by mechanical motion rather than buoyancy; and the air flow may be turbulent rather than laminar. Chapter 4 addresses pollutant deposition under these other conditions. The mass-transport-limited deposition rate is analyzed for three air flow regimes: (1) natural convection driven by a temperature difference between the surface and the nearby air; (2) forced laminar flow parallel to the surface; and (3) homogeneous turbulence in the core of the room. Theoretical predictions for these regimes are compared against published data on the mass-transport-limited deposition velocity of pollutants to surfaces of rooms.

In Chapters 6-8, the emphasis shifts from the general problem of modeling the dynamics of indoor pollutants to the specific issue of protecting works of art from soiling due to particle deposition in museums. Chapter 6 addresses the dynamics of airborne particles in three Southern California museums. Time-dependent measurements of the chemical composition and size distribution of the outdoor aerosol are reported for 24-hour periods at each site. Properties of the buildings that influence aerosol concentrations and fates are also given. The mathematical model of Chapter 5 is applied using these data to predict the concentration and fate of the indoor aerosol. A comparison of predicted and measured indoor aerosol characteristics provides a basis for evaluating the model's performance. Predictions of the rate of soiling are made, based on the modeling and measurement results. These predictions show that under present conditions, perceptible soiling of some surfaces in these museums may occur over periods ranging from one year at one of the museums to a few tens of years at the other two sites. These time scales are notably short relative to the period that art objects are to be preserved.

Only a small fraction (generally 1% or less for the three cases studied) of the airborne fine particles brought into a museum from outdoors deposit onto vertical surfaces. Consequently, the comparison between measurements and predictions of the aerosol size distribution in Chapter 6 does not constitute a sensitive test of the predicted deposition rates onto vertical surfaces. Nevertheless, the soiling hazard to works of art such as paintings may still be substantial, particularly since it is desired to preserve these objects indefinitely. In Chapter 7, predictions are developed of the average particle deposition velocity onto walls within five Southern California museums. These predictions are based on the deposition calculations developed in Chapters 3 and 4, and on experimental measurements of the near-wall air velocity and wall-air temperature difference at the five sites. The predictions are compared against the results of direct experimental measurements of the particle deposition velocity onto these surfaces.

The results presented in Chapters 6 and 7 demonstrate that a reasonable level of understanding has been attained of the dynamic factors governing indoor aerosol concentrations and deposition rates. In Chapter 8, this understanding is distilled into a simpler model than presented in Chapter 5, that captures the essential factors governing the rate of soiling of indoor surfaces. An examination of the central equation resulting from this analysis suggests several options for controlling the soiling rate. The options are (1) reducing the rate of exchange of indoor air with outdoor air; (2) improving particle filtration; (3) reducing particle deposition velocities; (4) using display cases or framing; (5) limiting sources of indoor aerosol; and (6) ensuring that the site has low outdoor aerosol concentrations. Using the mathematical model developed in Chapter 5 and experimental data presented in Chapter 6 for the museum site with the highest soiling rate, the potential effectiveness of each of these options is appraised. This chapter shows that a variety of practical techniques are available to control the rate of particle deposition onto objects displayed in museums. Through application of these techniques, the rate of soiling may be reduced by two orders of magnitude, or more, relative to uncontrolled

conditions. Thus, using the principles developed in this thesis, deliberate control of soiling rates can be engineered into the design of a museum gallery or industrial facility.

Chapter 9 provides a summary of the findings of this thesis and suggestions for further avenues of research.

1.5 References

Alzona, J., Cohen, B. L., Rudolph, H., Jow, H. N., and Frohliger, J. O. (1979) Indoor-outdoor relationships for airborne particulate matter of outdoor origin, *Atmospheric Environment* **13**, 55-60.

Anderson, D. J., and Hites, R. A. (1988) Chlorinated pesticides in indoor air, *Environmental Science and Technology* **22**, 717-720.

Baer, N. S., and Banks, P. N. (1985) Indoor air pollution: Effects on cultural and historic materials *International Journal of Museum Management and Curatorship* **4**, 9-20.

Biersteker, K., de Graaf, H., and Nass, Ch. A. G. (1965) Indoor air pollution in Rotterdam homes, *International Journal of Air and Water Pollution* **9**, 343-350.

Cohen, A. F., and Cohen, B. L., Protection from being indoors against inhalation of suspended particulate matter of outdoor origin, *Atmospheric Environment* **14**, 183-184.

Committee on Indoor Pollutants (1981) *Indoor Pollutants*, National Research Council, National Academy Press: Washington.

Committee on Preservation of Historical Records (1986) *Preservation of Historical Records*, National Research Council, National Academy Press: Washington.

Cooper, D. W. (1986) Particulate contamination and microelectronics manufacturing: An introduction, *Aerosol Science and Technology* **5**, 287-299.

Derham, R. L., Peterson, G., Sabersky, R. H., and Shair, F. H. (1974) On the relationship between the indoor and outdoor concentrations of nitrogen oxides, *Journal of the Air Pollution Control Association* **24**, 158-161.

Esmen, N. A. (1978) Characterization of contaminant concentrations in enclosed spaces, *Environmental Science and Technology* **12**, 337-339.

Gammage, R. B. and Gupta, K. C. (1984) Formaldehyde, in *Indoor Air Quality*, Walsh, P. J., Dudney, C. S., and Copenhaver, E. D., eds., CRC Press: Boca Raton, Florida, Chapter 7.

Hollowell, C. D., and Miksch, R. R. (1981) Sources and concentrations of organic compounds in indoor environments, *Bulletin of the New York Academy of Sciences* **57**, 962-977.

Hollowell, C. D., Budnitz, R. J., Case, G. D., and Traynor, G. W. (1976) *Combustion-Generated Indoor Air Pollution I. Field Measurements 8/75 - 10/75*, Report LBL-4416, Lawrence Berkeley Laboratory: Berkeley, California.

Hopke, P. K., ed. (1987) *Radon and Its Decay Products: Occurrence, Properties and Health Effects*, ACS Symposium Series 331, American Chemical Society: Washington.

Ishizu, Y. (1980) General equation for the estimation of indoor pollution, *Environmental Science and Technology* **14**, 1254-1257.

Leaderer, B. P. (1982) Air pollutant emissions from kerosene space heaters, *Science* **218**, 1113-1115.

MacLeod, K. E. (1981) Polychlorinated biphenyls in indoor air, *Environmental Science and Technology* **15**, 926-928.

Mathey, R. G., Faison, T. K., Silberstein, S., Woods, J. E., Johnson, W. B., Lull, W. P., Madson, C. A., Turk, A., Westlin, K. L., Banks, P. N. (1983) *Air Quality Criteria for Storage of Paper-Based Archival Records*, report NSBIR 83-2795, National Bureau of Standards: Washington.

Mueller, F. X., Loeb, L., and Mapes, W. H. (1973) Decomposition rates of ozone in living areas, *Environmental Science and Technology* **7**, 342-346.

Nazaroff, W. W., and Nero, A. V., eds. (1988) *Radon and Its Decay Products in Indoor Air*, Wiley: New York.

Nero, A. V. (1988) Controlling indoor air pollution, *Scientific American* **258(5)**, 42-48.

Özkaynak, H., Ryan, P. B., Allen, G. A., and Turner, W. A. (1982) Indoor air quality modeling: Compartmental approach with reactive chemistry, *Environment International* **8**, 461-471.

Pellizzarri, E. D., Hartwell, T. D., Perritt, R. L., Sparacino, C. M., Sheldon, L. S., Zelon, H. S., Whitmore, R. W., Breen, J. J., and Wallace, L. Comparison of indoor and outdoor residential levels of volatile organic chemicals in five U.S. geographical areas, *Environment International* **12**, 619-623.

Repace, J. L., and Lowrey, A. H. (1980) Indoor air pollution, tobacco smoke, and public health, *Science* **208**, 464-472.

Ryan, P. B., Spengler, J. D., and Halfpenny, P. F. (1988) Sequential box models for indoor air quality: Application to airliner cabin air quality, *Atmospheric Environment* **22**, 1031-1038.

Sabersky, R. H., Sinema, D. A., and Shair, F. H. (1973) Concentrations, decay rates, and removal of ozone and their relationship to establishing clean indoor air, *Environmental Science and Technology* **7**, 347-353.

Schafer, N., and Kotz, D. A. (1987) Successful clean room design, *ASHRAE Journal* **29(9)**, 25-28.

Schiller, G. E. (1984) *A Theoretical Convective-Transport Model of Indoor Radon Decay Products*, Ph. D. Thesis, University of California, Berkeley, California.

Sexton, K., Letz, R., and Spengler, J. D. (1983) Estimating human exposure to nitrogen dioxide: An indoor/outdoor modeling approach, *Environmental Research* **32**, 151-166.

Sexton, K., and Wesolowski, J. J. (1985) Safeguarding indoor air quality, *Environmental Science and Technology* **19**, 305-309.

Shair, F. H., and Heitner, K. L. (1974) Theoretical model for relating indoor pollutant concentrations to those outside, *Environmental Science and Technology* **8**, 444-451.

Solomon, W. R., and Burge, H. A. (1984) Allergens and pathogens, in *Indoor Air Quality*, Walsh, P. J., Dudney, C. S., and Copenhaver, E. D., eds., CRC Press: Boca Raton, Florida, Chapter 10.

Spengler, J. D., and Sexton, K. (1983) Indoor air pollution: A public health perspective, *Science* **221**, 9-17.

Thompson, C. R., Hensel, E. G., and Kats, G. (1973) Outdoor-indoor levels of six air pollutants, *Journal of the Air Pollution Control Association* **23**, 881-886.

Thomson, G. (1978) *The Museum Environment* Butterworths: London.

Traynor, G. W., Anthon, D. W., and Hollowell, C. D. (1982) Technique for determining pollutant emissions from a gas-fired range, *Atmospheric Environment* **16**, 2979-2986.

Tu, K.-W., and Knutson, E. O. (1988) Indoor outdoor aerosol measurements for two residential buildings in New Jersey, *Aerosol Science and Technology* **9**, 71-82.

Turk, A. (1963) Measurements of odorous vapors in test chambers: theoretical, *ASHRAE Journal* **5(10)**, 55-58.

Wallace, L. A., Pellizzarri, E. D., Hartwell, E. D., Sparacino, C. M., Sheldon, L. S., and Zelon, H. (1985) Personal exposures, indoor-outdoor relationships and breath levels of toxic air pollutants measured for 355 persons in New Jersey, *Atmospheric Environment* **19**, 1651-1661.

Yocum, J. E., Clink, W. L., and Cote, W. A. (1971) Indoor/outdoor air quality relationships, *Journal of the Air Pollution Control Association* **21**, 251-259.

CHAPTER 2

MATHEMATICAL MODELING OF CHEMICALLY REACTIVE POLLUTANTS IN INDOOR AIR

2.1 Abstract

A general mathematical model is presented for predicting the concentrations of chemically reactive compounds in indoor air. The model accounts for the effects of ventilation, filtration, heterogeneous removal, direct emission, and photolytic and thermal chemical reactions. The model is applied to the induction of photochemically reactive pollutants into a museum gallery and the predicted NO, NO_x-NO, and O_3 concentrations are compared to measured data. The model predicts substantial production of several species due to chemical reaction, including HNO_2, HNO_3, NO_3, and N_2O_5. Circumstances in which homogeneous chemistry may assume particular importance are identified and include buildings with glass walls, indoor combustion sources, and direct emission of olefins.

Reference: Nazaroff, W. W., and Cass, G. R. (1986) Mathematical modeling of chemically reactive pollutants in indoor air, *Environmental Science and Technology* **20**, 924-934.

2.2 Introduction

Considerable progress has been made recently in developing mathematical models for predicting pollutant concentrations in ambient air. In modeling urban air basins, state-of-the-art approaches utilize a spatially-resolved grid with explicit treatment of advective transport, photochemical reactions, deposition to the earth's surface, and pollutant emissions (McRae et al., 1982a, McRae and Seinfeld, 1983). Regional models, used in the study of acid deposition, incorporate many of the above features plus transformation processes involving pollutant reaction within aqueous droplets (Ruff et al., 1985).

By comparison, most approaches to modeling pollutant concentrations in indoor air have been relatively primitive, treating pollutant species as chemically independent, and assuming the building interior to be a single, well-mixed volume (e.g., Shair and Heitner, 1974; Traynor et al., 1982a; Yamanaka, 1984; Fisk, 1984). Extended developments have included (1) multichamber formulations (Hernandez and Ring, 1982; Özkaynak et al., 1982; Davidson et al., 1984); (2) a model for predicting radon progeny concentrations, which incorporated a description of natural convection (Schiller, 1984); and (3) explicit treatment of the kinetics of the primary photolytic cycle (Özkaynak et al., 1982). To date, however, there has not been an indoor air pollution model with the capability of explicitly treating an arbitrary chemical kinetic mechanism.

Despite the moderate success of the models cited above, there are many reasons that argue for development of a model for indoor air pollution that explicitly incorporates reactive chemistry. Data on indoor pollutant concentrations suggest that chemical reactions may proceed at rates comparable to, or even much greater than, the ventilation rate (for example, $NO + O_3$ and $NO_2 + O_3$). A major element of the mass-balance models cited above—the "reactivity" (Traynor et al., 1982a) or "indoor sinks" (Shair and Heitner, 1974)—is not well understood, and there are discrepancies between the wall-loss rates determined in chamber studies and field experiments (Sabersky et al., 1973; Shair,

1981). Some secondary pollutants produced, for example, in photochemical smog may not be well-determined by the simple mass-balance approach. And finally, it is becoming increasingly apparent that many indoor environments are as complex in their constitution—if not more so—than polluted outdoor environments (e.g., Berglund et al., 1984). It is reasonable to expect, given the wide range of pollutants that may be emitted directly indoors, the introduction of pollutants from outdoor air via the ventilation system, and the wide range of indoor lighting levels (and hence photolytic reaction rates), that there are numerous circumstances in which a chemically explicit model is needed to accurately predict indoor pollutant concentrations.

In this chapter, a general mathematical model is formulated that describes the time dependence of indoor air pollutants in a chemically reacting system. An important contribution of this formulation over previous work is the explicit treatment of gas-phase photolytic and thermal reactions. The model also is formulated to compute for each species the production rates associated with ventilation, chemical reaction, and direct emission, and the removal rates associated with ventilation, chemical reaction, filtration and wall loss. As a partial validation of the model, a case is simulated in which outdoor air, containing photochemically reactive air pollutants, is introduced into a museum gallery. The simulated indoor concentrations of ozone, nitric oxide and NO_x-NO are compared with measured data during a two-day period in November 1984. Several interesting perturbations from this base case are considered to study the likely effects of pollutant sources and altered building materials on indoor air chemistry.

2.3 Model Formulation

Two fundamental postulates form the basis of the model:

(1) The building can be represented as a set of chambers, with the air flow rate from each chamber to all others known as a function of time. Each chamber is visualized as a room or group of rooms. The core of each chamber is considered to be well-mixed

and separated from the building surfaces by a thin concentration boundary layer. The details of the boundary layer affect the rate of pollutant removal at fixed surfaces, but may otherwise be neglected in determining pollutant concentrations.

(2) Within each chamber, the rate of change of the concentration of each chemical species may be described by an equation of the form

$$\frac{dC}{dt} = S - L\,C \qquad (2.1)$$

where S represents the sum of all sources: direct emission, advective transport from other chambers (including the mechanical ventilation system and outdoors), and production by chemical reaction. L represents the sum of all sinks: loss by homogeneous chemical reaction, transformation and removal processes occurring on surfaces, and removal by transport from the chamber. S and L are, in general, functions of time and of the concentrations of all pollutant species in all chambers.

The following subsections present details of the manner in which the various elements of the problem are treated in the model.

2.3.1 Ventilation. The treatment of ventilation is an extension of the formulation of Shair and Heitner (1974) to incorporate an arbitrary number of chambers. A schematic illustration of the approach is presented in Figure 2.1. For each chamber, air may enter directly from outside (infiltration), from the mechanical ventilation system (supply), and from each of the other chambers (cross-ventilation). Air may be removed to the outside (exfiltration or exhaust), to the mechanical ventilation system (return), and to each of the other chambers. The mechanical ventilation system is treated as a special chamber having zero volume. In addition to the return air from each chamber, air from outdoors (make-up) may be supplied directly to the mechanical ventilation system. Pollutant removal devices ("filters") may be specified for each return-air line and for the make-up

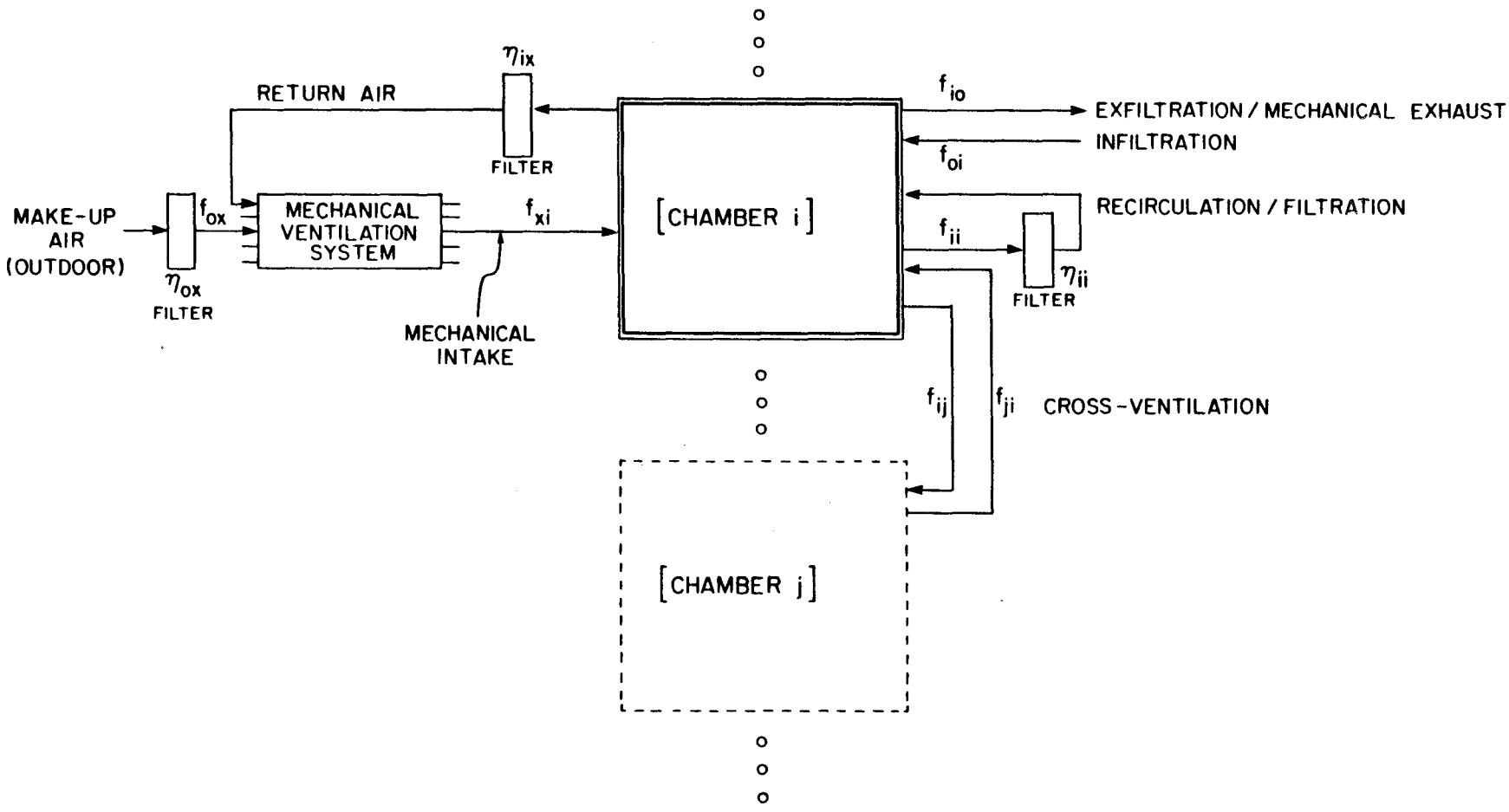

Figure 2.1 Schematic representation of the ventilation components of the multichamber indoor air quality model.

air line. Also, within each chamber, air may be recirculated through a filter. For each pollutant species, the filtration efficiency may be specified by the user.

Mathematically, if we consider a chemically inert compound, the effects of the ventilation system may be represented as follows:

$$\frac{dC_i}{dt} = \sum_{j=0}^{n} \left[\frac{f_{ji} C_j - f_{ij} C_i}{V_i}\right] + \left[\frac{f_{xi} C_x - f_{ix} C_i}{V_i}\right] - \frac{\eta_{ii} f_{ii} C_i}{V_i} \qquad (2.2)$$

and

$$C_x = \frac{\sum_{j=0}^{n} (1-\eta_{jx}) f_{jx} C_j}{\sum_{j=0}^{n} f_{xj}} \qquad (2.3)$$

where C_i = the concentration of the compound in chamber i, V_i = the volume of chamber i, f_{ij} = the volume flow rate from chamber i to chamber j, η_{ij} = the efficiency of removal of the compound by the filter located in the air stream connecting chamber i to chamber j, and subscripts x and 0 refer respectively to the mechanical ventilation system and to outdoor air. Equation (2.2) can readily be converted into the form of equation (2.1).

Ventilation data for a specific building can be obtained in several ways. Tracer gas experiments may be used to determine flow rates between pairs of chambers (Sinden, 1978). Under the uniform-mixing assumption, flow rate measurements in ventilation system ducts may be used to provide the necessary data. In buildings without mechanical ventilation systems, such as many residences, simple models may be used to predict infiltration (Sherman, 1980).

2.3.2 Chemical Kinetics. The model can be adapted to incorporate any of the kinetic mechanisms commonly employed in outdoor photochemical air quality models, and can

be modified to explicitly treat special problems occurring from the indoor emission of unusual chemical substances. For the examples illustrated in this chapter, a modified version of the Falls and Seinfeld chemical mechanism is used (Hecht and Seinfeld, 1972; Hecht et al., 1974; Falls and Seinfeld, 1978; McRae et al., 1982a; McRae and Seinfeld, 1983; Russell et al., 1985). More than 50 simultaneous chemical reactions are considered. Because the current form of the mechanism is not available in a single reference, it is presented in Table 2.1.

2.3.3 Photolysis Rates. A number of important atmospheric chemical reactions are photolytic in nature. Rates of such reactions depend on the spherically integrated photon flux, and are commonly expressed as

$$k_p = \int_0^\infty \sigma[\lambda]\ \phi[\lambda]\ I[\lambda;t]\ d\lambda \qquad (2.4)$$

where $\sigma[\lambda]$ is the absorption cross-section of the molecule (cm^2), $\phi[\lambda]$ is the quantum yield, $I[\lambda;t]$ is the photon flux density (photons $cm^{-3}\ s^{-1}$), and λ is the wavelength of light (cm).

The most accurate calculation of photolysis rates within a given building requires data on the spectral, spatial, and temporal distribution of the ambient lighting, and the model is capable of handling information provided at that level of detail. However, in many cases lighting levels indoors are so much lower than those outdoors that many otherwise important photolytic reactions proceed at small or even negligible rates. For such cases an approximate approach is provided.

Table 2.1. Kinetic mechanism (Baulch et al., 1982; McRae, 1982; McRae et al., 1982a; McRae and Seinfeld, 1983; Russell et al., 1985).

	Reaction	Rate Constant (ppm min K units)
1	$NO_2 + h\nu \rightarrow NO + O(^3P)$	a
2	$O(^3P) + O_2 + M \rightarrow O_3 + M$	$0.346\ T^{-2} \exp(510/T)$
3	$O_3 + NO \rightarrow NO_2 + O_2$	$9.245 \times 10^5\ T^{-1} \exp(-1450/T)$
4	$NO_2 + O(^3P) \rightarrow NO + O_2$	$3.99 \times 10^6\ T^{-1}$
5	$NO + O(^3P) \rightarrow NO_2$	$1.67 \times 10^5\ T^{-1} \exp(584/T)$
6	$NO_2 + O(^3P) \rightarrow NO_3$	$8.81 \times 10^5\ T^{-1}$
7	$O_3 + NO_2 \rightarrow NO_3 + O_2$	$5.19 \times 10^4\ T^{-1} \exp(-2450/T)$
8	$NO_3 + NO \rightarrow 2\ NO_2$	$8.81 \times 10^6\ T^{-1}$
9	$NO + OH \rightarrow HNO_2$	$5.07 \times 10^6\ T^{-1}$
10	$HNO_2 + h\nu \rightarrow NO + OH$	a
11	$HO_2 + NO_2 \rightarrow HNO_2 + O_2$	$17.3\ T^{-1} \exp(1006/T)$
12	$HNO_2 + OH \rightarrow H_2O + NO_2$	$2.91 \times 10^6\ T^{-1}$
13	$NO_2 + HO_2 \rightarrow HNO_4$	$1.73 \times 10^4\ T^{-1} \exp(1006/T)$
14	$HNO_4 \rightarrow HO_2 + NO_2$	$1.80 \times 10^{15} \exp(-9950/T)$
15	$HO_2 + NO \rightarrow NO_2 + OH$	$3.58 \times 10^6\ T^{-1}$
16	$RO_2 + NO \rightarrow NO_2 + RO$	$3.58 \times 10^6\ T^{-1}$
17	$RCO_3 + NO\ (+O_2) \rightarrow NO_2 + RO_2 + CO_2$	$1.13 \times 10^6\ T^{-1}$
18	$NO_2 + OH \rightarrow HNO_3$	$4.401 \times 10^{17}\ T^{-1} \times (280/T)^{1/2}\ 10^{-(11.6T/(17.4+T))}$
19	$CO + OH\ (+ O_2) \rightarrow HO_2 + CO_2$	$1.31 \times 10^5\ T^{-1}$
20	$O_3 + h\nu \rightarrow O(^3P) + O_2$	a
21	$HCHO + h\nu\ (+ 2\ O_2) \rightarrow 2\ HO_2 + CO$	a
22	$HCHO + h\nu \rightarrow H_2 + CO$	a
23	$HCHO + OH\ (+ O_2) \rightarrow HO_2 + H_2O + CO$	13890
24	$RCHO + h\nu\ (+ 2O_2) \rightarrow HO_2 + RO_2 + CO$	a
25	$RCHO + OH\ (+ O_2) \rightarrow RCO_3 + H_2O$	25680
26	$C_2H_4 + OH \rightarrow RO_2$	11660
27	$C_2H_4 + O(^3P) \rightarrow HO_2 + RO_2$	1219
28	$OLE + OH \rightarrow RO_2$	89142
29	$OLE + O(^3P) \rightarrow RO_2 + RCO_3$	22118
30	$OLE + O_3 \rightarrow 0.5\ RCHO + 0.5\ HCHO + 0.3\ HO_2 + 0.31\ RO_2 + 0.14\ OH + 0.03\ RO$	0.136

Table 2.1. (Cont.)

Reaction		Rate Constant (ppm min K units)
31	$ALK + OH \rightarrow RO_2$	4700
32	$ALK + O(^3P) \rightarrow RO_2 + OH$	99.8
33	$ARO + OH \rightarrow RO_2 + RCHO$	16112
34	$RO \rightarrow HO_2 + 0.5\ HCHO + RCHO$	2.0×10^5
35	$RONO + h\nu \rightarrow RO + NO$	a
36	$RO + NO \rightarrow RONO$	$4.38 \times 10^6\ T^{-1}$
37	$RO + NO_2 \rightarrow RNO_3$	$2.19 \times 10^6\ T^{-1}$
38	$RO + NO_2 \rightarrow RCHO + HNO_2$	$1.91 \times 10^5\ T^{-1}$
39	$NO_2 + RO_2 \rightarrow RNO_4$	$1.64 \times 10^6\ T^{-1}$
40	b	
41	$RNO_4 \rightarrow NO_2 + RO_2$	$1.80 \times 10^{15} \exp(-9950/T)$
42	$RCO_3 + NO_2 \rightarrow PAN$	$6.17 \times 10^5\ T^{-1}$
43	$PAN \rightarrow RCO_3 + NO_2$	$4.77 \times 10^{16} \exp(-12516/T)$
44	$NO_2 + NO_3 \rightarrow N_2O_5$	$7.48 \times 10^5\ T^{-1}$
45	$N_2O_5 \rightarrow NO_2 + NO_3$	$4.07 \times 10^{16} \exp(-11080/T)$
46	$H_2O + N_2O_5 \rightarrow 2\ HNO_3$	$5.66 \times 10^{-4}\ T^{-1}$
47	$O_3 + OH \rightarrow HO_2 + O_2$	$6.62 \times 10^5\ T^{-1} \exp(-1000/T)$
48	$O_3 + HO_2 \rightarrow OH + 2\ O_2$	$4.85 \times 10^3\ T^{-1} \exp(-580/T)$
49	$NO_3 + h\nu \rightarrow NO + O_2$	a
50	$HO_2 + HO_2 \rightarrow H_2O_2 + O_2$	$3.4 \times 10^4\ T^{-1} \exp(1100/T) + 5.8 \times 10^{-5}\ T^{-2} \exp(5800/T)\ [H_2O]$ [c]
51	$H_2O_2 + h\nu \rightarrow 2\ OH$	a
52	$RO_2 + RO_2 \rightarrow 2\ RO + O_2$	$2.04 \times 10^4\ T^{-1} \exp(223/T)$
53	$NO_3 + HCHO\ (+ O_2) \rightarrow HNO_3 + HO_2 + CO$	0.86
54	$NO_3 + RCHO\ (+ O_2) \rightarrow HNO_3 + RCO_3$	3.6
55	$NO_3 + h\nu \rightarrow NO_2 + O(^3P)$	a
56	$NO_3 + OLE \rightarrow RPN$ [d]	$3288\ T^{-1}$
57	$NO_2 + NO_3 \rightarrow NO_2 + NO + O_2$	$175\ T^{-1}$

[a] Rate depends on photon flux; see Table 2.2.

[b] Reaction in earlier mechanisms that was subsequently eliminated.

[c] $[H_2O]$ is water vapor concentration in ppm.

[d] Nitroxyperoxyalkyl nitrates and dinitrates, not considered to participate in further chemistry.

In the approximate case, light is treated as having two components, ultraviolet (300 - 400 nm) and visible (400 - 760 nm). Within each component, the spectral distribution is assumed to be flat. Consequently,

$$k_p = h_{uv} I_{uv} + h_{vis} I_{vis} \tag{2.5}$$

$$h_{uv} = (100\ nm)^{-1} \int_{300\ nm}^{400\ nm} \sigma \phi\, d\lambda \tag{2.6}$$

$$h_{vis} = (360\ nm)^{-1} \int_{400\ nm}^{760\ nm} \sigma \phi\, d\lambda \tag{2.7}$$

In equation (2.5), I_{uv} and I_{vis} represent the spherically integrated (spatially averaged) photon flux (photons $cm^{-2}\ s^{-1}$) in the ultraviolet and visible bands, respectively. The constants h_{uv} and h_{vis} are determined from published data (Baulch et al., 1982; McRae, 1982) and are presented in Table 2.2.

In the model, the ultraviolet and visible fluxes are each assumed to have two components, one due to artificial lighting, the other due to sunlight entering through windows or skylights. For the former, hourly values of the photon flux are specified in each band. For the latter, hourly values of ultraviolet and visible attenuation factors are specified. These factors are then applied to the outdoor photon fluxes determined using a solar simulator (McRae, 1982).

For calculations of outdoor radical concentrations, outdoor photolysis rates are required. Here, the approach of McRae (1982) is followed without modification.

Table 2.2. Coefficients used to determine photolysis rates (Baulch et al., 1982; McRae, 1982).

Reaction		h_{uv} (10^{-20} cm^2)	h_{vis} (10^{-20} cm^2)
1	$NO_2 + h\nu \rightarrow NO + O(^3P)$	39.4	0.95
10	$HNO_2 + h\nu \rightarrow NO + OH$	8.1	0
20	$O_3 + h\nu \rightarrow O(^3P) + O_2$	0.16	0.21
21	$HCHO + h\nu (+ 2\ O_2) \rightarrow 2\ HO_2 + CO$	0.58	0
22	$HCHO + h\nu \rightarrow H_2 + CO$	0.43	0
24	$RCHO + h\nu (+ 2\ O_2) \rightarrow HO_2 + RO_2 + CO$	0.56	0
35	$RONO + h\nu \rightarrow RO + NO$	8.7	0.21
49	$NO_3 + h\nu \rightarrow NO + O_2$	0	11.5
51	$H_2O_2 + h\nu \rightarrow 2\ OH$	0.13	0
55	$NO_3 + h\nu \rightarrow NO_2 + O(^3P)$	0	99.1

Data on indoor light levels sufficient to exercise the model for a specific building may be obtained with a radiometer and ultraviolet light meter (Hall, 1967; Thomson, 1967) as described in a later section of this chapter. Ultraviolet photon flux also may be inferred by measuring the photolysis rate of NO_2 (Jackson et al., 1975).

2.3.4 Treatment of Highly Reactive Species. In the indoor model calculations, the pseudo-steady state approximation (PSSA) (Seinfeld, 1986) is applied for O, OH, and RO. The PSSA is also used to determine the outdoor concentrations of these three species and of HNO_4, HO_2, NO_3, N_2O_5, RCO_3, RNO_4, and RO_2 as has been done in simulating outdoor air pollution (McRae et al., 1982b).

2.3.5 Heterogeneous Reactions. In addition to photolytic and thermal reactions occurring in the gas phase, important processes may occur on fixed surfaces such as the floor, walls and ceiling, and on or within airborne particles. Considerable evidence demonstrates that such processes have substantial impact on both outdoor (e.g., Russell et al., 1985) and indoor (e.g., Shair and Heitner, 1974) pollutant concentrations.

In previous indoor air pollution models, these processes have been lumped into a first-order decomposition rate, k_S, often assumed to take place entirely on fixed surfaces. An alternative, but nearly equivalent, formulation is in terms of deposition velocity, v_g, which is defined as the ratio of the pollutant flux to a surface, to the free-stream concentration. The rate of change of pollutant concentration due to this process alone is then given by

$$\frac{dC}{dt} = - k_S C = - v_g \frac{A}{V} C \qquad (2.8)$$

where A/V represents the superficial surface-to-volume ratio of the room.

This approach is far from ideal. Processes such as the catalytic conversion of one pollutant species to another, and adsorption followed a substantial time later by desorption, are not accommodated by this approach. Yet recent evidence suggests that NO_2 may be converted to NO on walls (Yamanaka, 1984), and that, in the presence of NO_2, nitrous acid is formed at substantial rates by heterogeneous reaction (Pitts et al., 1985a; Besemer and Nieboer, 1985). Too little is currently known to incorporate an explicit description of important surface reactions other than unimolecular decomposition and irreversible adsorption.

Measurements of heterogeneous reaction rate or deposition velocity have been reported for several species, as summarized in Table 2.3.

The loss rate depends, in general, on not only the combined reactivity of the compound and the surface, but also on the degree of air movement. Since direct evidence on surface-loss rates of some highly reactive species in the model do not exist (e.g., for HNO_3), it is appropriate that evidence pertaining to the transport-limited deposition velocity be considered.

Although seldom realized in rooms, the case of perfectly still air represents the lower bound on transport-limited deposition velocity. Here, the deposition velocity is of order 10^{-3} cm s^{-1}, determined by the molecular diffusion coefficient divided by a characteristic dimension of the room.

For rooms in which the air is not still, the analogy between heat and mass transfer can be used to obtain estimates of the transport-limited deposition velocity. Gadgil (1980) developed a model to predict the rate of heat transfer from room walls due to natural convection. In simulating a $3 \times 3 \times 3$ m enclosure with one wall maintained at 4.5 °C higher than the other surfaces, he found an average Nusselt number of 145 for the hot wall. For a compound with a diffusion coefficient of 0.2 cm^2 s^{-1}, the transport-limited deposition velocity to this wall would be 0.1 cm s^{-1}. This compares well to the deposition velocity of 0.13 cm s^{-1}, obtained by applying the von Kármán integral

Table 2.3. Measurements of indoor deposition velocity

Species	Dep. Vel. (cm s^{-1})	Notes
O_3	0.036±0.021	24 measurements in 13 buildings; one excluded due to suspected NO source (Shair and Heitner, 1974).
	0.02-0.07	inferred from measurements of ozone loss rate in a single residence (Sabersky et al., 1973).
	0.001-0.11 (New) 0.0005-0.015 (Aged)	for various materials exposed in a chamber study (Sabersky et al., 1973).
	0.027[a] (Aluminum) 0.015 (Stainless Steel) 0.036 (Office) 0.061 (Bedroom)	inferred from measurements of ozone loss rate in experimental chambers and rooms (Mueller et al., 1973).
	0.001-0.20	for various typical indoor materials exposed in a test room (Sutton et al., 1976).
NO	-0.0001±0.001	decay rate in a house of emissions from gas-fired range; assumed A/V = 2 m^{-1} (Traynor et al., 1982b).
	0.0008	decay rate in a house of emissions from gas-fired range; assumed A/V = 2 m^{-1} (Wade et al., 1975).
	0.0017±0.0014	analysis of data from gas-stove emissions experiment using simplified kinetic model; assumed A/V = 2 m^{-1} (Özkaynak et al., 1982).
	0.0000-0.003	for various indoor surface materials, measured in test chamber; 20-26 °C, 40-60% RH (Miyazaki, 1984).
NO_2	0.018±0.009	concentration decay rate from gas-stove emission experiment in test room; 11 runs; includes homogeneous reactions; assumed A/V = 2 m^{-1} (Traynor et al., 1982a).
	0.011	decay rate in a house of emissions from gas-fired range; assumed A/V = 2 m^{-1} (Wade et al., 1975).
	0.006 (50% RH) 0.011 (60% RH) 0.017 (70% RH)	analysis of decay rates from emissions due to gas- and kerosene-fired unvented heaters; attempt to exclude homogeneous reactions (Yamanaka, 1984).
	0.0003-0.12	for various indoor surface materials, measured in test chamber; 20-26 °C, 40-60% RH (Miyazaki, 1984).
HCHO	0.005±0.003	analysis of concentration decay rate from gas-stove emission experiment in test room; 5 runs; includes homogeneous reactions; assumed A/V = 2 m^{-1} (Traynor et al., 1982a).

[a] Data show strong positive correlation with relative humidity, varying from 0.0007 cm s^{-1} at 5% RH to 0.028 cm s^{-1} at 87% RH.

momentum balance to a 3-m long, vertically-oriented plate, heated to 4.5 °C above the free-stream air (Eckert and Drake, 1972). Wilson (1968) measured the relaxation time for air temperature in a suddenly cooled room. His results suggest a transport-limited deposition velocity of 0.07 cm s^{-1} for natural convection and 0.18 cm s^{-1} for stirred air, again assuming a diffusion coefficient of 0.2 cm^2 s^{-1}.

Somewhat higher values are indicated by experimental studies of the behavior of unattached decay products of radon in rooms. The deposition velocity for these species, which are believed to be removed at surfaces at the transport-limited rate, have been found to be 0.06 - 0.6 cm s^{-1}, with the consensus value of 0.2 cm s^{-1} (Knutson, 1988). The diffusion coefficient of these species is approximately 0.05 cm^2 s^{-1}, smaller than that for gaseous pollutants with lower molecular weights.

The results from Wilson and from the theoretical heat-transfer studies suggest that for circumstances in which room air is not highly stirred, the average transport-limited deposition velocity is within 50% of 0.07 cm s^{-1}. Further research is needed to resolve the discrepancy with studies of radon decay-product removal at surfaces.

2.3.6 Outdoor Concentrations. With the current chemical mechanism the model requires as input the hourly-averaged outdoor concentration of 15 species or groups of species. These data may be obtained by direct outdoor measurement or from a photochemical air quality model that describes the chemical evolution of the outdoor air over time (McRae et al., 1982a; Russell et al., 1985). For the application reported in this chapter, an approach was used, which combines outdoor monitoring data with inferences based on detailed experimental and modeling studies.

2.3.7 Initial Conditions. The initial indoor pollutant concentrations are treated in the same way as the outdoor concentrations: concentrations of fifteen species are specified and the remaining ten are computed assuming that steady-state conditions prevail. For most buildings, simulation results are relatively insensitive to changes in the initial

conditions: the limiting characteristic time associated with a perturbed initial condition is given by the inverse air-exchange rate, which in many cases is less than an hour.

2.3.8 Direct Emissions. The model accepts as input the direct indoor emission of any species other than O, OH, and RO. As currently formulated, hourly-averaged values are specified, and linear-interpolation is used to obtain the emission rate at any instant during the simulation. This rate is added directly to the source term S in equation (2.1).

2.3.9 Numerical Solution Technique. The procedure used for solving the system of coupled differential equations that constitutes the model is known as the asymptotic integration method (Young and Boris, 1977). The implementation used in the current model was slightly modified from that established by McRae et al. (1982b). The program is written in VAX-11 Fortran and is run on a VAX-11/750. A 24-hour simulation of a single chamber with an average integration time step of 10 s requires approximately 8 minutes of CPU time.

2.4 Model Application: Virginia Steele Scott Gallery

2.4.1 Introduction. Control of indoor pollutants is sought to prevent adverse health effects and to limit the rate of materials damage. Some of the most stringent standards for indoor air quality are specified for museums, archives, and rare book libraries. Since these collections must be preserved indefinitely, even very slow rates of deterioration could lead to unacceptable accumulated damage. Recommended objectives for indoor SO_2, NO_x, and O_3 concentrations in such facilities are a few parts per billion (Baer and Banks, 1985). Strong acids (e.g., HCl), organic acids (e.g., acetic acid) and formaldehyde are to be controlled to the lowest possible levels (Mathey et al., 1983).

Analytical tools are needed to predict the levels of chemically complex mixtures that will occur in new buildings prior to their construction, and to diagnose the source of pollutants present in existing facilities. Surface loss of pollutants is particularly important

in museums as it indicates the dose delivered to the collection. In this chapter, simulations are conducted of pollutant levels in a newly constructed museum, based on data taken for this purpose at the Virginia Steele Scott Gallery in San Marino, California. First, the model is exercised to verify that it correctly represents indoor pollutant levels in this building as it was constructed. Next, the effect of a series of hypothetical perturbations on that building's design are analyzed. These cases illustrate circumstances in which homogeneous chemistry in indoor air assumes added significance in determining the concentrations of photochemically reactive pollutants.

2.4.2 Description of the Site. Figure 2.2 shows a floor plan of the gallery and the ventilation flow rates, taken from the architectural plans and engineering specifications. The conditioned volume of the building is 2530 m^3 and the superficial surface area is 3060 m^2. In the gallery areas, rooms 101 and 102, which constitute 86% of the conditioned volume, the floors are oak plank, and the walls are painted plaster and plywood. The ceiling consists of plaster-veneer coffered beams and plastic diffusers. Above room 101 are skylights; fluorescent lamps behind the diffusers provide background lighting to room 102. The lighting in both rooms is supplemented by track lamps. Floor coverings in the other rooms are granite or ceramic tile, or linoleum-type flooring. Walls and ceilings are, for the most part, gypsum dry-wall.

The ventilation system is designed to maintain a temperature of 70±1 °F and a relative humidity of 50±3% in the galleries. The only pollutant removal devices in the ventilation system are strainer mat-type filters (U.L. Class 2, Farr 30/30), designed to remove coarse particulate matter. When the internal recirculation fan is on, the total air flow rate through the mechanical ventilation system is 345 $m^3\ min^{-1}$. The outdoor make-up air flow rate assumes two values: 85 $m^3\ min^{-1}$ during the day and 14 $m^3\ min^{-1}$ at night. The daytime setting was maintained from approximately 7 AM to 6 PM during the study period. In each room, supply and return registers are located on the ceiling, raising

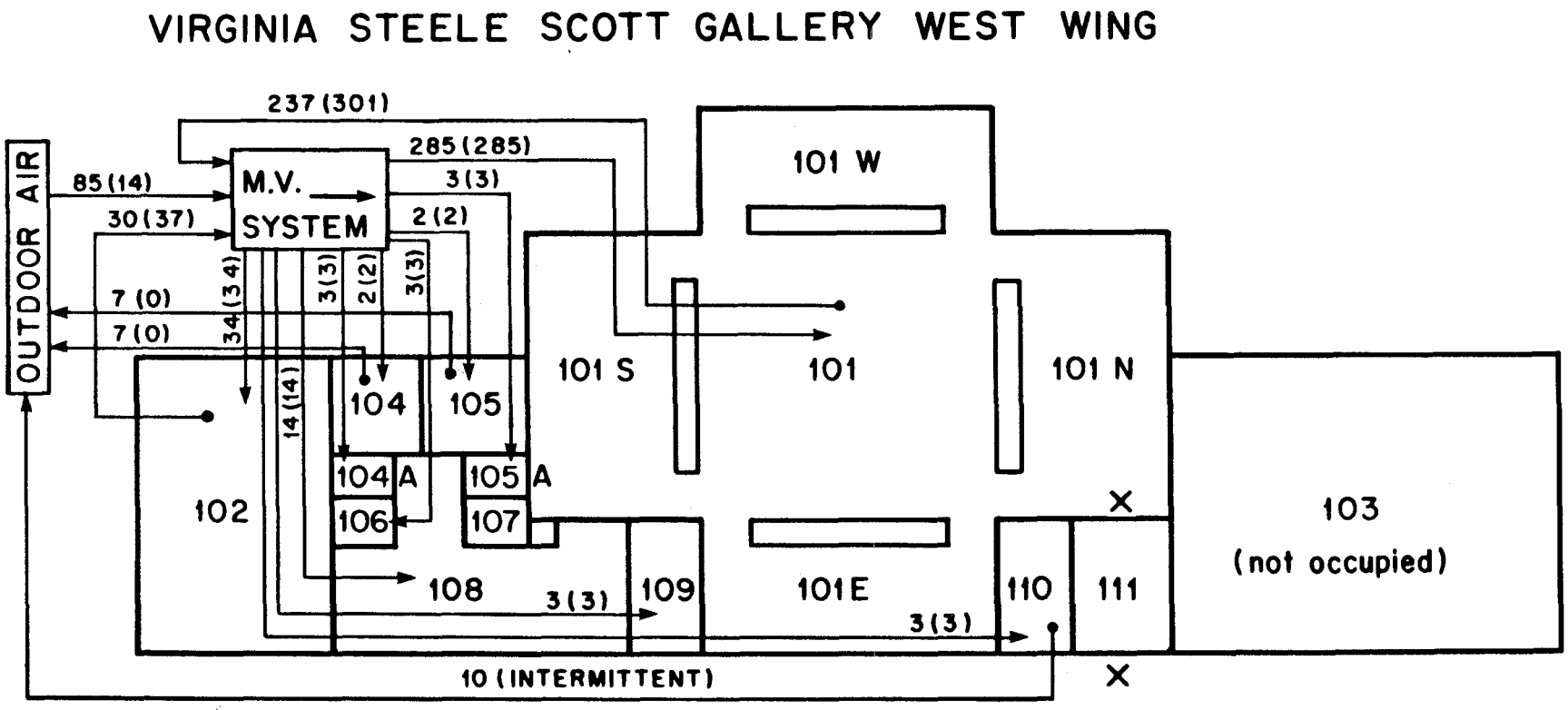

Figure 2.2 Floor plan of the west wing of the Virginia Steele Scott Gallery, San Marino, California. Daytime (nighttime) ventilation flow rates are given in units of $m^3\ min^{-1}$. Air sampling locations for the validation experiment are indicated by "x".

the possibility of ventilation "short-circuiting," which would lead to a smaller effective ventilation rate than suggested by the flow rate data. However, the relatively low outdoor-air exchange rate (0.3-2.0 h^{-1}) and the absence of rapid fluctuations in monitored pollutant concentrations, combined with the relatively large recirculation rate (8 h^{-1}), suggests that convection was sufficient to effect rapid mixing during the daytime. On the other hand, the indoor data show fluctuations in pollutant concentrations at night that could be due to incomplete mixing.

2.4.3 Monitoring Experiment. For a ten-day period beginning on October 30, 1984, O_3, NO, and NO_2 concentrations were monitored inside and outside the Scott Gallery. Ozone concentrations were measured with a pair of UV photometric ozone monitors (Dasibi models 1003-AH and 1003-PC). A pair of chemiluminescent NO_x monitors (Thermo Electron Corporation, model 14 B/E) was used to measure NO and NO_2. NO_2 values measured by this method include contributions from other nitrogen-containing species such as HNO_3 and PAN (Winer et al., 1974). The symbol NO_2* will be used to signify measurement data for this group of species, determined as NO_x-NO by the monitors. The NO_x monitors were calibrated daily against zero air and a known supply of 0.4 ppm NO in nitrogen. Data from all instruments were continuously registered on strip-chart recorders. Pollutant concentration values averaged over twelve-minute intervals throughout the experiment were extracted from the strip-chart records.

On two days during the monitoring period, November 4 and 5, peak outdoor O_3 concentrations exceeded 120 ppb in the presence of NO_x levels in excess of 200 ppb. Because of the relatively high pollution levels, model validation efforts were focused on these days.

2.4.4 Input Data for the Validation. Because of the large recirculation rate and the large fractional volume in room 101, the Scott Gallery was initially modeled as a single chamber. Ventilation rates were those indicated in the architectural specifications, as the

building had been balanced recently against those specifications. Filter efficiency was assumed to be zero for all gaseous species.

Ultraviolet and visible photon fluxes were computed from data taken both in room 101 and outdoors with a radiometer equipped with a UV cutoff filter (Eppley model PSP; filter GG 395) and a spot meter (UVC meter) designed to measure the ratio of radiance in the ultraviolet to the total illuminance (Hall, 1967; Thomson, 1967). From these measurements the skylights were estimated to transfer a photon flux equal to 0.7% of the visible light and 0.15% of the ultraviolet light falling on the roof of the building outdoors. Artificial lighting was estimated to contribute flux densities of 0.7×10^{15} and 2.3×10^{13} photons cm^{-2} s^{-1} in the visible and ultraviolet, respectively, between 9 AM and 6 PM.

For the "base case" simulation, deposition velocities reported in the literature for NO, NO_2, O_3, and HCHO have been used (see Table 2.4). Higher aldehydes were assumed to have the same surface removal characteristics as formaldehyde. Removal of highly reactive species (H_2O_2, PAN, HNO_2, RNO_2, RNO_4, HNO_3, N_2O_5, NO_3, HO_2, RO_2, HNO_4, and RCO_3) was taken to proceed at a transport-limited rate, based principally on Wilson's experiments. Other species (e.g., CO) are assumed to be sufficiently inert that their removal rates at building surfaces are negligible.

Data on outdoor concentrations of the fifteen pollutants required by the model were specified by the following approach.

The outdoor monitoring data on O_3, NO, and NO_2* collected on-site were used. Based on the results of monitoring studies (Tuazon et al., 1981; Hanst et al., 1982), outdoor HNO_3 and PAN concentrations in ppb were estimated as 10% and 5%, respectively, of the outdoor ozone concentration in ppb. The concentrations of HNO_3 and PAN were subtracted from the measured NO_x-NO concentration to correct for interference in determining the NO_2 values used in the validation study (Winer et al., 1974).

Table 2.4. Simulation input parameters

Base Case

Deposition Velocity (cm s-1):	O_3	0.036
	NO_2	0.006
	HCHO, RCHO	0.005
	PAN	0.035
	HNO_2, HNO_3, HNO_4, HO_2, H_2O_2, NO_3, N_2O_5, RCO_3, RNO_4, RONO, RO_2	0.07
	NO, ALK, ARO, CO, C_2H_4, OLE	0.0

All other input parameters discussed in text.

Low NO2 Wall Loss (WL)

Same as base case except deposition velocity for NO_2 changed to 0.0.

No Explicit Chemistry (No Chem)

Same as base case except rates of all reactions in kinetic mechanism set to 0.0.

Multichamber Case

Same as base case except building treated as four chambers:

Chamber 1 - Rooms 101, 101E, 101W, 101N, 101S
Chamber 2 - Room 102
Chamber 3 - Rooms 104, 104A, 105, 105A, 106, 107, 108, 109
Chamber 4 - Rooms 110, 111

Mechanical ventilation rates determined from architectural specifications (see Figure 2.2). Cross-ventilation flow rates taken as minimum necessary to balance air flows. Artificial lighting assumed same for each chamber. Daylighting only in chamber 1.

Indoor Hydrocarbon Source (HC Source)

Same as base case with added continuous indoor emission of hydrocarbons at following rates (ppb min^{-1}):

Alkanes - 46.7; Aromatics - 9.6; Olefins - 9.6

This corresponds approximately to evaporation of 10 cm^3 h^{-1} of gasoline (McRae, 1982) and is taken as a model either of the use of a naptha-based solvent as may occur in a preservation lab, or of the presence of an underground garage.

Indoor Oxides of Nitrogen Source (NOx Source)

Same as base case with added emission of combustion-generated pollutants during the hours 0700-1300 at following rates (ppb min^{-1})

Nitrogen dioxide - 2.5; Nitric oxide - 2.5; Carbon monoxide - 64.4; Formaldehyde - 0.6

Simulates the emissions due to gas-fired cooking equipment such as might be present in a cafeteria. Emissions data from Traynor et al. (1982a). Assumes 10 range-top burners and 5 ovens (residential sized) on continuously during 6-hour cooking period. Range hoods assumed to reduce emissions into the main volume to 40% of the total (Revzan, 1984).

Glass-Walled Building (Glass-Walled)

Changes from base case: (1) all deposition velocities reduced to 5% of base case values (based on chamber measurements of deposition rates on glass surfaces: Sabersky et al., 1973; Miyazaki, 1984); (2) indoor photolysis rates computed assuming indoor photon flux in visible range is 50% of that outdoors and that ultraviolet light is further attenuated according to the transmissivity data for window glass given in Summer (1962).

The outdoor data taken at the Scott Gallery were compared with NO, NO_x-NO, and O_3 measurements reported for the same time interval by the South Coast Air Quality Management District's (SCAQMD) monitoring station in Pasadena, located within 1.5 km of the Scott Gallery. Good agreement between these two data sets was found. Having established the close correspondence between these two monitoring sites, data for CO from the Pasadena station of the SCAQMD were used.

Hourly data on total hydrocarbons are measured by the SCAQMD at Azusa, California. These total hydrocarbon data were subdivided into formaldehyde, higher aldehydes, olefins, alkanes, aromatics and ethylene using the splitting factors determined by Russell and Cass (1986) based on detailed analysis of the composition of morning air in Los Angeles reported by Grosjean and Fung (1984).

Input data for concentrations of the remaining species in outdoor air (H_2O_2, HNO_2, and RNO_2) were determined from general experience in modeling ambient air pollution in the Los Angeles basin (A.G. Russell, Carnegie-Mellon University, personal communication, 1985). The hydrogen peroxide concentration was assumed to be 5% of the outdoor ozone concentration. Nitrous acid concentration was assumed to peak at 1.5 ppb during the hour after sunrise, falling to zero linearly over an hour on either side of the peak. The outdoor concentration of RNO_2 was assumed to be zero.

The initial indoor concentrations of NO, NO_2 and O_3 were specified based on values measured inside the Scott Gallery. For all other species, the initial concentration was computed by bringing the model to its steady state value based on the initial outdoor concentration, the air-exchange rate, the wall loss rate, and assuming no homogeneous chemical reaction. Since there are no known direct emissions of pollutants within the Scott Gallery, indoor pollutant source strengths were set to zero for the base case model calculations.

2.4.5 Perturbations of the Model Parameters. Six simulations in addition to the base case were run to examine the response of the model to changes in some of the input parameters (see Table 2.4). Three of these cases were run to examine the sensitivity of the results to assumptions about the input data. In particular, the "low NO_2 wall loss" case was run because indoor and outdoor monitoring data showed that the average total NO_x levels inside the Scott Gallery were very close to those outside. The case with "no explicit chemistry" was run to compare the predictions of previous model formulations with the present work. The "multichamber" case addresses the magnitude of errors resulting from assuming that this building may be represented as a single well-mixed chamber.

The three remaining cases were selected to examine how changes in building design or operation could influence indoor pollutant concentrations through chemical reaction. The case with an "indoor hydrocarbon source" could represent a situation in which fumes from an underground parking garage enter the building, or a case in which solvents are used within the building. The "indoor oxides of nitrogen source" considers the effect of operating combustion appliances. The "glass-walled building" case considers the effects of increased photolytic reaction rates and reduced wall loss rates associated with glass.

2.4.6 Results. A comparison of measured and simulated ozone concentrations is presented in Figure 2.3. Model results are shown for both the base case and the no-chemistry case. The full kinetic model is slightly better in predicting indoor ozone concentrations, particularly during the morning hours when the presence of a significant nitric oxide concentration constitutes a substantial sink for ozone by reaction 3. As indicated in Table 2.5, the heterogeneous wall loss rate is the dominant factor in accounting for the difference between indoor and outdoor ozone concentrations within this particular building. Chemical reaction is, however, a significant net sink.

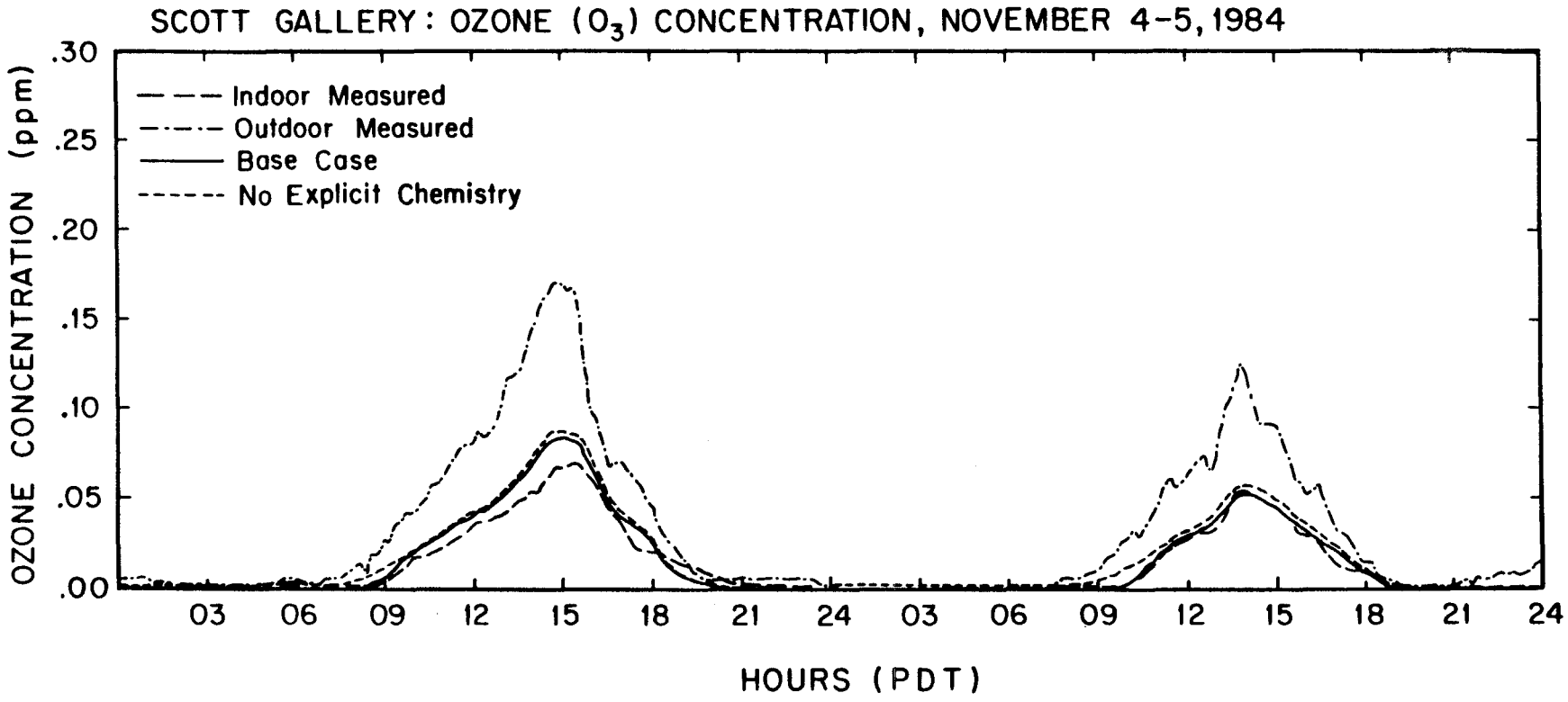

Figure 2.3 Comparison of modeled and measured ozone concentrations for a two-day period.

Table 2.5. Source and sink rates (ppb h^{-1}) in Scott Gallery for selected species and simulations: Average for November 4 and 5, 1984.

Simulation:		Base Case		HC Source		NOx Source		Glass-Walled	
Species	Process	Source	Sink	Source	Sink	Source	Sink	Source	Sink
NO	Ventilation	17.6	15.0	17.6	8.6	17.6	36.2	17.6	16.6
	Chemical Rxn	1.6	5.7	1.4	11.8	3.4	24.1	129	131
	Emission	0		0		38		0	
	Wall Loss		0		0		0		0
NO_2	Ventilation	69	58	69	54	69	99	69	67
	Chemical Rxn	172	172	666	666	154	136	418	418
	Emission	0		0		38		0	
	Wall Loss		12		13		19		1
O_3	Ventilation	58	29	58	20	58	21	58	65
	Chemical Rxn	2	8	1	25	3	23	131	123
	Emission	0		0		0		0	
	Wall Loss		23		15		17		3
HNO_2	Ventilation	0.029	0.025	0.029	0.064	0.029	0.046	0.029	0.134
	Chemical Rxn	0.051	0.0001	0.161	0.0004	0.104	0.0003	0.175	0.049
	Emission	0		0		0		0	
	Wall Loss		0.055		0.125		0.086		0.019
HNO_3	Ventilation	5.8	2.6	5.8	2.4	5.8	2.7	5.8	7.4
	Chemical Rxn	0.8	0	0.4	0	1.1	0	2.4	0
	Emission	0		0		0		0	
	Wall Loss		4.1		3.8		4.3		0.8
NO_3	Ventilation	0.007	0.008	0.007	0.004	0.007	0.005	0.007	0.007
	Chemical Rxn	29.6	29.6	12.8	12.8	24.7	24.7	43.1	43.1
	Emission	0		0		0		0	
	Wall Loss		0.013		0.007		0.009		0.001
N_2O_5	Ventilation	0.4	0.5	0.4	0.2	0.4	0.4	0.4	0.5
	Chemical Rxn	29.1	28.1	12.2	12.1	23.8	23.1	38.8	38.6
	Emission	0		0		0		0	
	Wall Loss		0.8		0.4		0.7		0.1
PAN	Ventilation	2.9	1.6	2.9	1.7	2.9	1.6	2.9	3.4
	Chemical Rxn	0.8	0.8	0.9	0.8	0.8	0.8	2.6	1.9
	Emission	0		0		0		0	
	Wall Loss		1.3		1.3		1.3		0.1
HCHO	Ventilation	14.3	13.1	14.3	23.9	14.3	21.2	14.3	18.1
	Chemical Rxn	1.0	0.03	13.7	0.06	1.1	0.1	4.3	0.5
	Emission	0		0		8.9		0	
	Wall Loss		2.2		4.0		3.1		0.2
RCHO	Ventilation	12.8	12.0	12.8	25.6	12.8	12.7	12.8	20.6
	Chemical Rxn	1.3	0.05	17.5	0.1	2.0	0.1	8.8	0.9
	Emission	0		0		0		0	
	Wall Loss		2.0		4.5		2.1		0.2
H_2O_2	Ventilation	2.9	1.2	2.9	2.0	2.9	1.1	2.9	2.9
	Chemical Rxn	0.1	0.0001	2.2	0.0002	0.1	0.0001	0.2	0.003
	Emission	0		0		0		0	
	Wall Loss		1.9		3.1		1.8		0.2

Comparisons between measurements and simulations for oxides of nitrogen are presented in Figure 2.4. At most times the measured NO_x and NO_2* concentrations are seen to lie between the results for the base case and "low NO_2 wall loss" simulations. The nitric oxide concentration, on the other hand, is underpredicted at most times by both simulations, supporting Yamanaka's inference that NO_2 is converted to NO at indoor surfaces (Yamanaka, 1984). The "low NO_2 wall loss" case predicts a total NO_x concentration that is closer to the measured value (5% high) than is the result for the base case simulation (14% low).

Tables 2.5 and 2.6 summarize the simulation results, giving average source and sink rates and average concentrations, respectively. Figure 2.5 presents average concentrations for selected species. Several of the findings are noteworthy.

Comparing the average concentrations for the base case and no chemistry simulations, we see that several nitrogen-containing species—HNO_2, HNO_3, HNO_4, NO_3, and N_2O_5—are produced at substantial net rates by chemical reaction indoors. For the latter two species, indoor concentrations exceed those outdoors. In a conventionally-lit building, formation of these species may occur indoors during the day by reaction pathways normally associated with nighttime chemistry outdoors (Russell et al., 1985). N_2O_5 recently has been implicated in the production of mutagenic compounds in outdoor air (Pitts et al., 1985b); the possibility that N_2O_5 is present at elevated levels indoors should be further studied.

Pitts et al. (1985a) experimentally demonstrated the production of nitrous acid in an indoor environment with elevated levels of NO_2, and inferred from their data a steady-state average ratio of HNO_2 to NO_2 of 15×10^{-3}. The base case indoor simulation also indicates that HNO_2 is formed indoors, but the HNO_2 to NO_2 ratio due to homogeneous gas-phase chemistry alone is lower, 0.4×10^{-3}. This discrepancy supports the hypothesis

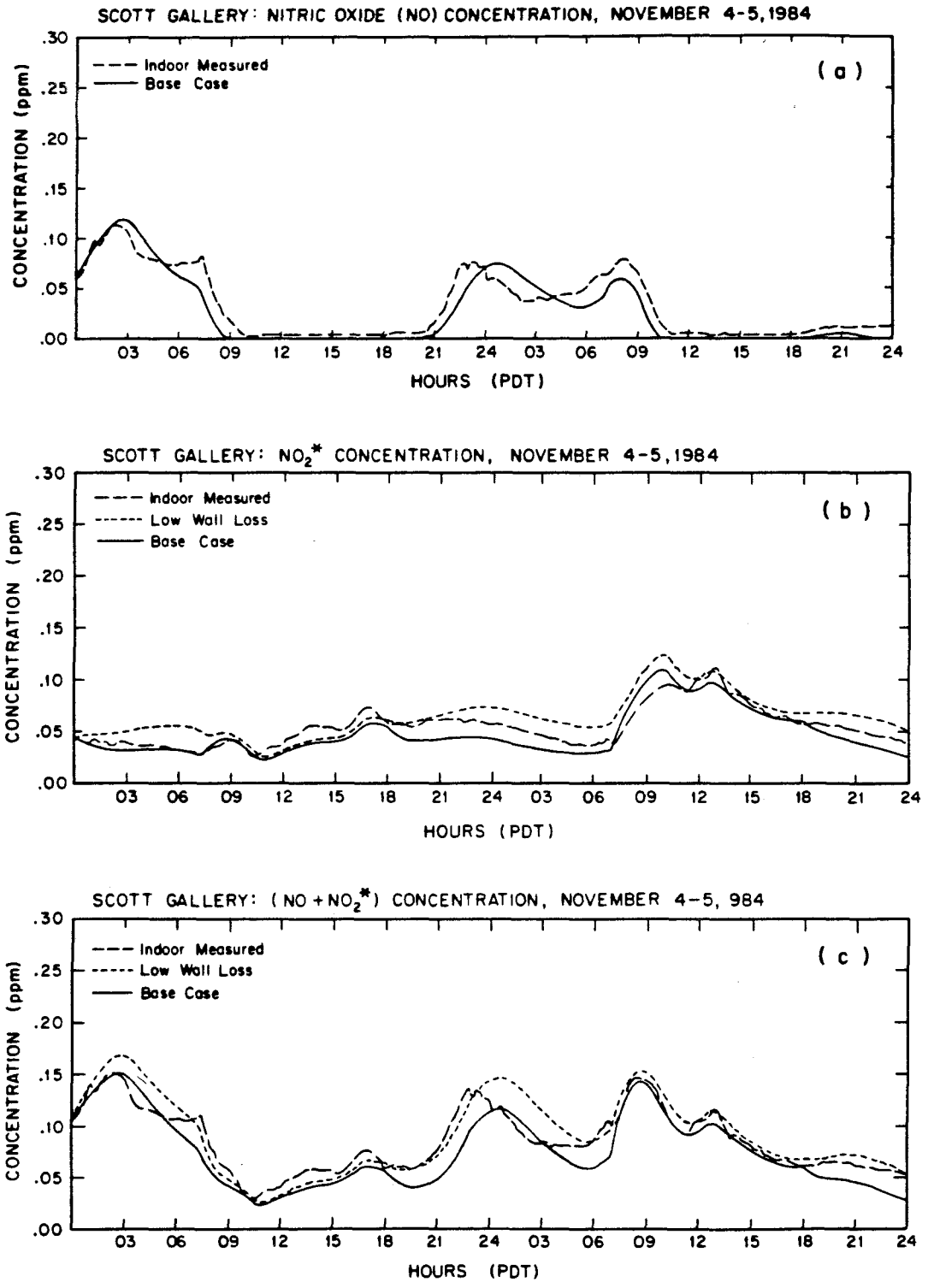

Figure 2.4 Comparison of modeled and measured concentrations of (a) nitric oxide, (b) nitrogen dioxide (NO_2^*, measured as NO_x - NO), and (c) total oxides of nitrogen for a two-day period. In the case of nitric oxide, the "base case" and "low (NO_2) wall loss" simulations produce essentially equivalent results.

Table 2.6. Species concentrations (ppb) in Scott Gallery: Average for November 4 and 5, 1984

	Outdoor:	Indoor:	Indoor Simulations						
Spec.	Meas/Sim.[a]	Meas.	Base Case	Low NO_2 WL	No Chem	Multichamber[b]	HC Source	NOx Source	Glass–Walled
NO	31.8	32.3	27.2	27.5	30.7	27.2	15.2	38.1	26.0
NO_2	59.8 [c]	52.4 [c]	45.9	61.6	45.0	46.5	48.5	70.4	61.0
O_3	31.2	14.0	15.1	14.9	16.8	15.5	9.8	11.1	34.1
HNO_2	0.063		0.018	0.018	0.007	0.019	0.041	0.028	0.124
HNO_3	3.12		1.35	1.36	1.17	1.43	1.25	1.39	4.96
HNO_4	0.343		0.176	0.181	0.133	0.184	0.646	0.135	0.304
NO_3	0.0035		0.0042	0.0041	0.0014	0.0044	0.0022	0.0029	0.0046
N_2O_5	0.181		0.258	0.285	0.072	0.277	0.110	0.211	0.350
PAN	1.56		0.86	0.86	0.85	0.89	0.87	0.85	1.96
RNO_4	0.87		0.44	0.44	0.34	0.47	2.21	0.34	0.78
RONO	0.0		0.00007	0.00006	0.0	0.00007	0.00205	0.00043	0.00107
HCHO	13.2		10.3	10.3	9.8	10.4	18.3	14.5	15.1
RCHO	11.7		9.5	9.5	8.8	9.6	21.0	9.8	16.3
HO_2	0.0151		0.0079	0.0072	0.0060	0.0082	0.0400	0.0049	0.0123
H_2O_2	1.56		0.61	0.60	0.59	0.64	1.02	0.59	1.69
O	1.31 E-06		6.21 E-09	6.92 E-09	0.0	6.24 E-09	5.10 E-09	12.0 E-09	4.62 E-07
OH	2.80 E-03		0.22 E-05	0.21 E-05	0.0	0.23 E-05	0.22 E-05	0.40 E-05	2.41 E-05
RCO_3	0.00042		0.00017	0.00015	0.00016	0.00018	0.00030	0.00011	0.00043
RO	6.03 E-07		0.37 E-07	0.35 E-07	0.0	0.38 E-07	4.62 E-07	1.08 E-07	5.10 E-07
RO_2	0.0146		0.0071	0.0063	0.0058	0.0074	0.0584	0.0044	0.0104

[a] Outdoor average concentrations for species not listed: ALK - 241 ppb, ARO - 63 ppb, CO - 3.04 ppm, C_2H_4 - 22 ppb, OLE - 15 ppb.

[b] Volume-weighted average for four chambers.

[c] Quantitative interference from HNO_3 and PAN assumed and subtracted from measured NO_x-NO. For indoor value, results from base case simulation used.

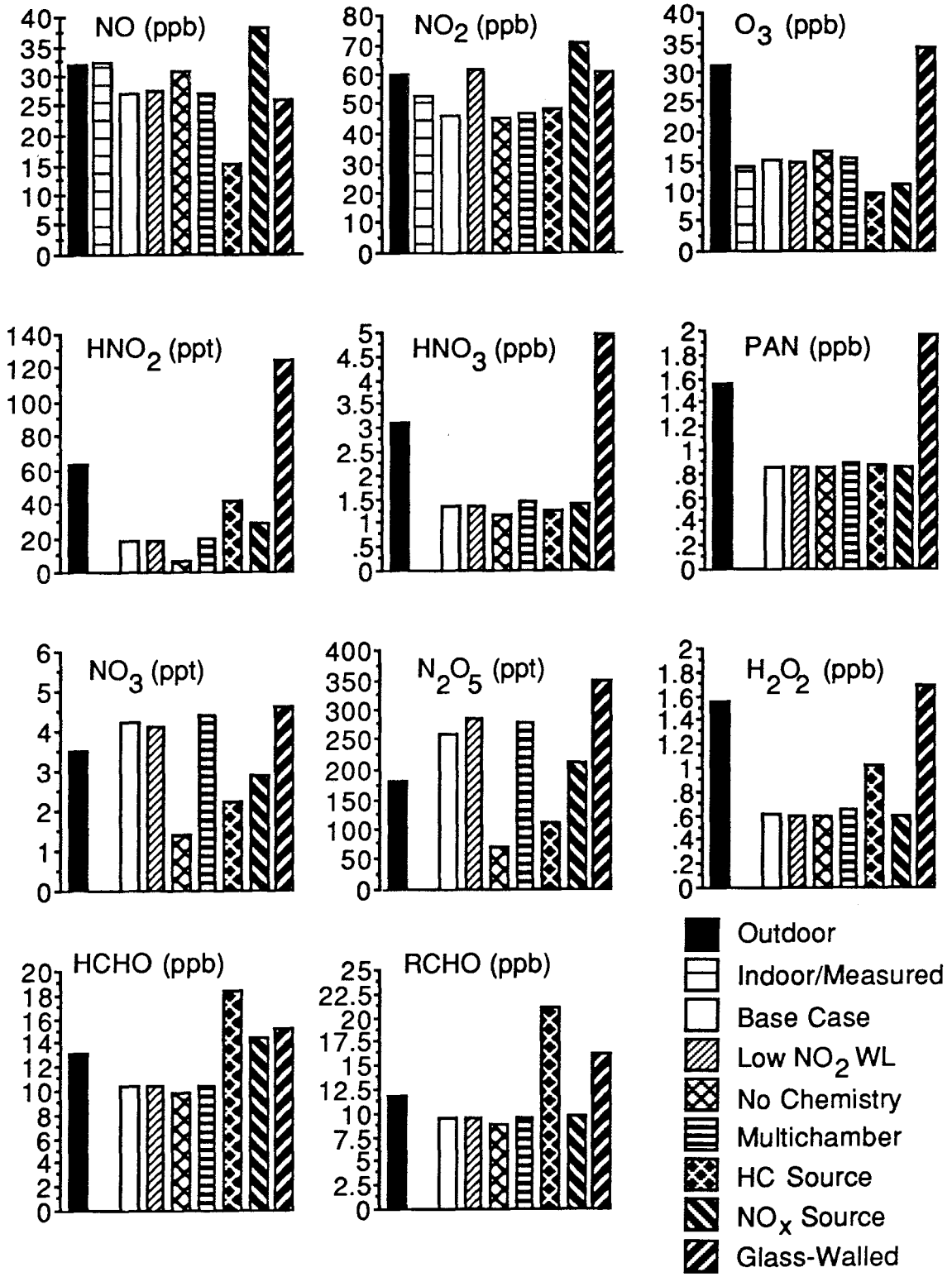

Figure 2.5 Average measured and modeled pollutant concentrations for the Scott Gallery, November 4-5, 1984.

that heterogeneous reactions (e.g., on building surfaces) may play an important role in nitrous acid production.

Information on the flux of reactive species to interior surfaces may be useful in assessing the potential for damage to materials displayed in museums. Under the assumptions of the base case simulation, the average fluxes of O_3 and HNO_3 to the walls during this two-day period were 38.4 and 8.8 $\mu g\ m^{-2}\ h^{-1}$, respectively.

The results of the multichamber simulation indicate that the treatment of this building as a single chamber is a reasonable approximation. Concentration variations among chambers are approximately 10% or less, due to the relatively high rate of recirculation through the mechanical ventilation system.

The two cases for which an indoor pollutant source is postulated show that such sources may either increase or decrease the concentration of species not directly emitted. For example, the hydrocarbon source leads to substantial reduction in the indoor concentration of O_3 and NO, but markedly increased concentrations of HNO_2, HNO_4, HCHO, and H_2O_2, among others. The indoor combustion source likewise leads to a consumption of O_3, but increased production of HNO_2 and HNO_3.

In the case of the glass-walled building, indoor concentrations of several key species—including O_3, HNO_2, HNO_3, PAN, and H_2O_2—are increased markedly over the base case values, and in fact are seen to exceed the outdoor levels. In this case, homogeneous chemical reactions are greatly enhanced by the combined effects of increased lighting (leading to higher photolysis rates), and reduced wall loss (leading to higher concentrations of reactive species).

2.5 Discussion

The results of this study indicate the importance of homogeneous chemistry as a pollutant transformation process in indoor atmospheres. Concentrations of many species (e.g., O_3) are significantly perturbed by chemical reaction, especially when outdoor air

pollutants are combined with direct indoor emissions. For other species (e.g., N_2O_5) an accounting of the effect of homogeneous chemical reactions is essential because the rates of chemical production in indoor air dominate other source terms.

The results of the present work—the reasonable agreement between measured and simulated pollutant concentrations, and the minor effect of treating the Scott Gallery as a four-chamber rather than a one-chamber building—indicate that the assumption that each chamber in the model is well-mixed did not interfere with obtaining accurate results. Additional work to relax the uniform mixing hypothesis is warranted. Efforts to determine the rates of mixing in indoor air and to examine the effect of poor mixing on the apparent rates of chemical reaction are recommended. One approach to relaxing the uniform-mixing assumption is to use the atmospheric diffusion equation (Seinfeld, 1986) in place of equation (2.1) to describe the time-rate-of-change of pollutant concentrations. To solve the problem using this approach, one requires information on localized indoor air velocities and eddy diffusivities. The basis for describing indoor air motion is partially established in numerical codes for natural convection in enclosures (Gadgil, 1980). A model that employs an explicit description of air motion at scales smaller than the dimension of the rooms would be considerably more difficult to validate and costly to apply than the present approach. Nevertheless, it could prove quite useful in examining the validity of the uniformly mixed model, and in treating the mass-transport aspects of surface reaction on a more fundamental basis.

The present model is also restricted in the scope of the transformation processes considered. The explicit description is limited to gaseous pollutants and gas-phase chemistry. The approach taken to account for pollutant interactions at fixed surfaces is a simplified one and possible interactions of gaseous pollutants with suspended particulate matter are not considered at all. The results reported here indicate that deposition on walls is a dominant route for removal of highly reactive pollutants (see Table 2.5). Also, as discussed above, there are indications that nitrogen-containing species may be

chemically transformed rather than simply removed at surfaces. Further research is needed to improve the understanding of these heterogeneous processes. Such work should include carefully designed experiments that account for both mass transport and surface-reaction kinetics.

The model as presently formulated has a number of important applications in addition to those discussed in this chapter. It may be used to assess the effects of filtration of selected compounds, to design indoor air quality control strategies based on ventilation scheduling, and to simulate specialized cases where unusual chemicals are present in an industrial setting. The model is formulated to be a general tool for studying chemically reactive air pollution systems. Within limits, one can specify an arbitrary chemical mechanism, modify the computer code in a straightforward manner, and simulate an indoor environment in which homogeneous chemical reactions play an important role in determining pollutant concentrations.

2.6 Acknowledgements

Discussions with Dr. A.G. Russell provided insight on several aspects of the related problem of modeling outdoor air quality. The research was supported by a contract with the Getty Conservation Institute and by an Earle C. Anthony Graduate Fellowship.

2.7 References

Baer, N. S., and Banks, P. N. (1985) Indoor air pollution: Effects on cultural and historic materials, *International Journal of Museum Management and Curatorship* **4**, 9-20.

Baulch, D. L., Cox, R. A., Crutzen, P. J., Hampson, R. F. , Jr., Kerr, J. A., Troe, J., and Watson, R. T. (1982) Evaluated kinetic and photochemical data for atmospheric chemistry: Supplement 1, *Journal of Physical and Chemical Reference Data* **11**, 327-496.

Berglund, B., Lindvall, T., and Sundell, J. , Eds. (1984) *Indoor Air*, Swedish Council for Building Research: Stockholm, 5 vol.

Besemer, A. C., and Nieboer, H. (1985) The wall as a source of hydroxyl radicals in smog chambers, *Atmospheric Environment* **19**, 507-513.

Davidson, C. I., Osborn, J. F., and Fortmann, R. C. (1984) Modeling and measurement of pollutants inside houses in Pittsburgh, Pennsylvania, In *Indoor Air: Chemical Characterization and Personal Exposure*, Berglund, B., Lindvall, T., Sundell, J. , Eds., Swedish Council for Building Research: Stockholm, Vol. 4, pp. 69-74.

Eckert, E. R. G., and Drake, R. M. , Jr. (1972) *Analysis of Heat and Mass Transfer*, McGraw-Hill: New York, p. 528.

Falls, A. H., and Seinfeld, J. H. (1978) Continued development of a kinetic mechanism for photochemical smog, *Environmental Science and Technology* **12**, 1398-1406.

Fisk, W. J. (1984) Ventilation for control of indoor air quality, In *Indoor Air: Buildings Ventilation and Thermal Climate*, Berglund, B., Lindvall, T., Sundell, J. , Eds., Swedish Council for Building Research: Stockholm, Vol. 5, pp. 187-192.

Gadgil, A. J. (1980) *On Convective Heat Transfer in Building Energy Analysis*, Ph. D. Thesis, University of California, Berkeley, California.

Grosjean, D., and Fung, K. (1984) Hydrocarbons and carbonyls in Los Angeles air, *Journal of the Air Pollution Control Association* **34**, 537-543.

Hall, E. T. (1967) Design of a UV light meter, In *London Conference on Museum Climatology*, International Institute for Conservation: London, pp 151-157.

Hanst, P. L., Wong, N. W., and Bragin, J. (1982) A long-path infra-red study of Los Angeles smog, *Atmospheric Environment* **16**, 969-981.

Hecht, T. A., and Seinfeld, J. H. (1972) Development and validation of a generalized mechanism for photochemical smog, *Environmental Science and Technology* **6**, 47-57.

Hecht, T. A., Seinfeld, J. H., and Dodge, M. C. (1974) Further development of generalized kinetic mechanism for photochemical smog, *Environmental Science and Technology* **8**, 327-339.

Hernandez, T. L., and Ring, J. W. (1982) Indoor radon source fluxes: Experimental tests of a two-chamber model, *Environment International* **8**, 45-57.

Jackson, J. O., Stedman, D. H., Smith, R. G., Hecker, L. H., and Warner, P. O. (1975) Direct NO_2 photolysis rate monitor, *Review of Scientific Instruments* **46**, 376-378.

Knutson, E. O. (1988) Modeling indoor concentrations of radon's decay products, In *Radon and Its Decay Products in Indoor Air* , Nazaroff, W. W., and Nero, A. V. , Eds., Wiley: New York, Chapter 5.

Mathey, R. G., Faison, T. K., Silberstein, S., Woods, J. E., Johnson, W. B., Lull, W. P., Madson, C. A., Turk, A., Westlin, K. L., and Banks, P. N. (1983) *Air Quality Criteria for Storage of Paper-Based Archival Records*, National Bureau of Standards: Washington, D. C. , NBSIR 83-2795.

McRae, G. J. (1982) *Mathematical Modeling of Photochemical Air Pollution*, Ph. D. Thesis, California Institute of Technology, Pasadena, California.

McRae, G. J., Goodin, W. R., Seinfeld, J. H. (1982a) Development of a second-generation mathematical model for urban air pollution—I. Model formulation, *Atmospheric Environment* **16**, 679-696.

McRae, G. J., Goodin, W. R., and Seinfeld, J. H. (1982b) Numerical solution of the atmospheric diffusion equation for chemically reacting flows, *Journal of Computational Physics* **45**, 1-42.

McRae, G. J., and Seinfeld, J. H. (1983) Development of a second-generation mathematical model for urban air pollution—II. Evaluation of model performance, *Atmospheric Environment* **17**, 501-522.

Miyazaki, T. (1984) Adsorption characteristics of NOx by several kinds of interior materials, In *Indoor Air: Chemical Characterization and Personal Exposure*,

Berglund, B., Lindvall, T., Sundell, J. , Eds., Swedish Council for Building Research: Stockholm, Vol. 4, pp. 103-110.

Mueller, F. X., Loeb, L., and Mapes, W. H. (1973) Decomposition rates of ozone in living areas, *Environmental Science and Technology* **7**, 342-346.

Özkaynak, H., Ryan, P. B., Allen, G. A., and Turner, W. A. (1982) Indoor air quality modeling: Compartmental approach with reactive chemistry, *Environment International* **8**, 461-471.

Pitts, J. N. , Jr., Wallington, T. J., Biermann, H. W., and Winer, A. M. (1985a) Identification and measurement of nitrous acid in an indoor environment, *Atmospheric Environment* **19**, 763-767.

Pitts, J. N. , Jr., Sweetman, J. A., Zielinska, B., Atkinson, R., Winer, A. M., and Harger, W. P. (1985b) Formation of nitroarenes from the reaction of polycyclic aromatic hydrocarbons with dinitrogen pentoxide, *Environmental Science and Technology* **19**, 1115-1121.

Revzan, K. L. (1984) Effectiveness of local ventilation in removing simulated pollution from point sources, in *Indoor Air: Building Ventilation and Thermal Climate*, Berglund, B., Lindvall, T., Sundell, J. , Eds., Swedish Council for Building Research: Stockholm, Vol. 5, pp. 65-72.

Ruff, R. E., Nitz, K. C., Ludwig, F. L., Bhumralkar, C. M., Shannon, J. D., Sheih, C. M., Lee, I. Y., Kumar, R., and McNaughton, D. J. (1985) Evaluation of three regional air quality models, *Atmospheric Environment* **19**, 1103-1115.

Russell, A. G., McRae, G. J., and Cass, G. R. (1985) The dynamics of nitric acid production and the fate of nitrogen oxides, *Atmospheric Environment* **19**, 893-903.

Russell, A. G., and Cass, G. R. (1986) Verification of a mathematical model for aerosol nitrate and nitric acid formation and its use for control measure evaluation, *Atmospheric Environment* **20**, 2011-2025.

Sabersky, R. H., Sinema, D. A., and Shair, F. H. (1973) Concentrations, decay rates and removal of ozone and their relation to establishing clean indoor air, *Environmental Science and Technology* **7**, 347-353.

Schiller, G. E. (1984) *A Theoretical Convective-Transport Model of Indoor Radon Decay Products*, Ph. D. Thesis, University of California, Berkeley, California.

Seinfeld, J. H. (1986) *Atmospheric Chemistry and Physics of Air Pollution*, Wiley: New York.

Shair, F. H., and Heitner, K. L. (1974) Theoretical model for relating indoor pollutant concentrations to those outside, *Environmental Science and Technology* **8**, 444-451.

Shair, F. H. (1981) Relating indoor pollutant concentrations of ozone and sulfur dioxide to those outside: Economic reduction of indoor ozone through selective filtration of the makeup air, *ASHRAE Transactions* **87 (Part I)**, 116-139.

Sherman, M. H. (1980) *Air Infiltration in Buildings*, Ph. D. Thesis, University of California, Berkeley, California.

Sinden, F. W. (1978) Multichamber theory of air infiltration, *Building and Environment* **13**, 21-28.

Summer, W. (1962) *Ultraviolet and Infra-Red Engineering*, Interscience Publishers: New York, p. 60.

Sutton, D. J., Nodolf, K. M., and Makino, K. K. (1976) Predicting ozone concentrations in residential structures, *ASHRAE Journal* **18(9)**, 21-26.

Thomson, G. (1967) Calibration and use of a UV monitor, In *London Conference on Museum Climatology*, International Institute for Conservation: London.

Traynor, G. W., Anthon, D. W., Hollowell, C. D. (1982a) Technique for determining pollutant emissions from a gas-fired range, *Atmospheric Environment* **16**, 2979-2987.

Traynor, G. W., Apte, M. G., Dillworth, J. F., Hollowell, C. D., and Sterling, E. M. (1982b) The effects of ventilation on residential air pollution due to emissions from a gas-fired range, *Environment International* **8**, 447-452.

Tuazon, E. C., Winer, A. M., and Pitts, J. N. , Jr. (1981) Trace pollutant concentrations in a multiday smog episode in the California South Coast Air Basin by long path length Fourier transform infrared spectroscopy, *Environmental Science and Technology* **15**, 1232-1237.

Wade, W. A. , III; Cote, W. A., and Yocum, J. E. (1975) A study of indoor air quality, *Journal of the Air Pollution Control Association* **25**, 933-939.

Wilson, M. J. G. , Indoor air pollution (1968) *Proceedings of the Royal Society (London)* **A307**, 215-221.

Winer, A. M., Peters, J. W., Smith, J. P., and Pitts, J. N., Jr. (1974) Response of commercial chemiluminescent NO-NO_2 analyzers to other nitrogen-containing compounds, *Environmental Science and Technology* **8**, 1118-1121.

Yamanaka, S. (1984) Decay rates of nitrogen dioxide in a typical Japanese living room, *Environmental Science and Technology* **18**, 566-570.

Young, T. R., and Boris, J. P. (1977) A numerical technique for solving stiff ordinary differential equations associated with the chemical kinetics of reactive-flow problems, *Journal of Physical Chemistry* **81**, 2424-2427.

CHAPTER 3

PARTICLE DEPOSITION FROM A NATURAL CONVECTION FLOW ONTO A VERTICAL ISOTHERMAL FLAT PLATE

3.1 Abstract

The deposition of particles from a laminar, natural convection boundary layer flow adjacent to a heated or cooled flat plate occurs due to a combination of thermophoretic drift and Brownian motion. In this chapter, scale analysis is used to determine the magnitudes of the concentration boundary layer thickness and the normalized particle flux. Scaling arguments are also used to show that thermophoresis dominates Brownian motion in the concentration boundary layer whenever $Le^{1/3} > (T_\infty / | \Delta T |)^{1/2}$, where Le is the Lewis number of the particle and ΔT is the difference between the temperature of the plate surface and that of the air outside the momentum boundary layer (T_∞). Using a similarity transformation, the governing partial differential equations are converted to a system of ordinary differential equations that are solved numerically. Dimensionless particle flux is determined as a function of particle diameter in the range 0.001-3.0 μm and ΔT from -10 to 10 K. The results have application in understanding and preventing the soiling of indoor surfaces, including works of art.

Nazaroff, W. W., and Cass, G. R. (1987) Particle deposition from a natural convection flow onto a vertical isothermal flat plate, *Journal of Aerosol Science* **18**, 445-455.

3.2 Introduction

The soiling of indoor surfaces due to the deposition of airborne particulate matter is a commonly observed phenomenon. Of particular concern is the potential for damage to paintings and other works of art. The aesthetic quality of such materials certainly would be deteriorated by an accumulated deposit of airborne particles. In addition, the useful lifetime of these objects may be limited to a small number of restorations, the frequency of which is determined, at least in part, by the rate of aerosol deposition.

In this context, the problem of relating the rate of deterioration of the visual quality of an object to the nature of its environment has two major components. One addresses the transport of particles from air to the surface; the other considers the interaction of the deposited particulate matter with the visual information transmitted from the object to the observer. The focus of the present work is the former problem.

Fluid circulation patterns in rooms are commonly driven by natural convection. Although many researchers have investigated the deposition of particles on surfaces, none have addressed the theoretical aspects of particle deposition onto a vertical isothermal surface in a natural convection flow. The combined effects of turbulence, Brownian motion, and gravitational settling on particle deposition in enclosures have been investigated theoretically (Corner and Pendlebury, 1951; Crump and Seinfeld, 1981) and experimentally (Crump et al., 1983; Okuyama et al., 1986). That work has recently been expanded to account for the effects of electrostatic forces, of particular interest for experiments conducted in Teflon-film smog chambers (McMurry and Grosjean, 1985; McMurry and Rader, 1985). The particle loss rate due to deposition on chamber surfaces under natural convection flow conditions has been investigated experimentally (Harrison, 1979). The surface accumulations of ionic substances have been related to indoor concentrations to determine the rates of particle deposition in a room (Sinclair et al., 1985). The deposition loss rate has also been studied experimentally (Scott, 1983;

Toohey et al., 1984) and theoretically (Schiller, 1984) for unattached radon decay products, which are believed to exist as very small particles with effective diameters in the range 0.001 to 0.01 μm. The influence of thermophoresis on particle migration near surfaces has also been investigated (Watson, 1936; Zernik, 1957; Goren, 1977; Talbot et al., 1980; Batchelor and Shen, 1985).

The definitive solution to the problem of heat and momentum transport to a vertical isothermal plate in a natural convection flow was reported by Ostrach (1953). Because of the analogy between heat and mass transfer, the extension of this solution to the deposition of highly reactive dilute gases is straightforward. However, for particles, because transport is influenced by factors in addition to advection and Brownian motion, the analogy does not hold. It shall be shown that, in particular, thermophoresis plays an important role in the migration of particles in the natural convection boundary layer, and must be incorporated into the description of particle deposition onto vertical surfaces.

In this chapter the rate of deposition of particles onto a surface is analyzed for the case of a semi-infinite, flat, vertical isothermal plate. By assumption, fluid extends without bound from one side of the plate. Outside a thin laminar boundary layer adjacent to the plate, the fluid has uniform temperature and is motionless. Scaling arguments are used first to simplify the governing transport equations, second to determine the conditions under which thermophoresis dominates Brownian motion in the concentration boundary layer, and third to determine the magnitude of the normalized particle flux onto the plate. A similarity transformation is used to convert the simplified partial differential equations to a set of ordinary differential equations that are then solved numerically. Application of the results to particle deposition onto vertical indoor surfaces is considered. Although only the case of air at ordinary environmental temperatures is considered explicitly, the calculation approach is suitable for analysis of particle deposition from a much broader class of fluids.

3.3 Analysis

3.3.1 Governing Equations. This problem is described by a system of partial differential equations accounting for the conservation of mass, momentum, energy, and particle concentration within a differential fluid element. For a monodisperse suspension of particles under steady-state conditions these equations are

$$\nabla \cdot \mathbf{u} = 0 \tag{3.1}$$

$$\mathbf{u} \cdot \nabla \mathbf{u} = - \beta (T-T_\infty) \mathbf{g} + \nu \nabla^2 \mathbf{u} \tag{3.2}$$

$$\mathbf{u} \cdot \nabla T = \alpha \nabla^2 T \tag{3.3}$$

$$\mathbf{u} \cdot \nabla n = D \nabla^2 n - \nabla \cdot \mathbf{f} n \tag{3.4}$$

where $\mathbf{u}$ is the fluid velocity vector, β is the coefficient of thermal expansion for the fluid ($\beta = T_\infty^{-1}$ for an ideal gas), T is the fluid temperature and T_∞ is the reference fluid temperature (i.e., the temperature outside the boundary layer), $\mathbf{g}$ is the gravitational acceleration vector, ν and α are the kinematic viscosity and thermal diffusivity of the fluid, respectively, n is the concentration of particles, D is the coefficient of Brownian diffusivity of the particles, and $\mathbf{f}$ is the velocity of the particles relative to the fluid, in particular due to gravitational settling and thermophoresis. These equations already incorporate several simplifications. Air is treated as a Newtonian fluid with constant kinematic viscosity and thermal diffusivity. The Boussinesq approximation is employed, meaning that air is considered to be incompressible, except in the body force term in the momentum equation. Heat generation due, for example, to viscous effects is neglected. Particle diffusivity is assumed to be constant, and, except for removal at the wall, the number of particles is conserved. The latter condition means that, among other things,

the concentration is dilute enough that particle coagulation in the boundary layer can be ignored. A comparison of time constants for transport in the boundary layer and for coagulation shows that this is valid for almost all indoor environments.

It is useful at this point to specify a coordinate system. The origin is taken to be at the leading corner of the plate. The x-coordinate is vertical, measuring the distance along the plate; the y-coordinate measures the horizontal distance from the plate. The velocity components in the x and y direction are u and v, respectively. The plate is considered to be infinitely wide so that the problem reduces to two dimensions. The plate also is assumed to extend infinitely from the leading edge in the direction of flow (i.e., downward for a cooled plate and upward for a heated plate).

Further simplifications of the governing equations can be made within the fluid boundary layer at locations where the boundary layer thickness is much smaller than the distance along the plate from the leading edge (see, e.g., Schlichting, 1979, Ch. VII; Bejan, 1984). The diffusion of momentum, heat and particles in the direction of the flow may be neglected. Also the y-component of the momentum equation reduces to a statement that the pressure is independent of y within the boundary layer. The temperature gradient is small in the x-direction, so the thermophoretic flux is considered in the y-direction only. Assuming an ideal gas, the resulting system of boundary layer equations is (see, e.g., Schlichting, 1979, pp. 315-321):

$$\frac{\partial u}{\partial x} + \frac{\partial v}{\partial y} = 0 \tag{3.5}$$

$$u\frac{\partial u}{\partial x} + v\frac{\partial v}{\partial y} = \nu\frac{\partial^2 u}{\partial y^2} + g\frac{|\Delta T|}{T_\infty}\theta \tag{3.6}$$

$$u\frac{\partial \theta}{\partial x} + v\frac{\partial \theta}{\partial y} = \alpha\frac{\partial^2 \theta}{\partial y^2} \tag{3.7}$$

$$u\frac{\partial\omega}{\partial x} + v\frac{\partial\omega}{\partial y} = D\frac{\partial^2\omega}{\partial y^2} - \frac{\partial(v_{t;y}\,\omega)}{\partial y} - v_g\frac{\partial\omega}{\partial x} \tag{3.8}$$

where $\theta = (T-T_\infty)/(T_w-T_\infty)$, $\Delta T = T_w-T_\infty$, $\omega = n/n_\infty$, $v_{t;y}$ is the y-component of the thermophoretic drift velocity, and v_g is the gravitational settling velocity. The subscripts 'w' and '∞' signify values at the wall and at great distance from the plate, respectively.

The gravitational settling term in equation (3.8) leads to difficulties in obtaining a solution to this system of equations. As shown in the Appendix, it is justified to neglect this term as small for particles with aerodynamic diameter less than several μm assuming $|\Delta T|$ greater than a few tenths of a degree K. The treatment in this chapter applies to those cases in which the gravitational settling term can be neglected.

The thermophoretic velocity is thought to vary linearly with the temperature gradient and is commonly expressed as

$$v_t = -K\frac{\nu}{T}\nabla T \tag{3.9}$$

The coefficient K depends on particle size and, for particles larger than the mean free path of air molecules (0.065 μm at 25 °C and 1 atm.), on the ratio of the thermal conductivity of the gas to that of the particle. In a recent review, Talbot et al. (1980) give an interpolation formula for spherical particles that is argued to be reasonably accurate for all particle sizes.

$$K = 2\,C_s\,\frac{\left[\frac{k_g}{k_p} + 2\,\frac{C_t\,\lambda}{d_p}\right]\left[1 + \frac{\lambda}{d_p}\left\{2.4 + 0.82\,\exp(-0.44\,\frac{d_p}{\lambda})\right\}\right]}{\left\{1 + 6\,C_m\,\frac{\lambda}{d_p}\right\}\left\{1 + 2\,\frac{k_g}{k_p} + 4\,\frac{C_t\,\lambda}{d_p}\right\}} \tag{3.10}$$

In this equation, k_g and k_p represent the thermal conductivity of the gas and particle, respectively, λ is the mean free path of air molecules, d_p is the particle diameter, and C_m, C_s, and C_t are coefficients of momentum exchange, thermal slip, and temperature jump,

respectively. The coefficients have values $C_m = 1.146$, $C_s = 1.147$, and $C_t = 2.20$. Batchelor and Shen (1985) illustrate the dependence of K on the conductivity ratio, k_g/k_p, and on the Knudsen number, $2\lambda/d_p$. For particles in air with $d_p \leq 3$ μm and k_g/k_p in the range 0.01 to 0.5, K varies between 0.1 and 0.6. A representative value of K is 0.5, particularly for particles smaller than 1 μm.

Using equation (3.9), the term accounting for thermophoresis in equation (3.8) becomes

$$- \frac{\partial(v_{t;y}\,\omega)}{\partial y} = K\nu \frac{\partial}{\partial y}\left[\frac{\omega}{T}\frac{\partial T}{\partial y}\right]$$

$$= K\nu\left[\frac{1}{T}\frac{\partial \omega}{\partial y}\frac{\partial T}{\partial y} - \frac{\omega}{T^2}\left(\frac{\partial T}{\partial y}\right)^2 + \frac{\omega}{T}\frac{\partial^2 T}{\partial y^2}\right] \qquad (3.11)$$

where K and ν have been assumed to be constant. The present interest is in systems in which the temperature differences are small compared with the absolute temperature, so in the coefficients involving $1/T$ and $1/T^2$, T may be approximated by T_∞. In addition, the concentration boundary layer thickness, δ_c, for particles of a size large enough for thermophoresis to play a significant role, is much smaller than the thickness, δ_t, of the thermal boundary layer. The first term on the right-hand side of equation (3.11) is larger than the remaining terms by the ratio δ_t/δ_c, and only this term shall be retained. (This approximation is most accurate for $|\Delta T|$ small or for a cool plate. For example, if $d_p = 0.3$ μm, and $\Delta T = -10$ K, $\delta_t/\delta_c \sim 10^3$, whereas if $\Delta T = 10$ K, $\delta_t/\delta_c \sim 10$.) Substituting into equation (3.8), the governing equation for particle concentration in the boundary layer becomes

$$u\frac{\partial \omega}{\partial x} + v\frac{\partial \omega}{\partial y} = D\frac{\partial^2 \omega}{\partial y^2} - \nu N_t \frac{\partial \omega}{\partial y}\frac{\partial \theta}{\partial y} \qquad (3.12)$$

where $N_t = K(T_w - T_\infty)/T_\infty$ is a dimensionless thermophoresis parameter.

It remains to specify boundary conditions for the system of equations (3.5)-(3.7), and (3.12). These are given below.

$$u(0,y) = u(x,0) = u(x,\infty) = 0 \tag{3.13}$$

$$v(x,0) = 0 \tag{3.14}$$

$$\theta(0,y) = \theta(x,\infty) = 0 \tag{3.15}$$

$$\theta(x,0) = 1 \tag{3.16}$$

$$\omega(0,y) = \omega(x,\infty) = 1 \tag{3.17}$$

$$\omega(x,0) = 0 \tag{3.18}$$

3.3.2 Scale Analysis. For air at atmospheric pressure and environmental temperatures, the Prandtl number ($Pr = \nu/\alpha$) is order one, taking a value of 0.72 at 20 °C (Bejan, 1984, Appendix). An implication is that the thickness of the thermal and momentum boundary layers are of the same magnitude. From arguments regarding the size of the terms in equations (3.5)-(3.7), it may be shown (e.g., Bejan, 1984, Ch. 4) that the magnitude of this thickness is given by

$$\delta \sim x\, Ra_x^{-0.25} \tag{3.19}$$

where Ra_x is the Rayleigh number,

$$Ra_x = \frac{g\,|\Delta T|\,x^3}{\alpha\,\nu\,T_\infty} \tag{3.20}$$

In the boundary layer, the peak fluid velocity along the plate scales as

$$u_p \sim \frac{\alpha}{x}\, Ra_x^{0.5} \tag{3.21}$$

The scale analysis may be extended to include equation (3.12), from which one obtains estimates of the thickness of the concentration boundary layer and of the normalized particle flux* onto the plate. The results of this analysis also indicate conditions under which thermophoresis dominates Brownian motion in the boundary layer.

Within the concentration boundary layer, the fluid velocity along the plate scales as

$$u_c \sim (\delta_c/\delta)\, u_p \sim \delta_c\, (\alpha/x^2)\, Ra_x^{0.75} \tag{3.22}$$

To satisfy the continuity equation, the terms on the left-hand side of equation (3.12) must have equal magnitude, which is $[\delta_c\, \alpha\, Ra_x^{0.75}\, x^{-3}]$. On the right-hand side, the diffusion term has magnitude $[D/\delta_c^2]$, and the thermophoresis term has magnitude $[N_t\, \nu\, Ra_x^{0.25}\, (x\, \delta_c)^{-1}]$.

Three cases must be considered, according to the relative magnitude of the particle diffusivity and the thermophoresis parameter, and according to whether the plate is warmer or cooler than the surrounding air.

3.3.2.1 Case I. | Nt | small, or D large. Thermophoresis is unimportant in this case. The thickness of the concentration boundary layer is obtained by balancing the advection and diffusion terms in equation (3.12)

$$\delta_c \sim x\, Le^{-1/3}\, Ra_x^{-1/4} \tag{3.23}$$

where $Le = \alpha/D$ is the particle Lewis number. The particle flux density is determined by the rate of diffusion of particles onto the plate. The magnitude of the normalized flux of particles onto the plate, v_d, is therefore

* The normalized particle flux is given by the ratio of the flux density onto the plate to the concentration of particles outside the boundary layer. This parameter has dimensions of a velocity and is commonly referred to in the air pollution literature as a deposition velocity.

$$v_d = D\left(\frac{\partial \omega}{\partial y}\right)_{y=0} \sim \frac{D^{2/3}\,\alpha^{1/3}}{x}\,Ra_x^{1/4} \tag{3.24}$$

3.3.2.2 Case II. | Nt | large, or D small; cool plate. The flux of particles to the plate is determined by the thermophoretic drift velocity, v_t,

$$v_d \sim v_t \sim \frac{\nu\,|\,N_t\,|}{x}\,Ra_x^{1/4} \tag{3.25}$$

Brownian motion is significant only within an extremely thin layer near the surface of the plate. The thickness of this layer is determined by a balance between the diffusion and thermophoretic terms, yielding

$$\delta_c \sim \frac{x}{Sc\,|\,N_t\,|\,Ra_x^{1/4}} \tag{3.26}$$

where $Sc = \nu/D$ is the particle Schmidt number.

The results of cases I and II may be used to determine the conditions under which either thermophoresis or Brownian motion dominates the other as a particle transport process. Comparing equation (3.24) with (3.25), and assuming $Pr \sim 1$ and $K \sim 1$, the two processes are seen to be of comparable magnitude if $Le^{1/3} = (T_\infty/|\,\Delta T\,|)^{1/2}$. The temperature difference implied by this condition for a range of particle sizes is illustrated in Figure 3.1. For temperature differences that are much larger than that needed to satisfy the equality, thermophoresis dominates Brownian motion as a transport process in the boundary layer. It is clear from Figure 3.1 that thermophoresis is a potentially important process in the deposition of airborne particles on vertical surfaces indoors.

3.3.2.3 Case III. | Nt | large, or D small; warm plate. In this case thermophoresis drives particles from the plate, and a thin layer, essentially free of particles, is formed. The existence of this layer has been investigated experimentally (Watson, 1936; Talbot et

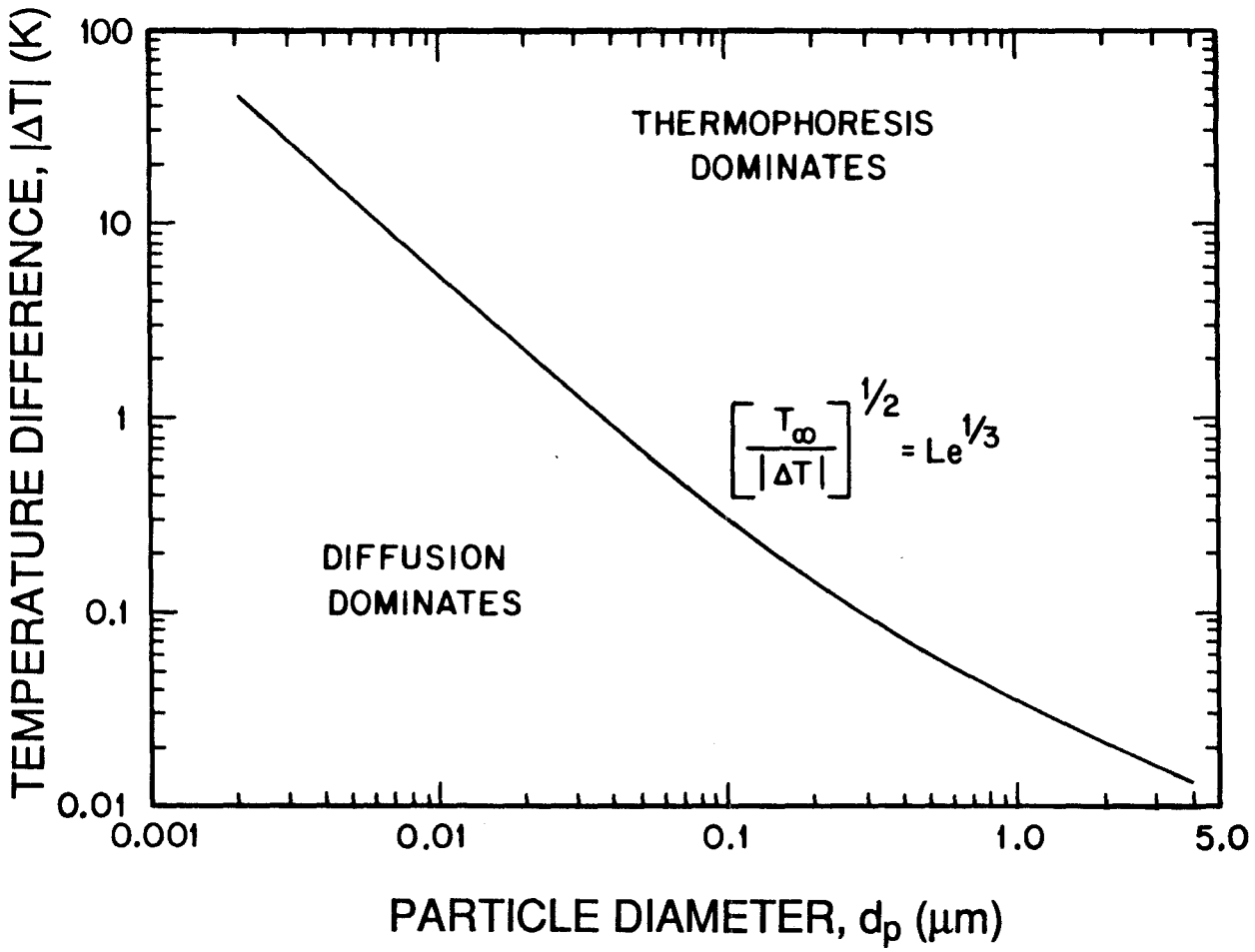

Figure 3.1 Relative importance of Brownian motion (diffusion) and thermophoresis for particle deposition from a natural convection boundary layer adjacent to a vertical isothermal flat plate. The line dividing the two regions is placed assuming Pr ~ 1 and K ~ 1.

al., 1980). The magnitude of the thickness of this layer is determined by a balance between thermophoresis and advection. For the case where Pr ~ 1,

$$\delta_c \sim \frac{x}{Ra_x^{1/4}} N_t^{1/2} \tag{3.27}$$

In this case, deposition of particles on the surface of the plate is negligible.

3.3.3 Similarity Solution. The classical problem of heat and momentum transfer for a vertical isothermal flat plate is reduced to a system of ordinary differential equations by means of a similarity transformation. This approach may be extended to analyze particle transport in the boundary layer.

Following Ostrach (1953) (see also Schlichting, 1979; Bejan, 1984), the continuity equation is transformed by writing the velocity components in terms of the stream function ψ:

$$u = \frac{\partial \psi}{\partial y}; \quad v = -\frac{\partial \psi}{\partial x} \tag{3.28}$$

A solution for ψ, θ, and ω is sought such that

$$\psi = 4 \nu c x^{3/4} \zeta(\eta) \tag{3.29}$$

$$\theta = \theta(\eta) \tag{3.30}$$

$$\omega = \omega(\eta) \tag{3.31}$$

where

$$c = \left[\frac{g |\Delta T|}{4 \nu^2 T_\infty}\right]^{1/4} \tag{3.32}$$

$$\eta = c\, y\, x^{-1/4} \tag{3.33}$$

Substituting into the partial differential equations (3.6), (3.7) and (3.12), the following ordinary differential equations are obtained.

$$\zeta''' + 3\,\zeta\,\zeta'' - 2\,(\zeta')^2 + \theta = 0 \tag{3.34}$$

$$\theta'' + 3\,Pr\,\zeta\,\theta' = 0 \tag{3.35}$$

$$\omega'' + 3\,Sc\,\zeta\,\omega' + N_t\,Sc\,\theta'\,\omega' = 0 \tag{3.36}$$

where primes indicate derivatives with respect to the independent variable η. The first two equations are the classical results describing momentum and heat transport in the boundary layer. Equation (3.36) describes particle transport in the boundary layer, with the terms on the left accounting for Brownian motion, advection, and thermophoresis, respectively.

The boundary conditions for these equations are

$$\zeta(0) = \zeta'(0) = 0;\ \zeta'(\infty) = 0 \tag{3.37}$$

$$\theta(0) = 1;\ \theta(\infty) = 0 \tag{3.38}$$

$$\omega(0) = 0;\ \omega(\infty) = 1 \tag{3.39}$$

The system of equations was solved numerically using the shooting method for transforming the boundary value problem into an initial value problem, and a fourth-order Runge-Kutta integration routine (Press et al., 1986).

Initially, to verify that the numerical procedure worked properly, and to obtain precise boundary conditions for $\zeta''(0)$ and $\theta'(0)$ that satisfied the conditions at $\eta\rightarrow\infty$, the system (3.34), (3.35), (3.37), and (3.38) was solved for Pr=0.72 and compared with the results of Ostrach (1953). Agreement was obtained within $\pm$ 0.0002 for all parameters and all values of η, except one. The exception appears to be due to a transposition error in Ostrach's table: for η=3.8, F=0.5753 rather than 0.5735.

Having obtained the solution to the momentum and heat transport equations, these equations were converted to an initial value problem by altering the boundary conditions (3.37) and (3.38):

$$\zeta(0) = \zeta'(0) = 0;\ \zeta''(0) = 0.675955 \tag{3.40}$$

$$\theta(0) = 1;\ \theta'(0) = -0.504599 \tag{3.41}$$

The system of equations (3.34)-(3.36) was then solved subject to the boundary conditions (3.39)-(3.41). Solutions were obtained for a range of values of N_t corresponding to air-plate temperature differences from -10 to 10 K (assuming T_∞=293 K, and K = 0.5) and for a range of Schmidt numbers corresponding to particle diameters in the range 0.001-3.0 μm (assuming T_∞=293 K).

3.4 Results

Selected concentration profiles are presented in Figure 3.2. For $Sc = 5.44 \times 10^5$ (d_p = 1.0 μm), the effect of thermophoresis is clearly dominant, even for $|N_t|$ as small as 0.0017 (ΔT = 1 K, K = 0.5). For the cool plate, the particle concentration rises steeply at $\eta = 0$, indicating a large normalized particle flux. The concentration boundary layer thickness is small: at x = 1 m and ΔT = 1 K, $\eta = 0.006$ corresponds to a distance of only 77 μm from the plate. For the warm plate, particles are driven from the surface by thermophoresis. A zone that is essentially free of particles extends out to $\eta = 0.02$. The normalized particle flux to the wall is very small, as indicated by the slope of the profile at $\eta = 0$.

By contrast, the effect of thermophoresis for $Sc = 2.22 \times 10^4$ (d_p = 0.1 μm), while not negligible, is much smaller. For this case, and for the small temperature difference considered, no particle-free zone occurs.

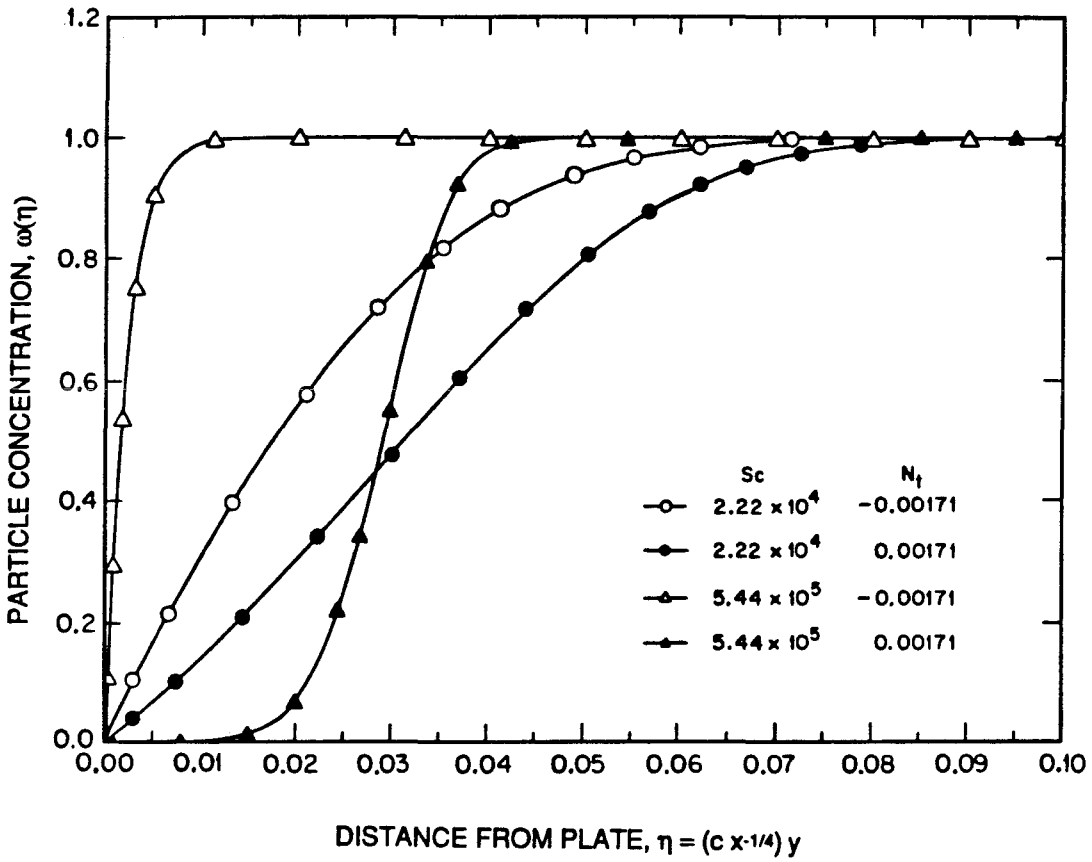

Figure 3.2 Particle concentration profiles in the natural convection boundary layer adjacent to a vertical isothermal flat plate. The Schmidt numbers of 2.22×10^4 and 5.44×10^5 correspond to particles of diameter 0.1 μm and 1.0 μm, respectively, in air at 293 K. The thermophoresis parameter $N_t = \pm 0.00171$ corresponds to a temperature difference between the plate and air of ± 1 K assuming K=0.5 and T_∞=293 K.

The dimensionless particle flux is presented in Figure 3.3 for the full range of particle sizes and temperature differences considered. The normalized particle flux in dimensional form is obtained from this figure by the equation

$$v_d = 0.77\ \alpha^{1/3}\ D^{2/3}\ \frac{Ra_x^{1/4}}{x}\ \{\omega'(0)/Le^{1/3}\} \tag{3.42}$$

The numerical factor in this equation corresponds to $(4\ Pr)^{-0.25}$, and arises from the definition of the coefficient c, equation (3.32). For $d_p = 0.001$ μm (the size of unattached radon decay products), the effect of thermophoresis is negligible compared with Brownian motion. However for particles as small as 0.1 μm, the effect of thermophoresis is substantial over the range of N_t considered. For particles with diameters of order 1 μm, the difference in dimensionless particle flux for heated and cooled walls is striking. A large fraction of urban aerosol mass, including most black soot, is found in particles with diameters of a few μm or smaller.

Normalized particle fluxes are presented in dimensional form in Table 3.1 for a range of particle sizes and temperature differences at x = 1 m, assuming $T_\infty = 293$ K and K = 0.5. Characteristic thicknesses of the particle concentration boundary layers are indicated in Table 3.2. The particle flux at a different distance along the plate is easily computed, noting that v_d scales as $x^{-1/4}$.

From the normalized particle flux, $v_d(d_p)$, and the aerosol size distribution function $n(d_p)$ (e.g., Friedlander, 1977), the rate of coverage of a surface, Ψ, due to the deposition of particles may be determined:

$$\Psi = \int_0^\infty \frac{\pi}{4} d_p^2\ v_d(d_p)\ n(d_p)\ d(d_p) \tag{3.43}$$

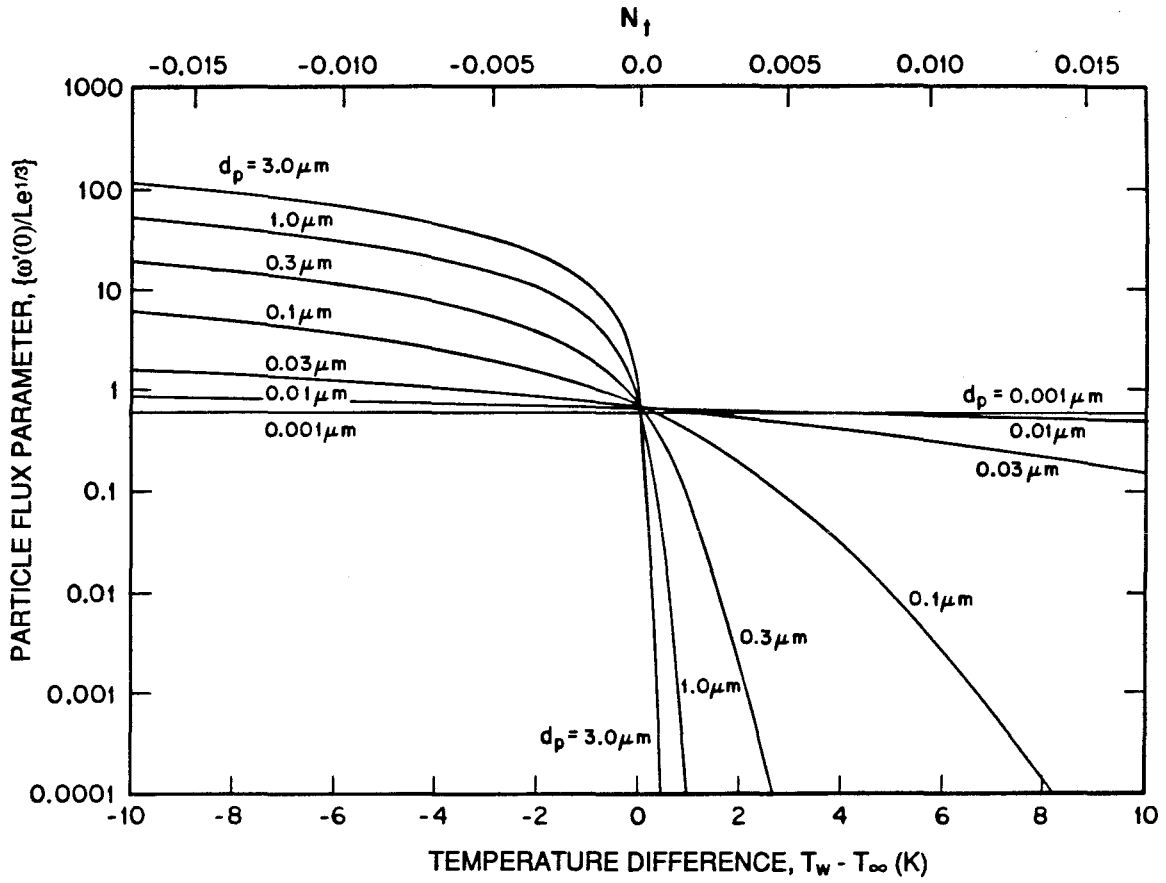

Figure 3.3 Dimensionless particle flux onto a vertical isothermal plate for particle diameters in the range 0.001-3.0 μm (assuming air at T_∞=293 K), and for thermophoresis parameters in the range -0.017 to 0.017, corresponding to T_w-T_∞ in the range -10 to 10 K, assuming K=0.5. For conversion to dimensional form, see equation (3.42).

Table 3.1. Normalized particle flux (v_d, $\times 10^{-6}$ m s^{-1}) onto a vertical isothermal flat plate*.

	$T_w - T_\infty$ (K)									
d_p(μm)	-10	-4	-2	-1	-0.1	0.1	1	2	4	10
0.01	47.3	37.6	25.7	21.0	11.5	11.5	19.9	23.0	25.8	26.9
0.03	21.6	10.7	7.4	5.6	2.8	2.8	4.4	4.7	4.2	2.0
0.1	18.0	6.1	3.0	1.8	0.68	0.62	0.66	0.39	0.07	n
0.3	17.9	5.7	2.5	1.1	0.24	0.18	0.04	0.001	n	n
1.0	17.9	5.7	2.4	1.0	0.11	0.05	n	n	n	n
3.0	17.9	5.7	2.4	1.0	0.07	0.01	n	n	n	n

* Normalized particle flux (deposition velocity) is defined as the particle flux density onto the plate divided by the particle concentration outside the boundary layer. The results in this table are obtained for x = 1 m, and assuming T_∞ = 293 K, K=0.5. The entry "n" implies $v_d < 10^{-10}$ m s^{-1}.

Table 3.2. A characteristic thickness* of the particle concentration boundary layer (mm).

	$T_w - T_\infty$ (K)									
d_p(μm)	-10	-4	-2	-1	-0.1	0.1	1	2	4	10
0.01	0.63	0.87	1.07	1.29	2.33	2.34	1.34	1.14	1.00	0.87
0.03	0.19	0.34	0.47	0.59	1.12	1.14	0.68	0.61	0.59	0.65
0.1	0.03	0.08	0.14	0.22	0.52	0.55	0.40	0.43	0.52	0.67
0.3	0.005	0.01	0.03	0.07	0.28	0.33	0.36	0.44	0.53	0.68
1.0	(0.001)	(0.003)	0.008	0.02	0.14	0.23	0.37	0.45	0.54	0.68
3.0	(0.0003)	(0.001)	(0.002)	(0.006)	0.07	0.20	0.38	0.45	0.54	0.68

* Taken as the distance from the plate to the point where the normalized particle concentration, ω, is 0.5. The results are obtained for x = 1 m, and assuming T_∞ = 293 K, K=0.5.

Entries in parentheses are not significantly larger than the particle diameter. In such cases a concentration boundary layer does not exist: the particle concentration near the plate is essentially uniform, and the normalized particle flux is equal to the thermophoretic velocity.

This equation would be expected to hold until a significant fraction of the surface is covered with a layer of particles.

3.5 Discussion

Much of the theoretical work on particle deposition within enclosures has utilized a simplified description of fluid behavior in the near-wall region. In particular, it is commonly assumed that a thin boundary layer separates the well-mixed core from the walls of the enclosure (Corner and Pendlebury, 1951; Crump and Seinfeld, 1981; McMurry and Rader, 1985). Particle migration through the boundary layer is assumed to be due to Brownian and turbulent diffusion, gravitational settling, and, in the latest case, electrostatic drift. The effects of mean fluid motion and thermal gradients in the near-wall region are neglected. This description has been demonstrated to be adequate for determining the effect of deposition on the evolution of particle concentration in the core of an enclosure (Crump et al., 1983; McMurry and Grosjean, 1985; Okuyama et al., 1986). It would be unlikely to work as well if the focus of attention were soiling or material damage effects due to the deposited airborne particles. For example, the turbulent deposition model would predict deposition rates that are uniform over an entire flat wall and independent of the temperature of the surface. The analysis presented here shows that even small temperature differences between the fluid and the walls can have a major effect on deposition rates, and that deposition rates in this case are a function of distance along the wall. Although restricted to a simplified geometry, the work presented in this chapter could lead to improvements in the near-wall description of particle behavior in enclosures.

Other extensions of the present work are needed to address the full range of systems of practical interest. For example, the rate of loss of particles on chamber surfaces has been observed to depend on the nature of the surface (Harrison, 1979).

Theoretically, one would expect deposition to be enhanced if a characteristic dimension of the surface roughness were at least comparable in magnitude to the thickness of the particle concentration boundary layer. From Table 3.2, characteristic concentration boundary layer thicknesses for a building wall warmer than the adjacent air are in the range of a few tenths of a mm to a few mm. The typical roughness of a painted surface is probably comparable to the lower end of this range, and many surfaces have larger roughness elements. Thus, even though the predicted deposition rates onto warm walls are small for particles with d_p greater than a few tenths of a μm, this may not hold true if the walls are rough.

The present analysis was confined to laminar flow along the plate. Strictly, this limits the results to small temperature differences or short plate lengths. The transition to turbulence for this system begins at $Ra_x \sim 10^9$ (Bejan, 1984, Ch. 6); this corresponds to a length of only 1 m for a temperature difference of 10 K, or a temperature difference of only 0.3 K for a plate length of 3 m. One should extend this work to cover deposition from a natural convection boundary layer that is influenced by turbulence.

The effect of electrostatic fields on particle deposition has been shown to be important in Teflon-film smog chambers (McMurry and Rader, 1985). Whether electrostatic fields are important for particle deposition indoors is not known. If so, the similarity solution derived in this chapter could be extended to account for electrical migration only if the electric field varied in inverse proportion with distance from the plate. Otherwise, as in the case in which gravitational settling is included, a similarity transformation is not obtained, and an alternative solution technique must be sought.

In summary, the results of the present analysis should apply for an isolated isothermal flat plate for particle sizes up to a few μm in diameter and for $Ra_x \leq 10^9$. The results are also indicative of deposition rates and processes onto vertical walls of enclosures—at least, in the absence of strong turbulent mixing in the core—and suggest that in rooms, thermophoresis is a dominant transport process across the concentration

boundary layer for particles exceeding the order of 0.1 μm in diameter. An apparent implication is that cool vertical surfaces are soiled much more rapidly than warm surfaces. This is an important result with many practical implications. Experimental confirmation of these predictions is warranted.

3.6 Acknowledgements

This research was supported by a contract with the Getty Conservation Institute.

3.7 References

Batchelor, G. K., and Shen, C. (1985) Thermophoretic deposition of particles in gas flowing over cold surfaces, *Journal of Colloid and Interface Science* **107**, 21-37.

Bejan, A. (1984) *Convection Heat Transfer*, Wiley: New York.

Corner, J. and Pendlebury, E. D. (1951) The coagulation and deposition of a stirred aerosol, *Proceedings of the Physical Society (London)* **B64**, 645-654.

Crump, J. G., Flagan, R. C., and Seinfeld, J. H. (1983) Particle wall loss rates in vessels, *Aerosol Science and Technology* **2**, 303-309.

Crump, J. G., and Seinfeld, J. H. (1981) Turbulent deposition and gravitational settling of an aerosol in a vessel of arbitrary shape, *Journal of Aerosol Science* **12**, 405-415.

Friedlander, S. K. (1977) *Smoke, Dust and Haze*, Wiley: New York.

Goren, S. L. (1977) Thermophoresis of aerosol particles in the laminar boundary layer of a flat plate, *Journal of Colloid and Interface Science* **61**, 77-85.

Harrison, A. W. (1979) Quiescent boundary layer thickness in aerosol enclosures under convective stirring conditions, *Journal of Colloid and Interface Science* **69**, 563-570.

McMurry, P. H., and Grosjean, D. (1985) Gas and aerosol wall losses in Teflon film smog chambers, *Environmental Science and Technology* **19**, 1176-1182.

McMurry, P. H., and Rader, D. J. (1985) Aerosol wall losses in electrically charged chambers, *Aerosol Science and Technology* **4**, 249-268.

Okuyama, K., Kousaka, Y., Yamamoto, S., and Hosokawa, T. (1986) Particle loss of aerosols with particle diameters between 6 and 2000 nm in stirred tank, *Journal of Colloid and Interface Science* **110**, 214-223.

Ostrach, S. (1953) *An Analysis of Laminar Free-Convection Flow and Heat Transfer about a Flat Plate Parallel to the Direction of the Generating Body Force*, NACA Report 1111, U.S. Govt. Printing Office: Washington.

Press, W. H., Flannery, B. P., Teukolsky, S. A., and Vetterling, W. T. (1986) *Numerical Recipes: The Art of Scientific Computing*, Cambridge University Press: Cambridge.

Schiller, G. E. (1984) *A Theoretical Convective-Transport Model of Indoor Radon Decay Products*, Ph.D. Thesis, University of California, Berkeley, California.

Schlichting, H. (1979) *Boundary-Layer Theory*, Seventh edn, McGraw-Hill: New York.

Scott, A. G. (1983) Radon daughter deposition velocities estimated from field measurements, *Health Physics* **45**, 481-485.

Sinclair, J. D., Psota-Kelty, L. A., and Weschler, C. J. (1985) Indoor/outdoor concentrations and indoor surface accumulations of ionic substances, *Atmospheric Environment* **19**, 315-323.

Talbot, L., Cheng, R. K., Schefer, R. W., and Willis, D. R. (1980) Thermophoresis of particles in a heated boundary layer, *Journal of Fluid Mechanics* **101**, 737-758.

Toohey, R. E., Essling, M. A., Rundo, J., and Hengde, W. (1984) Measurements of the deposition rates of radon daughters on indoor surfaces, *Radiation Protection Dosimetry* **7**, 143-146.

Watson, H. H. (1936) The dust-free space surrounding hot bodies, *Transactions of the Faraday Society* **32**, 1073-1084.

Zernik, W. (1957) The dust-free space surrounding hot bodies, *British Journal of Applied Physics* **8**, 117-120.

3.8 Appendix: Gravitational Settling in the Concentration Boundary Layer

The conditions under which gravitational settling may be neglected are determined by comparing the settling velocity with the rates of other transport processes in the concentration boundary layer. For a spherical particle of density ρ_p, the settling velocity is given by (Friedlander, 1977)

$$v_g = \frac{d_p^2 \rho_p g C}{18 \mu} \tag{3.44}$$

where C is the Cunningham slip correction factor.

Three cases are considered separately. If Brownian motion dominates thermophoresis, then by (3.22) and (3.23) the vertical fluid velocity in the concentration boundary layer scales as

$$u_c \sim \frac{\alpha}{x} Le^{-1/3} Ra_x^{1/2} \tag{3.45}$$

The particle diameter at which this velocity is of the same magnitude as the gravitational settling velocity is given by

$$d_{p,\max} = 2.5\left[\frac{\alpha^2 \mu^2 kT Ra_x^{3/2}}{C^2 \rho_p^3 g^3 x^3}\right]^{\frac{1}{7}} \tag{3.46}$$

For representative conditions, $\rho_p = 2.0 \times 10^3$ kg m^{-3}, $Ra_x = 10^8$, x = 1.0 m, and T = 293 K. In this case, by (3.46), $d_{p,max} = 4.6$ μm. Flow along the plate is dominant for particle sizes that are much smaller. For particles of diameter 0.1 μm or less, gravitational settling in the concentration boundary layer occurs at less than 1% of the velocity of fluid flow along the plate. Therefore, it is reasonable to neglect gravitational settling in the boundary layer for particles small enough for Brownian motion to dominate thermophoresis.

In cases where thermophoresis dominates, gravitational settling may be neglected for particles that are somewhat larger. For a plate that is warmer than the surrounding air, thermophoresis causes the concentration boundary layer thickness to increase, and so the characteristic fluid velocity within the concentration boundary layer is also increased. Combining (3.22), (3.27) and (3.44), one may determine the particle diameter at which gravitational settling in the boundary layer is of the same magnitude as the characteristic fluid velocity along the plate:

$$d_{p,max} = \left[\frac{18\,\alpha\,\mu}{C\,\rho_p\,g\,x}\right]^{\frac{1}{2}} N_t^{1/4}\,Ra_x^{1/4} \tag{3.47}$$

For the same conditions considered above, and for K = 0.5 and ΔT = 1 K, $d_{p,max}$ is equal to 12 μm. Under these conditions, for particles of diameter up to several μm, gravitational settling is a small contribution to particle motion in the concentration boundary layer.

For the third case, that of a cooled plate in which thermophoresis dominates, the distance that a particle settles as it migrates through the concentration boundary layer is considered. The time of travel through the layer is determined from (3.25) and (3.26):

$$\tau = \frac{\delta_c}{v_t} \sim \frac{x^2}{|N_t|^2\,Sc\,\nu}\,Ra_x^{-1/2} \tag{3.48}$$

Consider, for example, a particle of diameter 1 μm, with the other conditions as given above. The characteristic time to migrate through the concentration boundary layer is 4.2 s during which time the particle settles through 0.3 mm, a distance of no consequence. Smaller particles would settle through an even smaller distance while traversing the concentration boundary layer. As indicated in Table 3.2, thermophoresis so greatly dominates Brownian motion for larger particles that a concentration boundary layer is effectively absent.

CHAPTER 4

MASS-TRANSPORT ASPECTS OF POLLUTANT REMOVAL AT INDOOR SURFACES

4.1 Abstract

The mass-transport-limited rate of pollutant deposition onto indoor surfaces is examined in this chapter. Transport of both particles and highly reactive gases through the boundary layer of air adjacent to a surface is analyzed for three model airflow conditions: (1) natural convection flow along room surfaces, (2) forced laminar flow parallel to room surfaces, and (3) homogeneous turbulence in the core of the room. Transport mechanisms considered include convective diffusion, thermophoresis, and gravitational sedimentation. The predicted mass-transport-limited deposition velocity, averaged over the surfaces of a room, varies from order 10^{-6} to 10^{-2} m s^{-1} over the range of pollutant diffusivities and particle sizes encountered. Theoretical predictions are in rough agreement with the limited experimental data that have been taken inside rooms. Results show that if buildings were designed and operated such that natural convection or forced laminar flow conditions prevailed with surface temperatures a few degrees K warmer than the room air, then soiling of vertical surfaces due to deposition of soot particles in the size range 0.1-1 μm diameter could be greatly reduced.

Reference: Nazaroff, W. W., and Cass, G. R. Mass-transport aspects of pollutant removal at indoor surfaces, submitted to *Environment International.*

4.2 Nomenclature

Symbols

a	Constant, $[g \mid \Delta T \mid / (4 \nu^2 T_\infty)]^{1/4}$
C	Pollutant concentration (mass m^{-3})
C_c	Slip coefficient (dimensionless)
C_m	Momentum exchange coefficient, 1.146
C_s	Thermal slip coefficient, 1.147
C_t	Temperature jump coefficient, 2.20
C_∞	Pollutant concentration in the core of the room (mass m^{-3})
d_p	Particle diameter (m)
D	Diffusion coefficient ($m^2 s^{-1}$)
D_e	Eddy diffusion coefficient ($m^2 s^{-1}$)
g	Acceleration of gravity, 9.8 m s^{-2}
h	Heat transfer coefficient (W $m^{-2} K^{-1}$)
H	Height of the room (m)
k	Boltzmann's constant, 1.38×10^{-23} J K^{-1}
k_g	Thermal conductivity of air (W $m^{-1} K^{-1}$)
k_o	Von Kármán's constant
k_p	Thermal conductivity of particles (W $m^{-1} K^{-1}$)
K	Thermophoresis coefficient (dimensionless)
K_e	Turbulence intensity parameter (s^{-1})
Kn	Knudsen number, $Kn = 2\lambda/d_p$
L	Characteristic length of a surface (m)
Le	Lewis number, α/D
N_t	Thermophoresis parameter, $K(T_S - T_\infty)/T_\infty$

Nu	Nusselt number, $h\ x/k_g$
Pr	Prandtl number, ν/α
Ra_H	Rayleigh number based on height, $[g\ \beta \mid \Delta T \mid H^3] / \alpha\nu$
Ra_L	Rayleigh number based on characteristic length, $[g\ \beta \mid \Delta T \mid L^3] / \alpha\nu$
s_g	Surface orientation coefficient (dimensionless)
S_i	Area of the ith surface (m^2)
Sc	Schmidt number, ν/D
Sh	Sherwood number, $v_d\ x/D$
t	Time (s)
T	Temperature (K)
T_s	Surface temperature (K)
T_∞	Air temperature in the core of a room (K)
u	Fluid velocity parallel to a surface ($m\ s^{-1}$)
u_{max}	Peak air velocity along a vertical surface due to natural convection ($m\ s^{-1}$)
u_∞	Fluid velocity parallel to a surface outside of the momentum boundary layer ($m\ s^{-1}$)
v	Fluid velocity normal to a surface ($m\ s^{-1}$)
v_{CP}	Deposition velocity according to the theory of Corner and Pendlebury (1951) ($m\ s^{-1}$)
v_d	Deposition velocity ($m\ s^{-1}$)
v_D	Pollutant flux per unit surface area per unit atmospheric concentration associated with convective diffusion ($m\ s^{-1}$)
v_g	Gravitational settling velocity ($m\ s^{-1}$)
v_t	Migration velocity associated with thermophoresis ($m\ s^{-1}$)
V	Volume of room (m^3)
x	Distance along a surface (m)
X	Length of a surface in the direction of flow (m)

y	Distance normal to surface (m)

Greek Symbols

α	Thermal diffusivity of air ($m^2\ s^{-1}$)
β	Coefficient of thermal expansion (K^{-1})
δ	Fluid boundary layer thickness (m)
ΔT	Temperature difference, $T_s - T_\infty$ (K)
η	Independent variable of position in similarity transform (dimensionless)
ζ	Stream function (dimensionless)
λ	Mean free path of air molecules (0.065 μm at 298K and 1.0 atm.)
μ	Dynamic viscosity of air ($kg\ m^{-1}\ s^{-1}$)
ν	Kinematic viscosity of air ($m^2\ s^{-1}$)
ρ_p	Particle density ($kg\ m^{-3}$)
θ	Normalized temperature, $\frac{T-T_\infty}{T_s-T_\infty}$ (dimensionless)
ψ	Stream function ($m^2\ s^{-1}$)
ω	Normalized pollutant concentration, C/C_∞ (dimensionless)

Other Symbols

[overbar]	Mean value
[prime]	Derivative with respect to independent variable
∂	Partial derivative operator (dimensionless)
∇	Gradient operator (m^{-1})

4.3 Introduction

Pollutant deposition onto indoor surfaces is an important process in the context of two major indoor air quality concerns. First, for chemically reactive gases and ultrafine particles, it constitutes a major loss term, leading to substantially lower airborne concentrations, and therefore lower exposures to occupants than would otherwise occur. The second concern is material damage, including soiling by particles of all sizes and chemical deterioration due to deposition of reactive particles and gases. In this case, the deposition process is a delivery mechanism that may govern the rate of damage.

Pollutant deposition may be thought of as a two-stage process: first, fluid-mechanical mass-transport mechanisms govern pollutant delivery to surfaces, and then, subsequent chemical or physical interactions occur between the pollutants and the surface materials. If these processes proceed with substantially different characteristic times, the overall deposition rate is determined by the rate of the slower process. The rate of transport of pollutants to the surface is often the limiting step for particles and for highly reactive gases.

In this chapter, the mass-transport-limited deposition rate is analyzed for three model air flow conditions: (1) natural convection flow along the room surfaces, (2) forced laminar flow parallel to the room surfaces, and (3) homogeneous turbulence in the core of the room. The results are reported in terms of the deposition velocity, a term that is defined in the following section. The published data on the mass-transport-limited deposition velocity of pollutants to surfaces of rooms are reviewed and compared with the theoretical predictions.

4.4 Deposition Velocity

The deposition velocity is a useful concept for reporting theoretical and experimental rates of pollutant deposition. Denoted by v_d, it is defined as the pollutant

flux density to a surface (units: mass per area per time) divided by the pollutant concentration (units: mass per volume) at a large distance from the surface.

For the deposition velocity to be a useful concept in the present context, what is considered a "large" distance from the surface must be small with respect to the dimensions of the room. Under most circumstances in indoor air this condition holds; rooms can generally be considered to have a well-mixed core with any reduction in pollutant concentrations due to deposition observed only within several cm of a surface. Exceptions would be expected on a transient basis due to short-term pollutant emissions, such as the lighting of a match, and on a longer time scale in cases where the air is stably stratified, i.e., when air near the ceiling is much warmer than that near the floor. In the latter case, convection is suppressed, and pollutant concentrations may not be uniform throughout the core of a room. However, in such a case the deposition velocities, except for the settling of large particles, are so small as to be unimportant. Thus, the focus of attention in this chapter is on cases in which the room has a well-mixed core and the deposition velocity is determined by the rate of transport of pollutants through the boundary layer adjacent to a surface.

4.5 Theory

4.5.1 Introduction. The motion of both gases and particles is influenced by random collisions with surrounding gas molecules. The resulting migration is termed molecular diffusion in the case of gases and Brownian motion for particles. In addition, particles may be acted on by external forces that cause additional migration relative to the surrounding air. Particularly important processes in this regard are gravitational sedimentation and thermophoresis. These processes are described further in the next section. Other migration processes are not considered in this chapter. Inertial deposition, which occurs when large particles are unable to follow bending streamlines, is unlikely to be important at the low velocities prevalent indoors. Electric field effects may be

important (see, for example, McMurry and Rader, 1985); however, data on the electric field strength in rooms are lacking.

To make the analyses tractable, certain restrictions are applied. Airborne particles are assumed to be spherical and to have known density. Surfaces are considered to be smooth and to be oriented either vertically or horizontally. The deposition velocity onto each surface is assumed to be independent of deposition onto any other surface. The last condition means that the total rate of pollutant loss to surfaces in a room is related to the deposition velocities to the individual surfaces, v_{d_i}, by the expression

$$\frac{dC}{dt} = -\frac{C}{V}\sum_i v_{d_i} S_i \qquad (4.1)$$

where C is the pollutant concentration in the core of the room, S_i is the area of the ith surface in the room, V is the room volume, and t is time.

The three air flow conditions considered in this chapter are intended to represent limiting conditions that may be found in rooms. The natural convection representation is appropriate for conditions in which there is little forced air flow in the room and the flow near a surface is dominated by heat transfer from that surface to the room air. The case of laminar flow parallel to a surface may apply when the flow near a surface is dominated by the operation of a mechanical ventilation system with the air discharged in such a way as to produce a large convective loop with minimum turbulence. The case of homogeneous turbulence is appropriate when near-surface air flows are dominated by random air movement in the core of the room.

4.5.2 Pollutant Migration Processes

4.5.2.1 Molecular diffusion or Brownian motion. The pollutant flux to a surface that results from random molecular motion can be obtained from Fick's law. For the case of

indoor air pollutants, for which the volume fractions are always much less than one, this relationship may be written as

$$\mathbf{v_D} = -\frac{D}{C_\infty} \nabla C \tag{4.2}$$

where $\mathbf{v_D}$ is the pollutant flux per unit surface area per unit atmospheric pollutant concentration, D is the diffusion coefficient and C_∞ is the pollutant concentration outside of the boundary layer.

The diffusion coefficient of a pollutant in air varies according to the mass and the size of the species. Experimental measurements have been reported for many gases (Marrero and Mason, 1972, give an extensive bibliography); illustrative data are presented in Table 4.1. However, few measurements of the diffusivity of reactive gases have been made. For these cases, an estimate can be obtained by theoretical means (Reid et al., 1977).

The Brownian diffusion coefficient of particles in air is described by the following expression (see, e.g., Seinfeld, 1986):

$$D = \frac{k\,T\,C_c}{3\pi\,\mu\,d_p} \tag{4.3}$$

where $k = 1.38 \times 10^{-23}$ J K^{-1} is Boltzmann's constant, T is the temperature, μ is the dynamic viscosity of air (1.81×10^{-5} kg m^{-1} s^{-1} at 293 K) and d_p is the particle diameter. C_c is a slip coefficient that varies according to the particle Knudsen number, $Kn = 2\lambda/d_p$, where $\lambda = 0.065$ μm at 298 K is the mean free path of air molecules. An empirical expression for the slip coefficient is given in Davies (1945), based on prior experimental work involving oil droplets and glass beads:

$$C_c = 1 + Kn\left[1.257 + 0.400 \exp\left(-\frac{1.10}{Kn}\right)\right] \tag{4.4}$$

Table 4.1. Gaseous diffusion coefficients. [a]

Gas Pair	Temp. (K)	D_{meas} (10^{-5} m^2 s^{-1})	Reference
H_2 - Air	291.5	7.60 ± 0.07 [b]	Suetin and Ivakin (1961)
NH_3 - Air	295.1	2.47 ± 0.02	Ivakin and Suetin (1964)
H_2O - Air	293	1.83	Petit (1965)
HCN - Air	273	1.73	Klotz and Miller (1947)
CH_3OH - Air	295	1.59	Katan (1969)
H_2O_2 - Air	333	1.88 ± 0.04	McMurtie and Keyes (1948)
CO_2 - Air	288.6	1.72 ± 0.01[c]	Suetin and Ivakin (1961)
HCOOH - Air	298	1.53 ± 0.02	Lugg (1968)
CH_3COOH - Air	298	1.24 ± 0.02	Lugg (1968)
SO_2 - Air	293	1.22 ± 0.05	Andrew (1955)
Benzene - Air	298	0.932 ± 0.015	Lugg (1968)
Toluene - Air	298	0.849 ± 0.011	Lugg (1968)
m-xylene - Air	298	0.688 ± 0.010	Lugg (1968)
$CHCl_3$ - Air	298	0.888 ± 0.019	Lugg (1968)
Rn - Air	288	1.20	Hirst and Harrison (1939)
CCl_4 - Air	298	0.828 ± 0.006	Lugg (1968)
CO - N_2	295.8	2.12 ± 0.02	Ivakin and Suetin (1964)
NO - N_2	293.2	2.06 ± 0.01	Weissman (1964)
HCl - N_2	324.1	1.74	Mian et al. (1969)

[a] Measured at atmospheric pressure, 1.01×10^5 Pa, unless noted otherwise.

[b] Pressure = 9.3×10^4 Pa.

[c] Pressure = 9.2×10^4 Pa.

Phillips (1975) has developed a more general expression from approximate theoretical analysis.

4.5.2.2 Thermophoretic velocity. Thermophoresis refers to the tendency of particles suspended in a fluid to migrate along a thermal gradient toward colder temperatures. For particles that are small relative to the mean free path of air, this behavior is easily understood: fluid molecules striking the particle on the warm side impart more kinetic energy than those striking the particle on the cool side, and thus there is a net force in the direction from hot to cold. For large particles, the process is more complex: the thermophoretic force depends not only on the temperature gradient but also on the relative thermal conductivities of the particle and the fluid.

The resulting drift velocity (relative to the fluid) is determined by a balance between the thermophoretic force and the viscous drag and is commonly expressed as

$$\mathbf{v_t} = - K \frac{\nu}{T} \nabla T \tag{4.5}$$

where ν is the kinematic viscosity of the fluid (1.50×10^{-5} m^2 s^{-1} for air at 293 K). The coefficient K can be determined from an interpolation formula (Talbot et al., 1980):

$$K = 2\, C_s \frac{\left(\frac{k_g}{k_p} + C_t\, Kn\right)\left[1 + Kn\left\{1.2 + 0.41 \exp\left(-\frac{0.88}{Kn}\right)\right\}\right]}{(1 + 3\, C_m\, Kn)\,(1 + 2\frac{k_g}{k_p} + 2\, C_t\, Kn)} \tag{4.6}$$

In this expression, k_g and k_p represent the thermal conductivity of the fluid and particle, respectively. The coefficients have values $C_m = 1.146$, $C_s = 1.147$ and $C_t = 2.20$. For particles in air with $d_p \leq 3$ μm and k_g/k_p in the range 0.01-0.5, K varies between 0.1 and 0.6.

4.5.2.3 Gravitational settling velocity. Particles suspended in air attain a terminal settling velocity within a characteristic time of ms or less (Seinfeld, 1986). The settling velocity is determined by a balance between gravitational force and fluid drag:

$$v_g = \frac{d_p^2 \rho_p g C_c}{18 \mu} \tag{4.7}$$

where ρ_p is the particle density, and g is the acceleration of gravity, and C_c is the slip correction factor.

4.5.3 Particle Deposition from a Natural Convection Flow

4.5.3.1 Preliminary comments. Natural convection flows arise from temperature differences among parcels of air. An air parcel that is cooler than the surrounding air has a higher density and tends to settle; conversely, a warm parcel is buoyant and tends to rise. Some natural convection flow is likely to be present under most circumstances in indoor rooms. For example, a temperature difference between a wall and the air of 0.85 K is sufficient to induce a peak natural convection velocity of ~ 0.06 m s^{-1} along the wall (Schiller, 1984). Temperature differences of this magnitude are almost unavoidable, and much larger temperature differences are expected in some circumstances. For the present problem, the effect of natural convection flows is to bring the pollutants into the proximity of a surface much more rapidly than would occur by Brownian motion or molecular diffusion alone in still air.

Although a comprehensive theoretical treatment of pollutant deposition in an enclosure with natural convection flow is not possible at present, useful estimates can be obtained by imposing certain restrictions and using empirical results in combination with theoretical analysis. For the case of laminar natural-convection flow adjacent to a vertical wall, particle deposition fluxes can be predicted from boundary-layer theory. For turbulent natural-convection flow adjacent to vertical walls, and for natural-convection-induced deposition onto floors and ceilings, theoretical treatments are unavailable. In the

latter cases, an estimate of pollutant fluxes will be made by analogy between heat transfer and mass transfer, using data on natural-convection heat transfer rates that are available in the literature. Because fundamental results for heat and mass transfer onto surfaces of arbitrarily sized complete enclosures are unavailable, deposition onto enclosure surfaces will have to be estimated by summing separate predictions made for the walls, floor and ceiling of a room of a given size. In making such estimates in the present chapter, the surfaces are considered to be independent, i.e. a natural convection flow is taken to be determined by the difference in temperature of the surface and the nearby air without regard for flows arising, for example, from other surfaces. In addition, the analysis is carried out for the case of isothermal surfaces, and the air temperature outside the boundary layer is assumed to be uniform.

The analogy between heat and mass transfer arises because the governing equations for the temperature distribution and pollutant concentration for dilute, highly reactive gases in a forced convection flow are of analogous form. The normalized pollutant concentration, $\omega = C/C_\infty$, is analogous to the normalized temperature difference, $1-\theta$, where $\theta = (T-T_\infty)/(T_S - T_\infty)$, and T_S is the surface temperature. The pollutant diffusivity, D, is analogous to the thermal diffusivity, α. However, because density differences resulting from temperature gradients generate natural convection flows, but density differences resulting from differences in pollutant concentration are too small to do so, the analogy does not strictly hold for the case of natural convection flows. Nevertheless, the approximation that this analogy still holds provides the most accurate practical tool currently available for obtaining estimates of pollutant deposition velocities. For gaseous pollutants, the analogy can be applied by substituting the Schmidt number, $Sc = \nu/D$ for the Prandtl number, $Pr = \nu/\alpha$, and by substituting the Sherwood number, $Sh = v_d\, x/D$, for the Nusselt number, $Nu = h\, x/k_g$, in empirical expressions for the heat transfer rate observed in natural convection flows. In these expressions, x represents the distance along the surface from the leading edge in the direction of flow, h is the heat

transfer coefficient (units W m^{-2} K^{-1}), and k_g is the thermal conductivity of air (units W m^{-1} K^{-1}). A major body of research on natural convection heat transfer is summarized by Bejan (1984) and Incropera and DeWitt (1984), from which the heat-transfer-based pollutant deposition estimates given in this chapter will be taken.

For the case of airborne particles, the same substitutions are made to estimate particle deposition rates due to convective diffusion from the natural-convection heat-transfer data. A warning: the Schmidt number for particles in air is generally much higher than the Prandtl number of fluids. Thus any failure of the heat transfer results to extrapolate well to high Prandtl numbers will lead to inaccurate results. Unlike the solution for gaseous species, particle migration is affected by thermophoresis and gravitational sedimentation. As these effects are not embodied in the heat transfer analogy, they will be accounted for by vectorially adding the deposition flux due to those processes to the flux due to convective deposition:

$$v_d = v_D + v_t + s_g v_g \tag{4.8}$$

where s_g is a surface orientation coefficient equal to -1 for a downward-facing surface, 0 for a vertical surface, and +1 for an upward-facing surface. If the result of equation (4.8) is negative, the deposition velocity for that surface is set to zero.

The temperature gradient near the surface is needed to compute the thermophoretic velocity. This may be obtained directly from the empirical expressions for the Nusselt number, Nu, and the definition of the heat transfer coefficient. In the results presented below, one of two relationships is used to determine the thermophoretic velocity from the empirically determined Nusselt number, according to whether a horizontal dimension, L, of the surface, or the height, H, of the wall or of the enclosure is used in the definition of Nu:

$$v_{t,L} = -N_t \left(\frac{\nu}{L}\right) \overline{Nu_L} \tag{4.9}$$

$$v_{t,H} = -N_t \left(\frac{\nu}{H}\right) \overline{Nu_H} \tag{4.10}$$

Here the coefficient N_t is a thermophoresis parameter, defined by $N_t = K\,(T_s - T_\infty) / T_\infty$, and the overbar denotes an average over the surface.

4.5.3.2 Deposition onto vertical surfaces

4.5.3.2.1 Laminar flow. Particle deposition to a vertical isothermal semi-infinite flat plate in laminar natural convection flow was analyzed in Chapter 3. In this chapter, the problem formulation and solution technique are sketched and the results are presented. In addition, the analysis is extended to include reactive gases, which were not considered in the original work.

The treatment explicitly includes the effects of thermophoresis; sedimentation is neglected as a minor factor. A system of governing boundary-layer equations is developed to describe the transport of mass, momentum, heat and particles in the air adjacent to the surface:

$$\frac{\partial u}{\partial x} + \frac{\partial v}{\partial y} = 0 \tag{4.11}$$

$$u\frac{\partial u}{\partial x} + v\frac{\partial u}{\partial y} = \nu\frac{\partial^2 u}{\partial y^2} + g\frac{|\Delta T|}{T_\infty}\theta \tag{4.12}$$

$$u\frac{\partial \theta}{\partial x} + v\frac{\partial \theta}{\partial y} = \alpha\frac{\partial^2 \theta}{\partial y^2} \tag{4.13}$$

$$u\frac{\partial \omega}{\partial x} + v\frac{\partial \omega}{\partial y} = D\frac{\partial^2 \omega}{\partial y^2} + \nu\, N_t \frac{\partial \omega}{\partial y}\frac{\partial \theta}{\partial y} \tag{4.14}$$

In these expressions, u and v represent the air velocities along the wall and normal to the wall, respectively; x represents the distance along the wall in the direction of flow; y represents the distance normal to the wall; and $\Delta T = T_s - T_\infty$.

The boundary conditions for this system of equations state that the air is motionless at the wall and outside the boundary layer, and that the air outside the boundary layer has uniform temperature and particle concentration. In addition, the temperature of the wall is uniform and the wall is a perfect sink for particles so that the particle concentration at the wall is zero.

The problem is converted from a system of coupled partial differential equations to a system of coupled ordinary differential equations by means of a similarity transformation. The solution is obtained numerically for many values of Sc, representing changes in particle size, and of N_t, representing both changes in temperature difference and in the thermophoresis coefficient, K. The results are presented in Figure 4.1, which shows a particle flux parameter as a function of N_t and particle diameter. To obtain the average deposition velocity in dimensional form from this figure, the following expression is used:

$$v_d = \frac{4}{3} a\, \alpha^{1/3}\, D^{2/3}\, H^{-1/4}\, \{\omega'(0)/\, Le^{1/3}\} \qquad (4.15)$$

where H is the height of the wall, $Le = \alpha/D$ is the Lewis number, and $a = \left[\frac{g\,|\,\Delta T\,|}{4\nu^2\, T_\infty}\right]^{1/4}$.

This analysis can be directly extended to the case of reactive gases. The same governing equations and boundary conditions apply with ω representing the concentration of the gaseous species, and $N_t = 0$. Analyses were carried out for pollutant diffusivities in the range $(0.5\text{-}8.0) \times 10^{-5}$ m^2 s^{-1}, and the results are presented in Figure 4.2. A typical case is a 3-m wall with $\Delta T = 2$ K and $D = 1.5 \times 10^{-5}$ m^2 s^{-1}; $v_d = 8.4 \times 10^{-4}$ m s^{-1} for these conditions. For gases, as for ultrafine particles, the deposition velocity is independent of the sign of the temperature difference, owing to the relatively high rate of diffusive transport for these smaller species.

4.5.3.2.2 Turbulent flow. For moderate to large values of $|\,\Delta T\,|$, and for tall walls, the natural convection flow may become turbulent. In the case of an isolated flat plate, the

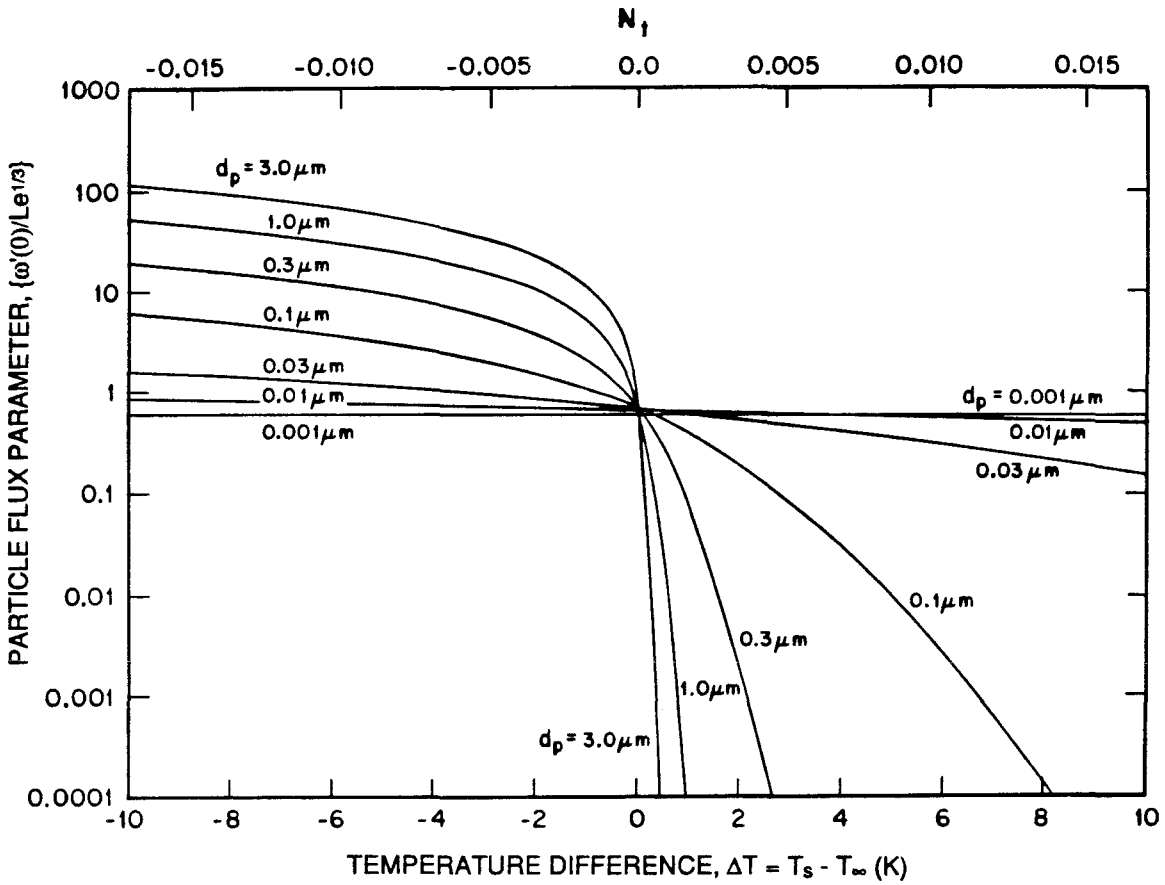

Figure 4.1 Particle flux parameter onto a vertical isothermal plate as a function of particle diameter and temperature difference. An air temperature, T_∞ = 293 K, and a thermophoresis coefficient, K=0.5, have been assumed. The average deposition velocity to a vertical surface in natural convection flow is obtained using the results in this figure in equation 4.15. See also Chapter 3.

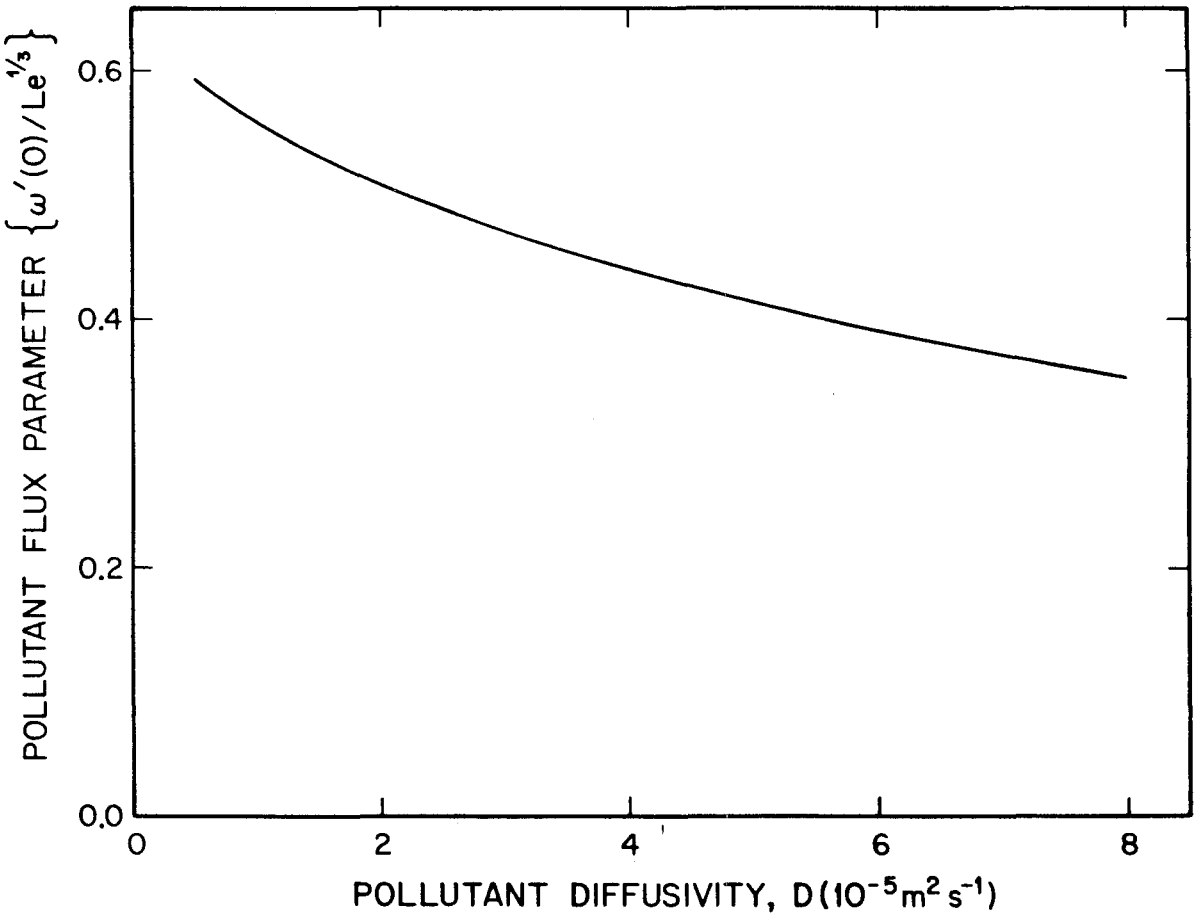

Figure 4.2 Pollutant flux parameter onto a vertical isothermal plate as a function of diffusivity for highly reactive gaseous pollutants. An air temperature, T_∞ = 293 K has been assumed. The average deposition velocity to a vertical surface in natural convection flow is obtained using these results in equation 4.15.

transition to turbulence occurs at $Ra_H \sim 10^9$ (Ede, 1967), where Ra_H is the Rayleigh number, defined by

$$Ra_H = \frac{g \beta | \Delta T | H^3}{\alpha \nu} \tag{4.16}$$

where β is the coefficient of thermal expansion ($\beta = 1/T$ for an ideal gas). Churchill and Chu (1975) have developed an empirical correlation for natural convection heat transfer to a vertical plate that covers both laminar and turbulent flow conditions. Applying the analogy between mass and heat transfer to their result, and adding the thermophoretic deposition velocity vectorially, one obtains

$$v_d = v_{t,H} + \frac{D}{H}\left[0.825 + \frac{0.387\, Ra_H^{1/6}}{\left\{1 + (0.492/Sc)^{9/16}\right\}^{8/27}}\right]^2 \tag{4.17}$$

where the thermophoretic velocity, $v_{t,H}$ is determined from equation (4.10). The average Nusselt number is given by

$$\overline{Nu_H} = \left[0.825 + \frac{0.387\, Ra_H^{1/6}}{\left\{1 + (0.492/Pr)^{9/16}\right\}^{8/27}}\right]^2 \tag{4.18}$$

This expression is intended to be applied for the entire range of Ra_H and Pr from 0 to ∞. However, since equation (4.15) was developed from more rigorously applicable assumptions, it is used in favor of equation (4.17) for $Ra_H < 10^9$. Furthermore, since the effect of turbulence is to enhance deposition, the larger of the two results obtained from equations (4.15) and (4.17) is used for $Ra_H > 10^9$.

The predicted deposition velocity for natural convection along walls is shown for a range of temperature differences and pollutant diffusivities in Figure 4.3. Thermophoresis plays a very important role in deposition of particles with diameter

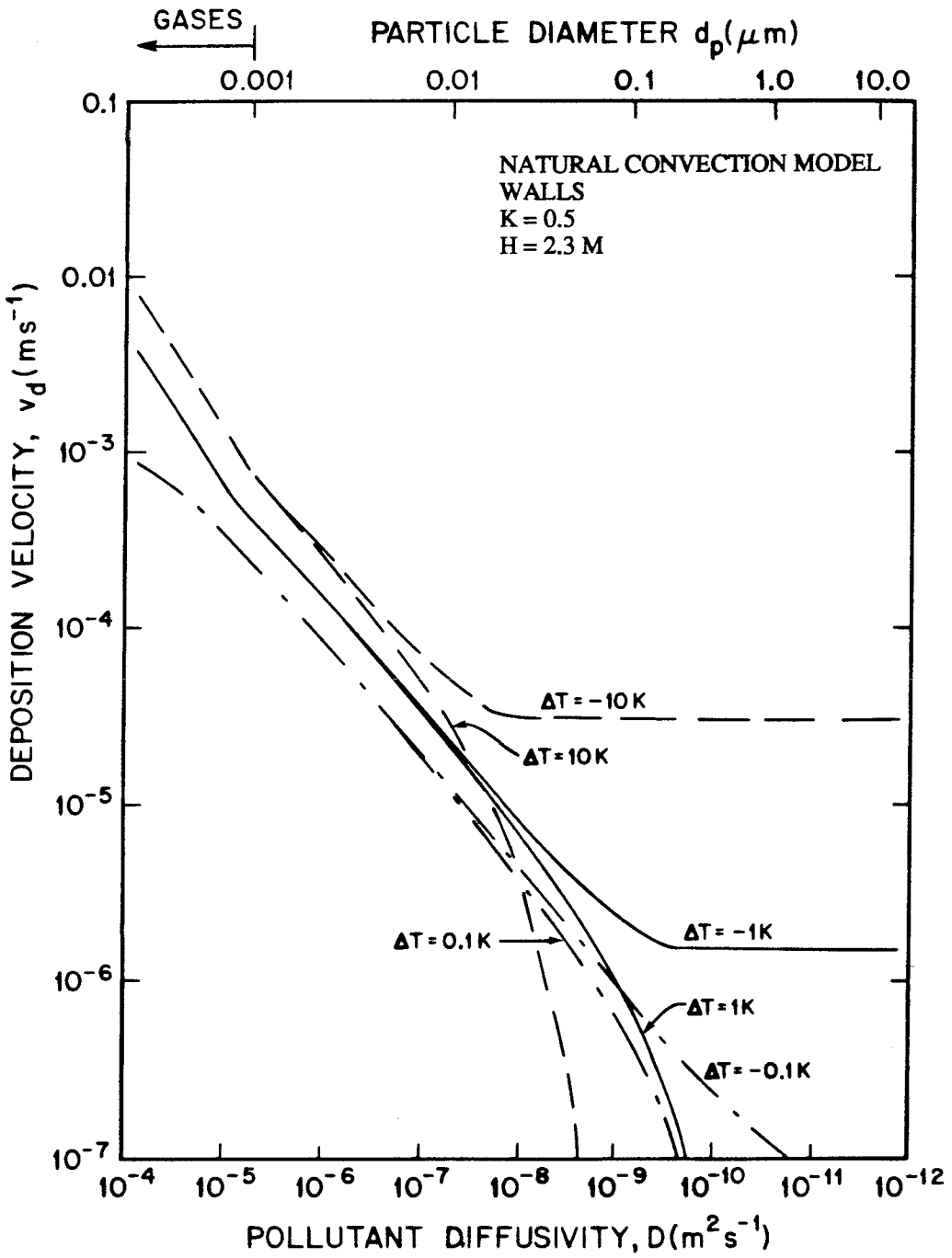

Figure 4.3 Mass-transport-limited deposition velocity averaged over height, H=2.3 m, of a wall according to the natural convection model (equations 4.15-4.18). ΔT is the temperature difference between the wall, T_S, and the air, T_∞ = 293 K. Thermophoresis accounts for the difference in deposition velocity for larger particles between cool walls and warm walls. The thermophoresis coefficient, K in equation 4.5, is taken to be 0.5.

greater than about 0.05 μm. For example, for particles of 0.22 μm diameter (a representative size of cigarette smoke), the deposition velocity is more than ten times greater to a wall that is 1K cooler than the air than to a wall that is 1K warmer. Thus, vertical surfaces are expected to soil much more rapidly if they are cool instead of being warm relative to the room air.

4.5.3.3 Deposition onto horizontal surfaces. There are no theoretical descriptions of natural convection flow near horizontal surfaces that are analogous to the boundary-layer description of laminar natural convection flow adjacent to a vertical wall. Consequently, one must rely entirely on empirical correlations as a basis for estimating the mass-transport-limited deposition velocity of pollutants onto horizontal surfaces.

It is necessary to distinguish surfaces according to whether they are "enclosed" or "isolated." For the present purposes, an enclosed horizontal surface is one with vertical surfaces extending from it along all sides. Ceilings and floors are common examples of enclosed horizontal surfaces. An example of an isolated horizontal surface is a desk top. The distinction is made because there are stable temperature differences for enclosed surfaces, whereas for isolated surfaces any temperature difference induces flow.

4.5.3.3.1 Enclosed surfaces. For an enclosed horizontal surface, no flow occurs if the surface is upward facing and cooler than the air, or if the surface is downward facing and warmer than the air. In addition, no flow occurs whenever $Ra_H < O(10^3)$ (Bejan, 1984); however, such a small value of Ra_H is unlikely for a room. For the no-flow condition, the pollutant concentration and temperature profiles are approximated as the steady-state solutions to the one-dimensional diffusion and conduction equations, respectively. Under this approximation, a constant gradient between the surface and the midline of the room is obtained. The resulting transport velocity due to diffusion is the diffusion coefficient divided by half the height of the room. Thus,

$$v_d = s_g v_g + v_{t,H} + 2\frac{D}{H} \tag{4.19}$$

And, in determining the thermophoretic transport velocity, the mean Nusselt number is given by

$$\overline{Nu_H} = 2 \tag{4.20}$$

If the temperature gradient leads to an unstable atmosphere, convective flow is induced and the deposition velocity is enhanced. In this case, the deposition velocity is estimated by the analogy between heat and mass transfer from the following expressions, derived from the work of Globe and Dropkin (1959), and appropriate for $3 \times 10^5 < Ra_H < 1.4 \times 10^9$:

$$v_d = s_g v_g + v_{t,H} + \frac{D}{H}\{0.087\, Ra_H^{1/3}\, Sc^{0.074}\} \tag{4.21}$$

$$\overline{Nu_H} = 0.087\, Ra_H^{1/3}\, Pr^{0.074} \tag{4.22}$$

Representative results from these expressions are presented in Figures 4.4 and 4.5. For gases and small particles (<~0.003 μm) the predominant transport process is convective diffusion. Thermophoresis plays an important role for particles in the size range 0.003-0.3 μm. For larger particles, sedimentation dominates the other transport mechanisms.

4.5.3.3.2 Isolated surfaces. In the correlations that follow, the characteristic length, L, of the surface is the area of the surface divided by the perimeter. For an upward facing heated surface, or a downward facing cool surface, the deposition velocity may be estimated from the analogy between heat and mass transfer by the following expressions (Incropera and DeWitt, 1984):

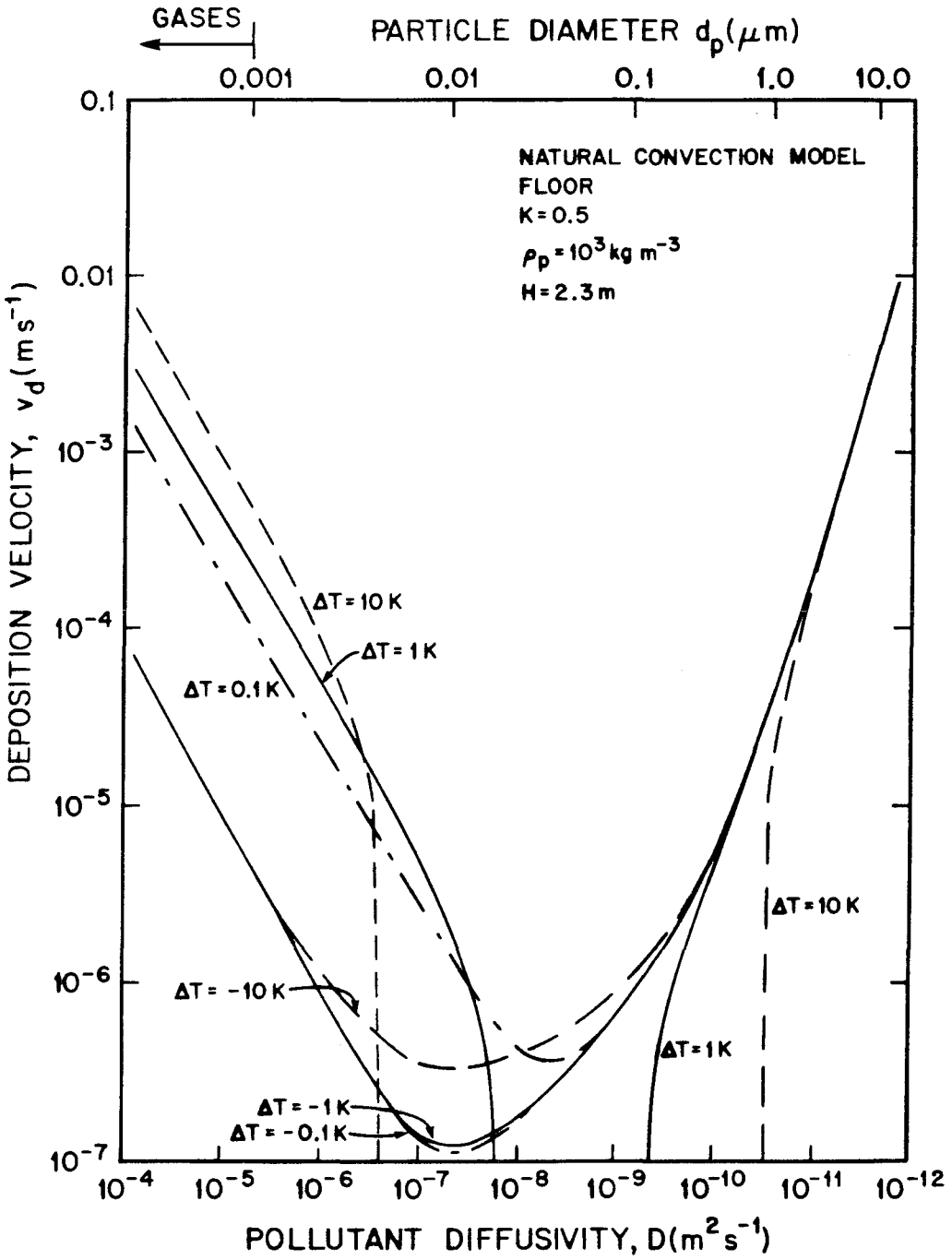

Figure 4.4 Mass-transport-limited deposition velocity to the floor of a room according to the natural convection model (equations 4.19-4.22). Particles are assumed to have unit density, i.e. $\rho_p = 10^3$ kg m^{-3}. See Figure 4.3 caption for further assumptions.

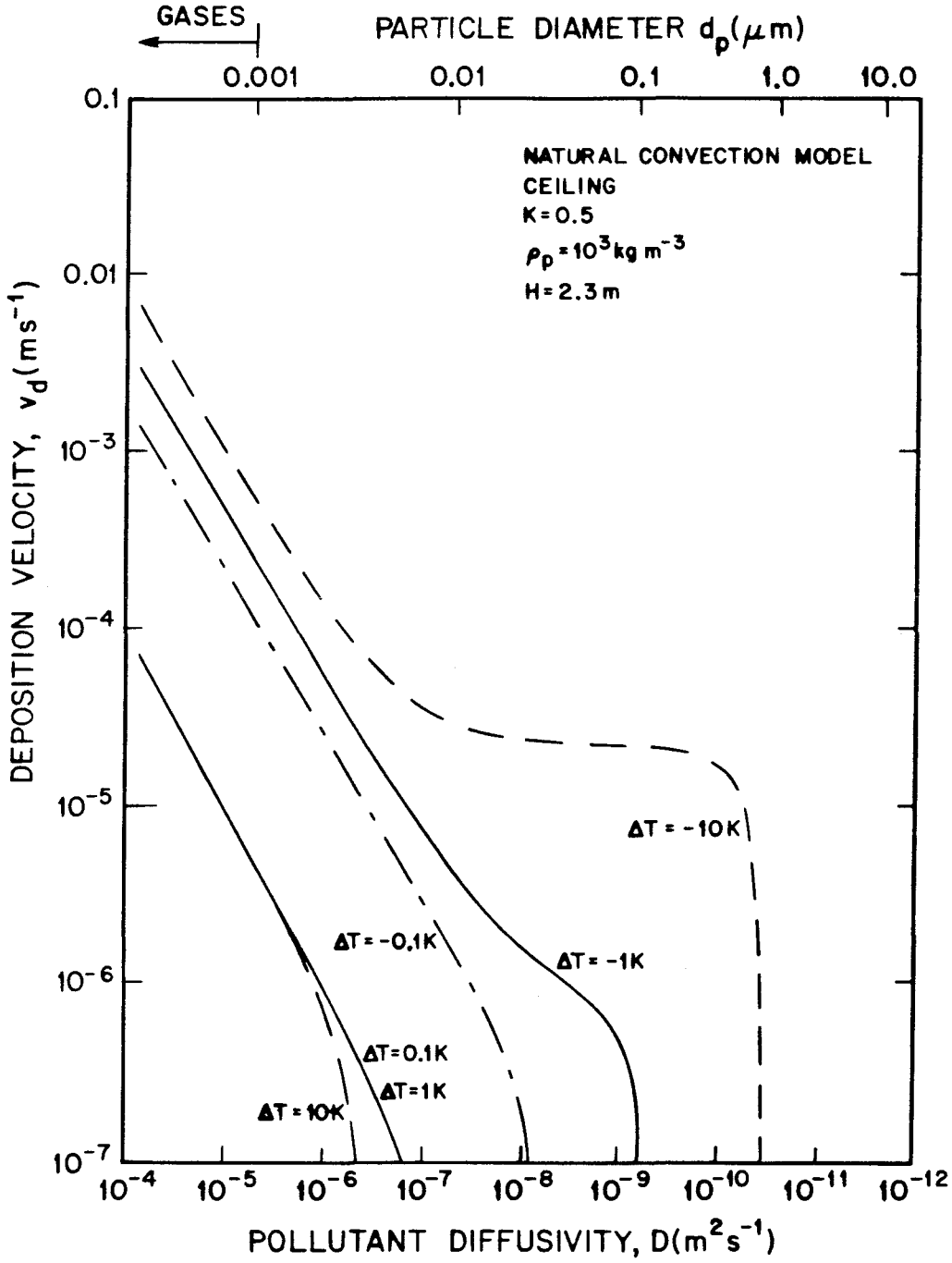

Figure 4.5 Mass-transport-limited deposition velocity to the ceiling of a room according to the natural convection model (equations 4.19-4.22). Particles are assumed to have unit density, i.e. $\rho_p = 10^3$ kg m^{-3}. See Figure 4.3 caption for further assumptions.

For $10^4 < Ra_L < 10^7$:

$$v_d = s_g v_g + v_{t,L} + \frac{D}{L}\{0.54\ Ra_L^{1/4}\} \tag{4.23}$$

$$\overline{Nu_L} = 0.54\ Ra_L^{1/4} \tag{4.24}$$

For $10^7 < Ra_L < 10^{11}$:

$$v_d = s_g v_g + v_{t,L} + \frac{D}{L}\{0.15\ Ra_L^{1/3}\} \tag{4.25}$$

$$\overline{Nu_L} = 0.15\ Ra_L^{1/3} \tag{4.26}$$

For a downward facing heated surface or an upward facing cool surface, and for $10^5 < Ra_L < 10^{10}$ the following expressions are appropriate:

$$v_d = s_g v_g + v_{t,L} + \frac{D}{L}\{0.27\ Ra_L^{1/4}\} \tag{4.27}$$

$$\overline{Nu_L} = 0.27\ Ra_L^{1/4} \tag{4.28}$$

4.5.4 Particle Deposition from a Forced Laminar Flow. Near-surface flows in several situations may be represented by a forced laminar flow parallel to a surface. The air flow along the walls of a laminar-flow clean room is one example. As a second example, Schiller (1984) noted that numerical simulations of a two-dimensional enclosure with one warm and one cool vertical side produced air flow profiles near the adiabatic bottom and top sides that were similar to forced flow parallel to a flat plate.

In this chapter, an idealized case is considered: the direction of flow is parallel to the surface which is assumed to extend infinitely from the leading edge, the edge being normal to the direction of free stream air flow. The surface is considered in isolation, and

the air velocity and air temperature are constant outside of a thin boundary layer adjacent to the surface. The surface may have a temperature different from that of the air, in which case thermophoresis may contribute to particle migration in the boundary layer. However, the temperature difference between the surface and the air is assumed to be small enough that the effects of buoyancy on the momentum of air can be neglected. Practically, this is a reasonable assumption for a vertical surface if the free-stream air velocity, u_∞, is much larger than the peak air velocity that would be attained in a pure natural convection flow for the given temperature difference. For reference, the peak air velocity along an isolated, isothermal vertical surface in natural convection flow is (Schlichting, 1979)

$$u_{max} = 0.55\left[\frac{g \times |\Delta T|}{T_\infty}\right]^{\frac{1}{2}} \tag{4.29}$$

If, for example, the plate length is 2 m and $\Delta T = 1$ K, then $u_{max} = 0.14$ m s^{-1}.

The particle deposition velocity is obtained by solving the same system of equations as for the natural convection case, except that the buoyancy term is omitted from the momentum equation.

$$\frac{\partial u}{\partial x} + \frac{\partial v}{\partial y} = 0 \tag{4.30}$$

$$u\frac{\partial u}{\partial x} + v\frac{\partial u}{\partial y} = \nu\frac{\partial^2 u}{\partial y^2} \tag{4.31}$$

$$u\frac{\partial \theta}{\partial x} + v\frac{\partial \theta}{\partial y} = \alpha\frac{\partial^2 \theta}{\partial y^2} \tag{4.32}$$

$$u\frac{\partial \omega}{\partial x} + v\frac{\partial \omega}{\partial y} = D\frac{\partial^2 \omega}{\partial y^2} + \nu N_t \frac{\partial \omega}{\partial y}\frac{\partial \theta}{\partial y} \tag{4.33}$$

The boundary conditions for this problem also distinguish it from the natural convection case and are given below

$$u(0,y) = u(x,\infty) = u_\infty \tag{4.34}$$

$$u(x,0) = v(x,0) = 0 \tag{4.35}$$

$$\theta(0,y) = \theta(x,\infty) = 0 \tag{4.36}$$

$$\theta(x,0) = 1 \tag{4.37}$$

$$\omega(0,y) = \omega(x,\infty) = 1 \tag{4.38}$$

$$\omega(x,0) = 0 \tag{4.39}$$

As for the solution of the natural convection flow problem (Chapter 3), a similarity transform is introduced to convert the system of partial differential equations into a system of ordinary differential equations. The continuity equation (4.30) is satisfied by writing the velocity components in terms of the stream function ψ:

$$u = \frac{\partial \psi}{\partial y}; \quad v = -\frac{\partial \psi}{\partial x} \tag{4.40}$$

A solution for ψ, θ, and ω is sought such that

$$\psi = (\nu \times u_\infty)^{1/2} \zeta(\eta) \tag{4.41}$$

$$\theta = \theta(\eta) \tag{4.42}$$

$$\omega = \omega(\eta) \tag{4.43}$$

where

$$\eta = y\left[\frac{u_\infty}{\nu x}\right]^{\frac{1}{2}} \tag{4.44}$$

Substituting into the partial differential equations (4.31)-(4.33), the following ordinary differential equations are obtained:

$$\zeta''' + \frac{1}{2}\zeta\,\zeta'' = 0 \tag{4.45}$$

$$\theta'' + \frac{1}{2}\mathrm{Pr}\,\zeta\,\theta' = 0 \tag{4.46}$$

$$\omega'' + \frac{1}{2}\mathrm{Sc}\,\zeta\,\omega' + N_t\,\mathrm{Sc}\,\theta'\,\omega' = 0 \tag{4.47}$$

where primes indicate derivatives with respect to the independent variable η. The first two equations describe momentum and heat transport in the boundary layer of the forced convection flow. Equation (4.47) describes particle transport in the boundary layer, with the terms on the left accounting for Brownian motion, advection, and thermophoresis, respectively.

The boundary conditions for these equations are

$$\zeta(0) = \zeta'(0) = 0;\ \zeta'(\infty) = 1 \tag{4.48}$$

$$\theta(0) = 1;\ \theta(\infty) = 0 \tag{4.49}$$

$$\omega(0) = 0;\ \omega(\infty) = 1 \tag{4.50}$$

The system of equations was solved numerically in two steps using the shooting method to transform the boundary value problem into an initial value problem, and a fourth-order Runge-Kutta integration routine (Press et al., 1986). In the first step, the system (4.45), (4.46), (4.48) and (4.49) was solved to obtain boundary conditions for $\zeta''(0)$ and $\theta'(0)$ that satisfied the conditions at $\eta \to \infty$. The momentum and heat transport equations were then converted to an initial value problem by altering the boundary conditions (4.48) and (4.49):

$$\zeta(0) = \zeta'(0) = 0;\ \zeta''(0) = 0.33206 \tag{4.51}$$

$$\theta(0) = 1;\ \theta'(0) = -0.295805 \tag{4.52}$$

Finally, the system of equations (4.45)-(4.47) was solved subject to the boundary conditions (4.50)-(4.52), to obtain $\omega'(0)$ for a range of values of Sc and N_t.

For horizontal surfaces, the effect of gravity is incorporated by vectorially summing the gravitational settling velocity to the deposition velocity associated with advective diffusion and thermophoresis. The average total deposition velocity onto a surface from a forced laminar flow is then determined as

$$v_d = 2\,D\left[\frac{u_\infty}{\nu\,L}\right]^{\frac{1}{2}}\omega'(0) + s_g\,v_g \tag{4.53}$$

Results for a vertical surface are illustrated in Figure 4.6. Note that for equation (4.53) to be valid, the Reynolds number of the flow must be less than (2-6) $\times$ 10^5, a range of values that marks the onset of the transition to turbulence for this system (Schlichting, 1979).

4.5.5 Particle Deposition from a Homogeneously Turbulent Flow. Corner and Pendlebury (1951) analyzed the deposition of particles onto the surfaces of a rectangular chamber assuming homogeneous turbulence in the air in the core of the chamber. In this section, their analysis is first summarized, then extended to include the case of reactive gases and to account for the effects of thermophoresis. Subsequent experimental and theoretical developments based on their work are reviewed. The implications of the theory are assessed, and some comments are made on its applicability to indoor environments.

The model formulated by Corner and Pendlebury derives from several key assumptions and approximations: (a) there is a boundary layer of thickness δ adjacent to each surface in which the mean air motion is parallel to the surface; (b) the gradient of the

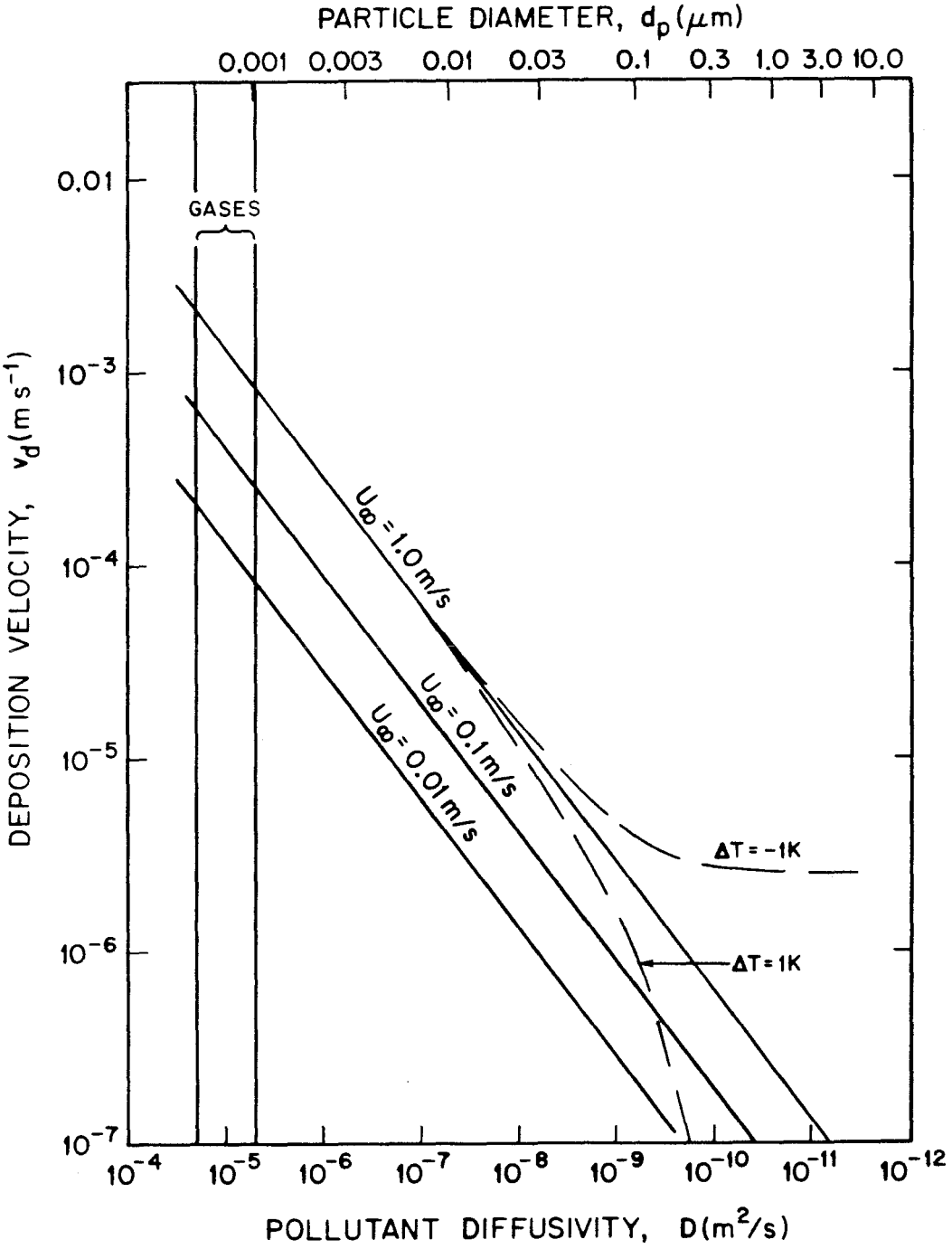

Figure 4.6 Mass-transport-limited deposition velocity to the walls of a room according to the forced laminar air flow regime (equation 4.53). The solid lines are based on isothermal conditions. For the dashed lines, the thermophoresis coefficient, K, is taken to be 0.5.

mean velocity is constant within the boundary layer; (c) the particle concentration is uniform outside of the boundary layer; (d) particle transport through the boundary layer occurs by sedimentation, Brownian motion, and eddy (turbulent) diffusion; (e) the eddy diffusion coefficient has the form $D_e = K_e y^2$ where y is the distance normal to the surface, and $K_e = k_o^2$ du/dy, where k_o is von Kármán's constant (commonly taken to be 0.4), and du/dy is the velocity gradient; (f) that transient effects can be neglected in computing the flux to surfaces; and (g) that turbulent diffusion dominates Brownian motion at the edge of the boundary layer, i.e. $D << K_e \delta^2$.

From these assumptions, a mass balance in the boundary layer leads to a set of three governing equations:

$$\text{Vertical surfaces: } \frac{\partial}{\partial y}\left[(K_e y^2 + D)\frac{\partial C}{\partial y}\right] = 0 \tag{4.54}$$

$$\text{Downward-facing surfaces: } \frac{\partial}{\partial y}\left[(K_e y^2 + D)\frac{\partial C}{\partial y}\right] - v_g \frac{\partial C}{\partial y} = 0 \tag{4.55}$$

$$\text{Upward-facing surfaces: } \frac{\partial}{\partial y}\left[(K_e y^2 + D)\frac{\partial C}{\partial y}\right] + v_g \frac{\partial C}{\partial y} = 0 \tag{4.56}$$

The boundary conditions are identical for the three cases:

$$C(0) = 0;\ C(\delta) = C_\infty \tag{4.57}$$

These equations are solved for the concentration profile. The deposition velocities according to the Corner and Pendlebury analysis, v_{CP}, are computed from these results and from the definition of the deposition velocity.

$$\text{Vertical surfaces: } v_{CP} = \frac{2}{\pi}(D\,K_e)^{1/2} \tag{4.58}$$

Downward-facing surfaces: $$v_{CP} = \frac{v_g}{\left[\exp\left(\frac{\pi}{2}\frac{v_g}{\sqrt{DK_e}}\right) - 1\right]} \quad (4.59)$$

Upward-facing surfaces: $$v_{CP} = \frac{v_g}{\left[1 - \exp\left(-\frac{\pi}{2}\frac{v_g}{\sqrt{DK_e}}\right)\right]} \quad (4.60)$$

The limiting behavior of equations (4.59) and (4.60) is consistent with expectations: for large particles, $v_g >> (2/\pi)\ (D\ K_e)^{1/2}$, and so $v_{CP} \rightarrow 0$ for downward surfaces and $v_{CP} \rightarrow v_g$ for upward surfaces; for small particles, $v_g << (2/\pi)\ (D\ K_e)^{1/2}$, and so $v_{CP} \rightarrow (2/\pi)\ (D\ K_e)^{1/2}$ for all surfaces, independent of orientation.

The small particle limit points to the extension of this model to the case of reactive gases. In this case, gravity does not influence pollutant motion, so there is no difference in deposition velocity according to surface orientation. Thus, $v_{CP} = (2/\pi)\ (D\ K_e)^{1/2}$ for deposition of reactive gases onto all surfaces, provided that each of the approximations introduced by Corner and Pendlebury applies. In fact, if the turbulence intensity is small, approximation (g) begins to fail for small particles and gases. A more accurate analysis yields the following expression for this case:

$$v_{CP} = \frac{1}{\tan^{-1}\left(\delta\sqrt{\frac{K_e}{D}}\right)}\left[D\ K_e\right]^{1/2} \quad (4.61)$$

where the boundary layer thickness, δ, can be estimated in relation to K_e (cf. Corner and Pendlebury, 1951, p. 651) by $\delta \sim 1.2\ (\nu/K_e)^{4/9}\ X^{1/9}$, X being the length of the surface in the direction of flow.

The analysis by Corner and Pendlebury accounts for the influence of Brownian motion, eddy diffusion, advection, and gravitational settling. By not including thermophoresis, the analysis strictly applies only when the surfaces are at the same temperature as the air. However, for indoor environments, the rate of heat transfer across

surfaces may be large, leading to significant temperature differences between surfaces and the indoor air, even when the air in the core of the room is turbulently stirred. The effects of thermophoresis may be estimated for use in this analysis, as was done for some of the natural convection cases, by vectorially adding the deposition flux due to thermophoresis to that given by equations (4.58)-(4.60). As in the analysis of forced laminar flow, buoyancy effects on air movement are not considered, a reasonable approximation if the rate of heat transfer at the surface due to the prevailing turbulence intensity is much larger than would result from natural convection alone. Under these conditions, the temperature gradient in the air at any surface may be obtained by solving equation (4.54) with the thermal diffusivity, α, substituted for D; the normalized temperature difference, θ, substituted for C; and boundary conditions $\theta(0) = 1$ and $\theta(\delta) = 0$. The total deposition velocity is then given by

$$v_d = v_{CP} + v_t \tag{4.62}$$

where

$$v_t = - N_t \nu \frac{(K_e/\alpha)^{1/2}}{\tan^{-1}[\delta (K_e/\alpha)^{1/2}]} \tag{4.63}$$

Figure 4.7 depicts the deposition velocity as a function of turbulence intensity, particle size, and temperature difference for the homogeneous turbulence flow regime.

Several additional extensions of this model have been suggested. Crump and Seinfeld (1981) derived expressions for an enclosure of arbitrary shape and for the specific case of a spherical enclosure. They also obtained expressions for a more general form of the eddy diffusivity: $D_e = K_e y^n$. McMurry and Rader (1985) analyzed the rate of particle deposition in a spherical chamber in which electrostatic effects were significant. Shimada et al. (1987) considered deposition in the case of a stirred chamber with sand-roughened surfaces.

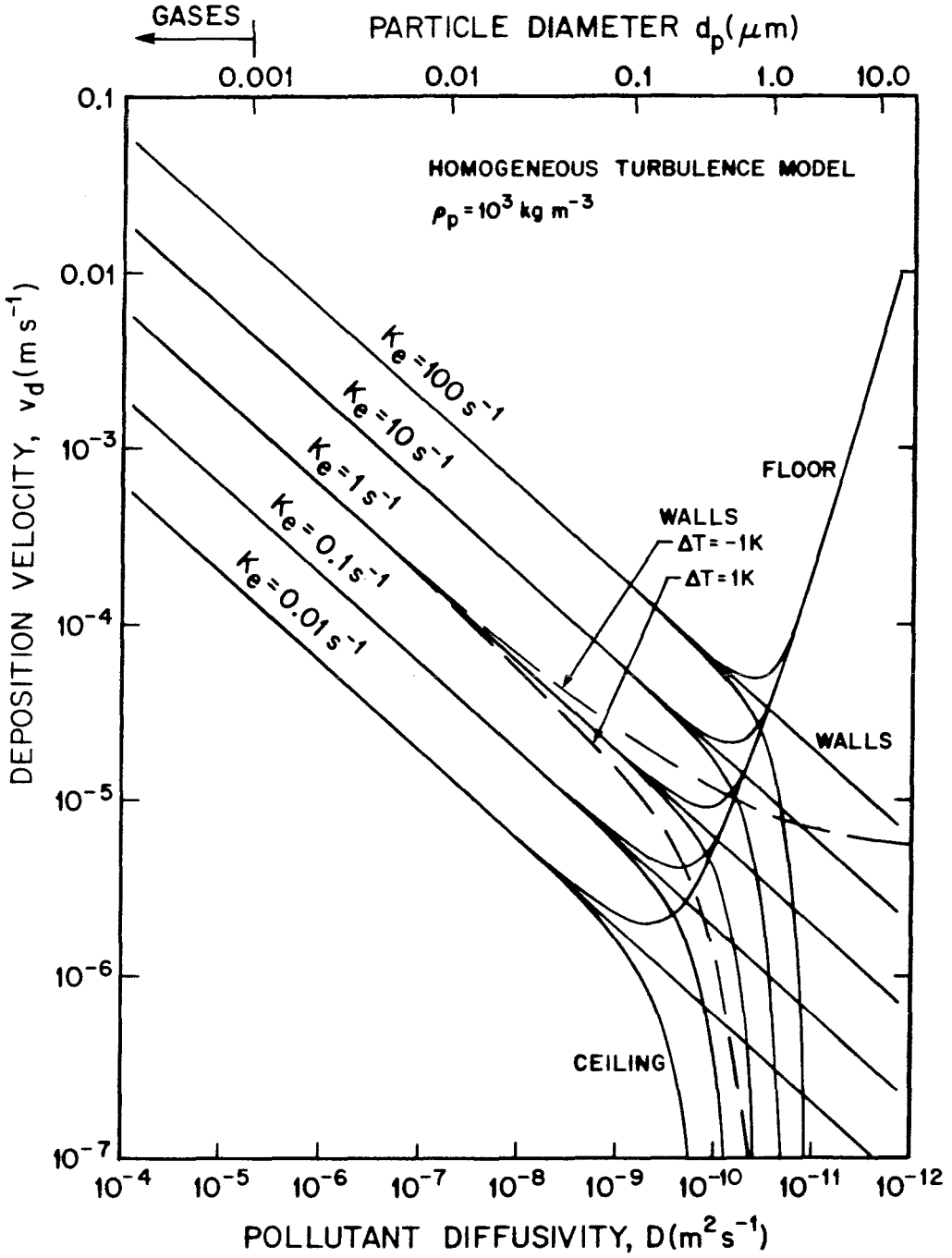

Figure 4.7 Mass-transport-limited deposition velocity of pollutants to surfaces of a room according to the homogeneous turbulence model (equations 4.58-4.63). The parameter K_e indicates the turbulence intensity. The difference between ceiling, floor and walls for larger particles results from gravitational settling, and is computed assuming unit particle density, ρ_p. The solid lines are based on isothermal conditions. Dashed lines indicating an estimate of the thermophoretic effect are supplied only for the case of $K_e = 1\ s^{-1}$, but an analogous effect would be seen at other values of K_e. For the dashed lines, K=0.5.

The model of Corner and Pendlebury, including its extensions, has been validated with moderate success in experimental vessels much smaller than a room. Corner and Pendlebury themselves compared their theory with experimental data obtained by Langstroth and Gillespie (1947) for a 1 m^3 stirred chamber. In this case, as in those summarized below, the theory has been tested by measuring the loss rate of particles from the core of the vessel rather than by direct measurement of the deposition rate of particles onto the surfaces.

Crump et al. (1983) compared model predictions with experimental measurements in a spherical glass chamber of 0.118 m^3 volume. In this case, the value of K_e was not determined independently, but rather obtained by fitting the measured rates of particle loss from the air. For given mixing conditions, a single value of K_e provided a moderately good fit to the measurement results for particles with diameters in the range 0.02-0.8 μm. McMurry and Rader (1985) measured the loss rate of neutral and singly charged particles from a 0.25 m^3 FEP Teflon film bag. By adjusting the turbulence parameter, K_e, and the mean electric field, a good fit between model and experiment was obtained. These investigators also found that the turbulent deposition model with electrostatic effects provided a good fit to particle loss rates observed in a large (60 m^3) Teflon smog chamber.

Okuyama et al. (1986) have studied the loss rate of monodisperse neutral particles in a small (0.0026 m^3) cylindrical stirred tank. In their studies, the turbulence intensity was determined from the power consumption of the stirrer, rather than being allowed to vary to fit the particle loss data. However, values of the coefficient κ and the exponent m in $D_e = \kappa\, y^m\, du/dy$ were adjusted to fit the data. Good agreement between experiment and theory was obtained for particles in the size range 0.006-0.2 μm, and for K_e greater than approximately 10 s^{-1}. That the theory underpredicted observed loss rates for larger particles was attributed to the effects of particle inertia. Shimada et al. (1987)

used the same chamber with the inner surface lined with sandpaper to conduct experiments designed to validate their extension of the model.

Application of the Corner and Pendlebury model to a typical indoor room has not been reported.

4.6 Experimental Results

4.6.1 Introduction. Although numerous studies have been published reporting pollutant loss rates to surfaces, few are directly relevant for assessing the mass-transport-limited loss rate in actual rooms. Even when data are taken in an actual room, deposition velocities are usually inferred from incomplete data. For example, a common technique involves measuring the rate of disappearance of a species from the core of the enclosure. Of the experiments described in this chapter, only those of Bigu (1985) for radon decay products are based on direct measurement of deposited species with simultaneous measurement of airborne concentrations.

4.6.2 Reactive Gases. Wilson (1968) studied the loss rate of SO_2 in a room after having painted the surfaces with sodium carbonate to ensure that the SO_2 was removed at a transport-limited rate. One may infer from his experiments a mean deposition velocity of 7.8×10^{-4} m s^{-1} for unstirred conditions and 22×10^{-4} m s^{-1} when the air was stirred sufficiently to move loose papers. The diffusion coefficient for SO_2 in air is 1.22×10^{-5} m^2 s^{-1} (Andrew, 1955, see Table 4.1).

4.6.3 Radon Decay Products. Measurements of the deposition velocity of unattached radon decay products have been made by several investigators. Of particular interest are the experiments of Scott (1983), Toohey et al. (1984), and Bigu (1985) conducted respectively in a commercial building, in a utility room of a house, and in a 26 m^3 chamber. The results are in the range 6×10^{-4} to 53×10^{-4} m s^{-1}, with 22×10^{-4} m s^{-1} recommended by Knutson (1988) as a representative average over the surfaces of a

typical room. The diffusion coefficient of the unattached decay products has been found to vary over the range (0.3-1.0) $\times$ 10^{-5} m^2 s^{-1} (Phillips et al., 1988).

4.6.4 Particles. Offermann et al. (1985) measured the evolution of the particle size distribution following the combustion of a cigarette in a room with a low air-exchange rate. For the present chapter, the aerosol size distributions measured at 91 and 241 min. after combustion were used to determine the deposition velocity as a function of particle size. (See Table 4.2.) Correction for the effect of coagulation was made by numerically computing the rate of change in the size distribution due to Brownian coagulation at the beginning and end of the analysis period and subtracting the average value from the observed decay rate. Correction was also made for loss by air-exchange, and by filtration associated with the operation of sampling instruments. The remaining loss rate is presumed to reflect the effect of deposition averaged over all surfaces of the room. The mean deposition velocity so determined is in the range 2.7×10^{-6} - 1.3×10^{-4} m s^{-1} for particles with a diameter in the range 0.07-0.91 μm.

Sinclair et al. (1985) measured surface accumulations of several ionic species on equipment frames in two telephone switching offices. These results, which apparently reflect ionic material collected over periods of several years, were combined with measurements of airborne concentrations, made over periods of a month, to estimate the deposition velocities. For fine (< 2.5 μm) particles, the determinations were based on sulfate, the most prevalent ion, and yielded deposition velocities of 3×10^{-5} and 5×10^{-5} m s^{-1} for the two sites. For coarse (2.5-15 μm) particles, the deposition velocities for the two sites were determined from calcium ion data to be 0.01 and 2×10^{-3} m s^{-1}.

4.7 Comparison of Theory with Experimental Data

Experimental measurements of deposition velocity in rooms have not been augmented by sufficient information on air flow patterns and temperature differences to permit a critical assessment of the applicability of the theories. Nevertheless,

Table 4.2. Mean deposition velocity of airborne particles to the surface of a room.[a]

Diameter (μm)	Loss rate (h^{-1})[b]	Loss (gain) due to coagulation (h^{-1})[c]	Loss due to deposition (h^{-1})[d]	$\overline{v_d}$ (10^{-5} m s^{-1})
0.07	0.446	0.251	0.132	1.72
0.10	0.223	0.139	0.021	0.27
0.12	0.183	0.091	0.029	0.38
0.17	0.143	0.051	0.029	0.38
0.22	0.112	0.013	0.036	0.47
0.26	0.100	(0.031)	0.068	0.89
0.35	0.117	(0.009)	0.063	0.82
0.44	0.116	(0.014)	0.067	0.87
0.56	0.222	(0.016)	0.075	0.98
0.72	0.172	(0.007)	0.116	1.51
0.91	1.056	(0.009)	1.002	13

[a] Room dimensions: 3.4 m × 4.6 m × 2.3 m high; total surface area, incl. furnishings: 74.8 m^2; total net volume: 35.1 m^3.

[b] Determined from Figure 4 of Offermann et al. (1985), measurements at 1156 and 1426.

[c] Mean of rates computed from size distribution at 1156 and 1426.

[d] Total loss rate minus loss due to coagulation and minus loss due to air-exchange (0.05 h^{-1}) and loss due to instrument-induced filtration (0.013 h^{-1}).

approximate comparisons may be made, as shown for the case of the natural convection air flow regime in Figure 4.8 and for the homogeneous turbulence air flow regime in Figure 4.9. In both cases, the room geometry was taken to be identical to the case studied by Offermann et al. (1985). The mean deposition velocity, $\overline{v_d}$, was computed as follows:

$$\overline{v_d} = \frac{1}{S_T} \sum_i v_{d_i} S_i \tag{4.64}$$

where $S_T = \sum_i S_i$.

For the natural convection air flow regime, all surfaces were assumed to have the same temperature, with T_s-T_∞ ranging from -10 K to 1 K. For the turbulence air flow regime, the turbulence intensity parameter is in the range 0.1-10 s^{-1}, which is judged to encompass typical indoor circumstances.

Given the approximate nature of the comparison, the experimental results are seen to generally lie within the range of values expected according to either the turbulence or the natural convection air flow regime. The turbulence regime seems to better accommodate the observations for unattached radon decay products; however, the results of Offermann et al. (1985) are more consistent with the natural convection regime assuming $\Delta T \sim -3$ K than with the turbulence regime assuming any single value of K_e. The results of Sinclair et al. (1985) are higher than can be explained by the models. This may be associated with the differences in geometry between equipment frames on which ionic substances were measured and enclosure surfaces (walls, floor and ceiling), for which the theoretical predictions apply. It may also reflect, in part, the inaccuracies that result from estimating deposition velocities based on airborne concentration data taken over a month in conjunction with data on deposits accumulated over several years on equipment surfaces.

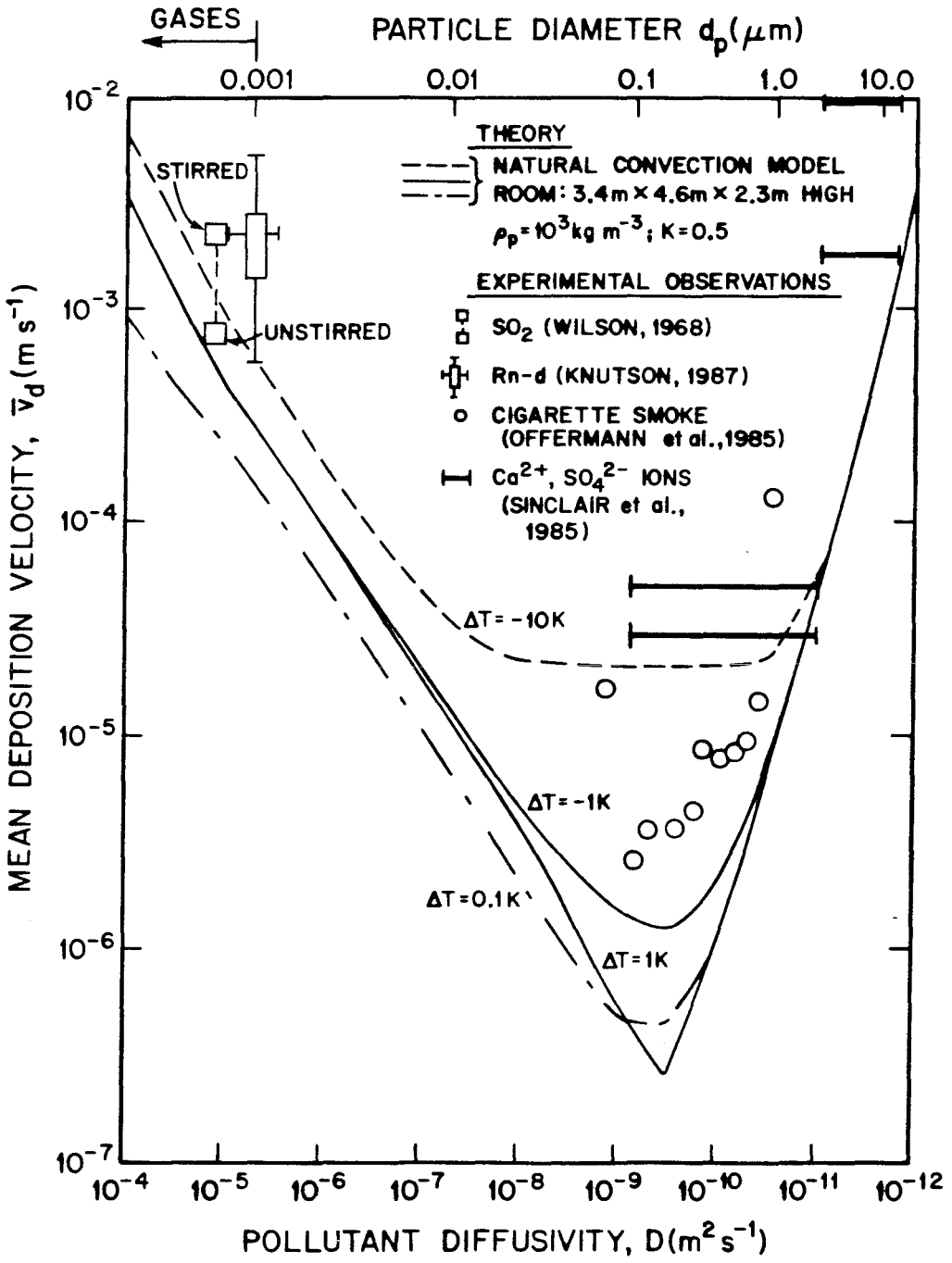

Figure 4.8 Comparison of the natural convection deposition model with experimental data.

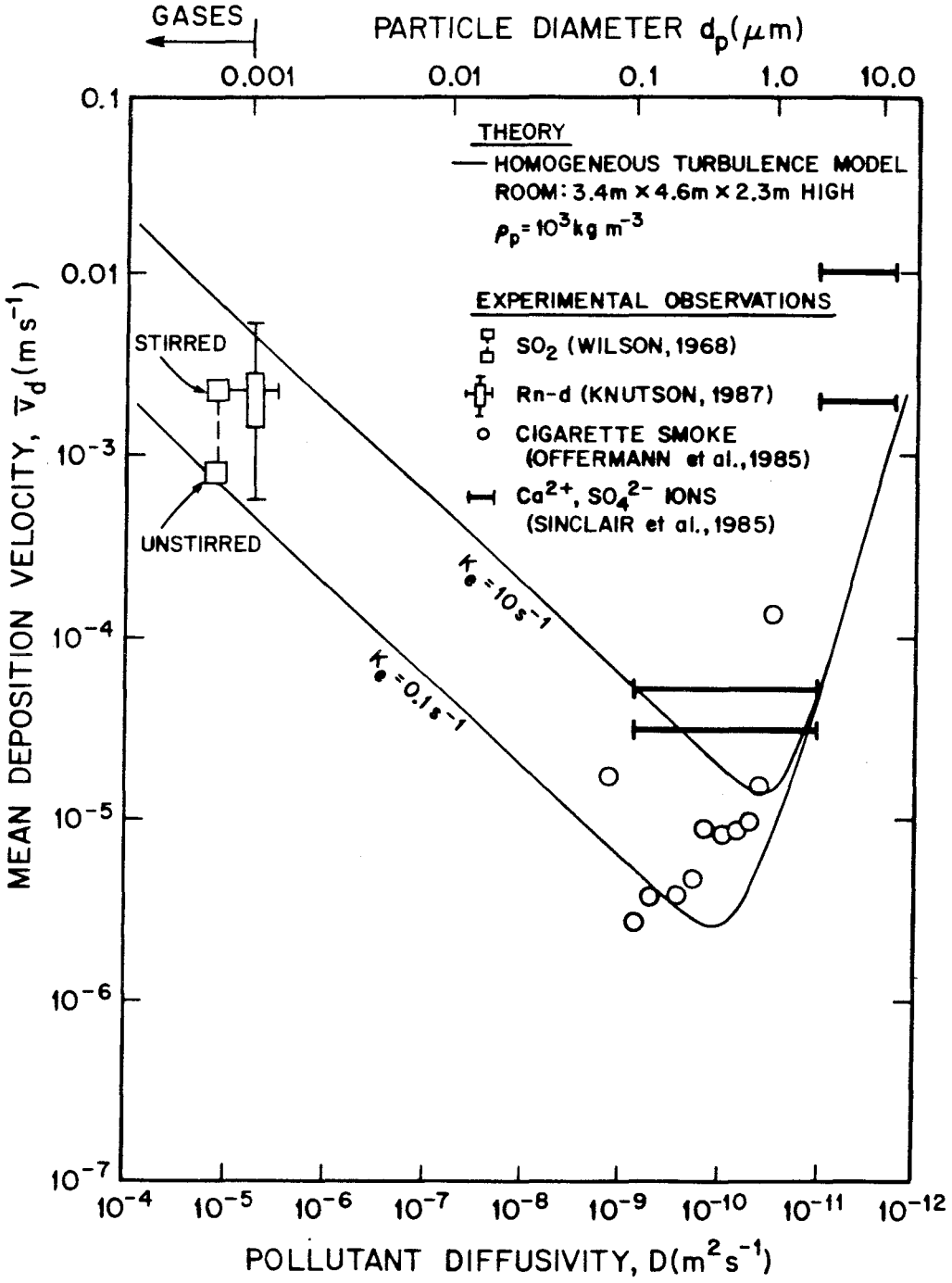

Figure 4.9 Comparison of the homogeneous turbulence deposition model with experimental data.

4.8 Conclusions

The air flow regimes considered in this chapter represent an important subset of the conditions that are expected to be prevalent in indoor environments. Predictions of the models are roughly consistent with existing experimental data. Moreover, the models establish a framework for future experiments designed to elucidate deposition mechanisms and rates.

With respect to the soiling of indoor surfaces, particles in the size range 0.05-1 μm, which includes much of the black soot component (e.g., Ouimette, 1981) are likely to be very important. Although all three flow regimes show a similar dependence of deposition velocity on particle size, there are important differences. For a given mean air velocity near a surface, the deposition rates are highest for the homogeneous turbulence flow regime, lowest for the forced laminar flow regime, and the differences in magnitude are large. Through careful design of a ventilation system to achieve forced laminar flow along surfaces, the soiling rate of indoor surfaces can be substantially reduced.

Another possibility for reducing soiling rates is to exploit thermophoresis. For all three flow regimes, the deposition velocity for particles larger than 0.1 μm is much smaller for a warm wall than for a cool wall, even for temperature differences between the wall and the air as small as 1 K.

Thus, if through altered building design or operation, natural convection, or particularly laminar forced flow conditions could be deliberately created with vertical surfaces slightly warmer than the room air, then it may be possible to greatly reduce the rate of soiling of these surfaces due to the deposition of airborne soot particles.

There is a clear need for additional experimental work on this topic. In addition to the experimental techniques that have been used in the past, several other methods may be used to determine pollutant deposition velocities in indoor environments. For

example, measurements of the rate of heat transfer from indoor surfaces could be used to determine the mass-transport-limited deposition velocity for gases and very small (d_p ~ 0.001 μm) particles. Measurement of the surface accumulation of monodisperse fluorescein particles injected into a room could be used to test the theories at smaller values of the diffusion coefficient. In either case, it is important to measure air velocities, particularly near surfaces, and the air and surface temperatures. Such experimental studies, in combination with further theoretical investigations, would lead to a more complete understanding of the deposition of reactive gases and particles onto room surfaces.

4.9 Acknowledgement

This work was supported by a contract with the Getty Conservation Institute, Marina del Rey, California.

4.10 References

Andrew, S. P. S. (1955) A simple method of measuring gaseous diffusion coefficients, *Chemical Engineering Science* **4**, 269-272.

Bejan, A. (1984) *Convection Heat Transfer*, Wiley: New York.

Bigu, J. (1985) Radon daughter and thoron daughter deposition velocity and unattached fraction under laboratory-controlled conditions and in underground uranium mines, *Journal of Aerosol Science* **16**, 157-165.

Churchill, S. W., and Chu, H. H. S. (1975) Correlating equations for laminar and turbulent free convection from a vertical plate, *International Journal of Heat and Mass Transfer* **18**, 1323-1329.

Corner, J., and Pendlebury, E. D. (1951) The coagulation and deposition of a stirred aerosol, *Proceedings of the Physical Society* **B64**, 645-654.

Crump, J. G., Flagan, R. C., and Seinfeld, J. H. (1983) Particle wall loss rates in vessels, *Aerosol Science and Technology* **2**, 303-309.

Crump, J. G., and Seinfeld, J. H. (1981) Turbulent deposition and gravitational sedimentation of an aerosol in a vessel of arbitrary shape, *Journal of Aerosol Science* **12**, 405-415.

Davies, C. N. (1945) Definitive equations for the fluid resistance of spheres, *Proceedings of the Physical Society* **57**, 259-270.

Ede, A. J. (1967) Advances in free convection, *Advances in Heat Transfer* **4**, 1-64.

Globe, S., and Dropkin, D. (1959) Natural-convection heat transfer in liquids confined by two horizontal plates and heated from below, *Journal of Heat Transfer* **81**, 24-28.

Hirst, W., and Harrison, G. E. (1939) The diffusion of radon gas mixtures, *Proceedings of the Royal Society* **A169**, 573-586.

Incropera, F. P., and DeWitt, D. P. (1985) *Fundamentals of Heat and Mass Transfer*, Wiley: New York, Chapter 9.

Ivakin, B. A., and Suetin, P. E. (1964) Diffusion coefficients of some gases measured by the optical method, *Soviet Physics—Technical Physics* **8**, 748-751.

Katan, T. (1969) Diffusion coefficients of vapors measured with a moving boundary, *Journal of Chemical Physics* **50**, 233-238.

Klotz, I. M., and Miller, D. K. (1947) Diffusion coefficients and molecular radii of hydrogen cyanide, cyanogen chloride, phosgene and chloropicrin, *Journal of the American Chemical Society* **69**, 2557-2558.

Knutson, E. O. (1988) Modeling indoor concentrations of radon's decay products, in *Radon and Its Decay Products in Indoor Air*, Nazaroff, W. W., and Nero, A. V., eds., Wiley: New York, Chapter 5.

Langstroth, G. O., and Gillespie, T. (1947) Coagulation and surface losses in disperse systems in still and turbulent air, *Canadian Journal of Research* **B25**, 455-471.

Lugg, G. A. (1968) Diffusion coefficient of some organic and other vapors in air, *Analytical Chemistry* **40**, 1072-1077.

McMurry, P. H., and Rader, D. J. (1985) Aerosol wall losses in electrically charged chambers, *Aerosol Science and Technology* **4**, 249-268.

McMurtie, R. L., and Keyes, F. G. (1948) A measurement of the diffusion coefficient of hydrogen peroxide vapor into air, *Journal of the American Chemical Society* **70**, 3755-3758.

Marrero, T. R., and Mason, E. A. (1972) Gaseous diffusion coefficients, *Journal of Physical and Chemical Reference Data* **1**, 3-118.

Mian, A. A., Coates, J., and Cordiner, J. B. (1969) Binary gaseous diffusion coefficients of N_2-HCl, A-HBr, and N_2-HBr systems as a function of temperature, *Canadian Journal of Chemical Engineering* **47**, 499-502.

Offermann, F. J., Sextro, R. G., Fisk, W. J., Grimsrud, D. T., Nazaroff, W. W., Nero, A. V., Revzan, K. L., and Yater, J. (1985) Control of respirable particles in indoor air with portable air cleaners, *Atmospheric Environment* **19**, 1761-1771.

Okuyama, K., Kousaka, Y., Yamamoto, S., and Hosokawa, T. (1986) Particle loss of aerosols with particle diameters between 6 and 2000 nm in stirred tank, *Journal of Colloid and Interface Science* **110**, 214-223.

Ouimette, J. (1981) *Aerosol Chemical Species Contributions to the Extinction Coefficient*, Ph.D. Thesis, California Institute of Technology, Pasadena, California.

Petit, M. C. (1965) Étude de la diffusion de la vapeur d'eau dans l'air, *Compte Rendus de l'Academie des Sciences (Paris)* **260**, 1368-1370.

Phillips, W. F. (1975) Drag on a small sphere moving through a gas, *Physics of Fluids* **18**, 1089-1093.

Phillips, C. R., Khan, A., and Leung, H. M. Y. (1988) The nature and determination of the unattached fraction of radon and thoron progeny, in *Radon and Its Decay Products in Indoor Air*, Nazaroff, W. W., and Nero, A. V., eds., Wiley: New York, Chapter 6.

Press, W. H., Flannery, B. P., Teukolsky, S. A., and Vetterling, W. T. (1986) *Numerical Recipes: The Art of Scientific Computing*, Cambridge University Press: Cambridge.

Reid, R. C., Prausnitz, J. M., and Sherwood, T. K. (1977) *The Properties of Gases and Liquids*, 3rd ed., McGraw-Hill: New York.

Schiller, G. E. (1984) *A Theoretical Convective-Transport Model of Indoor Radon Decay Products*, Ph.D. Thesis, University of California, Berkeley, California.

Schlichting, H. (1979) *Boundary-Layer Theory*, Seventh edn, McGraw-Hill: New York.

Scott, A. G. (1983) Radon daughter deposition velocities estimated from field measurements, *Health Physics* **45**, 481-485.

Seinfeld, J. H. (1986) *Atmospheric Chemistry and Physics of Air Pollution*, Wiley: New York, Chapter 8.

Shimada, M., Okuyama, K., Kousaka, Y., and Ohshima, K. (1987) Turbulent and Brownian diffusive deposition of aerosol particles onto a rough wall, *Journal of Chemical Engineering of Japan* **20**, 57-64.

CHAPTER 5

MATHEMATICAL MODELING OF INDOOR AEROSOL DYNAMICS

5.1 Abstract

A general mathematical model is presented for predicting the concentration and fate of particulate matter in indoor air. Using a multicomponent sectional representation, the model accounts for the effects of ventilation, filtration, deposition onto surfaces, direct emission, and coagulation. Model predictions are compared with the evolution over time of the measured aerosol size distribution following combustion of a cigarette in a single room with a low air-exchange rate. Reasonable agreement is obtained; however, further experiments are required for full validation of additional capabilities of the present model. Important environmental problems to which the model may be applied include analysis of the soiling of surfaces due to deposition of airborne particles, and control of human exposure to environmental tobacco smoke. The model may also serve as a foundation for improving the understanding of the risk of human exposure to radon decay products indoors.

Nazaroff, W. W., and Cass, G. R., Mathematical modeling of indoor aerosol dynamics, to be published in *Environmental Science and Technology*.

5.2 Introduction

Progress on some important environmental and industrial problems can be achieved with an improved understanding of the behavior of aerosols within buildings. Prominent examples include the indoor exposure of humans to pollutants such as environmental tobacco smoke (National Research Council, 1986; U.S. Department of Health and Human Services, 1986; Seifert et al., 1987) and radon decay products (Clemente et al., 1984; Hopke, 1987; Nazaroff and Nero, 1988), the soiling of works of art (Baer and Banks, 1985; Cortes-Cormerer, 1987), and the failure of semiconductors as a result of particle deposition (Larrabee, 1985; Cooper, 1986).

For addressing such problems, mathematical models describing the concentrations and fates of indoor aerosols constitute important tools. By serving as a framework within which to compare experimental results with theoretical predictions, models can be used to guide research. The power of experimental work may be enhanced, for example, by using a model to predict the depositional flux of pollutants onto surfaces, based on measurements of airborne concentrations. Models may also serve as tools for the design of environmental control systems in buildings.

Considerable progress has been achieved in the past decade in modeling aerosol dynamics (e.g., see Gelbard and Seinfeld, 1980; Warren and Seinfeld, 1985). Advanced models have been applied to nuclear-reactor containment vessels (Odom et al., 1981; Gelbard, 1982), industrial aerosol reactors (Wu, 1986), and even outdoor air (Pilinis et al., 1987).

By contrast, indoor aerosol modeling is considerably less advanced. The present state-of-the-art approach is based on a mass-balance that only determines the total concentration of suspended particulate matter (Alzona et al., 1979); no information on aerosol size or chemical composition is incorporated into that model. Yet particle size plays a major role in every aspect of aerosol behavior including the removal efficiency of

a filter, the rate of deposition onto surfaces, and the retention efficiency upon inhalation. In a like fashion, the ability to simultaneously track particles of differing chemical composition is important as a small proportion of black soot particles, mixed with the ambient aerosol, may be responsible for a disproportionately large fraction of the soiling hazard due to the deposition of airborne particles. Thus, an approach that considers aerosol mass concentration alone, without regard for particle size and composition, is inadequate for addressing many important issues concerning indoor aerosols.

The work described in this chapter was undertaken to advance the capabilities of modeling indoor aerosols. Both aerosol size distribution and chemical composition are simulated. Using a multichamber representation of a building, the model explicitly accounts for the effects of ventilation, filtration, deposition, direct indoor emission, and coagulation. The deposition calculations are especially detailed, to permit simulation of soiling problems. The aerosol model is coupled to a previously described model for gaseous pollutants (Chapter 2), permitting future calculations that account for gas-to-particle conversion processes.

In this chapter, the formulation of the model is described, then an application of the model is recounted to explain the results of an experiment in which the evolution of cigarette smoke in a poorly ventilated room was measured (Offermann et al., 1985). The model is shown to be reasonably successful in reproducing the experimental observations. However, further experiments are needed to thoroughly test its performance. Some potential applications of the model and future enhancements are discussed briefly.

5.3 Model Formulation

5.3.1 Aerosol Representation. The multicomponent sectional formulation of Gelbard and Seinfeld (1980) is used to represent the indoor aerosol. The complete aerosol size distribution is divided into a number of contiguous sections or bins, and within each section the aerosol mass may be comprised of many different chemical components. For

this representation to be unambiguous, an assumption must be made about the distribution of aerosol mass with particle size within a given section. Following Warren and Seinfeld (1985), the aerosol mass concentration within a section is assumed to be uniformly distributed with respect to the logarithm of the mass (or, equivalently, the diameter) of the particle. Particles are assumed to be spherical and to have equal densities so that a particle's mass is uniquely related to its diameter, and either may be used as a basis for specifying the size distribution. Components are assumed to be mixed internally, i.e., within a section all particles have the same composition.

To limit the computational requirements for simulating coagulation, a geometric constraint is imposed on the width of a section: the largest particle in each section must have a mass that is at least twice that of the smallest particle in the section. The user specifies the sectional boundaries, the number of sections, and the number of components, subject only to the geometric constraint and the program's dimensional limits.

5.3.2 Basic Model Postulates. The approach previously used for modeling gaseous pollutants (Chapter 2) is applied here. Briefly, the building is represented as a set of interconnected chambers, each having a well-mixed core. Within each chamber, the rate of change of aerosol mass concentration for each component within each section is given by a first-order differential equation

$$\frac{dC_{ijk}}{dt} = S_{ijk} - L_{ijk}\, C_{ijk} \qquad (5.1)$$

where C_{ijk} represents the mass concentration of component k in section j contained within chamber i, S_{ijk} represents the sum of all sources within chamber i of component k in section j: direct emission, advective transport from other chambers and outside, and coagulation of mass from smaller particles into the section. L_{ijk} represents the sum of all sinks within chamber i of component k in section j: loss to surfaces, removal by

ventilation and filtration, and loss to a larger size due to coagulation. The source and sink terms may, of course, vary with time.

5.3.3 Ventilation and Filtration. The treatment of ventilation and filtration is shown schematically in Figure 5.1. This approach is analogous to that developed for the gas-phase model (Chapter 2), with one clarification: the filter efficiency may vary with particle size but not according to particle composition. Thus, the efficiency of removing particles from each section may be specified independently for each filter. In mathematical terms, the effect of ventilation and filtration on aerosol species may be represented as follows:

$$\frac{dC_{ijk}}{dt} = \left(\sum_{h=0}^{n} \left[\frac{f_{hi}\, C_{hjk} - f_{ih}\, C_{ijk}}{V_i} \right] \right) + \left[\frac{f_{xi}\, C_{xjk} - f_{ix}\, C_{ijk}}{V_i} \right] - \frac{\eta_{iij}\, f_{ii}\, C_{ijk}}{V_i} \qquad (5.2)$$

$$C_{xjk} = \frac{\sum_{h=0}^{n} (1-\eta_{hxj})\, f_{hx}\, C_{hjk}}{\sum_{h=0}^{n} f_{hx}} \qquad (5.3)$$

where V_i is the volume of chamber i, f_{ih} = the volumetric flow rate of air from chamber i to chamber h, η_{ihj} = the efficiency of removal of aerosol section j by the filter located in the air stream flowing from chamber i to chamber h, the subscript x refers to the mechanical ventilation system supply air, and the index for chamber h=0 is reserved to denote outdoor air. Ventilation through doors and windows, infiltration, and exhaust flow to outdoors thus represent fluxes between chamber 0 and chambers 1 through n.

5.3.4 Aerosol Deposition onto Surfaces. In determining indoor aerosol concentrations, deposition is often of secondary importance, accounting for a rate of removal that is much smaller than that typically due to ventilation. However, accurate evaluation of particle

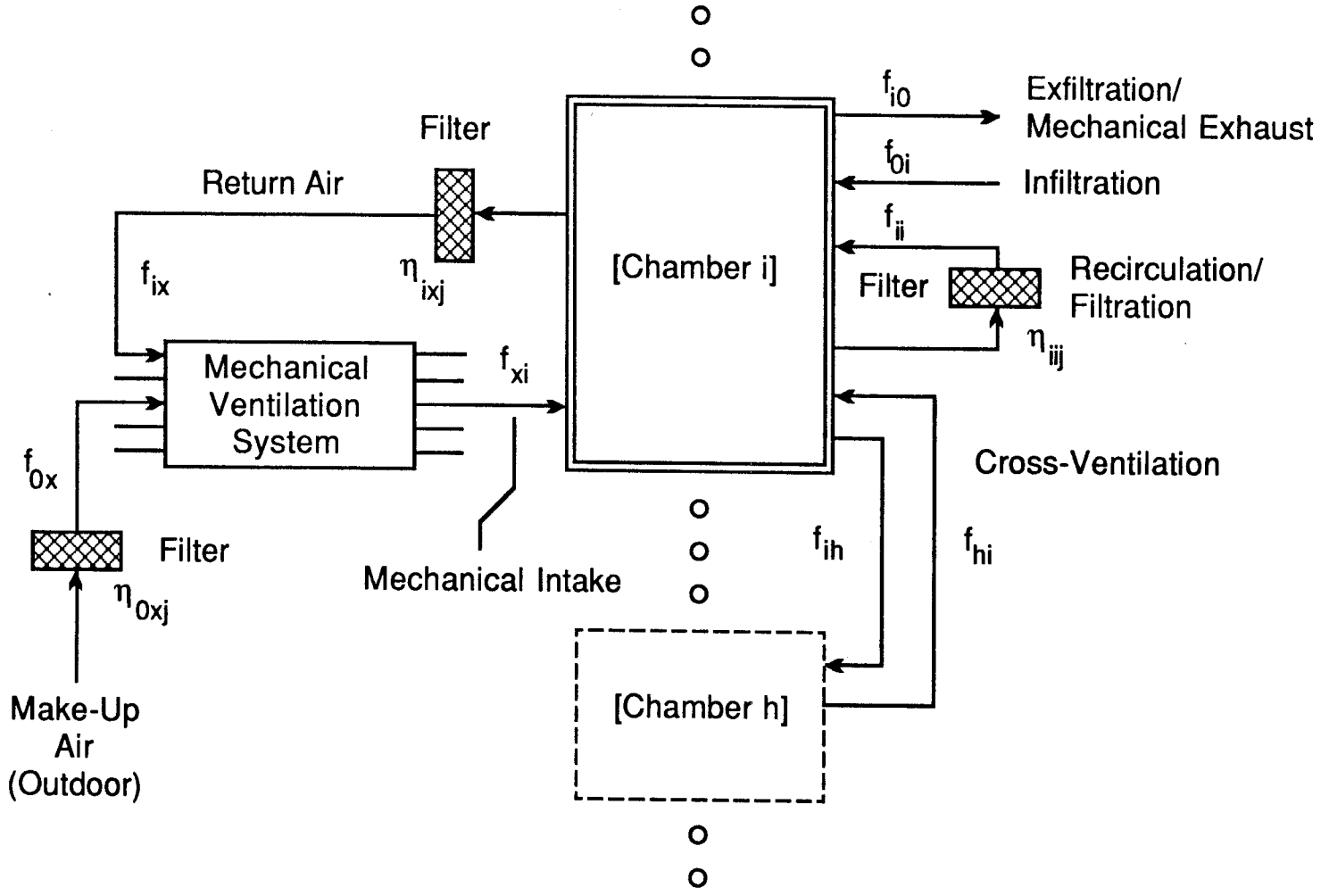

Figure 5.1 Schematic representation of the ventilation and filtration components of the indoor aerosol model.

deposition rates is extremely important in cases where deposition itself is the concern, such as for the soiling of works of art. To be able to meaningfully address these problems, the model is capable of making detailed calculations of particle deposition rates.

The rate of particle deposition onto surfaces is related to the loss of airborne particles through the deposition velocity, v_d, which is defined as the ratio of the aerosol mass flux to a surface to the airborne concentration in the core of the room. For a given chamber i, the rate of change of mass concentration of component k in section j, due only to deposition, is related to the deposition velocities to each surface by the expression

$$\frac{dC_{ijk}}{dt} = - \frac{C_{ijk}}{V_i} \sum_m v_{d_{imj}} A_{im} \qquad (5.4)$$

where $v_{d_{imj}}$ is the mean deposition velocity of particles in section j to the m^{th} surface of chamber i, and A_{im} is the superficial area of the m^{th} surface of chamber i.

The model requires that each surface (ceiling, floor, walls plus any items within the room) be designated to have one of three orientations: vertical, horizontal upward-facing, or horizontal downward-facing. For each orientation, the model contains three methods of evaluating $v_{d_{imj}}$, for each of three distinctly different mechanisms that may govern airflow along a surface: (1) natural convection driven by a temperature difference between the surface and the nearby air; (2) homogeneous turbulence in the core of the room; and (3) forced laminar flow parallel to a surface. The equations relating deposition velocity to particle size, surface orientation, and flow conditions are derived elsewhere (see Chapters 3 and 4). The equations for the cases of homogeneous turbulence and natural convection, to be used in the model application presented in this chapter, are presented in Table 5.1.

For those cases where particle deposition to surfaces is driven by turbulent mixing in the core of the room, the deposition flux is computed by a method based on the

Table 5.1. Particle deposition velocities, v_d. [a]

surface	deposition velocity	conditions
	homogeneous turbulence	
all	$v_d = v_{CP} + v_t$	all
all	$v_t = - N_t \nu \frac{(K_e/\alpha)^{1/2}}{\tan^{-1}[\delta (K_e/\alpha)^{1/2}]}$	all; see note b
vertical	$v_{CP} = \frac{2}{\pi} (D K_e)^{1/2}$	see note c
downward-facing	$v_{CP} = \frac{v_g}{\left[\exp\left(\frac{\pi}{2}\frac{v_g}{\sqrt{DK_e}}\right) - 1\right]}$	see note c
upward-facing	$v_{CP} = \frac{v_g}{\left[1 - \exp\left(-\frac{\pi}{2}\frac{v_g}{\sqrt{DK_e}}\right)\right]}$	see note c
	natural convection	
vertical	$v_d = \frac{4}{3}[g \lvert \Delta T \rvert / 4\nu^2 T_\infty]^{1/4} \alpha^{1/3} D^{2/3} H^{-1/4} \{\omega'(0)/ Le^{1/3}\}$	$Ra_H < 10^9$

Table 5.1 (continued).

surface	deposition velocity	conditions

natural convection (cont.)

vertical (cont.)

$$v_d = \text{maximum of } \left\{ \frac{4}{3}[g\,|\Delta T|\,/\,4\nu^2\,T_\infty]^{1/4}\,\alpha^{1/3}\,D^{2/3}\,H^{-1/4}\,\{\omega'(0)/\,Le^{1/3}\}\right\} \qquad 10^9<Ra_H<10^{12}$$

$$\text{or } \left\{ v_t + \frac{D}{H}\left[0.825 + \frac{0.387\,Ra_H^{1/6}}{\left\{1 + (0.492/Sc)^{9/16}\right\}^{8/27}}\right]^2\right\};$$

$$\text{where } v_t = -N_t\left(\frac{\nu}{H}\right)\left[0.825 + \frac{0.387\,Ra_H^{1/6}}{\left\{1 + (0.492/Pr)^{9/16}\right\}^{8/27}}\right]^2$$

horizontal, enclosed

$$v_d = s_g\,v_g - 2\,N_t\left(\frac{\nu}{H}\right) + 2\,\frac{D}{H} \qquad v_d \geq 0;\ Ra_H < 1100;$$

or upward-facing cooled or downward-facing heated surface

$$v_d = s_g\,v_g - N_t\left(\frac{\nu}{H}\right)\{0.087\,Ra_H^{1/3}\,Pr^{0.074}\} + \frac{D}{H}\{0.087\,Ra_H^{1/3}\,Sc^{0.074}\} \qquad v_d \geq 0;\ 3\times10^5 < Ra_H < 1.4\times10^9;$$

or upward-facing heated or downward-facing cooled surface

Table 5.1 (continued).

surface	deposition velocity	conditions
	natural convection (cont.)	
horizontal, isolated; and upward-facing heated or downward-facing cooled surface	$v_d = s_g v_g - N_t\left(\frac{\nu}{L}\right)\{0.54\ Ra_L^{1/4}\} + \frac{D}{L}\{0.54\ Ra_L^{1/4}\}$	$v_d \geq 0;\ 10^4 < Ra_L < 10^7$
	$v_d = s_g v_g - N_t\left(\frac{\nu}{L}\right)\{0.15\ Ra_L^{1/3}\} + \frac{D}{L}\{0.15\ Ra_L^{1/3}\}$	$v_d \geq 0;\ 10^7 < Ra_L < 10^{11}$
horizontal, isolated; and upward-facing cooled or downward-facing heated surface	$v_d = s_g v_g - N_t\left(\frac{\nu}{L}\right)\{0.27\ Ra_L^{1/4}\} + \frac{D}{L}\{0.27\ Ra_L^{1/4}\}$	$v_d \geq 0;\ 10^5 < Ra_L < 10^{10}$

[a] See Chapters 3 and 4.

[b] In the expression for deposition velocity, δ is the boundary layer thickness given approximately by $\delta \sim (1.2)\ (\nu/K_e)^{4/9}\ x_s^{1/9}$ where x_s is the length of the surface in the direction of flow.

[c] For very small particles, v_{CP} to a surface having any orientation is more accurately given by the expression $v_{CP} = (D\ K_e)^{1/2} / [\tan^{-1}\{\delta\ (K_e/D)^{1/2}\}]$, where δ is given in note b, above. For a particle to be sufficiently small for this expression to be appropriate, it must satisfy $D < 0.12\ \nu^{4/9}\ K_e^{1/9}\ x_s^{2/9}$. A typical set of conditions has $K_e = 0.1\ s^{-1}$ and $x_s = 1$ m, for which the inequality becomes $D < 0.05\ cm^2\ s^{-1}$, i.e.,that the particle must be smaller than 0.001 μm in diameter.

analysis of Corner and Pendlebury (1951). That analysis accounts for the combined effects of eddy diffusion, Brownian motion and gravitational settling, assuming that within a thin turbulent boundary layer adjacent to the surfaces of the enclosure the eddy diffusion coefficient for the particles, D_e, is related to the distance from the surface, y_s, according to $D_e = K_e\, y_s^2$. For the model presented here, the effects of thermophoresis have been added in a manner compatible with this boundary layer structure (see Chapter 4). The turbulence intensity parameter, K_e, has the dimensions of inverse time, and its value can be obtained by a fit to experimental data on the measured deposition flux to the surface of an enclosure. While a higher order description of the turbulent deposition process could be adopted, recent experiments by Crump et al. (1983) and Okuyama et al. (1986) have shown that Corner and Pendlebury's formulation of the problem produces deposition flux predictions that are close enough to experimental observations that a more elaborate treatment would not produce a practical improvement in the results of the indoor air quality model.

The natural convection equations apply when heat transfer between the surfaces of the room and the air governs the flow along surfaces. For the case of laminar natural-convection flow along a vertical surface, boundary layer equations are solved to simultaneously account for the effects on deposition of thermophoresis, advection and Brownian motion (see Chapter 3). For turbulent flow along a vertical surface and for horizontally oriented surfaces, experimental heat transfer correlations are used to estimate the rates of deposition due to advective diffusion and thermophoresis; these components, plus gravitational sedimentation, are combined vectorially to determine the total particle deposition rate (see Chapter 4).

For either flow regime, the mass-weighted mean deposition velocity for a sectional cut through the aerosol size distribution is determined by numerical integration under the assumption, already introduced, that the aerosol mass is distributed uniformly with respect to the logarithm of particle diameter within a single section.

As an alternative to these calculational approaches, the model permits the user to specify directly the mean deposition velocity for each section. This approach allows direct utilization of experimental data on deposition rates.

In addition to accounting for the effect of deposition on the evolution of airborne particle concentrations in the core of a chamber, the model can report the time-integrated deposition to each surface of each aerosol chemical component within each section of the aerosol size distribution. This capability is designed specifically for the investigation of soiling problems where the flux of black elemental carbon particles to surfaces is of particular interest.

5.3.5 Coagulation. The treatment of aerosol coagulation in the model is best considered in two stages: the calculation of the collision frequency between two particles and the integration of these probabilities to obtain the growth and loss rates for component masses within each section.

The total collision probability is taken as the linear sum of the rates due to two processes: differential sedimentation and Brownian motion. For the contribution of Brownian motion, the Fuchs interpolation formula (Fuchs, 1964, p. 291-294; Seinfeld, 1986, p. 397) is used. For the contribution of differential sedimentation, the result of Fuchs is used (Fuchs, 1964, sections 34 and 54). When computing the effect of differential sedimentation, only particle interception is considered; Brownian motion and impaction are neglected. In both calculations the slip correction factor is calculated according to the expression of Phillips (1975). The equations used to compute the collision frequency function are summarized in Table 5.2.

Collisions may occur as a result of other processes leading to relative motion of particles, such as laminar or turbulent shear (Saffman and Turner, 1956; Fuchs, 1964; Pruppacher and Klett, 1978; Seinfeld, 1986). Calculations for representative conditions show that the shear rates indoors would have to be unusually large for shear-induced

Table 5.2. Particle collision frequency function, $\beta(u,v)$.

Basic definitions

$$\beta = \beta(u,v); \qquad u = \frac{\pi}{6}\rho\, d_1^3; \quad v = \frac{\pi}{6}\rho\, d_2^3$$

Aggregation of component parts

$$\beta = \beta_{DS} + \beta_B$$

Differential sedimentation component (Fuchs, 1964)

$$\beta_{DS} = \frac{\pi}{4}\phi\,\kappa\,|\,v_{g1} - v_{g2}\,|\,[\max(d_1,d_2)]^2$$

$$\phi = (1+R)^2 - 1.5(1+R) + \frac{0.5}{1+R}; \quad R = \min\left(\frac{d_1}{d_2}, \frac{d_2}{d_1}\right)$$

$$v_{gi} = \frac{d_i^2\,\rho\, g\, C(Kn)}{18\,\mu}; \qquad i = 1,2$$

Brownian motion component (Fuchs, 1964; Phillips, 1975; Seinfeld, 1986)

$$\beta_B = \frac{2\pi\,(D_1+D_2)\,(d_1+d_2)\,\kappa}{\left(\frac{d_1+d_2}{d_1+d_2+2g_{12}}\right) + \frac{8(D_1+D_2)}{c_{12}(d_1+d_2)}}$$

$$g_{12} = (g_1^2 + g_2^2)^{1/2}; \quad g_i = \frac{1}{3\,d_i\,a_i}[(d_i+a_i)^3 - (d_i^2+a_i^2)^{3/2}] - d_i; \qquad a_i = \frac{8\,D_i}{\pi\,\overline{c_i}}; \quad i = 1,2$$

$$\overline{c_1} = \left[\frac{8kT}{\pi u}\right]^{1/2}; \qquad \overline{c_2} = \left[\frac{8kT}{\pi v}\right]^{1/2}; \qquad c_{12} = \left(\overline{c_1}^2 + \overline{c_2}^2\right)^{1/2}$$

$$D_i = \frac{k\,T\,C(Kn)}{3\pi\,\mu\,d_i}; \qquad i = 1,2$$

$$Kn = \frac{2\,\lambda}{d_i}; \qquad \lambda = \left[\sqrt{2}\,\pi\,\sigma^2\,\frac{PN_a}{RT}\right]^{-1}; \qquad \sigma = 3.711 \times 10^{-10}\ \text{m (Reid et al., 1977)}$$

$$C(Kn) = \frac{15 + 12B_1Kn + 9(B_1^2+1)\,Kn^2 + 18B_2\,(B_1^2+2)\,Kn^3}{15 - 3B_1Kn + (8+\pi\gamma)\,B_2\,(B_1^2+2)\,Kn^2}$$

$$B_1 = \frac{2-\gamma}{\gamma}; \qquad B_2 = \frac{1}{2-\gamma}$$

coagulation to become important; consequently, coagulation induced by shear flow is not included in the model, but it can be added in a straightforward manner should a circumstance arise in which it would be an important effect.

The approach developed by Gelbard and Seinfeld (1980) is used to integrate the collision probabilities to determine the mean values for each section. The equations are summarized in Table 5.3. For a given section, j, there are as many as four classes of collisions that can alter the mass concentration, with the classes distinguished by the sizes of the colliding particles: (1) two particles, each from a section smaller than j, collide to produce a particle in section j (valid for $1 < j \leq s$ where s is the total number of sections); (2) one particle from a section smaller than j collides with a particle in j to yield either (a) a particle larger than j or (b) a particle in j (valid for $1 < j \leq s$); (3) two particles in j collide to yield a particle larger than j (valid for $1 \leq j < s$); and (4) a particle in j collides with a particle larger than j (valid for $1 \leq j < s$). Each sectional mean coagulation coefficient in Table 5.3 is designated with a preceding superscript number that corresponds to one of these classes, in the order given above. Note that in this formulation the aerosol mass summed over all sections is conserved through coagulation, but that this is achieved by not allowing the loss of aerosol mass from the largest section. This limitation of the sectional description can be made to have negligible effect by choosing the largest section to contain particles large enough that coagulation in this section is unimportant.

The effect of coagulation on the evolution of the aerosol mass concentration of a given component, k, within chamber i, and section j, is expressed mathematically as

Table 5.3. Sectional mean coagulation coefficients (Gelbard and Seinfeld, 1980).

coefficient	conditions [a]	value [b]
1a $\overline{\beta}_{pqj}$	$p < j-1;\ q < j-1$	0
1a $\overline{\beta}_{pqj}$	$1 < j \le s;\ p = j-1;\ q < j-1$	$\int_{x_{q-1}}^{x_q} \int_{\ln(v_{j-1}-v)}^{x_{j-1}} \frac{\beta(u,v)}{u\,(x_q-x_{q-1})\,(x_{j-1}-x_{j-2})}\,dy\,dx$
1a $\overline{\beta}_{pqj}$	$1 < j \le s;\ p < j-1;\ q = j-1$	$\int_{x_{p-1}}^{x_p} \int_{\ln(v_{j-1}-v)}^{x_{j-1}} \frac{\beta(u,v)}{v\,(x_p-x_{p-1})\,(x_{j-1}-x_{j-2})}\,dy\,dx$
1a $\overline{\beta}_{pqj}$	$1 < j \le s;\ p = j-1;\ q = j-1$	$\int_{x_{p-1}}^{\ln(v_p-v_{p-1})} \int_{\ln(v_{j-1}-v)}^{x_{j-1}} \frac{\beta(u,v)}{v\,(x_{j-1}-x_{j-2})^2}\,dy\,dx + \int_{\ln(v_p-v_{p-1})}^{x_p} \int_{x_{j-2}}^{x_{j-1}} \frac{\beta(u,v)}{v\,(x_{j-1}-x_{j-2})^2}\,dy\,dx$
1b $\overline{\beta}_{pqj}$	$1 < j \le s;\ p \le j-1;\ q \le j-1$	1a $\overline{\beta}_{qpj}$
2a $\overline{\beta}_{pj}$	$1 < j < s;\ p < j$	1a $\overline{\beta}_{pj(j+1)}$
2a $\overline{\beta}_{pj}$	$j = s$	0

Table 5.3 (continued).

coefficient	conditions [a]	value [b]
$^{2b}\overline{\beta}_{pj}$	$1 < j \le s;\ p < j$	$\int_{x_{p-1}}^{x_p} \int_{x_{j-1}}^{\ln(v_j - v)} \frac{\beta(u,v)}{u\,(x_p - x_{p-1})\,(x_j - x_{j-1})}\,dy\,dx$
$^{3}\overline{\beta}_{jj}$	$1 \le j < s$	$2\left[{}^{1a}\overline{\beta}_{jj(j+1)}\right]$
$^{3}\overline{\beta}_{jj}$	$j = s$	0
$^{4}\overline{\beta}_{pj}$	$1 \le j < s;\ p > j$	$\int_{x_{p-1}}^{x_p} \int_{x_{j-1}}^{x_j} \frac{\beta(u,v)}{v\,(x_p - x_{p-1})\,(x_j - x_{j-1})}\,dy\,dx$
$^{4}\overline{\beta}_{pj}$	$j = s$	0

[a] s designates the largest aerosol section.

[b] $\beta(u,v)$ = collision frequency between particles of mass u and v (see Table 5.2); $x_q = \ln(v_q)$; v_q = mass of largest particle in section q; $u = e^y$; $v = e^x$.

follows (cf. Gelbard and Seinfeld, 1980):

$$\frac{dC_{ijk}}{dt} = \frac{1}{2}\left(\sum_{p=1}^{j-1} \sum_{q=1}^{j-1} \left[[^{1a}\overline{\beta}_{pqj}]\, C_{iqk} \left(\sum_k C_{ipk}\right) + [^{1b}\overline{\beta}_{pqj}]\, C_{ipk} \left(\sum_k C_{iqk}\right) \right] \right)$$

$$- \left(\sum_{p=1}^{j-1} \left[[^{2a}\overline{\beta}_{pj}]\, C_{ijk} \left(\sum_k C_{ipk}\right) - [^{2b}\overline{\beta}_{pj}]\, C_{ipk} \left(\sum_k C_{ijk}\right) \right] \right)$$

$$- \frac{1}{2} [^{3}\overline{\beta}_{jj}]\, C_{ijk} \left(\sum_k C_{ijk}\right) - C_{ijk} \left(\sum_{p=j+1}^{s} [^{4}\overline{\beta}_{pj}] \left(\sum_k C_{ipk}\right) \right) \qquad (5.5)$$

where s is the total number of sections in the aerosol representation. Of the six terms on the right hand side of this equation (with 1a, 1b, 2a, 2b, 3 and 4, respectively, as superscripts of $\overline{\beta}$), the first four are zero for the smallest aerosol section and, for the largest section, the third term and the last two terms are zero.

Expressing equation 5.5 in the form of equation 5.1 requires one additional approximation. The collision of two particles from the same section to produce one in the next larger section ($^{3}\overline{\beta}$) is a second-order, rather than a first-order loss process. Treating it as a first-order process, as is done in this model, introduces an insignificant error in almost all circumstances. The error would only become significant if the mass concentration in a single section were sufficiently large that coagulation among particles within that section represented a rapid loss process compared with numerical solution time scales. The error in such a case, which would represent an unusual situation, could be reduced by choosing a shorter solution time step.

5.3.6 Other Elements: Outdoor Concentrations, Initial Conditions, Indoor Emissions. The method for incorporating outdoor aerosol size distribution and chemical composition data and initial indoor particle characteristics is analogous to that used in the previous gas-phase model (Chapter 2): for each section and component, the user specifies the initial indoor mass concentration and the hourly-averaged values of outdoor mass concentration. The model applies linear interpolation to the latter data to obtain the outdoor concentrations at any given time.

Direct indoor emissions are treated by a more flexible method than in the gas-phase model. The model accepts sources having constant emission rates between start and stop times specified with one-minute precision. This permits simulation of sources that emit over relatively short time periods, such as a single cigarette. Time-varying sources can be represented in a discrete-step fashion by specifying multiple constant-emission sources with contiguous or overlapping emission periods.

5.3.7 Computer-Implementation Notes. In the computer model, equations 5.2, 5.4, and 5.5 are combined with direct emissions terms and cast into the form of equation 5.1. This equation is then solved numerically using the asymptotic integration method (Young and Boris, 1977), as implemented for the gas-phase indoor air quality model (Chapter 2). The program is written in VAX Fortran. The simulations described in the following section were run on a micro-VAX II, and required 40-60 min of CPU time to determine the evolution and fluxes over 11 hours of an aerosol represented by 16 sections having a single component in a single-chamber building.

The program has the capacity to trace a large number of parameters (in its current form the aerosol size distribution may be divided into 29 sections with 8 chemical components per section and be simulated in a building with up to 10 chambers over a period of 24 hours, and these limits may be easily extended). Even in its current configuration, it would require considerable computational power to make use of the full

capacity of the program. However, for most applications a much smaller number of parameters need to be simulated, and the program is designed to run efficiently for a restricted set of parameters. Furthermore, computation-intensive processes—coagulation and/or deposition—can be omitted from the analysis if they are deemed to be unimportant.

5.4 A Test of Model Performance: Evolution of Cigarette Smoke

5.4.1 Introduction. To develop confidence in the capabilities of the model, it is important to test its predictions against experimental data taken in rooms. Unfortunately, though, data on the evolution of indoor aerosols are sparse, and no experiments have been reported that include all of the important factors influencing the size distribution. The most suitable experimental data currently available for the purpose of testing the model recount the decay of cigarette smoke aerosol in a room having a low air-exchange rate (Offermann et al., 1985). Simulations of this experiment are described below, and it is shown that by assuming reasonable values for unmeasured variables, reasonable agreement between the measured and predicted aerosol size distribution is obtained.

5.4.2 Experiment. The experiment considered here was conducted as part of a study on the effectiveness of portable air cleaners. Details of the experimental protocol and study site can be found in Offermann et al. (1985). Key facts are summarized here.

The experiment was carried out in a closed, unoccupied room of a research "house." A single cigarette was smoked by machine within the room at a rate of two puffs of 35 ml per minute for a period of six minutes, then automatically extinguished. The aerosol size distribution was sampled continuously for a period of 24 hours using a laser-based optical particle counter (PMS, Model LAS-X), with results reported seven times per hour.

The air-exchange rate of the room was determined to be 0.05 h^{-1} by measuring the rate of decay of ^{222}Rn that had been injected to a concentration of ~ 18 kBq m^{-3} at the

outset of the experiment. An additional particle filtration rate of 0.013 h^{-1} resulted from air sampling.

No data were collected on air motion or surface temperatures.

5.4.3 Simulation. Because cigarette smoke emission rates are not known with high precision, the simulations were initialized at 30 minutes following cigarette ignition. The subsequent evolution of the aerosol size distribution was simulated for 11 hours; at the end of 11 hours the measured aerosol volume concentration had decayed to 23% of its initial value.

Due to the lack of direct measurements of airflow conditions along the walls during this experiment, simulations were run for a range of deposition conditions. The calculations for deposition driven by homogeneous turbulence in the core of the room were conducted at values of the turbulence intensity parameter ranging from 0.1-10 s^{-1}, which, based on a comparison of predicted and measured deposition velocities (Chapter 4), span those expected inside such a room. Deposition fluxes were also calculated for natural-convection driven flows using values of the temperature difference between surfaces and the air that range from -1 K to -5 K, which corresponds approximately in magnitude to the range of such temperature differences that we recently have measured in other buildings of similar construction. (To reduce the number of cases, all surfaces were assumed to have the same temperature.) Particle density was varied from 1.0 to 2.5 g cm^{-3}; however for the results presented here, a value of 1.4 g cm^{-3}, was used, based on simultaneous measurement of the cigarette smoke volume with the optical particle counter and gravimetric analysis of particles collected on a filter (F. J. Offermann, Indoor Environmental Engineering, San Francisco, California, personal communication, 1987).

5.4.4 Results and Interpretation. Predicted aerosol size distributions are compared against the experimental data in Figures 5.2 and 5.3. Both methods of predicting particle deposition rates are seen to yield model results that agree reasonably with the

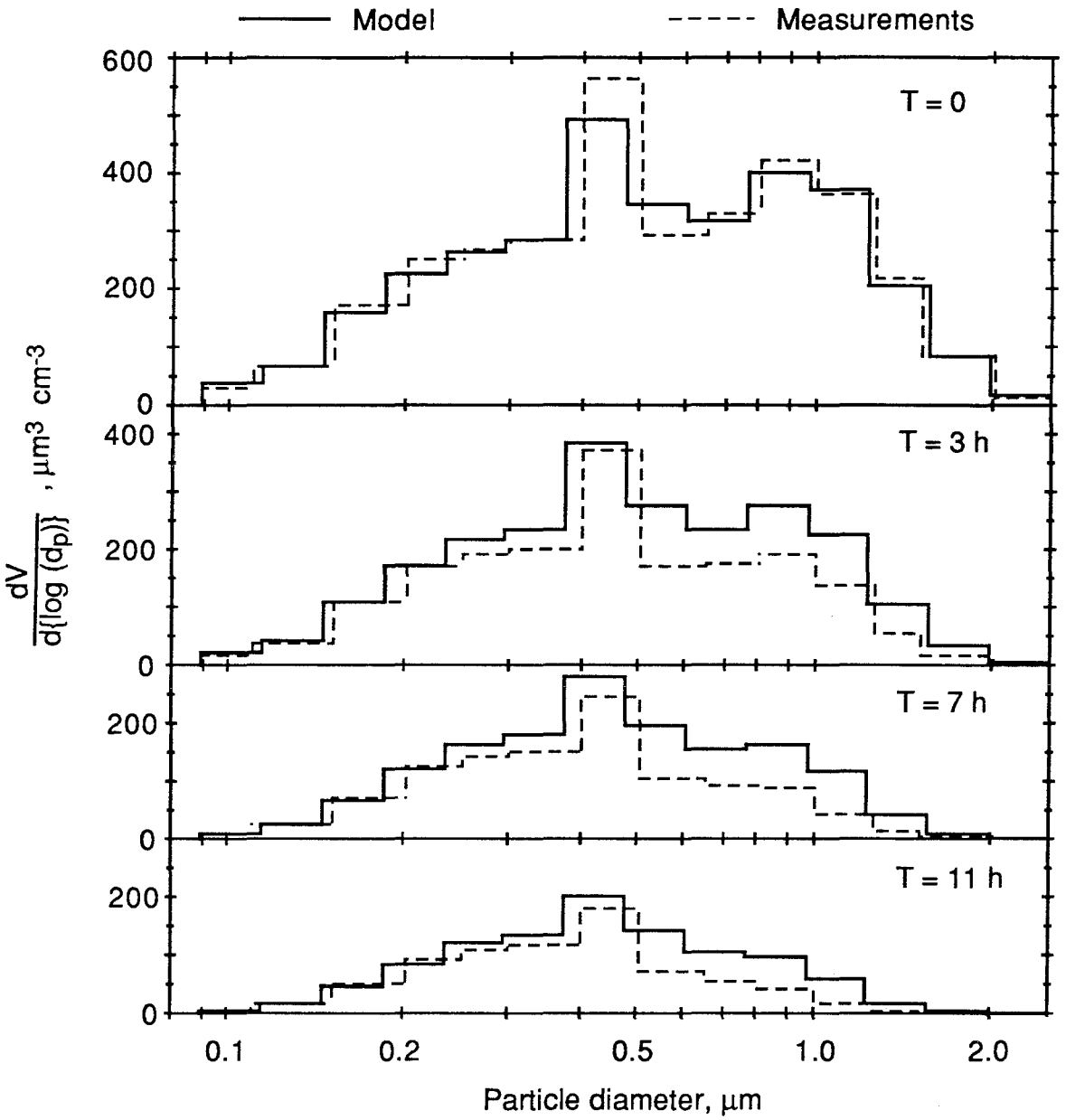

Figure 5.2 Evolution of the aerosol size distribution following combustion of a single cigarette. Measurements were conducted in a 35 m^3 room with a ventilation rate of 0.05 h^{-1} (Offermann et al., 1985). In the simulation, the natural convection description of airflow was used to account for particle deposition rates. All surfaces were assumed to be 1 K cooler than the air in the core of the room. Particle density was assumed to be 1.4 g cm^{-3}.

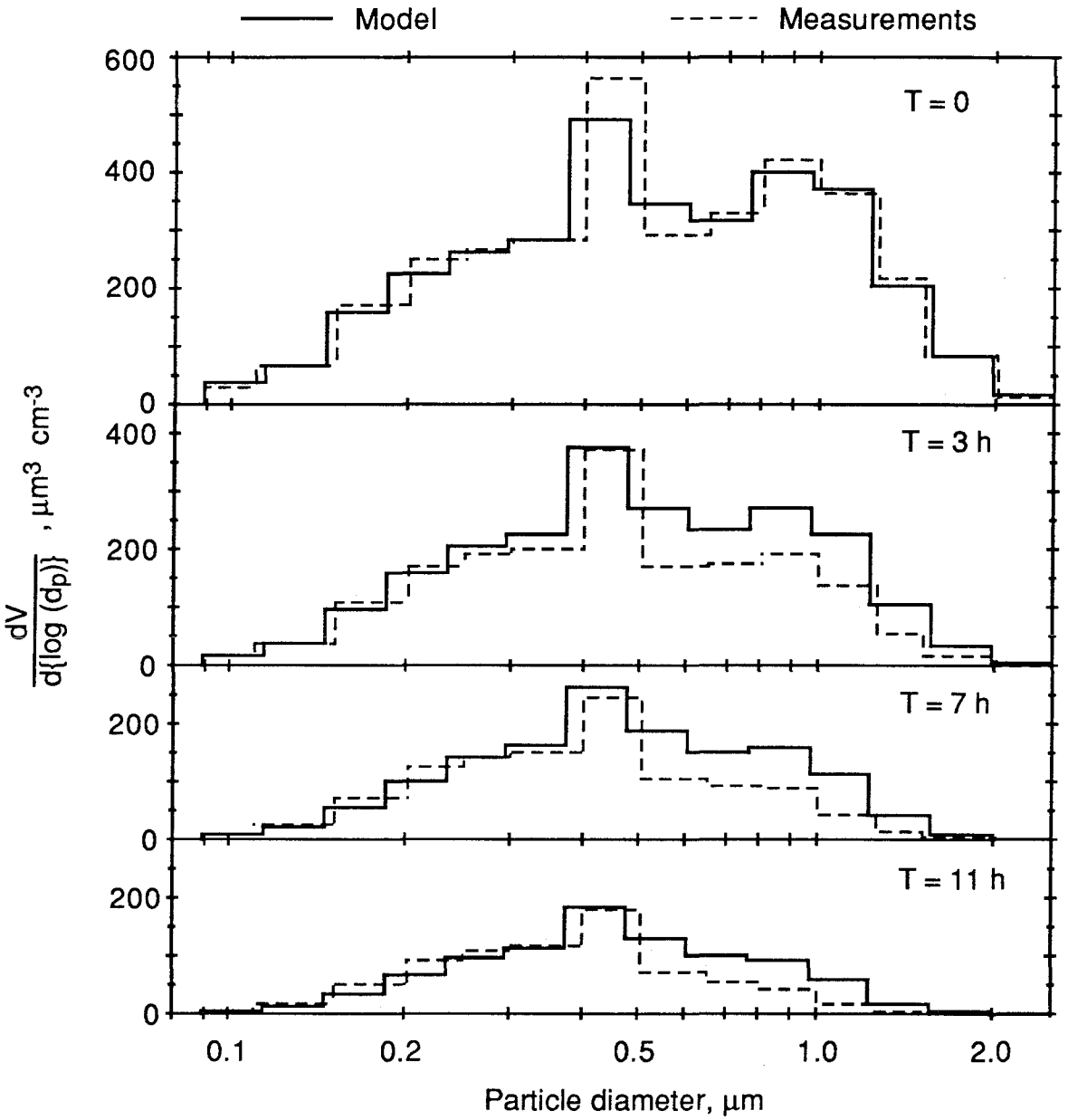

Figure 5.3 Evolution of aerosol size distribution following combustion of a single cigarette. Conditions unchanged from those of Figure 5.2, except the homogeneous turbulence description of airflow, with $K_e = 0.3\ s^{-1}$ and $\Delta T = 0$, was used to determine the particle deposition rates.

experimental measurements. Assumed values for the unmeasured parameters are plausible: surfaces 1 K cooler than the air for deposition driven by natural convection or a turbulence intensity parameter, K_e, of 0.3 s^{-1} for deposition driven by homogeneous turbulence. The agreement is particularly good for particles with a diameter in the range 0.09-0.4 μm. For particles in the range 0.5-1.0 μm, the model underpredicts the rate of loss of particle volume concentration when compared with the experimental data. Overall, the performance of the model appears to be satisfactory. From an initial aerosol volume concentration of 336 $\mu m^3\ cm^{-3}$, the predicted concentration after 11 hours is 93-107 $\mu m^3\ cm^{-3}$ for these two cases compared with a measured value of 78 $\mu m^3\ cm^{-3}$. Thus, in these simulations the model accounts for 90-95% of the aerosol volume lost from the room air.

Several possible explanations were explored in an attempt to account for the small remaining differences between model predictions and experimental data in the 0.5-1.0 μm diameter range. One class of explanations arises if the deposition of the particles to surfaces is underpredicted by the model, which could occur as follows: (1) the actual particle density was greater than the value 1.4 g cm^{-3} used in the model; (2) the actual temperature differences between the air and the surfaces were larger and the actual turbulence intensity was higher than assumed in the model calculations; (3) the actual particle deposition rate was higher than predicted because the model does not account for the particle migration due to inertial drift or electric fields; and (4) the actual particle deposition rate was higher than predicted due to surface roughness (Harrison, 1979; Shimada et al., 1987), a factor not considered in the model. The following explanations based on the possibility of measurement error also were explored: (5) the instrument systematically erred in determining particle size because of a difference in the index of refraction between cigarette smoke particles and the calibration aerosol (polystyrene latex); and (6) the coincident presence of two small particles in the sensing volume of the instrument led to erroneously high measured concentrations of larger particles. Among

all of these possible explanations for the differences between measurements and predictions, reason (6) appears most plausible. The probability of coincidence errors is proportional to the square of the particle concentration; thus, such errors would diminish through the course of the experiment. The net effect would be a measured loss rate of larger particles that is greater than actually occurs. This explanation is supported by the large number concentration (3×10^4 cm^{-3} with diameters in the range 0.09-2 μm) of particles following cigarette combustion relative to the maximum number concentration (1.7×10^4 cm^{-3}) given by the manufacturer of the optical particle counter as the limit before coincidence errors necessitate dead-time corrections.

The fate of the cigarette smoke aerosol as predicted by the simulation used to generate Figure 5.2 is shown in Figure 5.4. For these circumstances, coagulation is an important loss mechanism for particles of less than approximately 0.2 μm in diameter, shifting their mass to particles having a diameter in the vicinity of 0.5 μm. Small particles are affected by coagulation to a greater degree than are large particles because of the greater number concentration of small particles and because of their higher mobility. Deposition to surfaces is an important loss mechanism for particles larger than ~ 0.4 μm in diameter in this simulation. The large depositional losses for the largest particles are due to gravitational settling. In other situations, loss of particles due to ventilation would be a more important sink, but in this case the air-exchange rate for the room is unusually low.

The predicted size distribution of aerosol mass deposited during the 11-hour period onto different surfaces is shown in Figure 5.5 for the two alternative approaches used to calculate deposition fluxes. For the floor, most of the deposition is due to gravitational settling and so the results are similar for the two air flow regimes. This is the dominant site of deposition for particles larger than about 0.2 μm in diameter. For the walls and ceiling, the deposition predictions depend strongly on the assumptions concerning airflow. Using the natural convection model with the walls 1 K cooler than

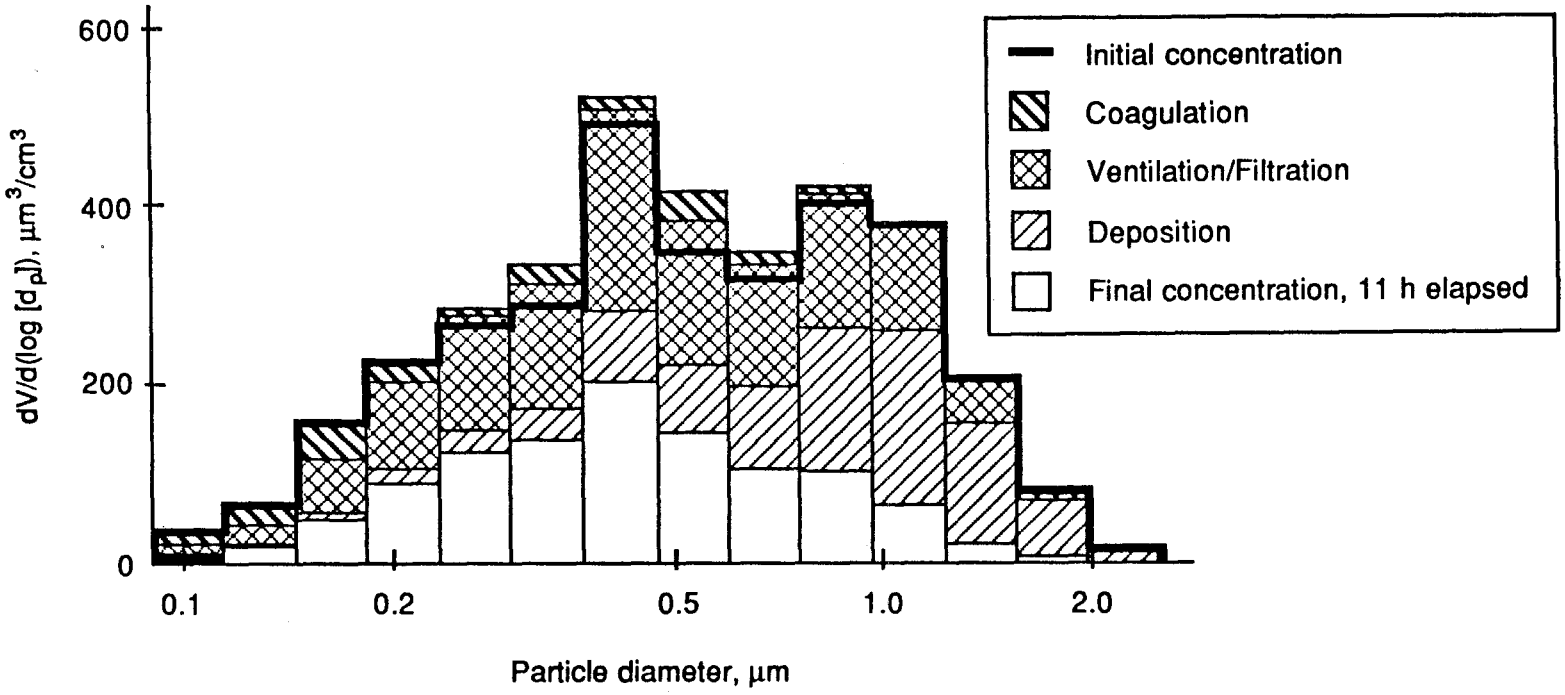

Figure 5.4 Predicted fate of cigarette smoke aerosol. The conditions of the simulation were the same as used to generate Figure 5.2. Note that coagulation represents a net sink for particles in the four smallest sections and a net source of particles in the larger sections.

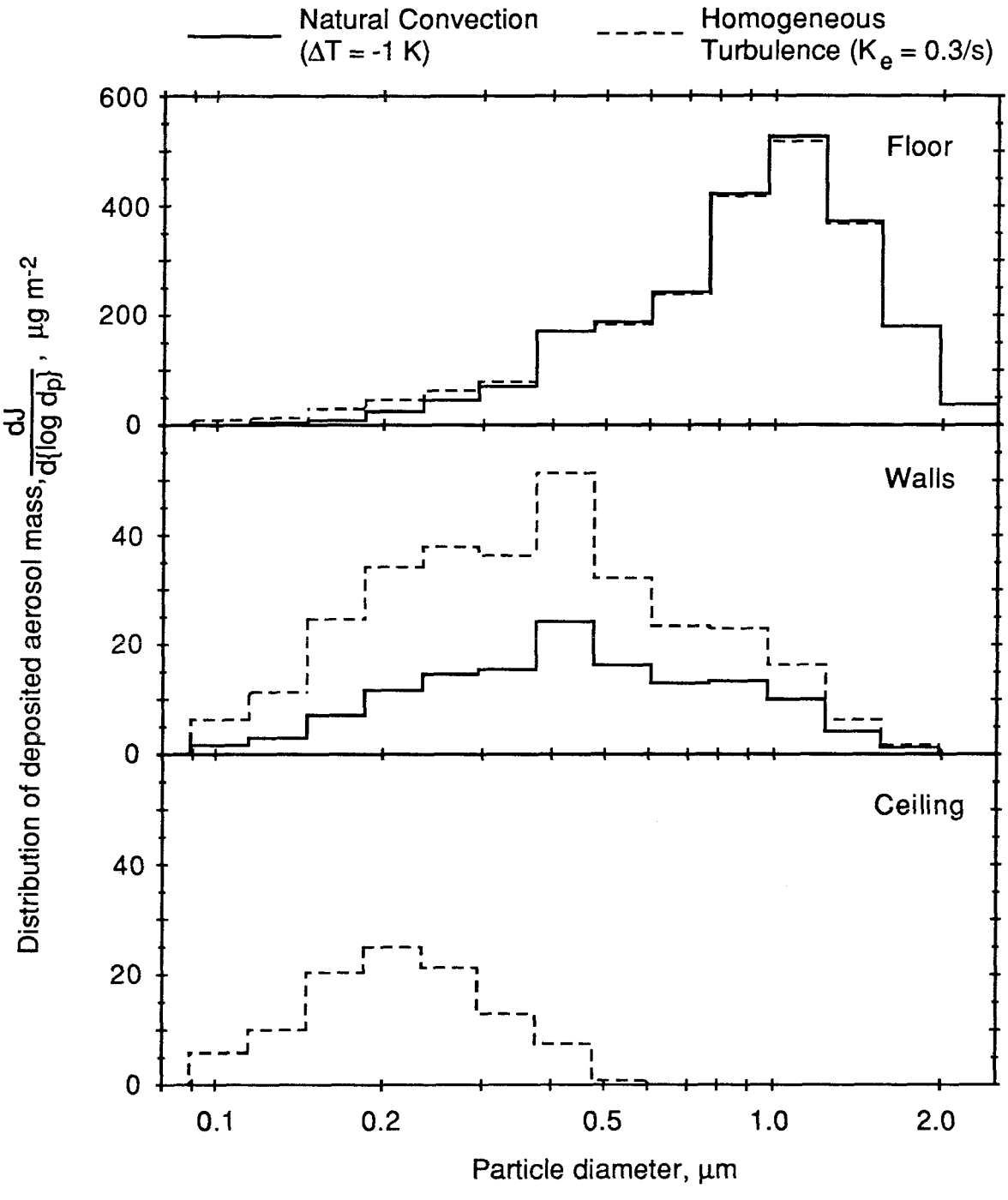

Figure 5.5 Predicted size distribution of cigarette smoke aerosol mass deposited per unit area onto different surfaces of the test chamber, $dJ/d(\log d_p)$. The average deposited mass per unit area is plotted for each size section for the eleven-hour period beginning 30 minutes after combustion of the cigarette. The simulation conditions correspond to those used to generate Figures 5.2 and 5.3.

the air, uniformly smaller deposition rates are predicted than with the homogeneous turbulence model assuming $K_e = 0.3\ s^{-1}$. Because of the competing effect of gravity, there is essentially no deposition onto the ceiling using the natural convection description; however, the assumed turbulence intensity is strong enough to overcome gravitational settling and cause some particle deposition onto the ceiling.

5.5 Discussion

5.5.1 Model Validation. Because of its complexity, no single experiment provides a thorough test of all features of the model. It would be desirable to compare model predictions against the results of experiments specifically designed to test separately the coagulation and deposition calculations. The effects of these elements of the model, clearly important in some circumstances, could be masked by the larger effects of direct emission and ventilation in many situations. It is also important that the overall performance of the model is compared against additional experimental data taken in buildings in normal operation. For mechanically ventilated buildings, such experiments would require, at a minimum, measurement of ventilation rates, filtration efficiencies, and, as a function of time, the indoor and outdoor aerosol size distribution. In addition, measurements of the indoor air flow characteristics, temperature distribution, and particle deposition fluxes would improve the basis for comparing model predictions with measurements.

5.5.2 Model Applications. As noted in the introduction, the model has application to several research topics of current interest. In this section, the methods by which such applications may be pursued are sketched.

One area of interest, and the immediate motivation for the present research, is the soiling of works of art. With information on outdoor aerosol concentrations, building operation characteristics, and indoor flow dynamics, the model can be used directly to compute the rate of deposition of airborne particles onto indoor surfaces such as a fresco.

It is a relatively short step from there to the evaluation of the rate of soiling, that is the rate of degradation of the transmission of visual information from the object to an observer. The present model should prove particularly useful in predicting the effect of control measures designed to reduce the rate of soiling.

A second topic of current concern is the exposure of nonsmokers to environmental tobacco smoke. The model can be used to address important aspects of the problem, such as how exposure characteristics vary with frequency of smoking and building ventilation conditions. The present model represents an important advance over previously available tools in that it directly simulates the aerosol size distribution that is necessary to relate accurately dose to exposure. The influence of coagulation and deposition on the aerosol size distribution may be quite substantial, as indicated in Figure 5.3. Consequently, explicit treatment of these processes by the present model also represents an important advance.

A third area of interest is the inhalation of radon decay products indoors. The total radiation dose and its distribution within the lung depend critically on the fractions of the decay product concentrations that are not attached to airborne particles, and on the size distribution of the attached fractions (James, 1984). Existing models of the dynamics of radon decay product behavior treat the indoor aerosol size distribution as a static, given entity (Knutson, 1988). As a result, certain problems, such as the influence of air cleaners that remove both airborne particles and radon decay products on dose to the lung, cannot be simulated adequately with existing tools. A module accounting for radon decay product dynamics could be added to the model described in this chapter to establish a means of addressing this and related issues.

The model does not currently account for all of the dynamic processes affecting the indoor aerosol. Simple calculations show that one might expect substantial gas-to-particle conversion in some cases. For example, because of the considerable temperature sensitivity of the equilibrium dissociation constant for ammonium nitrate (Russell et al.,

1983), the cooling of polluted outdoor air upon entry into an air-conditioned building could lead to substantial conversion of gaseous NH_3 and HNO_3 to aerosol phase NH_4NO_3. Incorporation of such gas-to-particle conversion processes is possible if the gas phase pollutant models described previously (Russell et al., 1983; and Chapter 2 of this work) are coupled to the present aerosol model. As another example, nucleation of fresh aerosol is clearly important indoors in connection with combustion sources, and the model treats such a process by accounting for direct indoor emissions. However, the model does not presently account for spatially distributed aerosol nucleation, which might also be important in some circumstances. Investigators are currently exploring whether distributed aerosol production may be promoted by the radioactive decay of ^{222}Rn and its decay products, often present in high concentrations indoors.

In summary, a mathematical model for indoor aerosol dynamics has been developed that links a flexible description of building and ventilation system structure to a mechanistically sound analysis of particle dynamics. The model tracks the evolution over time of the aerosol size distribution and the fate of distinct chemical constituents of that size distribution, as well as the loss of particles to indoor surfaces. The present model can be used to study problems as diverse as the soiling of art objects in museums and the exposure of office workers to environmental tobacco smoke. The calculation scheme may be readily combined with existing models for the behavior of chemically reactive gases indoors (Chapter 2) and outdoors (Russell et al., 1983) to study gas-to-particle conversion processes and with existing models of radon decay product behavior (Knutson et al., 1988) to study the relationship between exposure to radon decay products indoors and radiation dose to the lung.

5.6 Nomenclature

Symbols

A_{im}	area of the m^{th} surface of chamber i (m^2)
C(Kn)	slip correction factor (-)
C_{ijk}	mass concentration of aerosol component k in size section j within chamber i ($\mu g\ m^{-3}$)
D	coefficient of Brownian diffusivity of particles ($m^2\ s^{-1}$)
D_e	coefficient of eddy diffusion ($m^2\ s^{-1}$)
d_i	diameter of ith particle, i=1,2 (m)
d_p	particle diameter (μm)
$\frac{dJ}{d\{\log d_p\}}$	deposited mass density of particles having diameters between $\{\log [d_p]\}$ and $\{\log [d_p] + d(\log [d_p])\}$ ($\mu g\ m^{-2}$)
$\frac{dV}{d\{\log d_p\}}$	differential volume concentration of particles having diameters between $\{\log [d_p]\}$ and $\{\log [d_p] + d(\log [d_p])\}$ ($\mu m^3\ cm^{-3}$)
f_{ih}	rate of air flow from chamber i to chamber h ($m^3\ s^{-1}$)
g	gravitational acceleration (9.8 $m\ s^{-2}$)
H	height of room (m)
K	thermophoresis coefficient (see Chapter 3) (-)
K_e	turbulence intensity parameter (s^{-1})
Kn	particle Knudsen number (-)
k	Boltzmann's constant ($1.38 \times 10^{-23}\ J\ K^{-1}$)
L	characteristic dimension of surface: area divided by perimeter (m)
Le	particle Lewis number, α/D (-)
L_{ijk}	rate of loss of aerosol mass from component k and section j in chamber i (s^{-1})
N_a	Avogadro's number ($6.02 \times 10^{23}\ mol^{-1}$)

N_t	thermophoresis parameter, $K\frac{\Delta T}{T_\infty}$ (-)
P	pressure of air (Nt m^{-2})
Pr	Prandtl number of the fluid, ν/α (-)
R	universal gas constant (8.314 J K^{-1} mol^{-1})
Ra_H	Rayleigh number, $\frac{g\,\beta\,\lvert\Delta T\rvert\,H^3}{\alpha\nu}$, where β is the coefficient of thermal expansion of air (-)
Ra_L	Rayleigh number, $\frac{g\,\beta\,\lvert\Delta T\rvert\,L^3}{\alpha\nu}$ (-)
Sc	particle Schmidt number, ν/D (-)
S_{ijk}	rate of production of aerosol mass of component k in section j within chamber i ($\mu g\ m^{-3}\ s^{-1}$)
s_g	orientation coefficient, 1 for upward-facing, -1 for downward-facing (-)
T	temperature of air (K)
T_∞	air temperature outside of boundary layer (K)
t	time (s)
u	mass of particle (μg)
V_i	volume of chamber i (m^3)
v_{CP}	deposition velocity by theory of Corner and Pendlebury (1951) (m s^{-1})
v	mass of particle (μg)
v_{dimj}	mean deposition velocity of particles in size section j to the m^{th} surface of chamber i (m s^{-1})
v_g	gravitational settling velocity (m s^{-1})
v_j	mass of largest particle in section j (μg)
v_t	thermophoretic velocity of particles near surface (m s^{-1})
x	natural logarithm of the mass of a particle (mass expressed in μg)
x_s	length of a surface in the direction of flow (m)
y	natural logarithm of the mass of a particle (mass expressed in μg)

y_s	distance from a surface (m)

Greek Symbols

α	thermal diffusivity of air ($m^2\ s^{-1}$)
$\overline{\beta}_{pqj}$	mean rate of collision between particles in sections p and q yielding a particle in section j ($m^3\ \mu g^{-1}\ s^{-1}$)
$\overline{\beta}_{pj}$	mean rate of collision between particles in sections p and j ($m^3\ \mu g^{-1}\ s^{-1}$)
γ	accommodation coefficient (= 1 for present work) (-)
δ	boundary layer thickness for turbulent flow (m)
ΔT	temperature of surface (T_s) minus temperature of air outside boundary layer (T_∞) (K)
η_{ihj}	filter efficiency for removing particles in size section j from the air stream flowing from chamber i to chamber h (-)
κ	sticking coefficient (= 1 for present work) (-)
λ	mean free path of gas molecules (m)
μ	dynamic viscosity of air ($kg\ m^{-1}\ s^{-1}$)
ν	kinematic viscosity of air ($m^2\ s^{-1}$)
ρ	particle density ($kg\ m^{-3}$)
$\omega'(0)$	slope of normalized particle concentration at surface (see Chapter 3) (-)

Subscript Indices

h	chamber number
i	chamber number
j	aerosol size section
k	aerosol chemical component number
m	surface number
n	total number of chambers
p	aerosol size section

q	aerosol size section
s	total number of aerosol size sections
x	designates mechanical ventilation system
0	designates outdoor air

5.7 Acknowledgements

Support for this research was provided by a contract with the Getty Conservation Institute and by a fellowship from the ARCS Foundation.

5.8 References

Alzona, J., Cohen, B. L., Rudolph, H., Jow, H. N., and Frohliger, J. O. (1979) Indoor-outdoor relationships for airborne particulate matter of outdoor origin, *Atmospheric Environment* **13**, 55-60.

Baer, N. S., and Banks, P. N. (1985) Indoor air pollution: Effects on cultural and historic materials, *International Journal of Museum Management and Curatorship* **4**, 9-20.

Clemente, G. F., Eriskat, H., O'Riordan, M. C., and Sinnaeve, J., Eds. (1984) *Radiation Protection Dosimetry* **7**.

Cooper, D. W. (1986) Particulate contamination and microelectronics manufacturing: An introduction, *Aerosol Science and Technology* **5**, 287-299.

Corner, J., and Pendlebury, E. D. (1951) The coagulation and deposition of a stirred aerosol, *Proceedings of the Physical Society (London)* **B64**, 645-654.

Cortes-Comerer, N. (1987) Out from the shadows, *Mechanical Engineering* **109(9)**, 44-50.

Crump, J. G., Flagan, R. C., and Seinfeld, J. H. (1983) Particle wall loss rates in vessels, *Aerosol Science and Technology* **2**, 303-309.

Fuchs, N. A. (1964) *Mechanics of Aerosols*, Pergamon: New York.

Gelbard, F. (1982) *MAEROS User Manual*, U.S. Nuclear Regulatory Commission: Washington, NUREG/CR-1391 SAND80-0822 R7.

Gelbard, F., and Seinfeld, J. H. (1980) Simulation of multicomponent aerosol dynamics, *Journal of Colloid and Interface Science* **78**, 485-501.

Harrison, A. W. (1979) Quiescent boundary layer thickness in aerosol enclosures under convective stirring conditions, *Journal of Colloid and Interface Science* **69**, 563-570.

Hopke, P. K., Ed. (1987) *Radon and Its Decay Products: Occurrence, Properties and Health Effects*, American Chemical Society: Washington, ACS Symposium Series 331.

James, A. C. (1984) Dosimetric approaches to risk assessment for indoor exposure to radon daughters, *Radiation Protection Dosimetry* **7**, 353-366.

Knutson, E. O. (1988) Modeling indoor concentrations of radon's decay products, In *Radon and Its Decay Products in Indoor Air*, Nazaroff, W. W., Nero, A. V., Eds., Wiley: New York, Chapter 5.

Larrabee, G. B. (1985) A challenge to chemical engineers—Microelectronics, *Chemical Engineering* **92(12)**, 51-59.

National Research Council (1986) *Environmental Tobacco Smoke: Measuring Exposures and Assessing Health Effects*, National Academy Press: Washington.

Nazaroff, W. W., and Nero, A. V., Eds. (1988) *Radon and Its Decay Products in Indoor Air*, Wiley: New York.

Odom, J. P., Senglaub, M. E., Kelly, J. E., and Clauser, M. J. (1981) CONTAIN: A computer code for simulation of reactor accident containment, *Transactions of the American Nuclear Society* **38**, 328-330.

Offermann, F. J., Sextro, R. G., Fisk, W. J., Grimsrud, D. T., Nazaroff, W. W., Nero, A. V., Revzan, K. L., and Yater, J. (1985) Control of respirable particles in indoor air with portable air cleaners, *Atmospheric Environment* **19**, 1761-1771.

Okuyama, K., Kousaka, Y., Yamamoto, S., and Hosokawa, T. (1986) Particle loss of aerosols with particle diameters between 6 and 2000 nm in stirred tank, *Journal of Colloid and Interface Science* **110**, 214-223.

Phillips, W. F. (1975) Drag on a small sphere moving through a gas, *Physics of Fluids* **18**, 1089-1093.

Pilinis, C., Seinfeld, J. H., and Seigneur, C. (1987) Mathematical modeling of the dynamics of multicomponent atmospheric aerosols, *Atmospheric Environment* **21**, 943-955.

Pruppacher, H. R., and Klett, J. D. (1978) *Microphysics of Clouds and Precipitation*, D. Reidel: Dordrecht, Sect. 12.6.

Reid, R. C., Prausnitz, J. M., and Sherwood, T. K. (1977) *The Properties of Gases and Liquids*, 3rd ed., McGraw-Hill: New York, p. 678.

Russell, A. G., McRae, G. J., and Cass, G. R. (1983) Mathematical modeling of the formation and transport of ammonium nitrate aerosol, *Atmospheric Environment* **17**, 949-964.

Saffman, P. G., and Turner, J. S. (1956) On the collision of drops in turbulent clouds, *Journal of Fluid Mechanics* **1**, 16-30.

Seifert, B., Esdorn, H., Fischer, M., Rüden, H., and Wegner, J., Eds. (1987) *Indoor Air '87*, Institute for Water, Soil and Air Hygiene: Berlin, Vol. 2, pp. 1-179.

Seinfeld, J. H. (1986) *Atmospheric Chemistry and Physics of Air Pollution*, Wiley: New York.

Shimada, M., Okuyama, K., Kousaka, Y., and Ohshima, K. (1987) Turbulent and Brownian diffusive deposition of aerosol particles onto a rough wall, *Journal of Chemical Engineering of Japan* **20**, 57-64.

U.S. Department of Health and Human Services (1986) *The Health Consequences of Passive Smoking: A Report of the Surgeon General*, U.S. Department of Health and Human Services: Rockville, MD.

Warren, D. R., and Seinfeld, J. H. (1985) Simulation of aerosol size distribution evolution in systems with simultaneous nucleation, condensation and coagulation, *Aerosol Science and Technology* **4**, 31-43.

Wu, J. J. (1986) *Powder Synthesis in Aerosol Reactors*, Ph.D. Thesis, California Institute of Technology, Pasadena, California.

Young, T. R., and Boris, J. P. (1977) A numerical technique for solving stiff ordinary differential equations associated with the chemical kinetics of reactive-flow problems, *Journal of Physical Chemistry* **81**, 2424-2427.

CHAPTER 6

CONCENTRATION AND FATE OF AIRBORNE PARTICLES IN MUSEUMS

6.1 Abstract

Objects displayed in museums are subject to a soiling hazard due to the deposition of airborne particles. To investigate this hazard, time-resolved measurements were made of the indoor and outdoor aerosol size distribution and chemical composition in three Southern California museums. A mathematical model of indoor aerosol dynamics was applied to the three sites to relate the data on outdoor aerosol characteristics and building parameters to observed indoor aerosol properties. The predicted indoor aerosol characteristics agree well with the indoor measurements. For the two sites having mechanical ventilation systems, model calculations show that generally greater than 70% of the fine particles (0.05-2 μm in diameter) entering the building from outdoor air are removed by successive passes through the medium-efficiency air filters. At all three sites, the fraction of particles entering from outdoor air that deposit onto surfaces varies strongly with particle size, ranging from a minimum of 0.1-0.5% for particles having a diameter in the vicinity of 0.15 μm to greater than 90% for particles larger than 20 μm in diameter. Deposition calculations indicate that, at the rates determined for the study days, enough elemental carbon (soot) would accumulate on vertical surfaces in the museums to yield perceptible soiling in as little as one year at one site to as long as 10-40 years at the other two sites.

Nazaroff, W. W., Salmon, L. G., and Cass, G. R., Concentration and fate of airborne particles in museums, to be submitted to *Environmental Science and Technology*.

6.2 Introduction

Objects kept indoors may suffer damage due to exposure to air pollutants. The concern over this potential hazard is acute among museum curators (e.g., Thomson, 1978). The objects in their charge are often valued entirely for their visual quality, a characteristic that may be particularly susceptible to air pollution damage. Furthermore, it is desired to preserve these objects for centuries; thus, even modest rates of deterioration may yield a cumulative effect that is unacceptable.

Airborne particles constitute a major class of pollutants that may be hazardous to works of art. Deposition of particulate matter onto the surface of an object may cause chemical damage and/or soiling. Consequently, activities that generate particles, such as smoking, are restricted in museum galleries. However, particulate matter may enter the building with the outdoor air that is supplied for ventilation. Although some research has been reported on indoor/outdoor relationships for airborne particles (e.g., Yocum, 1982 and references therein), little is known about particle concentrations in museums, the factors that affect those concentrations, the fate of particles that enter museum atmospheres, and the magnitude of the potential soiling hazard posed by deposition of airborne particles (Baer and Banks, 1985). The present chapter addresses these issues.

Over periods of 24 hours, at each of three museums in Southern California, time-dependent measurements were made of the chemical composition and size distribution of the indoor and outdoor aerosol. Building characteristics that influence aerosol concentrations and fates were measured: ventilation rate, temperature differences between a wall and the air, fluid velocities adjacent to a wall, and the particle removal efficiency of filters in the mechanical ventilation system. From these data, the concentration and fate of the indoor aerosol was computed for each site, using a mathematical model previously developed for use in this study (Chapter 5). To evaluate the performance of the model, the predicted indoor aerosol properties—based on the outdoor aerosol data and

measured building characteristics—are compared against the results of the indoor measurements. The fate of particulate matter entering the museums is assessed through the use of the model, with emphasis on the deposition of particles—particularly those containing elemental carbon and soil dust—onto indoor surfaces. The results show that the principal soiling hazard to smooth vertical surfaces and to downward facing surfaces results from the deposition of particles with diameters in the vicinity 0.1 μm. For floors and other upward facing surfaces, both fine and coarse particles contribute significantly to the rate of soiling.

6.3 Study Sites

Three sites in Southern California were selected for the study: the Norton Simon Museum in Pasadena, the Scott Gallery on the Huntington Library grounds in San Marino, and the Sepulveda House at El Pueblo de Los Angeles State Historic Park in downtown Los Angeles. These were chosen from among five museums in which indoor and outdoor aerosol characteristics were measured on a 24-hour average basis every sixth day during the previous summer and winter seasons (Ligocki et al., 1988a). The range of values for the ratio of indoor to outdoor aerosol mass concentration thus was known approximately in advance, and the three sites were selected to span the range from very high to very low indoor aerosol concentration. Major characteristics of the buildings are summarized in Table 6.1 and in the following discussion.

The Norton Simon Museum and the Scott Gallery are modern buildings with custom-engineered heating, ventilation and air conditioning (HVAC) systems (see Figure 6.1). At the Norton Simon Museum, make-up air from outdoors passes through a fibrous mat filter (F_{A1}), and through an activated carbon filter (F_{A2}), before being blended with return air that has been passed through a fibrous mat filter (F_{A3}); the air mixture is then conditioned for proper temperature and humidity, and distributed to the building. The make-up air flow rate (Q_F) is lower than the original design value, as the supply-air

Table 6.1. Characteristics of the study sites

	Norton Simon	Scott Gallery	Sepulveda House
Dimensions			
No. of floors	2	1	2
Floor Area (m^2)	4930	535	330
Wall Area (m^2)	6950	1990	1050
Volume (m^3)	21540	2530	1200
Ventilation [a]			
Outdoor air-exchange (h^{-1})	0.37 [b]	0.28±0.01	3.6±1.4
Recirculation (h^{-1})	5.8	8.2	—
Monitoring period			
Start date	6 April 88 [c]	24 April 88	30 March 88
Start time	1000 PDT	1800 PDT	2100 PST

[a] Flow rate divided by building volume; mean±one standard deviation of measurements for 24 hour period.

[b] Based on hot-wire anemometry measurements of outdoor air flow rate into mechanical ventilation system. Tracer gas decay yielded 0.40 h^{-1} with 90% confidence bounds of 0.37-0.44 h^{-1}.

[c] Boundary layer flow and temperature differences measured for 24 hours commencing at 1200 PDT on 4 April 1988.

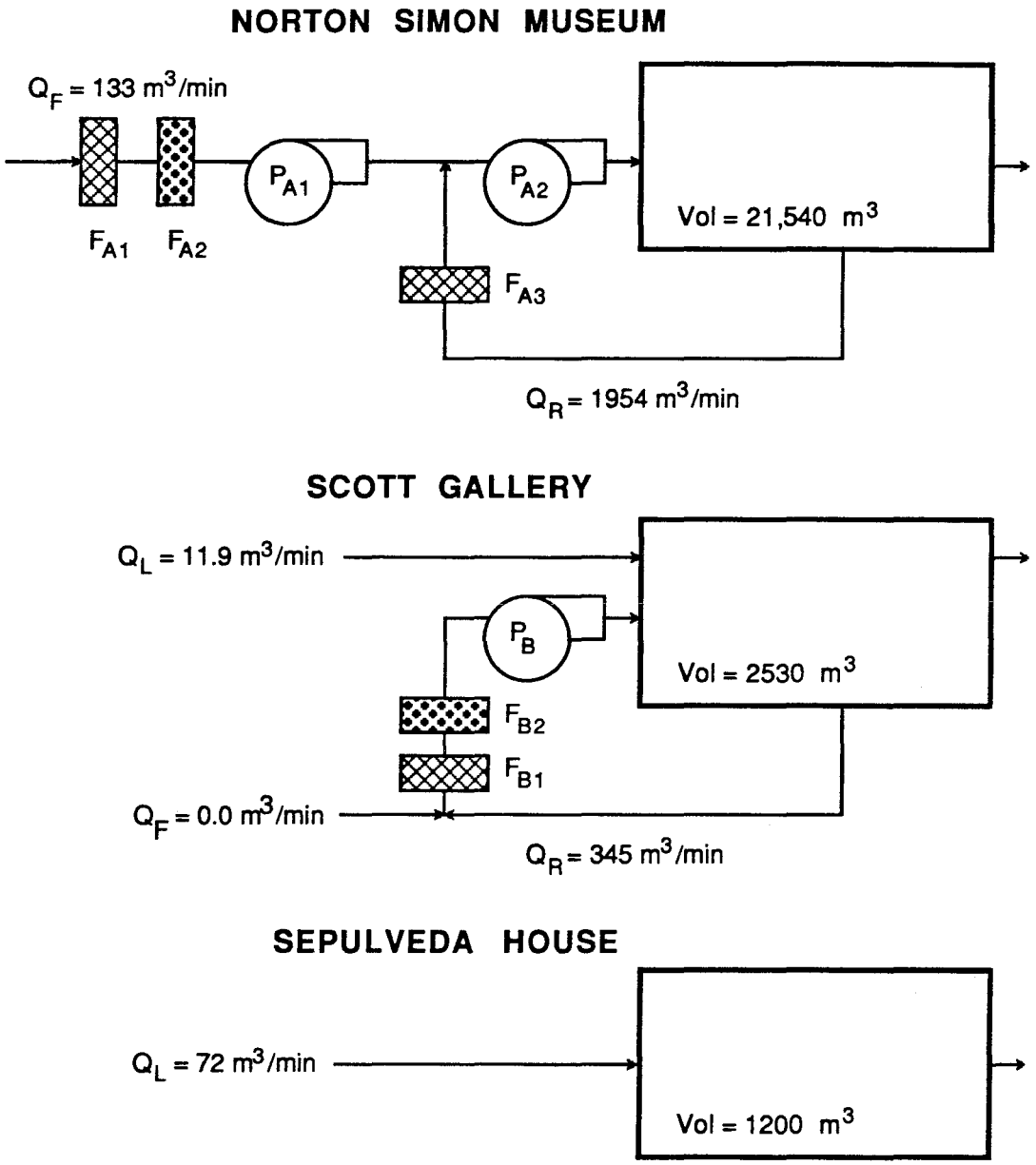

Figure 6.1 Schematic representation of the ventilation and filtration systems for the three study sites, showing the flow rates (Q), fans (P) and filters (F) in each system. For air flows, subscripts L, F, and R represent leakage (infiltration), forced supply (make-up), and recirculation, respectively. Filters F_{A2} and F_{B2} contain activated carbon for ozone removal; the other filters are mat-fiber type for removing particles.

blower (P_{A1}) has been shut off to improve temperature control. At the Scott Gallery, the building was originally operated with 25% make-up air, which would be blended with the return air, passed through a fibrous filter, conditioned, and then distributed to the building (as described in Chapter 2). More recently, an activated carbon filter was added to the system for ozone removal, and the flow rate of make-up air was reduced effectively to zero by closing the intake dampers (again for the purpose of improving thermal control). At the time of the present study, air-exchange between indoors and outside at the Scott Gallery occurred entirely due to infiltration through cracks in the building shell and through door openings.

The Sepulveda House is an historical museum with no system for regulating the air temperature, humidity, or ventilation rate. Air-exchange is provided by infiltration through relatively large openings in the building shell. When the building is open to the public (1000-1500 daily, except Sunday) and the weather is warm, two downstairs doors are kept open.

At each site, one wall was selected for investigation of boundary-layer air flows and temperature gradients that influence particle deposition rates. Measurements of particle deposition rate, reported elsewhere (Ligocki et al., 1988b; see also Chapter 7), were made on the same walls. Detailed description of the walls is provided in Chapter 7. Briefly, an interior wall with a painted dry-wall surface was selected for investigation at the Norton Simon Museum; a painted plywood panel mounted onto an interior wall with furring strips was selected at the Scott Gallery; and an outer brick wall having a painted, irregular plaster surface was chosen at the Sepulveda House.

Because the experiments would have been disruptive to normal museum operation, measurements at the Norton Simon Museum and at the Scott Gallery were conducted while the buildings were closed to the public (the museum staff were still present). Consequently, this study does not fully incorporate the effects of occupancy on

aerosol properties. The Sepulveda House was open to the public, as usual, from 10 AM to 3 PM on the day of monitoring.

6.4 Experimental Methods

Detailed, time-resolved information on the indoor and outdoor aerosol size distribution and chemical composition was collected at each site for a period of twenty-four hours. To measure the aerosol size distribution, two pairs of optical particle counters were operated, one pair sampling from a central indoor location with the second sampling from an outdoor location on the grounds of the site. One instrument in each pair (Particle Measuring Systems model ASASP-X, referred to subsequently as the "mid-range OPC") is capable of detecting particles over a nominal size range of 0.09-3 μm optical diameter and classifying them, according to the amount of light scattered in the forward direction, into 32 size channels. Sampling flow rates were measured at least hourly with rotameters that had been calibrated against a bubble flow meter; the flow rate was adjusted whenever it deviated by more than 10% from a nominal rate of 1 $cm^3\ s^{-1}$. The second instrument in each pair (Particle Measuring Systems model CSASP-100HV) detects and classifies light scattered from particles in the size range 0.5-47 μm diameter. All of the optical particle counters were operated continuously, with cumulative counts per channel recorded at six-minute intervals. The results of tests of instrument performance are discussed in the appendix to this chapter, Section 6.10.

Indoor and outdoor aerosol mass concentration and chemical composition were determined for the total suspended particulate matter (TSP) and for the fine particles ($< \sim 2$ μm diameter) using sampling devices and analysis methods similar to those described by Gray et al. (1986). Briefly, for both indoor and outdoor sampling locations, air was drawn through each of two sets of three 47-mm diameter filters—one quartz fiber (Pallflex 2500 QAO) and two Teflon membrane filters (Gelman, PTFE, ringed, 2.0 μm pore size). One filter set at each site was deployed in open-faced holders to collect the

TSP, while the other set was placed within in-line holders downstream of a cyclone separator (John and Reischl, 1980) to collect the fine particles. The air flow rate through each filter holder was nominally 30 l min^{-1}, and each of the fine particle filter holders was preceeded by its own cyclone separator. The sampling interval was typically 4 hours; however, because of access restrictions, 8-hour intervals were used at night at the Norton Simon Museum. The quartz filters were analyzed for elemental and organic carbon (Johnson et al., 1980; Cary, 1987). One of the Teflon filters was used to gravimetrically determine aerosol mass concentration and, by x-ray fluorescence, the concentrations of 34 trace metals (Dzubay, 1977). The second Teflon filter was analyzed for sulfate and nitrate concentrations by ion chromatography (Mulik et al., 1976) and for ammonium ion by colorimetry (Bolleter et al., 1961). For the purposes of this chapter, the elemental carbon concentrations are of great interest, as they govern the blackness, and therefore a major portion of the soiling hazard, of the fine particulate matter (Cass et al., 1984). In addition, the aluminum and silicon concentrations are of interest as markers for soil dust which may also lead to soiling.

Air-exchange rates were measured at each site using the tracer-gas decay technique, with sulfur hexafluoride (SF_6) as the tracer (ASHRAE, 1985). At the Scott Gallery and the Sepulveda House, SF_6 measurements were made continuously throughout the study period, with samples collected at intervals of ~ 10 minutes and analyzed with a portable gas chromatograph. At the Norton Simon Museum, because of access limitations, a single two-hour tracer decay measurement was made during the study period. The air flow rates through the mechanical ventilation system were determined by hot-wire anemometry at the Norton Simon Museum and on the basis of building design specifications at the Scott Gallery.

The air velocity adjacent to surfaces and the temperature difference between the surface and the adjacent air are important factors governing the deposition rate of fine particles (Chapters 3 and 4). During the study period, continuous measurements were

made of the temperature difference between the air and the surface of one wall using an array of thermistors (Yellow Springs Instrument, part no. 44202). Two thermistors were used to determine the temperature of the wall surface; one was mounted in a thin (1.5 mm) aluminum plate that was attached to the wall with thermal joint compound, the other was coated with thermal joint compound and set into a small hole drilled in the wall so that the thermistor was flush with the surface. Likewise, two thermistors were used to determine the air temperature at approximately 15 cm from the wall; one was shielded with insulating foam to eliminate radiant heat transfer, the other was unshielded. The temperature difference was determined as the difference between the mean of the two wall probes and the mean of the two air probes. The probes were individually calibrated and have an intrinsic uncertainty of ~ 0.02 °C. Differences between the temperatures measured by the two wall probes and by the two air probes were less than 0.1 °C in 53%, less than 0.2 °C in 83%, and less than 0.3 °C in 94% of the measurements made during the entire study.

Air velocity was measured adjacent to the same wall using two omnidirectional sensors (TSI model 1620), placed at approximately 0.6 and 1.2 cm from the surface of the wall. The temperatures and velocities were sampled with a microcomputer-based data logger at intervals of two seconds, and the mean value was recorded for each minute. At the Norton Simon Museum, again because of access limitations, surface and air temperatures and the air velocities were monitored for 24 hours two days prior to the aerosol monitoring period. At the other sites, the temperatures and velocities were measured simultaneously with the aerosol monitoring.

The particle removal efficiency of the filters found in the buildings' mechanical ventilation systems was measured as a function of particle size for each fiber filter by simultaneously measuring the upstream and downstream particle concentrations with the two sets of optical particle counters. The measurements at the Norton Simon Museum were done *in situ*. For filter F_{B1} at the Scott Gallery, a section of a used filter panel from

the site was obtained. At a Caltech laboratory (located about 1.5 km from the Scott Gallery), outdoor air was drawn through the filter section at the same face velocity as for actual use of the filter, and the percent particle removal as a function of particle size was determined.

6.5 Measurement and Modeling Results: Aerosol Size Distribution and Chemical Composition

6.5.1 Filter Efficiency. The filtration efficiency as a function of particle size for a single pass through the building ventilation system filters F_{A3} and F_{B1} is shown in Figure 6.2. The efficiency for particles in size interval i, η_i, was computed as

$$\eta_i = \frac{C_{u_i} - C_{d_i}}{C_{u_i}} \tag{6.1}$$

where C_{u_i} and C_{d_i} are the upstream and downstream particle volume concentration in size range i, respectively. The efficiency was computed for size ranges corresponding to the sections used in the indoor air quality model to represent the aerosol. For particles in the range (0.09-2.5 μm) optical particle counter data were used to determine C_{u_i} and C_{d_i}. The removal efficiencies for particles smaller than 0.09 μm and larger than 2.5 μm in diameter were taken to be equal to the efficiency measured for the nearest size section.

At the Norton Simon Museum, filter F_{A1} is composed of the same material as filter F_{A3}. However, whereas filter F_{A3} was sufficiently loaded with particulate matter to appear heavily soiled, new filter material had recently been installed for F_{A1}. Very little difference (<5%) between upstream and downstream particle concentrations was observed for all particle sizes measured for filter F_{A1}. (These observations are consistent with the general knowledge that particle filters become more efficient as the loading increases.) Measurements across the charcoal filter, F_{A2}, indicate that it also is ineffective in removing fine particles.

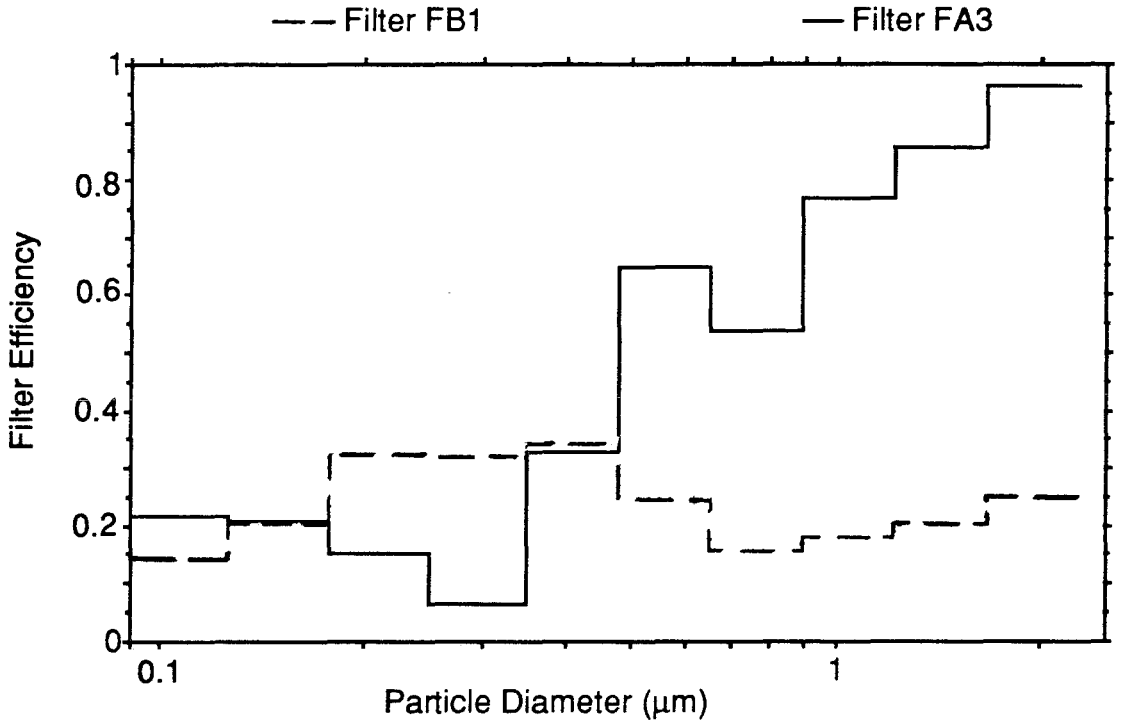

Figure 6.2 Filtration efficiency of particle filters as a function of particle size. The results are based on 21 and 4.5 hours of data for filters F_{A3} and F_{B1}, respectively. The corresponding operating flow velocities across the filter faces are 0.44 and 1.7 m s^{-1}. Filter media: Filter F_{A3} is Servodyne type SR-P1L; Filter F_{B1} is Servodyne type Mark 80. Filter F_{A1} was found to have less than 5% removal efficiency when new for particles smaller than 2.3 μm in diameter.

6.5.2 Temperature Differences and Boundary-Layer Flows. The results of monitoring temperature difference and near-surface air velocity at the three sites are shown in Figure 6.3. The prominent features of the temperature-difference profiles are readily understood. For example, the largest peak in T_{wall}-T_{air} at the Norton Simon Museum occurs in the late afternoon. At this time, the air temperature in this gallery increases, probably because of solar heating of the roof and of the south and west-facing walls. During this time, the mechanical ventilation system is supplying cool air in an attempt to maintain the set point temperature, thereby increasing T_{wall} - T_{air} (see also Chapter 7).* The large dip and rise in the profile at the Scott Gallery is associated with an inadvertent interruption in air-conditioning for the building. (It appears that the fans in the mechanical ventilation system continued to operate during this time, but that the cooling function ceased for almost four hours.) The indoor air temperature rises rapidly at 1200 PDT and heat is transferred to the wall. At approximately 1545 PDT, the air-conditioning system resumes operation, rapidly cooling the air, and heat is transferred from the wall back to the air. At the Sepulveda House, without any thermal control, the diurnal cycle is driven by the outdoor air temperature and the delayed thermal response of the brick wall. The maximum value of T_{wall}-T_{air} occurs just before dawn and the minimum occurs at 1400 PST, corresponding approximately to the peak outdoor air temperature.

At the Sepulveda House the near-wall air velocity is consistent with expectations for natural convection (Schiller, 1984; Bejan, 1984), driven by the temperature difference between the wall and the air, for the periods 0000-1000 and 1500-2400 PST, i.e., whenever the museum is closed. Note that during these periods, the maximum velocity occurs when the temperature difference is greatest; likewise, when the temperature

* During the long-term monitoring reported in Chapter 7, a west-facing window opposite the monitored wall was covered by foam board and curtains. Before the present study, the foam board was removed. Consequently, during the afternoon, a portion of the wall was in direct sun, which probably contributed to the peak in T_{wall} - T_{air}.

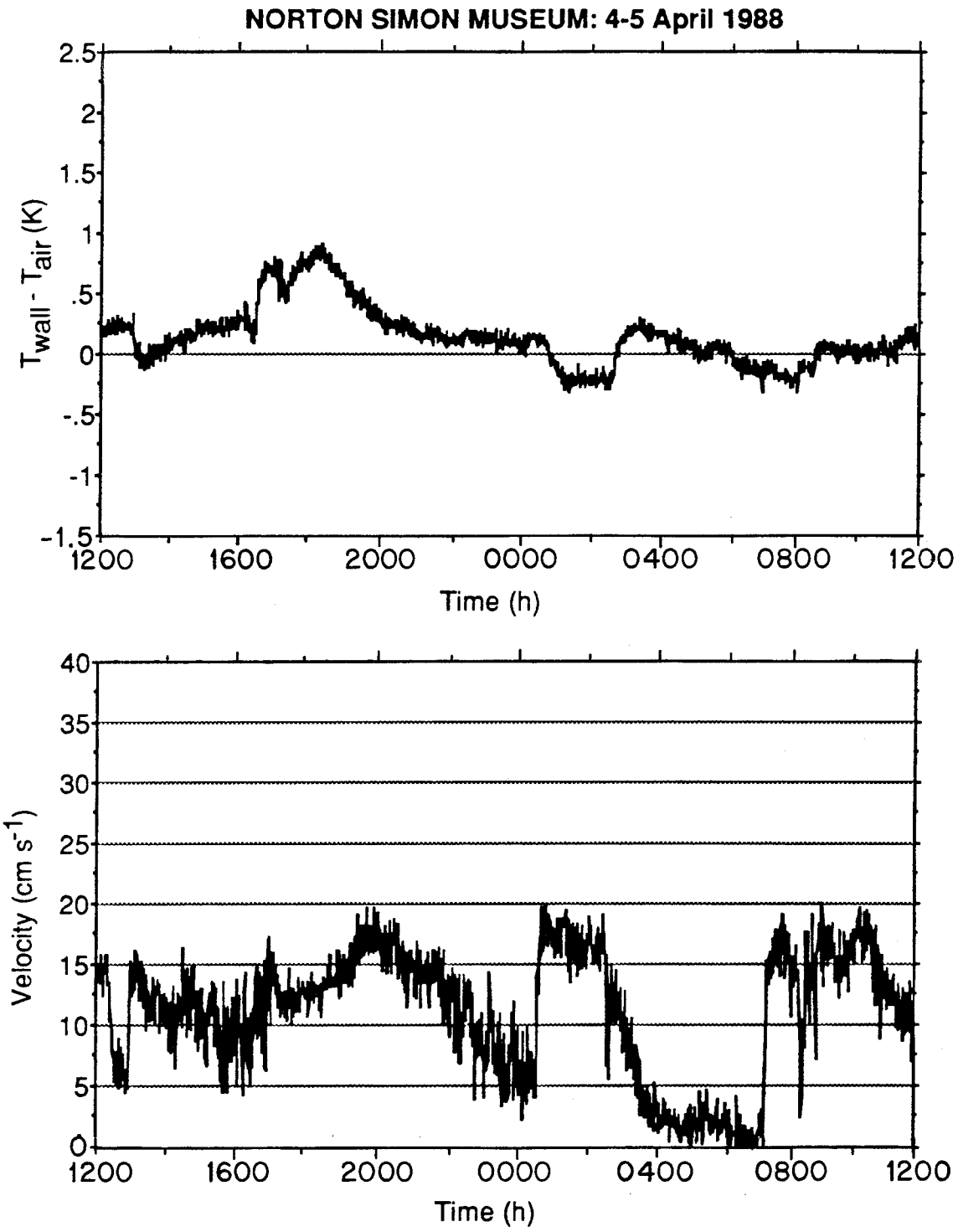

Figure 6.3 Temperature difference between the surface of a wall and the air, and the air velocity near the same wall vs. time for 24-hour periods at each site. The air velocity probe was located at a distance from the wall of 1.05 cm for the Norton Simon Museum, 1.3 cm for the Scott Gallery, and 1.2 cm for the Sepulveda House.

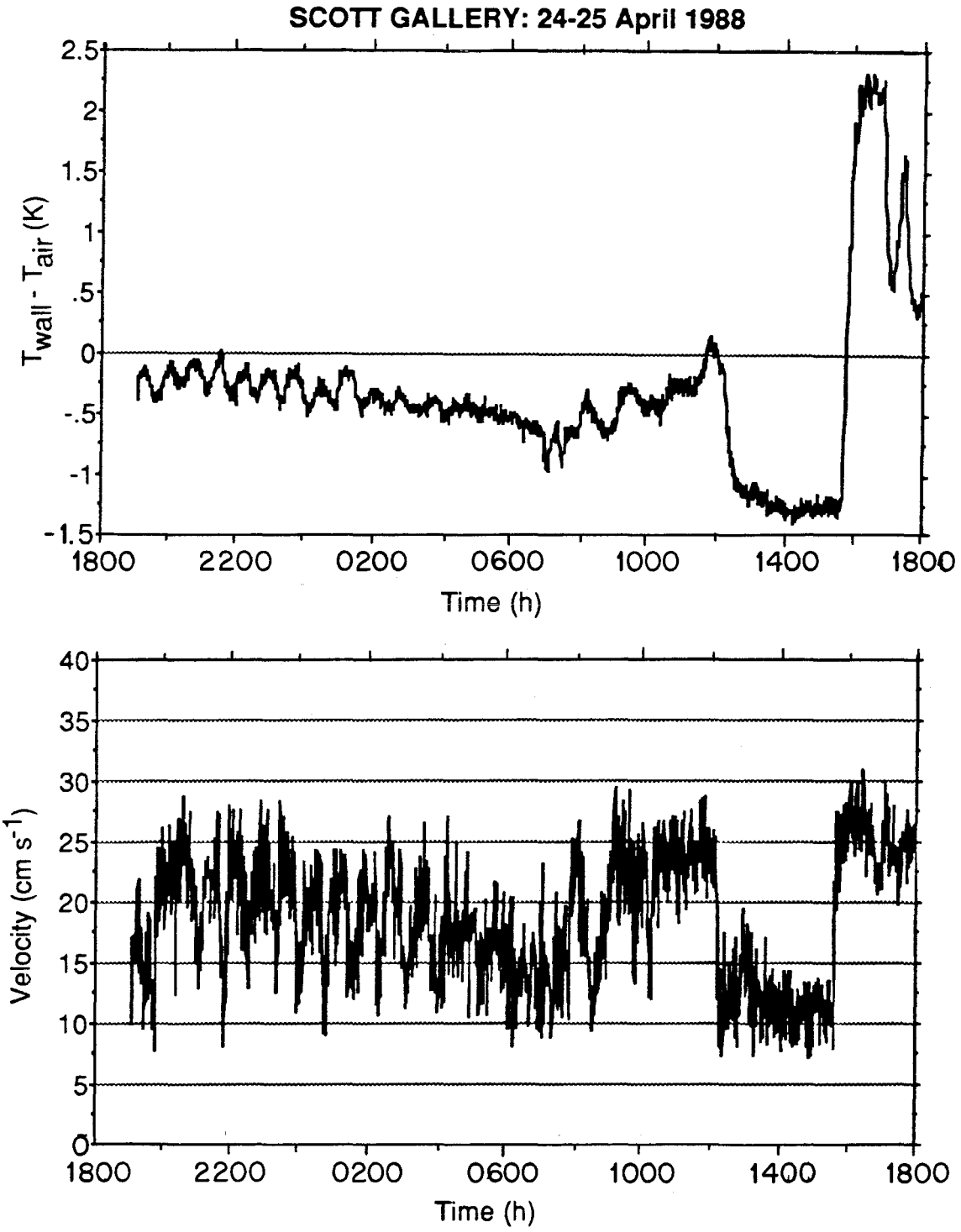

Figure 6.3 (Cont.)

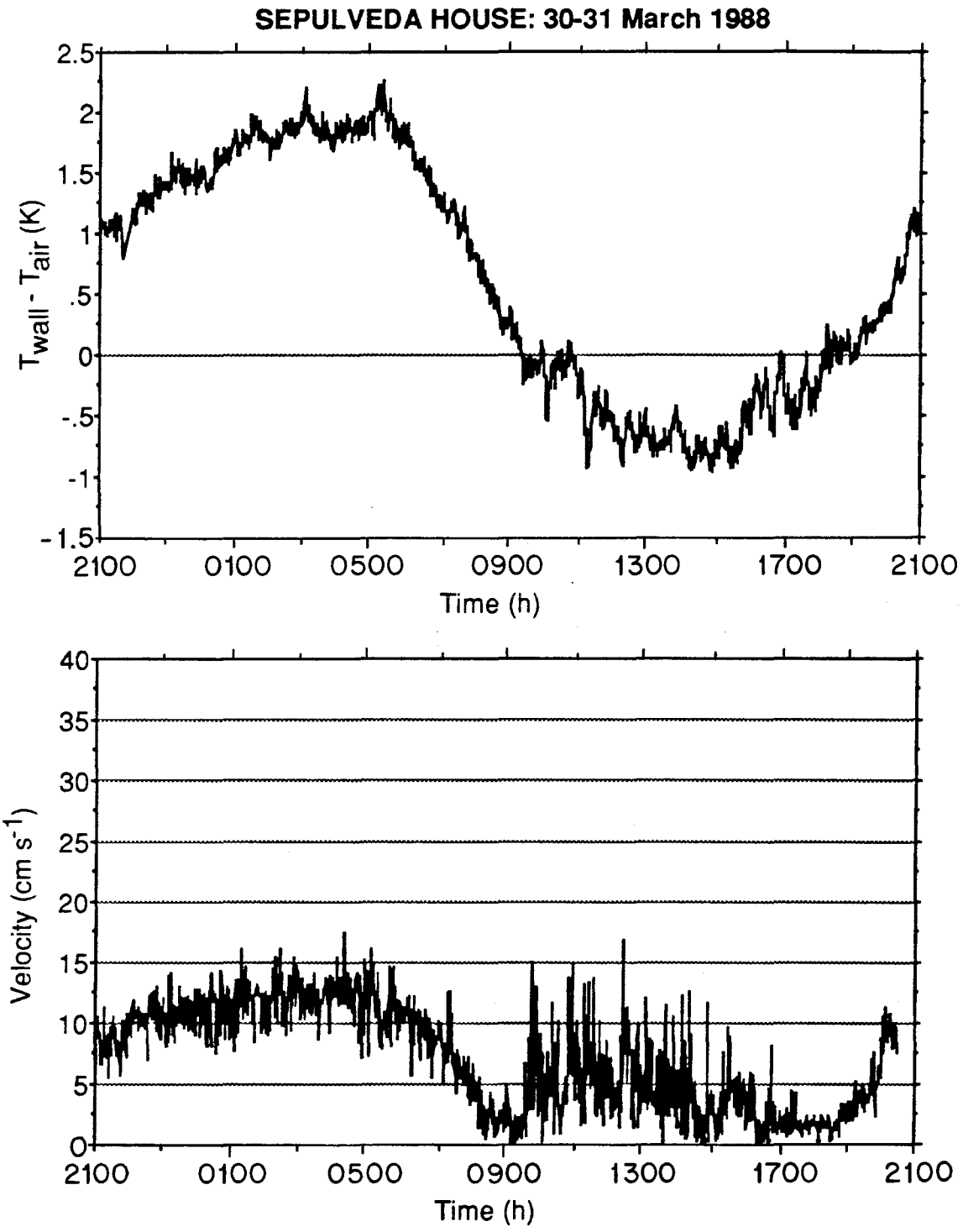

Figure 6.3 (Cont.)

difference is near zero, the air velocity is very small. When the museum is open, the air flow velocity adjacent to the wall is highly variable and appears to be driven predominantly by turbulent air movement in the core of the room.

At the Scott Gallery, the near-wall air velocity appears to be strongly dominated by the flow of air through the building due to the operation of mechanical ventilation system. At this site, the supply and return-air registers are located at the tops of the walls. The lower velocity observed during the period when air cooling failed probably results from the fact that the buoyant warm air entering the room from the ceiling registers would not promote convective mixing in the core of the room. After cooling is restored, peak near-wall air velocities are observed. A similar correlation between the wall-air temperature difference and the near-wall air velocity is observed at other times during the monitoring period, most notably for the first seven hours. During this interval $T_{wall} - T_{air}$ oscillates with an amplitude of ~ 0.3 K and a period of approximately 45 minutes; an envelope of the near-wall air velocity can be traced with an amplitude of approximately 5 cm s^{-1} and the same period. Some of the high-frequency fluctuations in the air velocity at the Scott Gallery may be a result of the fact that the sampling location was located near a door that was opened and closed approximately 10 times hourly during monitoring.

At the Norton Simon Museum, air is supplied to the gallery through perforated tiles that cover more than half of the ceiling. Air is returned to the ventilation system through the interior hallways of the building. Combining this circulation pattern with a lower recirculation rate (see Table 6.1), it is not surprising that the measured near-wall air velocities are generally lower at this site than at the Scott Gallery.

6.5.3 Modeling Aerosol Characteristics. The indoor aerosol size distribution and chemical composition were computed from measured outdoor aerosol properties for each site using the indoor air quality model previously reported (Chapter 5). That model tracks

the evolution of the indoor aerosol size distribution and chemical composition as it is affected by ventilation, filtration, emission, coagulation, and deposition. For the present study, the aerosol size distribution was represented by 15 sections spanning the diameter range 0.05-40 μm and by three chemical components—elemental carbon, soil dust, and "other."

Measured outdoor concentrations were used as input to the model as follows. Hourly averaged results from the outdoor mid-range OPC were used to compute the total mass concentration per section for sections 2-11, assuming the particle density to be 2.0 g cm^{-3} (see the appendix to this chapter). The total mass concentration for sections 12-15 was determined from filter-based coarse particle concentration measurements, assuming that the mass is distributed uniformly with the log of the particle diameter. Concentrations of elemental carbon and soil dust were determined from analyses of filter samples. The fine elemental carbon concentrations were partitioned into sections 1-11 using size distribution data reported by Ouimette (1981) for the Los Angeles and Pasadena elemental carbon aerosol. The concentration of soil dust was computed from the aluminum and silicon content of the aerosol using the data of Miller et al. (1972) on the percent of these elements in suspended samples of local soil dust. The fine soil dust was apportioned into sections 2-11 in proportion to the size distribution of the total 24-hour-average aerosol mass in these sections. For coarse particles both elemental carbon and soil dust were allocated to produce a constant value of $dM/d(\log d_p)$ across sections 12-15, where M is the aerosol mass concentration and d_p is the particle diameter. For section 1, spanning particle diameters in the range 0.05-0.09 μm, the total aerosol mass of material other than elemental carbon is unknown, and that other material will be neglected. For sections 2-15, the component "other" was determined by difference between the total aerosol mass and the soil dust plus elemental carbon mass.

For the model calculations, each site was represented as a single well-mixed chamber, with building size and ventilation characteristics as indicated in Figure 6.1 and

Table 6.1. A constant ventilation rate was adopted for the Norton Simon Museum, based on the apparent dominance of the constantly operated mechanical ventilation system over infiltration. Likewise, the rate of outdoor air-exchange at the Scott Gallery was taken to be constant, based on the small variance in results from tracer gas decay measurements. At the Sepulveda House, tracer decay data were used to obtain hourly averaged air exchange rates, which were then applied in the model calculations.

Particle removal efficiencies for filters F_{A3} and F_{B1} were based on measurements reproduced in Figure 6.2 for particles in the diameter range 0.09-2.25 μm. The efficiencies for particles smaller than 0.09 μm and larger than 2.25 μm in diameter were estimated by extrapolation. The charcoal filters, F_{A2} and F_{B2}, were assumed to have no effect on particle concentrations, based on measurements of the penetration efficiency for F_{A2}. To best reflect the prevailing conditions on the monitoring day for this study, the effectiveness in removing particles of the newly replaced filter F_{A1} was taken to be zero, based on measurements showing its effectiveness to be less than 5% at that time. An additional modeling run (Case C, see Table 6.2) was carried out with filter F_{A1} having the same effectiveness as filter F_{A3}. The latter case better represents ordinary conditions at the Norton Simon Museum. (The particle filter material is contained in large rolls. Routinely, the filters are advanced a small fraction (<10%) of their exposed length, thereby maintaining a fairly uniform degree of particle loading. Just prior to the day of monitoring in this study, a new roll of material was installed for filter F_{A1}.)

Aerosol deposition rates were computed for idealized flow conditions using the data on wall-air temperature differences and near-wall air velocities reproduced in Figure 6.3. These data were used to determine the hourly average temperature difference between the wall and the air. The temperature differences were then assumed to apply to all surfaces of the building. For the Sepulveda House, particle deposition was computed using the natural convection description of air flow during 0000-1000 and 1500-2400

Table 6.2. Deposition and filtration conditions simulated at study sites using the indoor air quality model.

Norton Simon Museum

Case A	Deposition: forced laminar flow; Filter F_{A1}: ineffective
Case B	Deposition: homogeneous turbulence in the core of the room; Filter F_{A1}: ineffective
Case C	Deposition: forced laminar flow; Filter F_{A1}: same efficiency as filter F_{A3}

Scott Gallery

Case A	Deposition: forced laminar flow
Case B	Deposition: homogeneous turbulence in the core of the room

Sepulveda House

Case A	Deposition: natural convection flow (0000-1000 and 1500-2400 h), homogeneous turbulence in the core of the room (1000-1500 h)

PST (Chapter 4). Homogeneous turbulence in the core of the building was assumed to dominate deposition processes for the remaining period at this site. At the Norton Simon Museum and at the Scott Gallery, deposition calculations were carried out for two representations of near-wall air flows. As shown in Table 6.2, the base case (Case A) calculations were made assuming laminar, forced flow, parallel to the surfaces. Case B calculations were made assuming that the near-wall flows were dominated by homogeneous turbulence in the core of the rooms. A comparison of model and measurement results for particle deposition velocity at these two sites suggests that the actual deposition rates lie between the values predicted for Case A and Case B conditions at the Scott Gallery and closest to the results for Case A conditions at the Norton Simon Museum (see Chapter 7).

For deposition calculations based on laminar, forced flow, the freestream air velocity, u_∞, is required to compute the deposition velocity. For laminar flow conditions, the air velocity probes located at ~0.6 and ~1.2 cm from the wall would be within the momentum boundary layer. The hourly averaged freestream air velocity was estimated from velocity measurements with these probes using the boundary layer velocity profile for an isolated flat plate (Schlichting, 1979). This freestream velocity was assumed to apply for all indoor surfaces. The mean hourly averaged value (± one standard deviation) of the freestream air velocity so obtained was 0.33±0.11 m s^{-1} for the Norton Simon Museum and 0.29±0.04 m s^{-1} for the Scott Gallery.

For calculations based on the assumption of homogeneous turbulence, the turbulence intensity parameter, K_e, was estimated on an hourly basis from the air velocity, linearly interpolated to a distance of 1 cm from the wall, using the relationship proposed by Corner and Pendlebury (1951):

$$K_e = k_o^2 \frac{0.073}{\mu} \frac{\rho u^2}{2} \left(\frac{\mu}{\rho u X}\right)^{\frac{1}{5}} \qquad (6.2)$$

where k_o is von Kármán's constant, taken to be 0.4, μ is the dynamic viscosity of air, ρ is the air density, u is the mean air velocity, and X is the length of the surface in the direction of the mean motion. This equation is based on a correlation for the turbulent drag on a flat plate in an infinite fluid moving parallel to the plate. The turbulence intensity parameter so obtained has a mean hourly averaged value ($\pm$ one standard deviation) of 0.56 ± 0.34 s^{-1} for the Norton Simon Museum, 1.25 ± 0.45 s^{-1} for the Scott Gallery, and 0.18 ± 0.04 s^{-1} for the period 1000-1500 PST at Sepulveda House. Note that the results of pollutant deposition velocity measurements inside buildings are bounded approximately by predictions based on the assumption of homogeneous turbulence with K_e in the range 0.1-10 s^{-1} (see Chapter 4, Figure 4.9).

For each site, a comparison is presented in Figure 6.4 of the results of outdoor measurements, indoor measurements, and the indoor model predictions (under Case A conditions) for the total fine particle concentration as a function of time and for the 24-hour-average aerosol size distribution. At both the Norton Simon Museum and the Scott Gallery, the fine particle mass concentration indoors is reduced to 15-20% of the outdoor value and coarse aerosol mass present indoors is less than 5% of the outdoor value. The agreement between the indoor model and measurement results ranges from excellent to good: the size distribution and total fine aerosol concentration is predicted quite accurately for the Scott Gallery, while at the Norton Simon Museum the agreement is good except that the aerosol mass concentration for particles having a diameter in the range 0.18-0.35 μm is overpredicted by the indoor air quality model.

At the Sepulveda House, there is little difference between the indoor and outdoor fine particle concentrations. The model reflects this fact; however the high frequency fluctuations in the indoor concentration, which result from the high air-exchange rate, are smoothed in the model calculations, an artifact of using hourly averages for outdoor concentrations in the model. (Although the model as used here employs outdoor aerosol concentration data on an hourly averaged basis, there is no intrinsic reason in the method

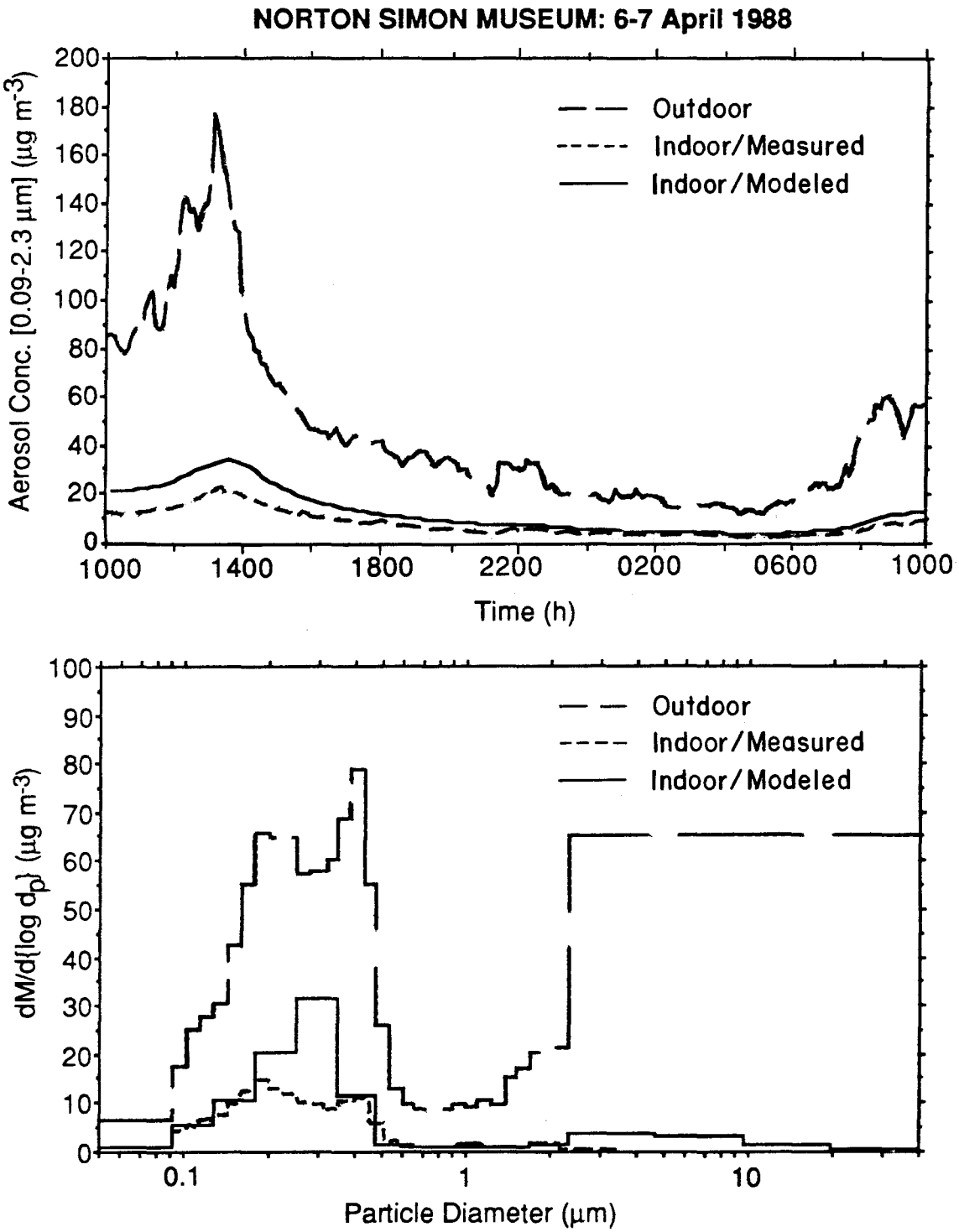

Figure 6.4 Fine aerosol mass concentration vs. time and 24-hour average aerosol size distribution for the three study sites. The figure compares outdoor measurements, indoor measurements and indoor modeling results. The measured fine particle concentrations are based on the mid-range optical particle counters. The coarse component, and the mass in the smallest section of the size distribution is based on analysis of filter samples. The modeling results for the Norton Simon Museum and the Scott Gallery reflect Case A conditions, defined in Table 6.2.

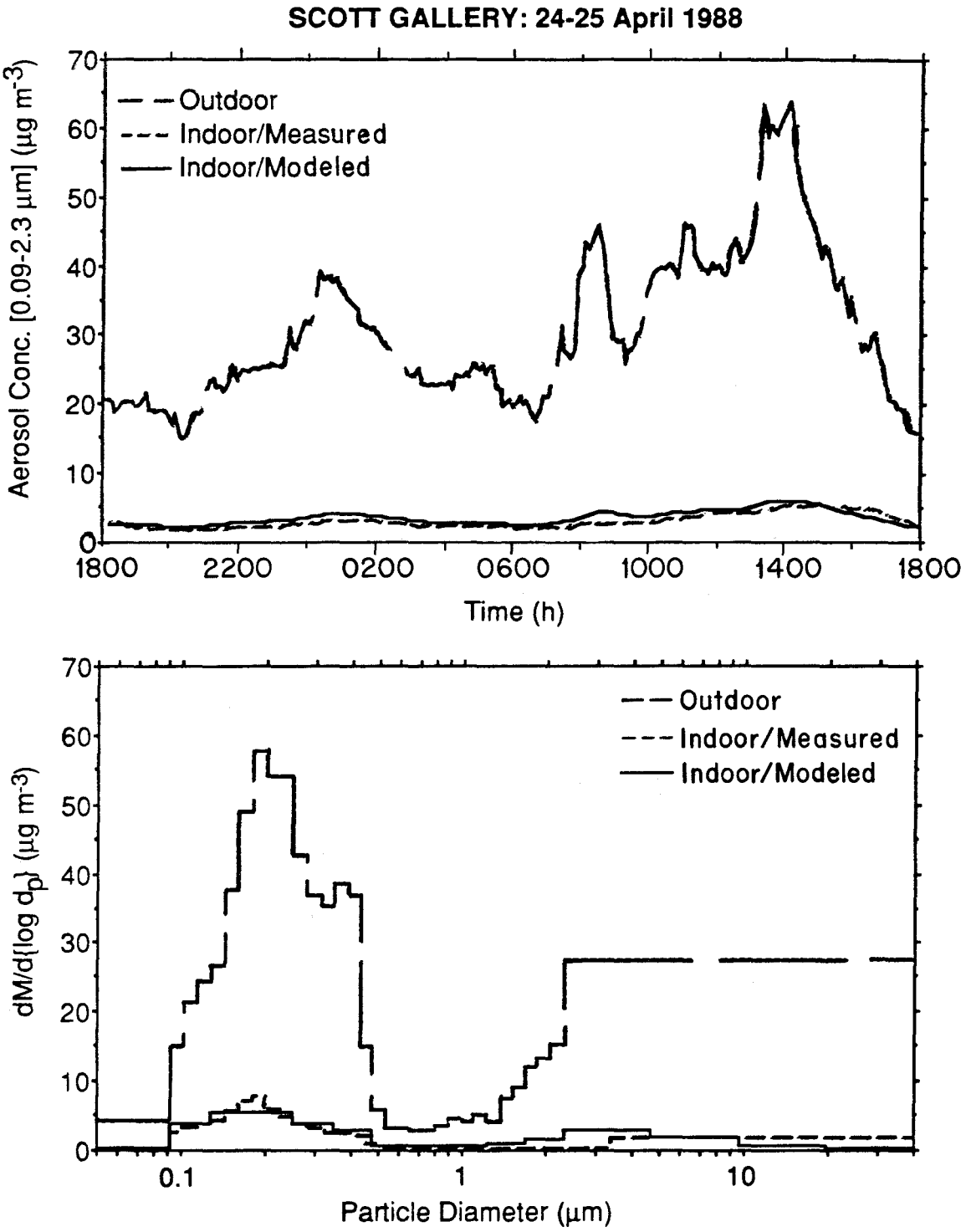

Figure 6.4 (Cont.)

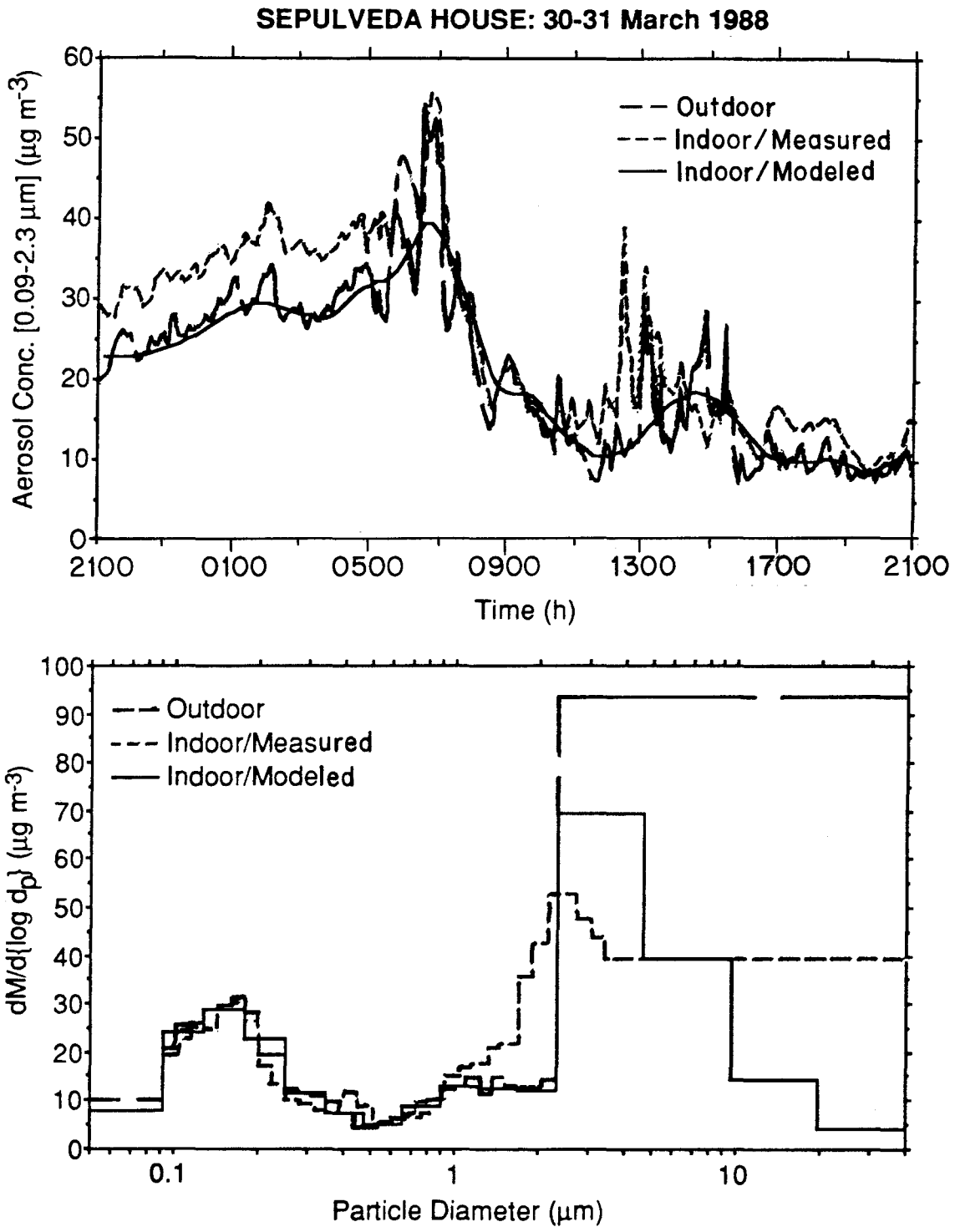

Figure 6.4 (Cont.)

of solution that precludes using data with finer time resolution.) One does not need a detailed mathematical model to predict the indoor concentrations of fine particles based on outdoor values if the building has a high air-exchange rate and no filtration. However, the estimates of particle flux to the walls and other surfaces of the Sepulveda House are complex and utilize the indoor air quality model's capabilities.

Table 6.3 compares measurements and predictions of the aerosol constituents, sorted according to particle size into coarse and fine modes. Again, the agreement is good, particularly for the fine particles for which the input data are more detailed.

Overall, the agreement between model calculations and measurement results justifies confidence in using the model to further consider the dynamics of indoor aerosols. The next two sections explore the fate of particles and the magnitude of the soiling hazard in museums.

6.6 Fate of the Particles Entering from Outdoor Air

The design of effective control measures for indoor aerosols can be facilitated by examining the relative strengths of particle sources and sinks. For the three sites considered in this chapter, the overwhelming source of indoor airborne particles during these experiments was due to the entry of outdoor air. The validity of this observation is substantiated by the agreement between measurement and model results. It remains to consider the relative strength of the aerosol sinks: filtration, removal by ventilation, and deposition onto interior surfaces. Coagulation, which serves as a sink for very fine particles, transferring their mass to larger particles, is also considered.

For each simulation and for each particle size section, the mean rate of removal of aerosol mass by the various sinks was computed, then normalized in each case by the mean rate of supply of aerosol mass in the section from outdoor air. The results for Case A, displayed in Figure 6.5, show that at the Norton Simon Museum and at the Scott Gallery the dominant fate of particles smaller than approximately 10 μm in diameter is

Table 6.3. Average mass concentrations ($\mu g\ m^{-3}$) of aerosol components for study periods from filter-based measurements and simulations.

	Fine			Coarse [a]		
	E. carbon	Soil dust	Total	E. carbon	Soil dust	Total
Norton Simon Museum						
Outdoor, measured	3.9	1.5	50	2.7	30	81
Indoor, measured	0.67	0.15	9.3	0.09	0.25	-2.0
Indoor, modeled, case A	0.83	0.36	12.5	0.10	1.0	2.9
Indoor, modeled, case B	0.82	0.36	12.4	0.10	1.0	2.9
Indoor, modeled, case C	0.62	0.30	10.1	0.004	0.04	0.11
Scott Gallery						
Outdoor, measured	1.5	0.75	26	0.95	6.9	37
Indoor, measured	0.16	0.09	4.1	0.01	0.13	2.3
Indoor, modeled, case A	0.23	0.08	3.7	0.05	0.32	1.8
Indoor, modeled, case B	0.22	0.08	3.6	0.05	0.32	1.8
Sepulveda House						
Outdoor, measured	5.0	2.6	34	1.3	41	117
Indoor, measured	5.6	0.86	24	0.75	23	57
Indoor, modeled, case A	4.9	2.5	22	0.49	14	40

[a] Coarse data are obtained by difference between mass concentration determined for filters in open-faced holders and filters downstream of cyclones with ~2.0 μm diameter cut-point. The negative measured value at the Norton Simon Museum results from subtraction of two small and nearly identical measurement results.

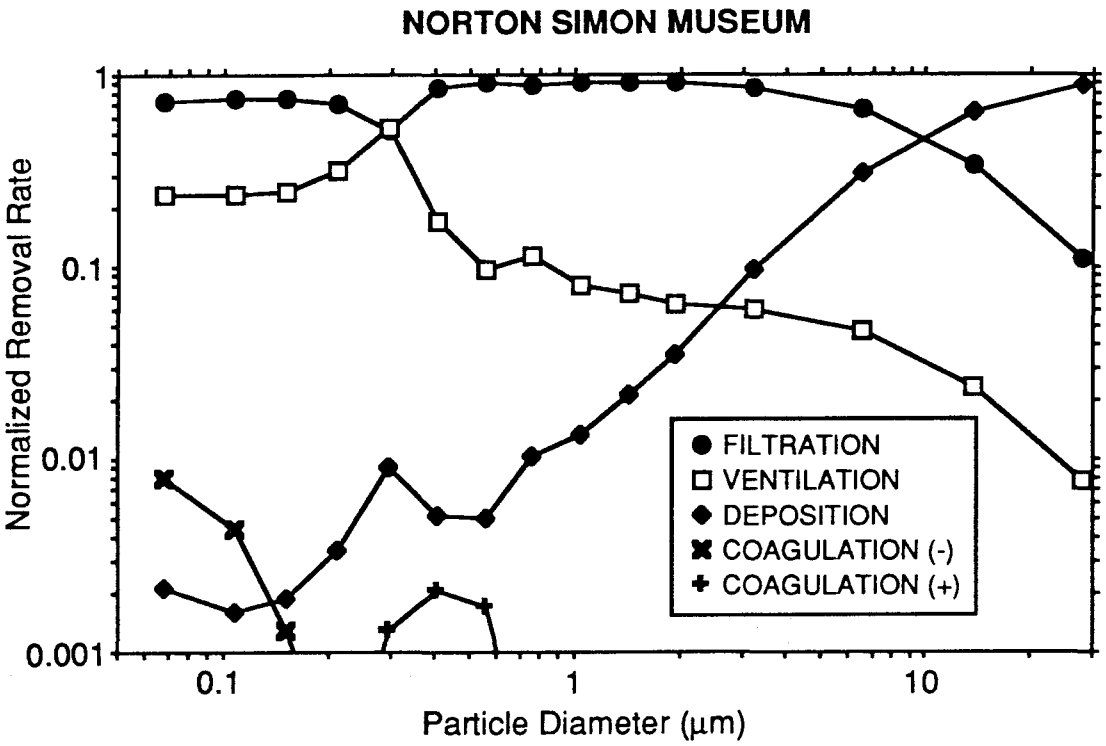

Figure 6.5 The predicted fate of particles introduced into the buildings from outdoors. The ordinate of each point represents the 24-hour average fraction of the mass in that section brought in from outdoors that is removed by the indicated process. The abscissa reflects the logarithmic midpoint of the range of diameters in the size section. "Coagulation (-)" indicates a net loss of aerosol mass in the section due to particle coagulation, and "Coagulation (+)" indicates a net gain. The results shown for the Norton Simon Museum and the Scott Gallery reflect the Case A conditions defined in Table 6.2.

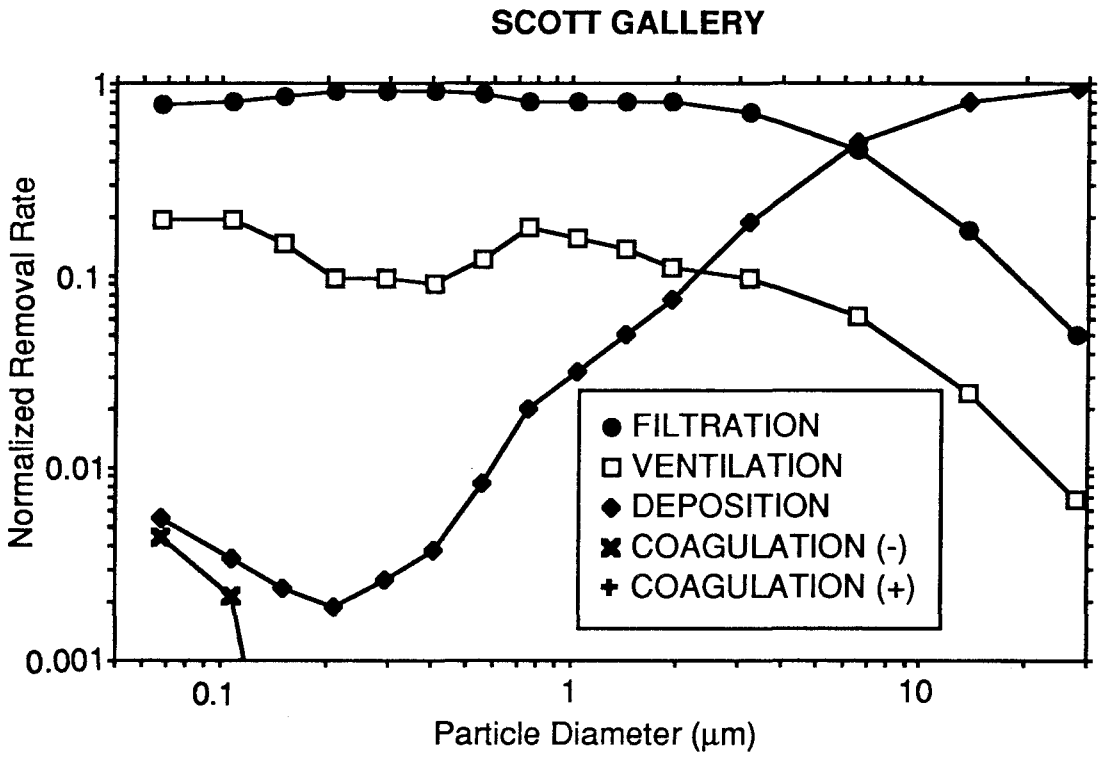

Figure 6.5 (Cont.)

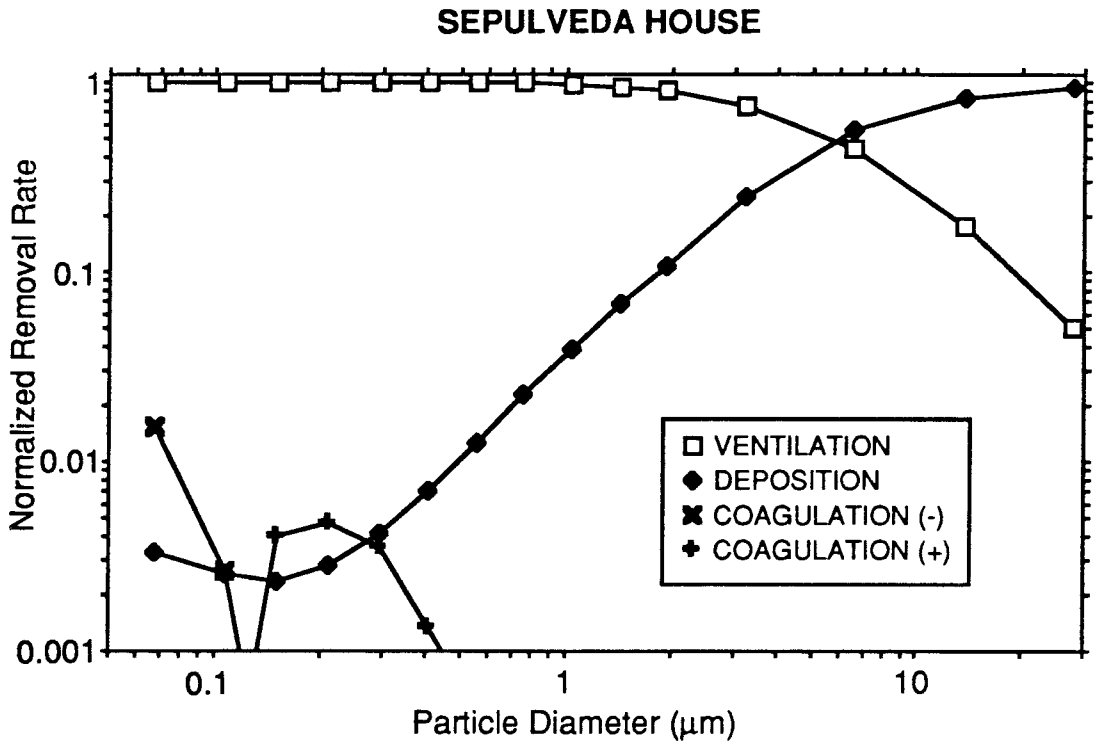

Figure 6.5 (Cont.)

removal by the filters. This result is obtained despite the moderately low particle filtration efficiencies, because during its residence time within these museums, air makes a large number of passes through the filters in the recirculating air ducts. At Sepulveda House, particles of this size are predominantly removed by ventilation. Surprisingly, at all three sites the dominant fate of larger particles is deposition onto surfaces, essentially entirely by gravitational settling onto the floor. This result demonstrates the importance of an effective filter for removing coarse particles from the ventilation supply air. Under ordinary conditions at the Norton Simon Museum, with filter F_{A1} partially loaded with particles rather than clean, it is expected that 95% of coarse particles are removed from the air entering the building.

Deposition constitutes a much smaller sink for fine particles; for example, for particles that are 0.1 μm in diameter only 0.1-0.5% of those that enter the buildings will ultimately deposit on a surface. This indicates that detailed calculations of deposition rates are not necessary to obtain accurate predictions of the indoor airborne concentrations of fine particles in these particular buildings.

At all three sites, and for all particle sizes, coagulation is seen to be of little importance. It is not correct to conclude, however, that particle coagulation is never important in indoor air. The study conditions at these three sites tend to minimize the rates of coagulation: low particle concentrations at the Norton Simon Museum and at the Scott Gallery imply low particle collision rates, and the high air-exchange rate at Sepulveda House doesn't allow sufficient time for coagulation to have a significant effect. On the other hand, previous analysis of the fate of cigarette smoke in a room having a low air-exchange rate showed that coagulation was an important sink for particles smaller than 0.2 μm in diameter (Chapter 5).

6.7 Particle Deposition onto Indoor Surfaces

Even though only a small fraction of the fine particles that enter a building deposit onto surfaces, the soiling hazard posed by particle deposition may still be significant. To assess the magnitude of the problem, the rates of particle accumulation onto the floor, walls and ceiling of each of the three sites were computed using the indoor air quality model for the 24-hour study periods. The results are displayed in Figure 6.6 in terms of the rate of mass accumulation per unit surface area, J, as a function of particle size and composition. Table 6.4 gives the total rate of accumulation of elemental carbon, soil dust, and of the total aerosol onto the walls, floors and ceilings for each of the three sites. Before considering the significance of the results, it is important to emphasize that the calculations at each site represent predictions for a single day. Thus, extrapolations to longer time periods must be regarded only as indicative estimates. In particular, differences in the deposition rates between sites may reflect differences in the outdoor conditions on the particular days studied, rather than differences in the long-term average rates of soiling. Note, also, that although the calculations are done specifically for the floor, walls and ceiling, the results are indicative of expected values for other surfaces, such as those of art objects, which have corresponding orientations.

The computed total rate of accumulation of elemental carbon particles onto the walls of the three sites is in the range 0.02-0.7 $\mu g\ m^{-2}\ day^{-1}$. The corresponding rates for the ceilings are smaller, 0.002-0.5 $\mu g\ m^{-2}\ day^{-1}$ and are very sensitive to the assumed nature of near-surface air flow. For forced laminar flow conditions (Case A), gravititational settling is effective in reducing deposition of ~0.1 μm particles onto the ceiling. For homogeneous turbulence (Case B), however, eddy diffusivity dominates gravitational settling for the very fine elemental carbon particles, and the deposition rate is about the same for the ceiling as for the walls. The rates of accumulation of elemental carbon onto the floors are much larger, 2-50 $\mu g\ m^{-2}\ day^{-1}$ for the Norton Simon Museum, 20 $\mu g\ m^{-2}\ day^{-1}$ for the Scott Gallery and almost 300 $\mu g\ m^{-2}\ day^{-1}$ for Sepulveda House.

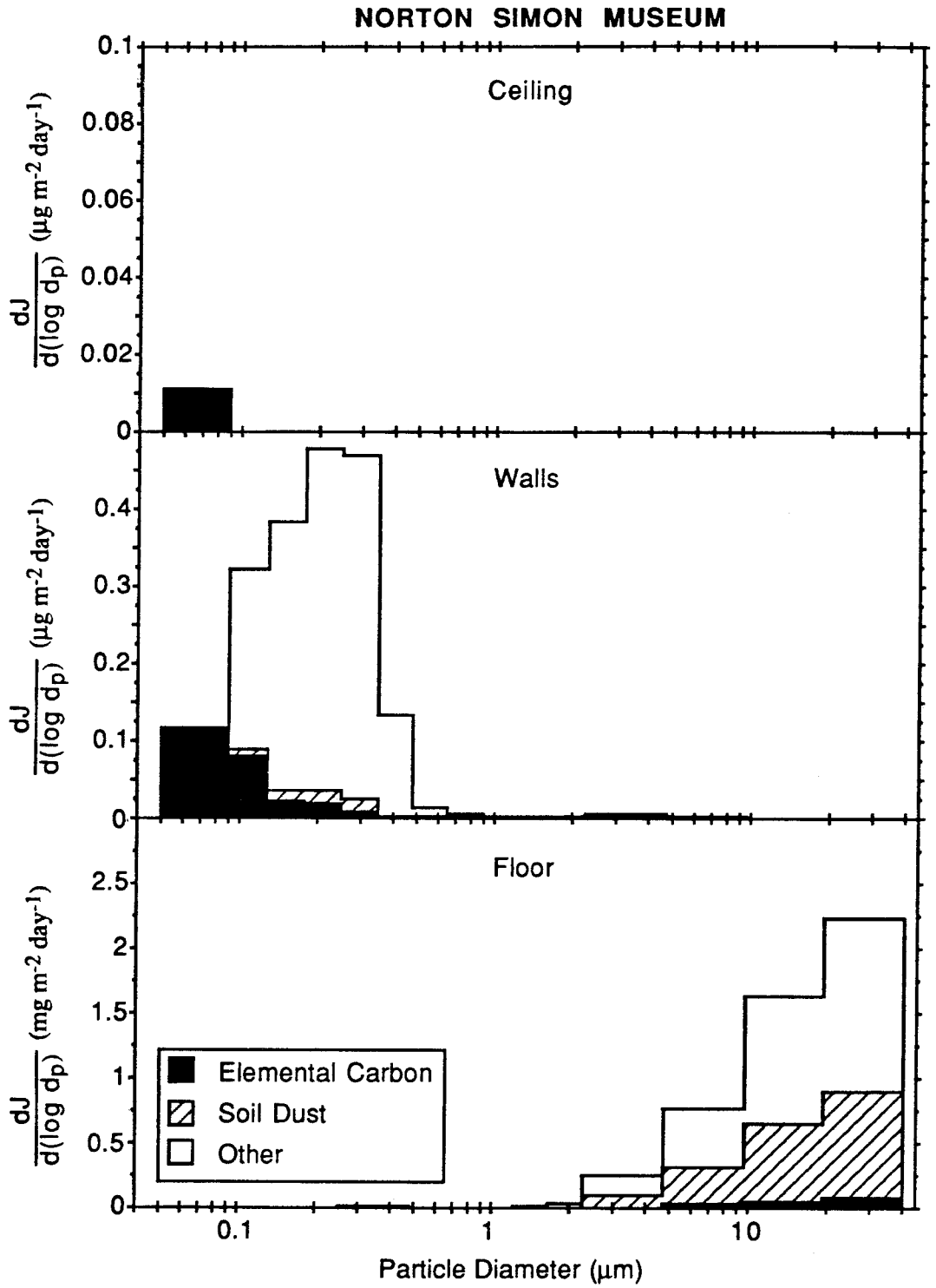

Figure 6.6 Predicted rate of accumulation, based on the single study day, of aerosol mass as a function of particle composition and size for three major surface orientations. Note that the vertical axes have different scales; in particular, the mass unit for the floors is mg, compared with μg for the other surfaces. The results shown for the Norton Simon Museum and the Scott Gallery reflect the Case A conditions defined in Table 6.2.

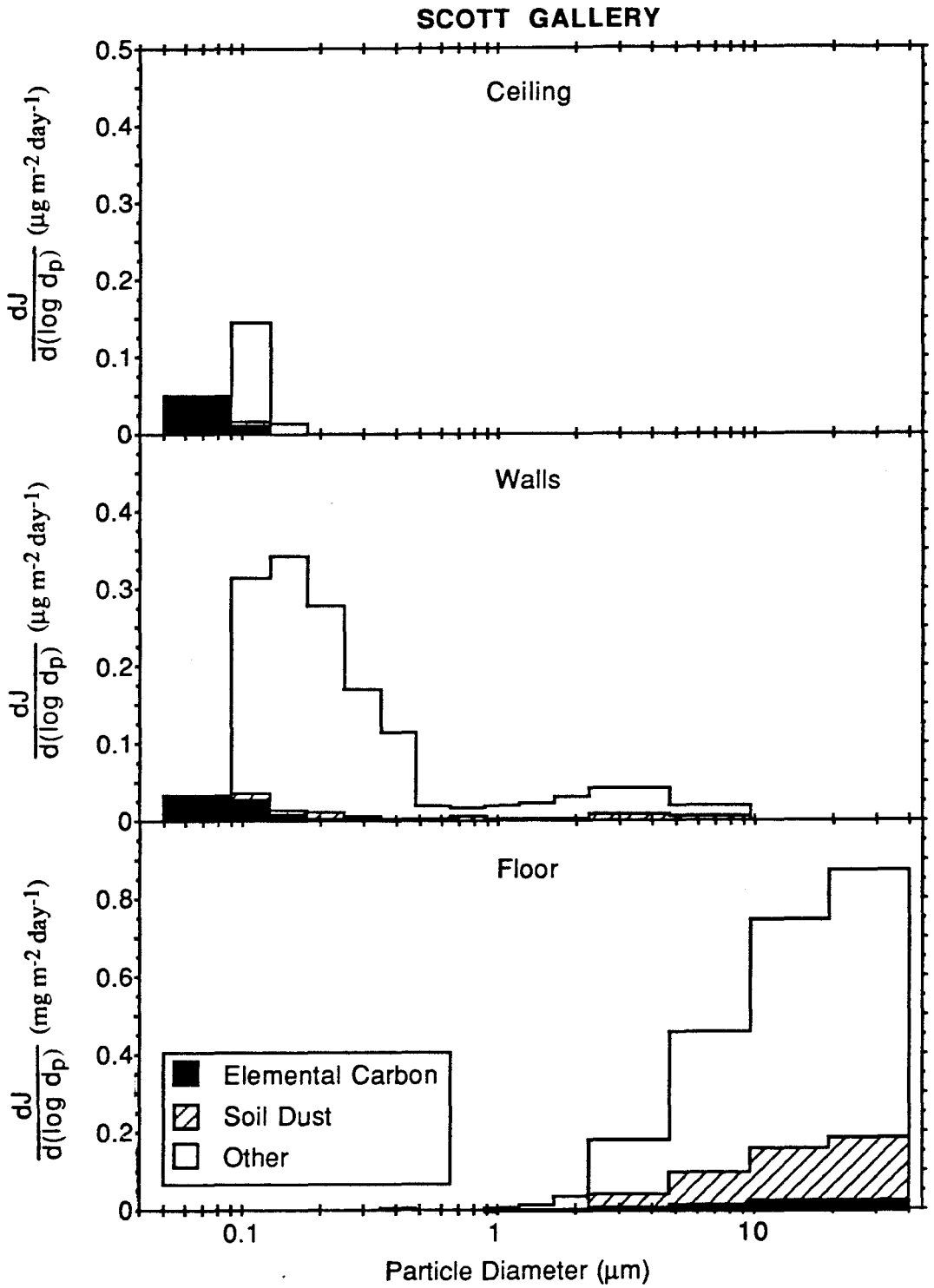

Figure 6.6 (Cont.)

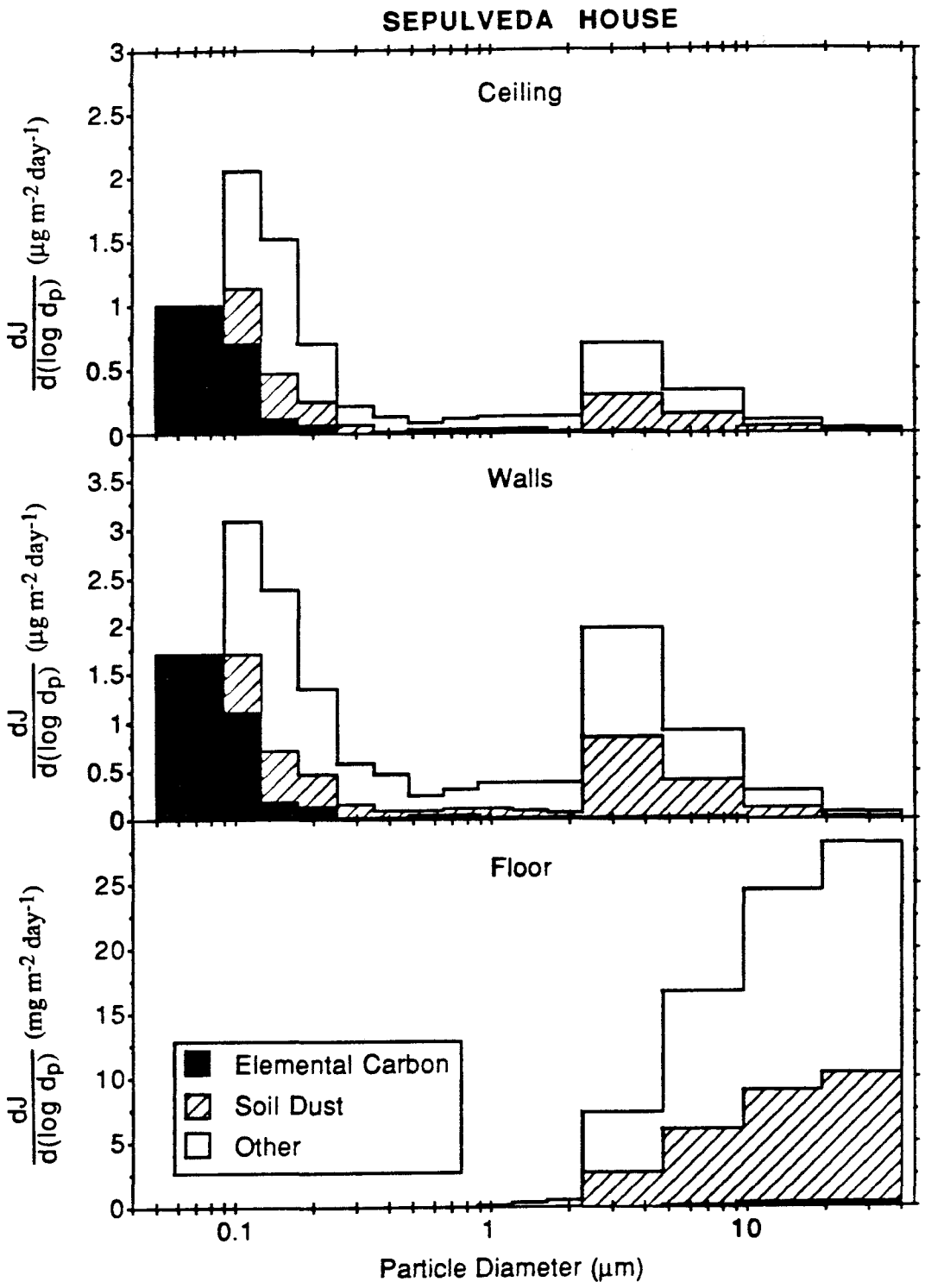

Figure 6.6 (Cont.)

Table 6.4. Average deposition rate of aerosol mass ($\mu g\ m^{-2}\ day^{-1}$) onto indoor surfaces based on simulations of study periods at each site.

	E. carbon	Soil dust	Total
Norton Simon Museum - Case A			
Ceiling	0.003	0.000	0.003
Walls	0.050	0.010	0.30
Floor	52	560	1540
Norton Simon Museum - Case B			
Ceiling	0.54	0.10	3.6
Walls	0.64	0.23	6.2
Floor	53	560	1540
Norton Simon Museum - Case C			
Ceiling	0.002	0.000	0.002
Walls	0.039	0.007	0.24
Floor	2.4	23	67
Scott Gallery - Case A			
Ceiling	0.015	0.001	0.036
Walls	0.017	0.008	0.22
Floor	19	130	710
Scott Gallery - Case B			
Ceiling	0.26	0.08	3.0
Walls	0.29	0.13	3.9
Floor	19	130	710
Sepulveda House - Case A			
Ceiling	0.40	0.32	1.4
Walls	0.69	0.70	2.8
Floor	280	8500	24,000

The particle sizes associated with volume-weighted elemental carbon deposition onto these surfaces are quite distinct: predominantly 0.05-0.3 μm for the walls and ceiling, compared with 4-40 μm for the floor. However, considered in terms of the rate of accumulation of projected particle cross-sectional area (probably the appropriate scale for assessing the rate of soiling [e.g., Carey, 1959]), the deposition of fine particles onto the floor has a significance comparable with the deposition of coarse particles.

Because of its lower rate of accumulation, soil dust appears to pose a smaller soiling hazard than elemental carbon for the ceiling and walls at the Norton Simon Museum and at the Scott Gallery. However, the rates of accumulation of soil dust onto the floor at those two sites are 7-10 times larger than those of soot. These differences are a consequence of the fact that soil dust, being mechanically generated, is found predominantly in the coarse particle mode and settles onto upward facing surfaces under the influence of gravity, whereas elemental carbon, produced in combustion systems, is found primarily in fine particles for which deposition occurs to surfaces of any orientation by a combination of advective diffusion and thermophoresis (Chapter 4).

The much higher flux density of particle mass to the floor compared with values for the ceiling and walls points to a limitation of the calculations employed here in assessing the soiling hazard for certain surfaces. In these calculations, vertical surfaces are assumed to be smooth; however, many real surfaces are rough. Through gravitational settling, large particles will deposit preferentially on the upward-facing portions of surface roughness elements. Because contrast is readily detected, nonuniform deposition of elemental carbon particles by such a process would probably lead to noticeable visual degradation of the object more rapidly than an equivalent rate of deposition spread uniformly over the surface.

To gain perspective on the significance of these results in the context of protecting museum collections, a characteristic time interval for soiling was computed. Previous studies have shown that a white surface is perceptibly darkened when 0.2% of its area is

effectively covered by either black dots that are too small to be distinguished individually (Carey, 1959) or by black particles (Hancock et al., 1976). Since the light absorbing properties of elemental carbon particles differ from those of soil dust, the degree of surface coverage needed to produce perceptible soiling probably differs for the two components. The information needed to combine the accumulation rate of the two components into a single soiling rate is lacking, and so, for the present study, the characteristic times for soiling by elemental carbon particles ($\tau_{s;EC}$) and by soil dust ($\tau_{s;SD}$) were estimated as the time required to achieve 0.2% coverage of a surface by these components independently. These times were computed for each surface orientation and each model case, given the deposition rates as a function of size (as displayed for Case A in Figure 6.6), and assuming that, within each section, the deposited elemental carbon or soil dust can be considered to exist as pure, spherical particles with a diameter equal to the logarithmic mean for the section. Then, the characteristic time for a perceptible deposit of either component to accumulate is given by

$$\tau_{s;c} = 0.002\left[\sum_{i}\left(\frac{3}{2d_i}\right)\left(\frac{\Delta J_{i;c}}{\rho}\right)\right]^{-1} \qquad (6.3)$$

where c represents the soiling component (EC or SD), d_i is the particle diameter for section i, $\Delta J_{i;c}$ is the rate of mass deposition of component c for section i, and ρ is the particle density.

The resulting values for $\tau_{s;c}$ are given in Table 6.5 for the three sites. For walls and ceilings, deposition of elemental carbon particles constitutes a greater soiling hazard than the deposition of soil dust. Characteristic soiling times associated with elemental carbon particle deposition are in the range 1-40 years for walls. For ceilings, the corresponding predictions are in the range 1-35 years except for the Norton Simon Museum under the assumption of forced laminar flow for which the estimated

Table 6.5. Characteristic time (years) for perceptible soiling to occur.[a]

	Ceiling		Walls		Floor	
	$\tau_{s;EC}$	$\tau_{s;SD}$	$\tau_{s;EC}$	$\tau_{s;SD}$	$\tau_{s;EC}$	$\tau_{s;SD}$
Norton Simon Museum						
Case A	180	-	12	170	1.2	0.2
Case B	1.2	12	1.1	8.4	0.6	0.2
Case C	230	-	16	210	4.7	3.0
Scott Gallery						
Case A	35	720	40	240	2.9	0.6
Case B	2.5	19	2.4	16	1.4	0.6
Sepulveda House						
Case A	1.5	6.2	0.9	4.1	0.15	0.01

[a] Based on the predicted deposition rates for the single study day at each site. The characteristic soiling time is computed as the time required for the accumulation of sufficient elemental carbon particles ($\tau_{s;EC}$) or soil dust particles ($\tau_{s;SD}$) onto a smooth surface to effectively cover 0.2% of the surface area. For black particles on a white surface, this degree of coverage by has been shown to yield perceptible soiling (Carey, 1959; Hancock et al., 1976).

characteristic soiling time is two centuries. For floors, predicted characteristic soiling times due to soil dust deposition are more rapid than those due to elemental carbon deposition. The values of $\tau_{s;SD}$ range from as short as three days at the Sepulveda House to as long as three years for the Norton Simon Museum with an effective intake filter (Case C). Among the three surface orientations, predictions for the ceilings must be regarded as the least certain, since, as with the walls, the deposition rates depend critically on near-surface air flows, and no measurements of flows near ceilings were made in this study.

With the exception of the few large values of τ_s for the ceiling of the Norton Simon Museum, these soiling periods are short relative to the time scales over which museum curators wish to preserve their collections. In some respects, these estimates are conservative. The degree of effective area coverage by black particles needed to produce perceptible soiling would be a minimum for a purely white surface for which the 0.2% result applies. The surfaces of heavily pigmented paintings, for example, could probably accrue a greater deposit before soiling became perceptible.

As expected, the soiling problem is most acute at the Sepulveda House because of its high ventilation rate and lack of particle filtration. Taking the geometric mean of the results for Cases A and B as a representative estimate of the true soiling rates at the Norton Simon Museum and the Scott Gallery, soiling rates due to elemental carbon deposition at these sites are approximately 5-10 times lower than at the Sepulveda House. For soiling dust deposition onto upward surfaces, the difference between the characteristic soiling time at the Sepulveda House and those at the other two sites are even greater. It is noteworthy that the effectiveness of the supply air filter at the Norton Simon Museum in lengthening the soiling periods (compare Cases A and C) is not large for soiling by elemental carbon particles. This result is obtained because the deposition of fine particles onto the floor contributes significantly to $\tau_{s;EC}$, and the inlet filter is relatively ineffective in removing these particles. On the other hand, an effective supply

air filter at the Norton Simon Museum does significantly extend the characteristic soiling time for the floor associated with soil dust deposition.

6.8 Discussion

The results of this study serve several purposes. First, they substantially increase the basis for confidence in the ability to predict the size distribution and chemical composition of the indoor aerosol using the indoor air quality model described in Chapter 5. Second, they provide considerable information beyond that previously available about the indoor-outdoor aerosol relationship for two types of buildings. (The Norton Simon Museum and the Scott Gallery are representative of modern commercial buildings, apart from their relatively high ratio of recirculated air to outdoor make-up air flow rates and the presence activated carbon filters. Sepulveda House is representative of many older buildings, at least those in temperate climates.) Third, the results constitute, to our knowledge, the first detailed estimates of the cause-and-effect relationships that lead to soiling of indoor surfaces. The information about the size of particles that contribute to soiling is crucial in designing efficient control measures. Estimates of the rate of soiling will help concerned officials make informed decisions about how much of their limited resources to devote for control measures.

Despite the progress marked by the results reported here, a number of issues must be left unaddressed. Model validation has not yet included a sensitive test of the deposition calculations. Also, as already mentioned, the deposition rates reported here are based on short-term measurements. Yet, soiling is a relatively long-term problem, so it is important to incorporate longer term data in assessing the hazard. In addition, the options available for controlling the soiling of indoor surfaces have not been addressed in detail. These issues are addressed in Chapters 7 and 8.

The other hazard for artwork associated with the deposition of particles—corrosion and other chemical attack—has not been addressed specifically here. In this

context, it is interesting to compare the rate of deposition onto surfaces of particles with the rates associated with other pollutants. For example, the rates of total aerosol mass accumulation to the walls and ceilings of the sites investigated in the present study are less than 0.25 $\mu g\ m^{-2}\ h^{-1}$ (Table 6.4). The corresponding rates are much higher for upward-facing surfaces including the floors, 3-1000 $\mu g\ m^{-2}\ h^{-1}$. By contrast, based on calculations for a two-day period, the mean rates of deposition of ozone and nitric acid to the surfaces of the Scott Gallery (prior to the installation of the activated charcoal filter and the reduction in the ventilation rate) were determined to be 38 and 9 $\mu g\ m^{-2}\ h^{-1}$ (Chapter 2). This comparison suggests that the chemical degradation hazard to surfaces having vertical or downward orientations may be dominated by the deposition of gaseous pollutants, rather than the deposition of particles. However, certain components that may damage materials, such as sea salt, may accumulate onto surfaces only through aerosol deposition. In such a case, as with soiling, even slow rates of accumulation may constitute a significant cumulative hazard to works of art over the long periods that they are to be preserved. Furthermore, large mass fluxes may result from gravitational settling of coarse particles onto upward-facing surfaces. Consequently, the potential for chemical damage caused to the surfaces of art objects from particle deposition should be investigated.

In addition to these topics, there is a need for further investigation of the relationship between the deposition rate of elemental carbon and other particles and the rate of optical degradation of surfaces. Results of such studies are needed to refine estimates of the time periods over which perceptible soiling occurs.

With the capability of testing candidate protection measures and ventilation system designs in advance of their construction by using a model such as the one employed here, the ability to protect artwork from soiling due to the deposition of airborne particles will improve. It may become not only possible, but practical, to greatly

increase the time periods over which artwork can be preserved while retaining the visual qualities given by the artist.

6.9 Acknowledgements

We thank Robert Harley, Michael Jones and Wolfgang Rogge for assisting with the field experiments; Timothy Ma for fabricating of the thermistor array and signal conditioning electronics; Luiz Palma for assisting with the performance evaluation of the optical particle counters; Richard Sextro for arranging a loan of a portable gas chromatograph; and the staffs of the three museum sites for their generous cooperation. The x-ray fluorescence analyses were carried out by Dr. John Cooper at NEA, Inc. Robert Cary at Sunset Laboratories measured the elemental carbon content of filter samples. This work was supported by a contract with the Getty Conservation Institute and by fellowships from the Switzer Foundation and the Air Pollution Control Association.

6.10 Appendix: Performance Checks of the Optical Particle Counters

Four independent means were applied to test the performance of the optical particle counters: (1) simultaneous sampling by paired instruments of atmospheric aerosol both before and after the monitoring program; (2) comparison of inferred particle mass concentration against simultaneous filter-based measurements; (3) laboratory sampling of monodisperse fluorescein particles to evaluate sampling and counting efficiency; and (4) laboratory sampling of monodisperse particles of dioctyl phthalate (DOP) to verify instrument size response. The laboratory-based studies utilized a vibrating-orifice aerosol generator (TSI model 3450, ref. Berglund and Liu, 1973) to produce monodisperse particles.

The large particle optical particle counters (OPC) (model CSASP-100-HV) failed to yield satisfactory results in these tests. One of the instruments had been purchased recently and appeared to have problems associated with its manufacture. The other

instrument performed well in the laboratory tests. Its mean counting efficiency for fluorescein particles with diameters in the range 1-5 μm was determined to agree within 15% of the manufacturer specifications. As shown in Figure 6.7, the instrument accurately sized DOP particles in the diameter range 0.5-25 μm. On this basis, accurate sizing of atmospheric particles might also be expected, since DOP has an index of refraction (1.485) closely approximating that expected for coarse atmospheric particles (Larson et al., 1988). However, a comparison of filter-based measurements of coarse particle mass and total volume concentration of coarse-particles by the large-particle OPC, depicted in Figure 6.8, yields unsatisfactory results. Although the correlation is reasonably good, the slope of the regression line implies an effective aerosol density of 0.25 g cm^{-3}, almost an order of magnitude lower than the expected value. These contradictory results cannot be rigorously explained with the available data. However, if even one percent of the particles with actual diameters in the range, say 1-4 μm, were sensed as being an order-of-magnitude larger, then the total coarse-particle volume would be overestimated by as much as an order of magnitude. In such a case, it would be virtually impossible to extract the correct coarse-particle aerosol size distribution from the data. Because of these problems, the data from the large-particle OPCs were not used in the analysis reported in this chapter.

In contrast, the performance of the mid-range OPCs was good in all of the tests. The fluorescein tests indicated mean sampling and counting efficiencies of 0.92±0.03 and 0.93±0.03 for fluorescein particles in the size range of 1-5 μm diameter. Instrument sizing of DOP particles in the diameter range of 0.56-2.85 μm showed small but consistent deviations from manufacturer specifications. The results of the DOP sampling runs were used to adjust the particle size assignments for the upper half of the instrument range. The width of the measured particle size spectrum in response to monodisperse DOP particles was sufficiently narrow that it is reasonable to consider instrument response to be ideal for the present purposes. For example, for 0.56 μm DOP particles,

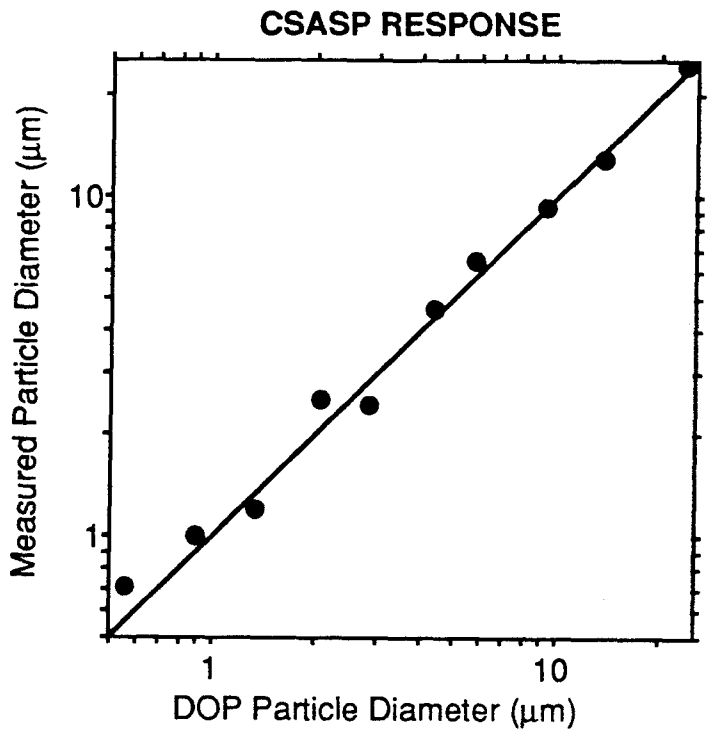

Figure 6.7 Response of a large-particle optical particle counter (CSASP) to spherical droplets of dioctyl phthalate (DOP). The ordinate of each point reflects the count-weighted mean particle diameter determined by the instrument and the abscissa indicates the diameter of the DOP particle as generated.

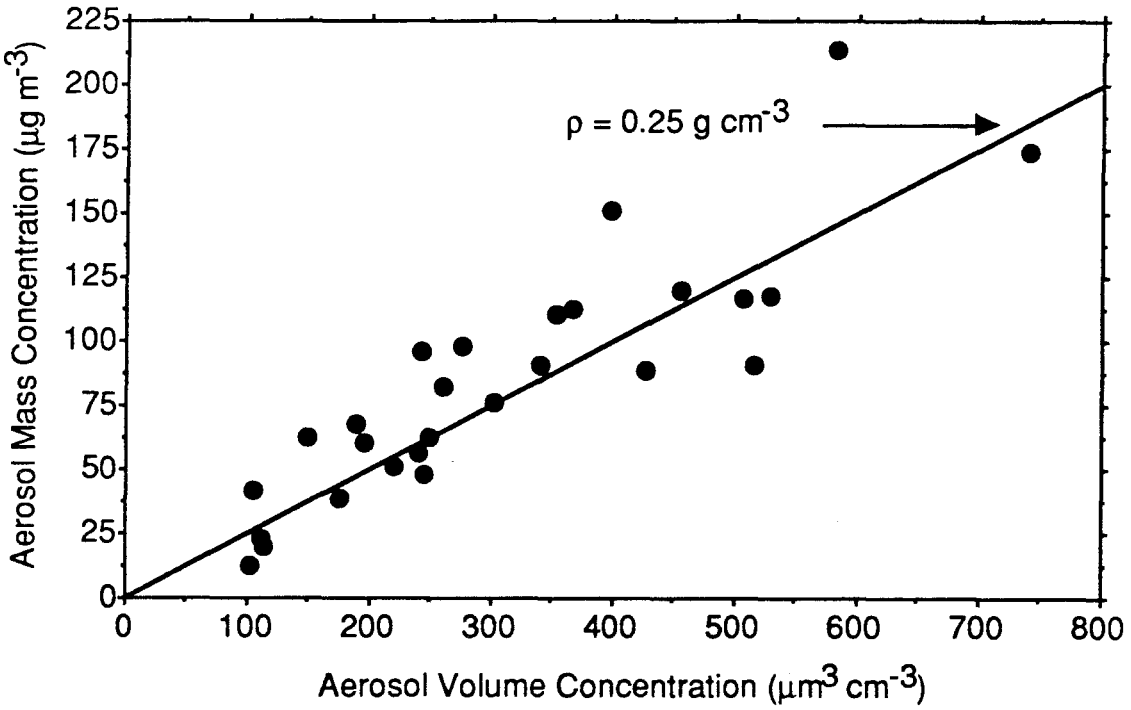

Figure 6.8 A comparison of the total volume concentration of coarse atmospheric particles measured by a large-particle optical particle counter with the simultaneously sampled dry mass of coarse particles. Each point represents a sampling interval of 4-8 h. Apparently, the OPC is substantially overpredicting the total aerosol volume concentration. For ideal instrument response, the points would fall along a line having a slope that corresponds to the particle density in units g cm^{-3}. The apparent particle density of 0.25 g cm^{-3} is well below the range of 1-2.5 g cm^{-3} that is expected for atmospheric aerosols.

96% and 86%, respectively, of the particles detected by the two instruments were placed within a contiguous band of three channels, which corresponds to the width of a size section used in the numerical simulations. (Note that the response of the instruments to atmospheric aerosols would undoubtedly be less precise than to DOP, which exists as spherical liquid droplets with a constant index of refraction. However, data on which to base an inversion calculation (see, e.g., Crump and Seinfeld, 1982) are lacking for optical particle counters sampling atmospheric aerosols.)

The results of simultaneous sampling of the atmospheric aerosol with the two instruments are depicted in Figure 6.9, using the adjusted channel definitions. The agreement is seen to be excellent for most particle sizes, with significant deviation occuring only in the diameter range of 0.2-0.4 μm. (The other such comparison showed good agreement in this size range, but some deviation for particles larger than 1 μm in diameter.)

Finally, in Figure 6.10 the fine particle mass determined by filter sampling is compared with the fine aerosol volume concentration determined by the mid-range OPCs. The points scatter reasonably about the line, which is the expected result for a mean particle density of 2 g cm^{-3}, as used in the numerical simulations. The excess number of points above the line is due entirely to measurements at the Sepulveda House which, being in proximity to the highest density of aerosol generation of any of the three sites, is expected to have the highest concentration of aerosol mass below the mid-range OPCs detection limit of 0.09 μm.

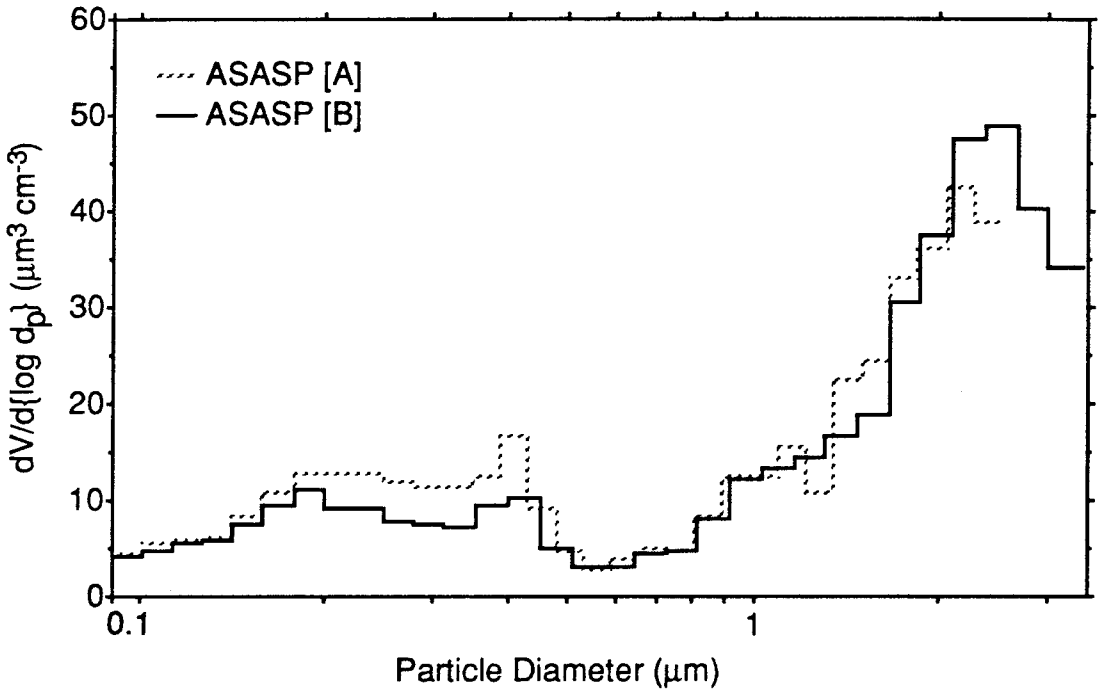

Figure 6.9 The results of simultaneous measurements of atmospheric aerosol size distribution by the two mid-range OPCs. The measurement was made on the roof of a Caltech laboratory during the period 1000-1630 on 4 May 1988.

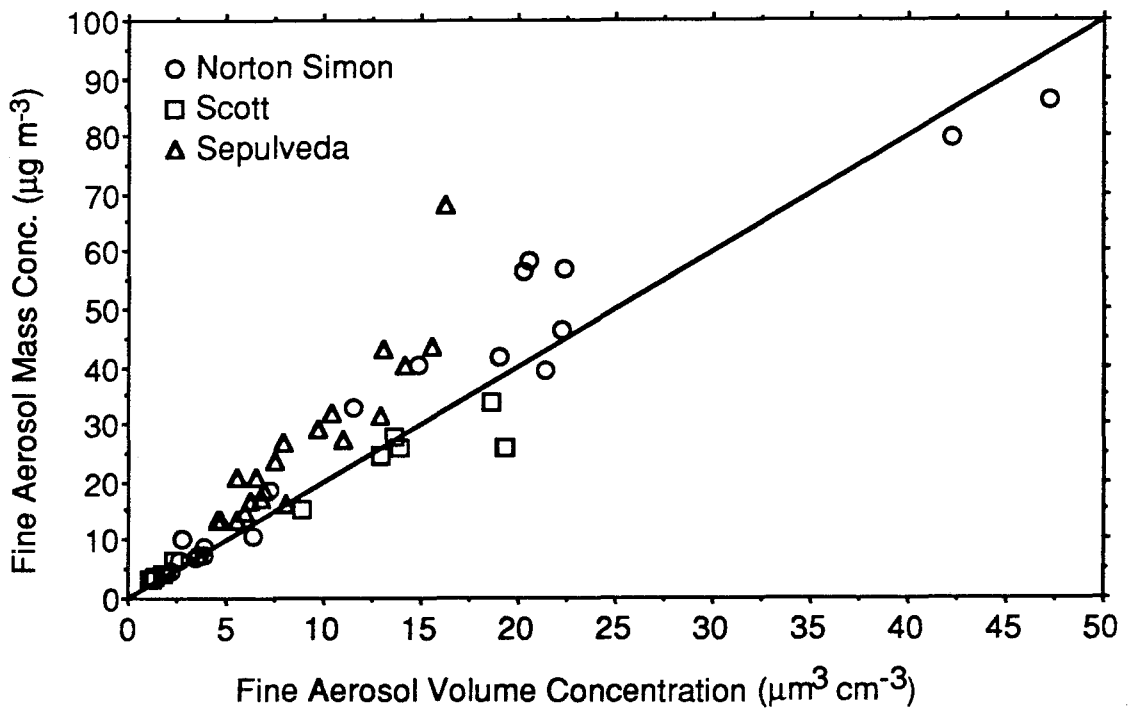

Figure 6.10 A comparison of the total volume concentration of fine atmospheric particles, measured by the mid-range optical particle counters, against the simultaneously sampled mass of fine dry particles. Each point represents a sampling interval of 4-8 h. The line represents the expected relationship for ideal instrument response, assuming that the particle density is 2 g cm^{-3} and that all of the fine particle mass occurs due to particles larger than 0.09 μm in diameter.

6.11 References

ASHRAE (1985) *ASHRAE Handbook: 1985 Fundamentals*, American Society of Heating, Refrigeration, and Air Conditioning Engineers: Atlanta, Georgia, Chapter 22.

Baer, N. S., and Banks, P. N. (1985) Indoor air pollution: Effects on cultural and historic materials, *International Journal of Museum Management and Curatorship* **4**, 9-20.

Bejan, A. (1984) *Convection Heat Transfer*, Wiley: New York.

Berglund, R. N., and Liu, B. Y. H. (1973) Generation of monodisperse aerosol standards, *Environmental Science and Technology* **7**, 147-153.

Bolleter, W. T., Bushman, C. T., and Tidwell, P. W. (1961) Spectrophotometric determination of ammonia as indophenol, *Analytical Chemistry* **33**, 592-594.

Carey, W. F. (1959) Atmospheric deposits in Britain: A study of dinginess, *International Journal of Air Pollution* **2**, 1-26.

Cary, R. (1987) Speciation of aerosol carbon using the thermal-optical method, presented at the Third International Conference on Carbonaceous Particles in the Atmosphere, Berkeley, California, October 1987.

Cass, G. R., Conklin, M. H., Shah, J. J., Huntzicker, J. J., and Macias, E. S. (1984) Elemental carbon concentrations: Estimation of an historical data base, *Atmospheric Environment* **18**, 153-162.

Corner, J., and Pendlebury, E. D. (1951) The coagulation and deposition of a stirred aerosol, *Proceedings of the Physical Society (London)* **B64**, 645-654.

Crump, J. G., Seinfeld, J. H. (1982) A new algorithm for inversion of aerosol size distribution data, *Aerosol Science and Technology* **1**, 15-34.

Dzubay, T. G. (1977) *X-ray Fluorescence Analysis of Environmental Samples*, Ann Arbor Science: Ann Arbor, MI.

Gray, H. A., Cass, G. R., Huntzicker, J. J., Heyerdahl, E. K., and Rau, J. A. (1986) Characteristics of atmospheric organic and elemental carbon particle concentrations in Los Angeles, *Environmental Science and Technology* **20**, 580-589.

Hancock, R. P., Esmen, N. A., and Furber, C. P. (1976) Visual response to dustiness, *Journal of the Air Pollution Control Association* **26**, 54-57.

John, W., Reischl, G. (1980) A cyclone for size selective sampling of ambient air, *Journal of the Air Pollution Control Association* **30**, 872-876.

Johnson, R. L., Shah, J. J., Cary, R. A., and Huntzicker, J. J. (1980) An automated thermal-optical method for the analysis of carbonaceous aerosol, In *Atmospheric Aerosols: Source/Air Quality Relationships*, Macias, E. S., and Hopke, P. K., Eds., American Chemical Society: Washington, pp. 223-233.

Larson, S. M., Cass, G. R., Hussey, K. J., and Luce, F. (1988) Verification of image processing-based visibility models, *Environmental Science and Technology* **22**, 629-637.

Ligocki, M. P., Salmon, L. G., Fall, T., Jones, M. C., Nazaroff, W. W., and Cass, G. R. (1988a) Characteristics of airborne particles inside Southern California museums, California Institute of Technology: Pasadena (manuscript in preparation).

Ligocki, M. P., Liu, H. I. H., Cass, G. R., and John, W. (1988b) Measurements of particle deposition rates inside Southern California museums, to be submitted to *Aerosol Science and Technology.*

Miller, M. S., Friedlander, S. K., and Hidy, G. M. (1972) A chemical element balance for the Pasadena aerosol, *Journal of Colloid and Interface Science* **39**, 165-176.

Mulik, J., Puckett, R., Williams, D., and Sawicki, E. (1976) Ion chromatographic analysis of sulfate and nitrate in ambient aerosols, *Analytical Letters* **9**, 653-663.

Ouimette, J. (1981) *Aerosol Chemical Species Contributions to the Extinction Coefficient*, Ph.D. Thesis, California Institute of Technology, Pasadena, California.

Schiller, G. E. (1984) *A Theoretical Convective-Transport Model of Indoor Radon Decay Products*, Ph.D. Thesis, University of California, Berkeley, California.

Schlichting, H. (1979) *Boundary-Layer Theory (7th edn.)*, McGraw-Hill: New York, pp. 315-321.

Thomson, G. (1978) *The Museum Environment*, Butterworths: London.

Yocum, J. E. (1982) Indoor-outdoor air quality relationships: A critical review, *Journal of the Air Pollution Control Association* **32**, 500-520.

CHAPTER 7

PARTICLE DEPOSITION IN MUSEUMS: COMPARISON OF MODELING AND MEASUREMENT RESULTS

7.1 Abstract

Deposition of airborne particles may lead to soiling and/or chemical damage of objects kept indoors, including works of art in museums. Measurements recently were made of the deposition velocity of fine particles (diameter range: 0.05-2 μm) and of sulfates onto surfaces mounted on walls within five Southern California museums. In this chapter, theoretical predictions of particle deposition velocity are developed for comparison against the experimental results. Deposition velocities are calculated from data on surface-air temperature difference and near-wall air velocity using idealized representations of the air flow field near the wall. For the five sites studied, the wall-air temperature differences were generally in the range of a few tenths to a few degrees K. Average air velocities measured at 1 cm from the wall were in the range 0.08-0.19 m s^{-1}. Based on a combination of modeling predictions and measurement results, the best estimate values of deposition velocity for the wall studied at each site are obtained. These values are in the range (1.3-20) $\times$ 10^{-6} m s^{-1} for particles with 0.05 μm diameter and (0.1-3.3) $\times$ 10^{-6} for particles with 1 μm diameter; the range of 15-30 in deposition velocity for a given particle size is due primarily to differences among sites in the near-wall air flow regime, with the low and high values associated with forced laminar flow and homogeneous turbulence in the core of the room, respectively.

Nazaroff, W. W., Ligocki, M. P., Ma, T., and Cass, G. R. (1988) Particle deposition in museums: Comparison of modeling and measurement results, to be submitted to *Aerosol Science and Technology*.

7.2 Introduction

Airborne particles that deposit onto indoor surfaces may cause soiling or chemical damage such as corrosion. For this reason, particles in museum atmospheres constitute a hazard for works of art. An art object may be very highly valued solely for its aesthetic qualities, and these qualities will be degraded if, for example, enough light absorbing particles accumulate on the object's surface.

Much of the work in this thesis is aimed at developing means to protect works of art from damage due to the deposition of airborne particulate matter. As part of this research effort, a mathematical model was developed to simulate the dynamics of indoor aerosols (Chapter 5), with emphasis on predicting the rate of particle deposition onto surfaces (Chapters 3 and 4). It was shown that this model is capable of accurate predictions of the time-dependent aerosol size distribution and chemical composition in museums (Chapter 6), characteristics that depend principally upon the concentration and composition of the outdoor aerosol and on the building ventilation and filtration system. For the three sites that were studied, model calculations show that generally less than 1% of the fine particles (0.05-2 μm in diameter) entering the museums were deposited onto walls. Thus, the agreement between predicted and measured indoor aerosol concentrations obtained in Chapter 6 does not constitute a stringent test of the accuracy of predicted particle deposition rates onto vertical surfaces.

Although only a small fraction of the fine airborne particles entering a museum deposit onto surfaces, soiling may still constitute a substantial hazard, particularly since it is desired to preserve art objects in their original condition for as long as possible. Thus, even slow rates of particle accumulation may lead to cumulative damage that is unacceptable. To gain confidence in model predictions of particle deposition rates, a sensitive test is required, based on a comparison of predictions against direct measurements of particle deposition rates. A companion paper to the present chapter

describes measurements of the deposition velocity of particles onto surfaces in museums (Ligocki et al., 1988a). These measurements are suitable for the purpose of this chapter: to compare model predictions of the particle deposition velocity onto vertical surfaces with direct experimental measurements.

7.3 Study Sites

Five Southern California museums were selected for the study. A detailed description of the sites is provided elsewhere (Ligocki et al., 1988b). The pertinent characteristics of these sites for the particle deposition predictions and measurements are summarized below.

Three sites—the Getty Museum, in Malibu; the Norton Simon Museum, in Pasadena; and the Virginia Steele Scott Gallery, in San Marino—are relatively modern buildings with conventional mechanical ventilation systems. At the Getty Museum, measurements discussed in this chapter were made in the Mosaics gallery, located on the main (antiquities) floor. The mechanical ventilation system serving the galleries on this floor operates from 0800 to 1800 hours daily. During these hours, air is discharged into the room from slits at ceiling level that are located at intervals near the room's perimeter. At each of the other two sites, ventilation is provided continuously, at a constant rate, by an engineered air-conditioning system. At the Scott Gallery, air enters the room from ventilation registers located near ceiling level, and is returned to the mechanical ventilation system through other registers also located at ceiling level. At the Norton Simon Museum, air from the ventilation system is supplied to the galleries through porous tiles that constitute approximately 75% of the ceiling area. There are no return air registers at the Norton Simon Museum. Instead, air is returned from the galleries to the mechanical ventilation system through large hallways. A fourth site—the Sepulveda House, in downtown Los Angeles—is an historic two-story building with no heating or cooling system. Ventilation is provided by uncontrolled leakage through relatively large

openings in the building shell. A large gap (~ 0.35 m^2 total area) around the perimeter of a carriage door downstairs, coupled with skylight vents in the upstairs ceiling, permits frequently strong buoyancy-driven air flow through the building. During times when the museum is open (1000-1500 hours daily except Sunday), if the weather is warm, downstairs doors are kept open, providing additional ventilation. The fifth site—the Southwest Museum, located in the Highland Park area of Los Angeles—is ventilated by a set of high-powered exhaust fans that draw outdoor air through the main portion of the building. Deposition velocity measurements were conducted in the California Room, which is not directly influenced by the exhaust fans. Instead, it contains a local forced-air heating and cooling system that, when operating, entrains air from the main portion of the building and discharges it into the room from registers located along a duct that traverses the length of the room about 4 m above the floor and 2 m below the ridge of a gabled roof. The fan in this ventilation system operates only on demand of the thermostat, which is generally on during the day (0700-1730 hours) and off at night.

One wall was selected at each site for deposition measurements. An objective, largely met, was to sample on a wall from which a painting or other object of art might be displayed. The characteristics of the surfaces, described in Table 7.1, span a substantial range of conditions that might influence particle deposition. Thus, the measured and predicted deposition velocities at each site reflect both the nature of the surface, such as its thermal characteristics, and the air flow conditions within the building.

7.4 Experimental Methods

Particle deposition rates are parameterized in terms of the deposition velocity (units: m s^{-1}), defined as the flux density of particles to a surface (number m^{-2} s^{-1}) divided by the concentration of particles in the air in the core of the room away from the surface (number m^{-3}). For the present work, the time-averaged particle deposition velocity was determined by measuring particle accumulation onto surfaces over extended

Table 7.1. Properties of the walls upon which deposition was studied at each site.

Getty Museum	Exterior, north-facing wall. Plaster over concrete. Wall height = 3.2 m, width = 1.1 m; deposition plate height approx. 2.3 m. Short-term boundary-layer probes at height of 1.2 m.
Norton Simon	Interior wall contained within single room. Gypsum board over sheet-metal frame construction. Deposition sampling carried out on side of wall facing west, opposite a large window that was covered with foam board and curtains during the study to block direct sunlight. Wall height = 5.2 m, width = 4.9 m; deposition plate height approx. 3 m. Short-term boundary layer probes at 1.8 m height.
Scott Gallery	Interior wall. Deposition sampling carried out on painted plywood panel mounted with furring strips onto wall; all paintings in gallery are hung from such panels. The panel height and width are approximately 2.7 and 0.7 m, respectively, and the base of the panel is approx. 1 m above the floor. The ceiling height is 4.5 m. The deposition plates were mounted approx. 2.4 m above the floor, and the short-term boundary layer probes sampled at 1.8 m height.
Sepulveda	Exterior wall made of irregular plaster over brick. Outer surface of wall abuts to adjacent building. Wall height and width 3.8 and 3.7 m, respectively. Deposition plates located 2.9 m above the floor, and the short-term boundary layer probes sampled at 1.9 m height.
Southwest	Plywood panel mounted 15 cm away from exterior concrete wall. The panel extends upward about 1 m from a concrete shelf that forms the top of a display case, approx. 2.5 m above the floor. The deposition plates and short-term boundary-layer probes sampled at the middle height of the panel. The width of the panel, and of the room, is approx. 9 m.

periods and sampling the airborne particle concentrations during those periods. Measurements also were made of the air velocity near the walls and the surface-air temperature difference to support the predictions of the deposition velocity.

Deposition velocities were measured as a function of size for particles having diameters in the approximate range 0.05-1 μm, and for sulfates. The measurement of particle deposition rate and mean concentration used to determine the deposition velocity is summarized briefly here; the complete description of these experiments can be found in the companion paper (Ligocki et al., 1988a).

To measure particle accumulation rates, a number of collection plates were deployed on the chosen wall at each site. Particles were collected by deposition onto sets of plates exposed during three extended periods: ten weeks during the summer of 1987, ten weeks during the autumn and winter of 1987-88, and a year beginning in the summer of 1987. Such lengthy collection periods were necessary to accumulate sufficient particles for analysis, and are appropriate for considering soiling or corrosion, which are long-term hazards.

For single-particle analysis, deposition plates were comprised of a thin sheet of freshly cleaved mica, coated with a carbon film. Some of these plates were mounted directly onto the wall, attached with a thin layer of thermal joint compound. Other plates were mounted onto small, unframed, stretched canvasses which were hung on the walls. Following each collection period, the plates were analyzed with an automated scanning electron microscope (SEM) to determine the number and size distribution of the deposited particles from which the mean rate of particle deposition (number of particles per area per time) was computed as a function of particle diameter.

For sulfate analysis, the deposition plates consisted of membrane filter material (Gelman, Zefluor 8" × 10" sheets of supported PTFE, 1 μm pore size), flush-mounted in a thin aluminum frame. The deposition plates were machined with beveled edges to minimize disruption of the boundary layer flow. These plates were coupled to the wall

with thermal joint compound. After sampling, material deposited on the filter was extracted and analyzed by ion chromatography.

To determine average indoor particle concentrations, air was sampled through filters for 24-hour intervals every sixth day during the summer and autumn/winter study periods. Samplers and analysis methods were similar to those described by Gray et al. (1986). The sulfate content of fine (<2 μm) particles was determined by ion chromatographic analysis of particulate matter collected on Teflon membrane filters located downstream of a cyclone separator. Single-particle analysis using the SEM was performed on airborne particle samples collected on polycarbonate membrane filters (Nuclepore, 47 mm, 1.0 or 0.4 μm pore size) that had been precoated with a layer of vapor-deposited carbon. In this case, because of resource constraints, only a subset of the filters collected (5-6 filters per season at each site) were analyzed by the SEM technique.

The total 24-hour average dry aerosol mass of fine and coarse particles was determined gravimetrically from the filter-based air samplers for each sampling day. The results were used to weight the deposition velocity model predictions made on a daily basis, to determine long-term average values.

For fine particle deposition onto an indoor surface, the deposition velocity depends on the nature of the air flow adjacent to the surface, the intensity of the air motion, and on the temperature gradients in the boundary layer. (Deposition velocity may vary with other factors, such as surface roughness; this factor was not considered here, as the sampling plates were smooth.) To provide data on which to base predictions of the deposition velocity, surface-air temperature differences were monitored, and air velocity adjacent to the chosen wall at each site was sampled.

Two thermistors (part no. 44202, Yellow Springs Instrument Co., Yellow Springs, OH) were used at each site to monitor the surface-air temperature difference. One thermistor was mounted within an aluminum deposition plate that was secured to the wall with thermal joint compound; the second was exposed to the air at about 5 cm from the

wall. Signal-conditioning electronics produced an output voltage that was proportional to the difference in temperature between the thermistor mounted in the plate and the one in the air. This output signal was recorded continuously either by a strip-chart recorder or by a microcomputer-based data acquisition system. From these records, hourly-averaged temperature differences were extracted for each site, for both seasons, and for each of the particle sampling days.

Near-wall flow characteristics were investigated for a one-day period at each site during the summer of 1987. An omnidirectional flow sensor (TSI model 1620) was placed at a central location along the wall (see Table 7.1 for details) approximately 1 cm from the surface. An array of eight thermistors was used to simultaneously measure the temperature of the wall surface, the temperatures at five successive distances from the wall within the boundary layer adjacent to the wall, and two air temperatures outside the boundary layer (one probe was shielded from radiant heat transfer, the other unshielded). The sensor output was monitored by a data acquisition system that recorded the air velocity at 2-s intervals and the average temperature at each point every minute. Sampling was conducted continuously for a 21-hour period at each site.

7.5 Air Flows and Temperature Differences Near Walls

Air movement within buildings results from a combination of mechanically induced flows, such as the discharge of air from a ventilation register, and thermally induced flows, such as the flow of air downward along a cold window. Although investigations into the nature of indoor air flows have been conducted (e.g., Gadgil, 1980; Camuffo, 1983; Kurabuchi and Kusuda, 1987), the problem is complex and, at present, not well understood. Consequently, the information collected on near-wall air flows and temperature differences in this study must be discussed in some detail.

A summary of the data on air velocity and surface-air temperature differences measured over 21-hour periods is presented in Figure 7.1. Overall, the air velocities at 1

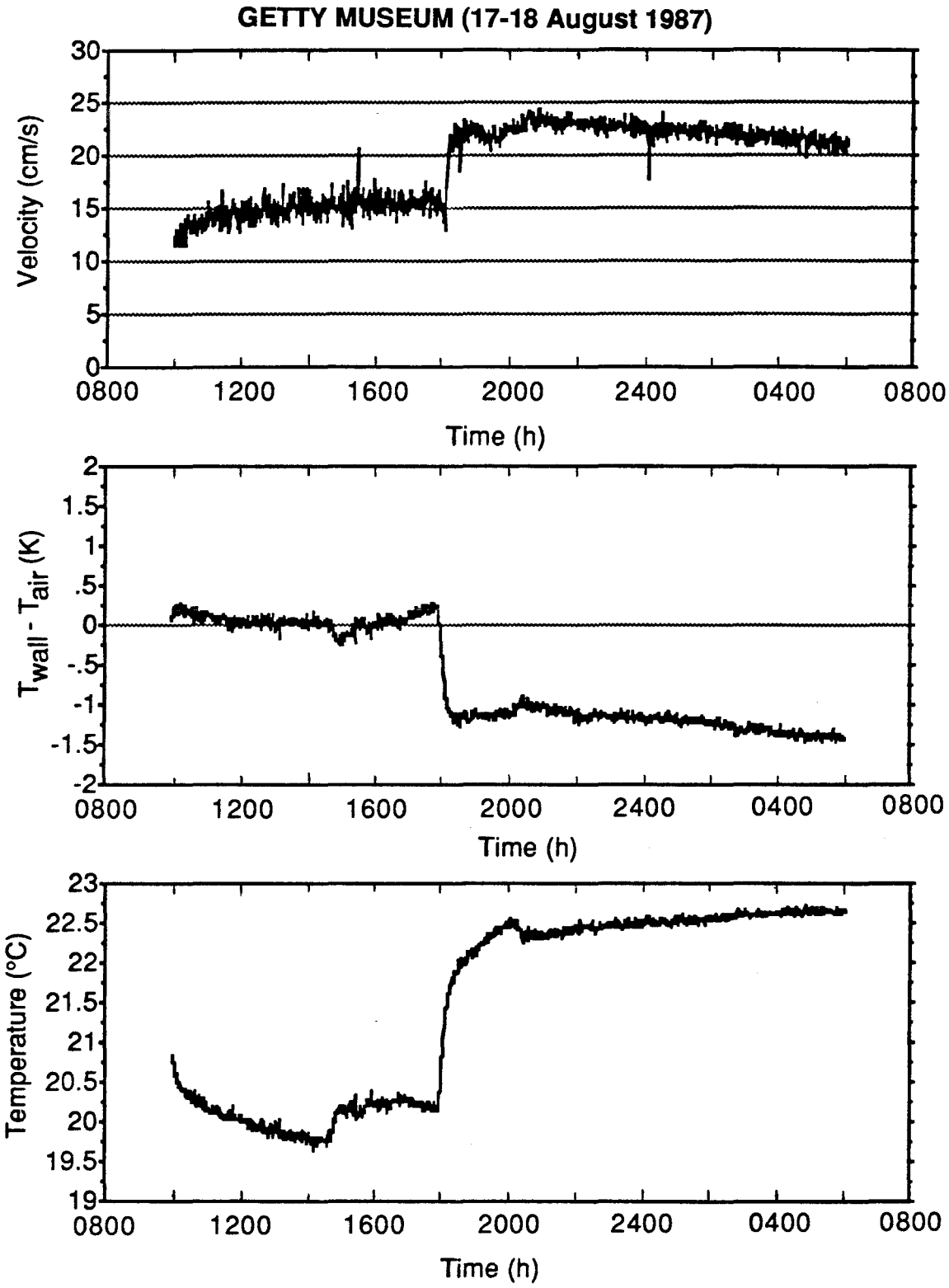

Figure 7.1 Results of short-term sampling of near-wall air velocity, wall-air temperature difference, and indoor air temperature at each of the five study sites. Sampling was conducted over a 21-hour period at each site. Air velocity was measured 1 cm from the surfaces described in Table 7.1.

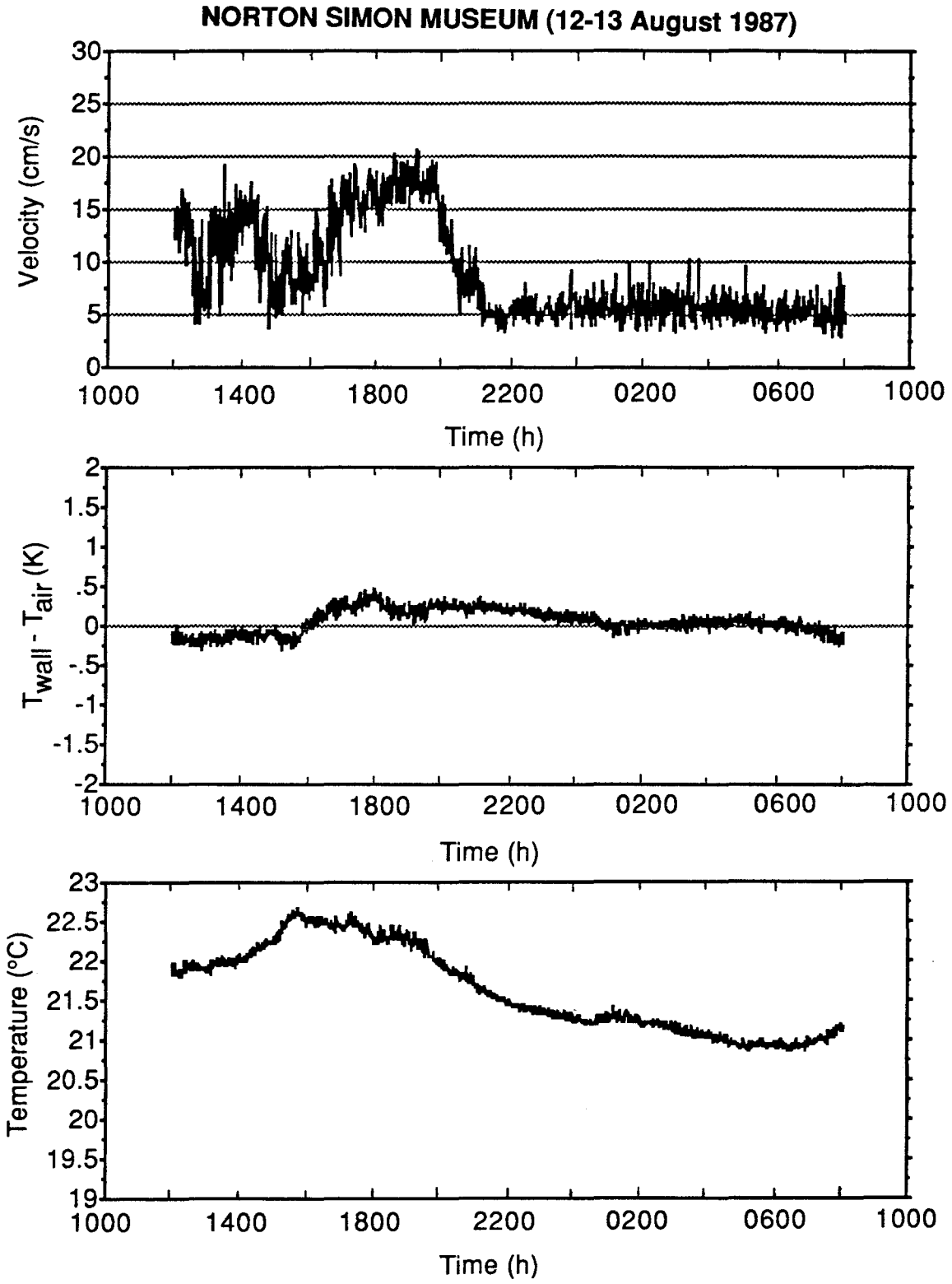

Figure 7.1 (cont.)

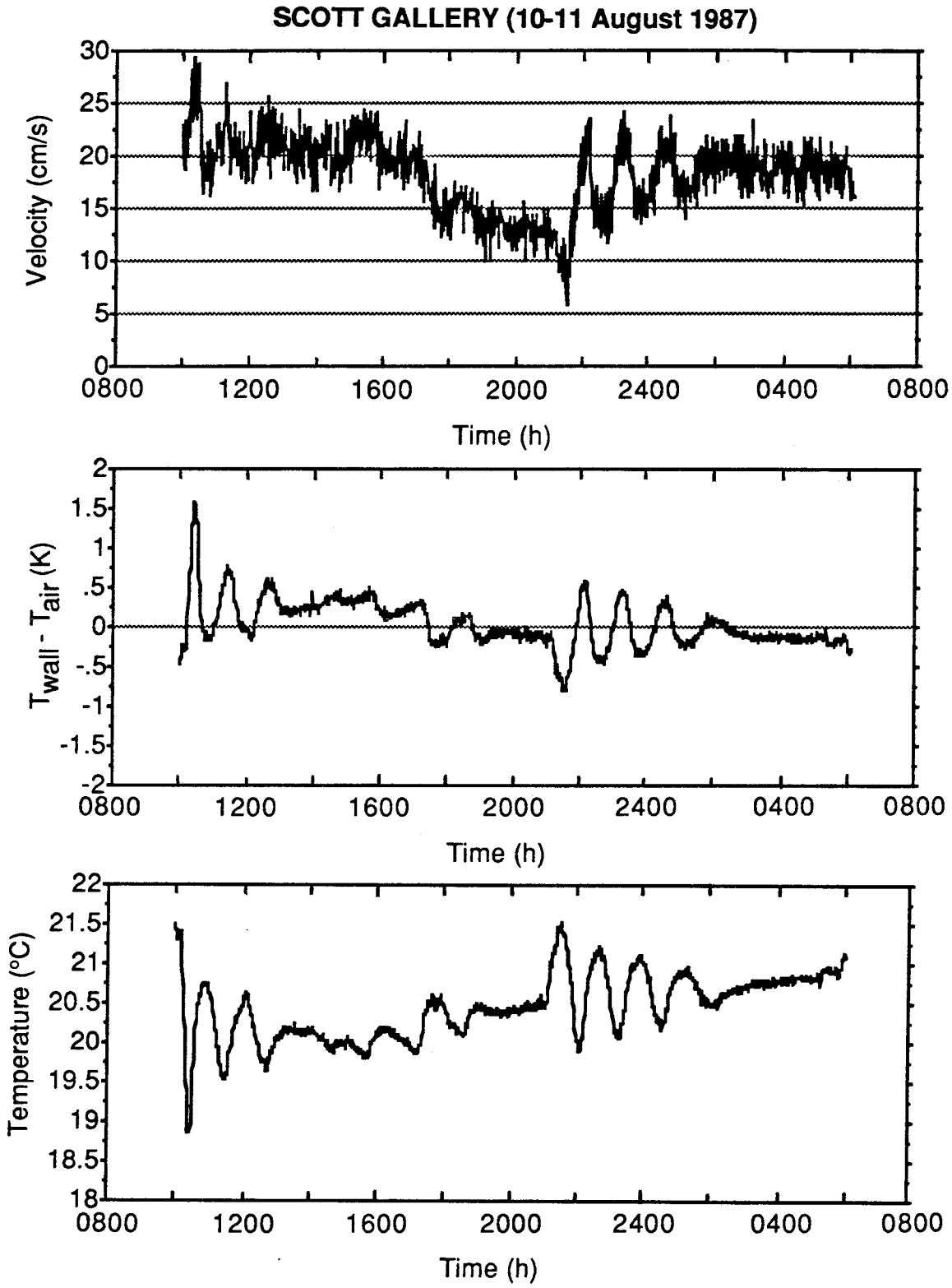

Figure 7.1 (cont.)

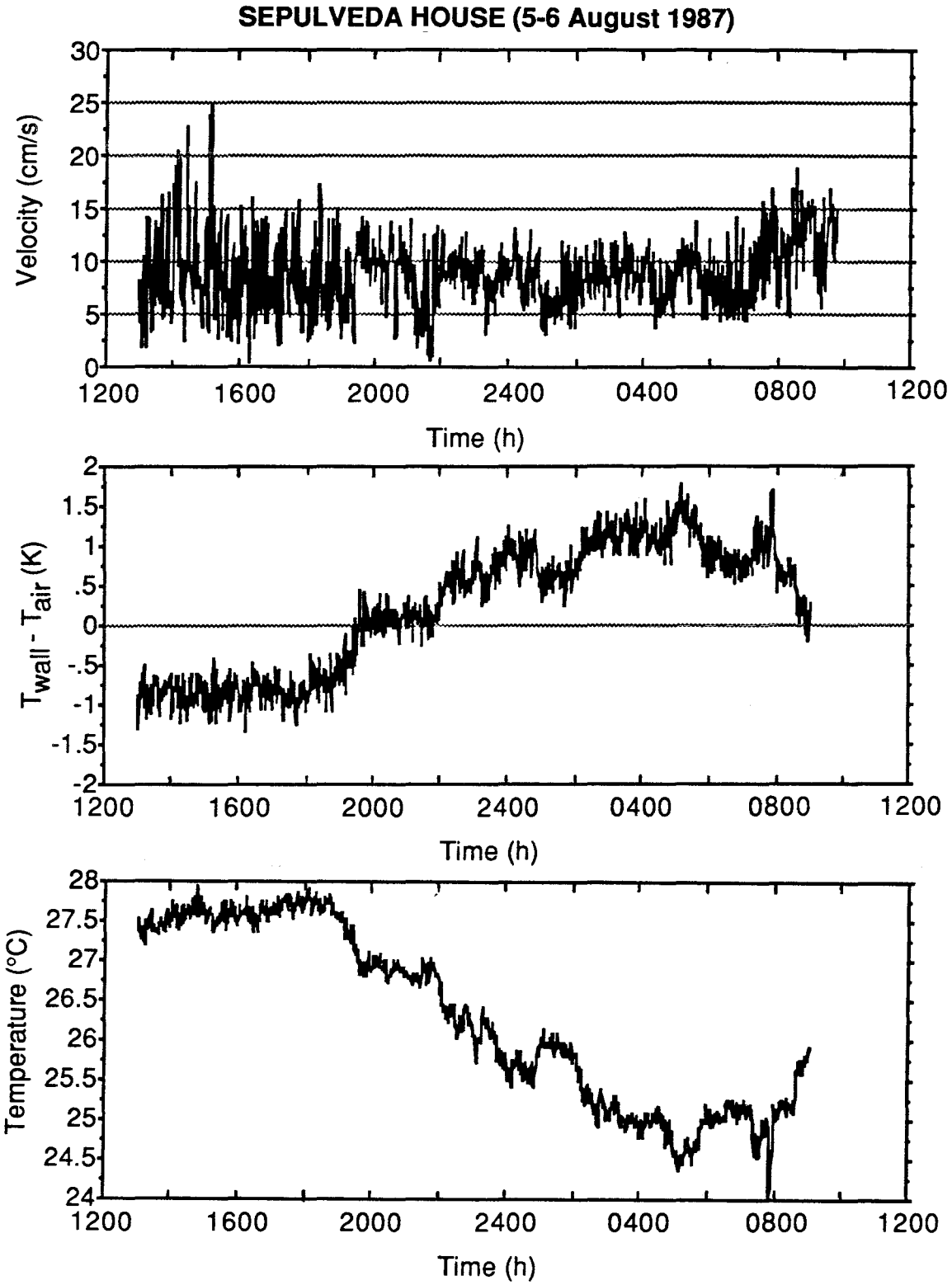

Figure 7.1 (cont.)

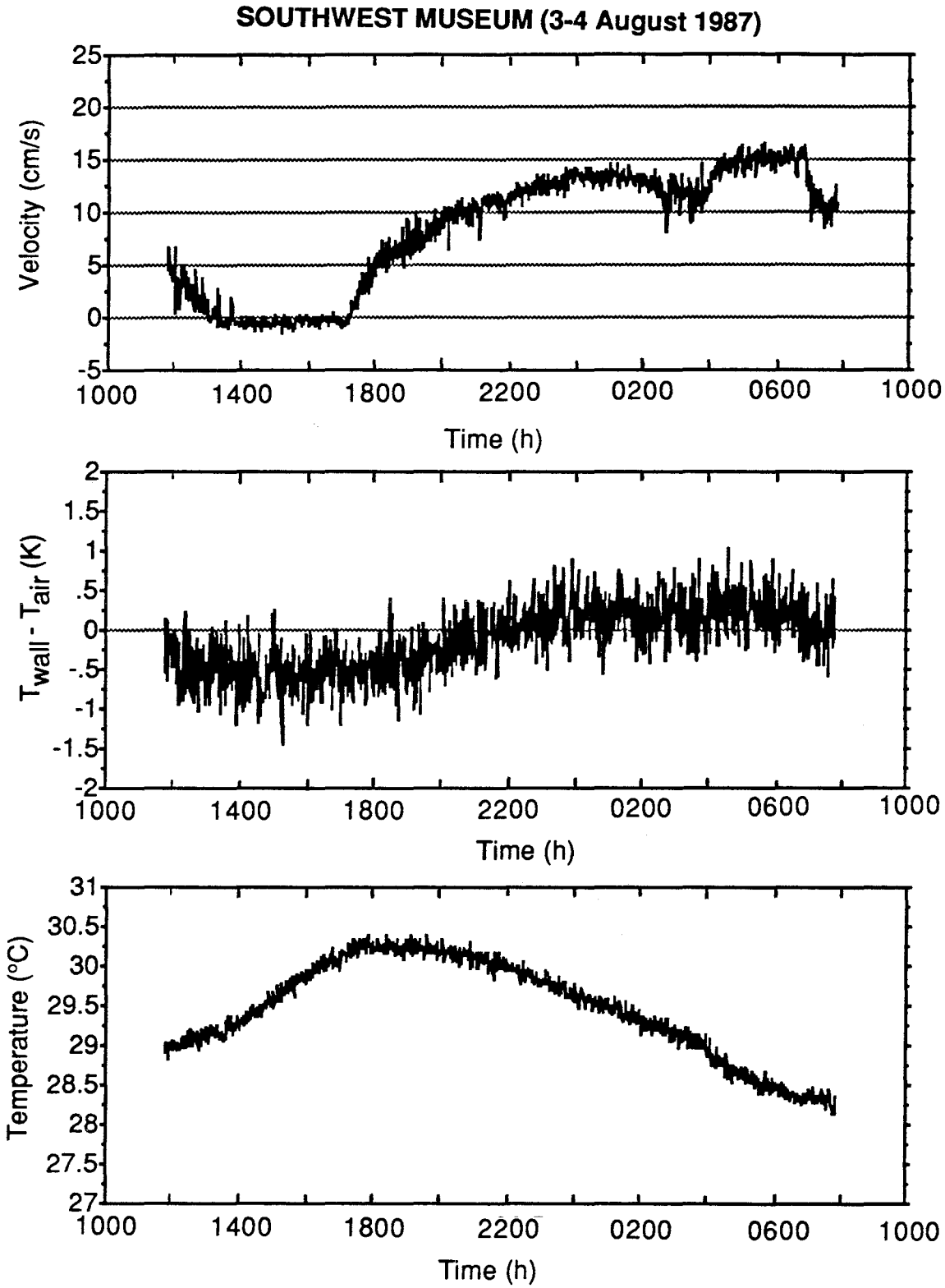

Figure 7.1 (cont.)

cm from the surfaces, averaged over 1-minute intervals, range from effectively zero to almost 30 cm s^{-1}. The absolute value of the surface-air temperature difference is generally in the range of a few tenths to 2 degrees K. The indoor air temperature at each site varies 2-4 degrees K over the course of the day.

Long-term average data on the surface-air temperature differences are presented in Figure 7.2, with the traces in each frame based on the analysis of data from the 11-12 aerosol sampling days for each season. Higher surface temperatures relative to the air temperature generally are observed in the summer, whereas higher air temperatures relative to the surface occur in the winter. This finding is consistent with the tendency for the air to be cooled by climate control systems in the summer and heated in the winter. The difference between summer and winter conditions is smallest at the Sepulveda House, where no thermal conditioning occurs.

The results of the short-term and long-term measurements are sufficiently distinct at each site to merit brief independent discussions. Results at the Getty Museum show clear evidence of the operation of the mechanical ventilation system from 800-1800 hours daily, particularly in Figure 7.2 where a consistent difference is observed in $T_{wall} - T_{air}$ between periods in which the ventilation system is on and periods in which it is off. Figure 7.1 illustrates additional details of the effect of turning off the ventilation system at 1800: the indoor air temperature rises, and the mean air velocity along the wall also rises. During periods when the mechanical ventilation system is on, the observed air movement along the walls is probably forced by the ventilation air flow: the magnitude is consistent with observations of mechanically induced flows at other sites and the temperature difference is much too small to induce the observed flow rate via buoyancy driven effects. When the mechanical ventilation system is off, the observed air flow might be due to natural convection downward along the cool wall. The mean velocity, 20-25 cm s^{-1}, is comparable in magnitude, although a little larger than one would expect for flow driven by the surface-air temperature difference, given the measured ΔT of 1.2-1.5 K and the

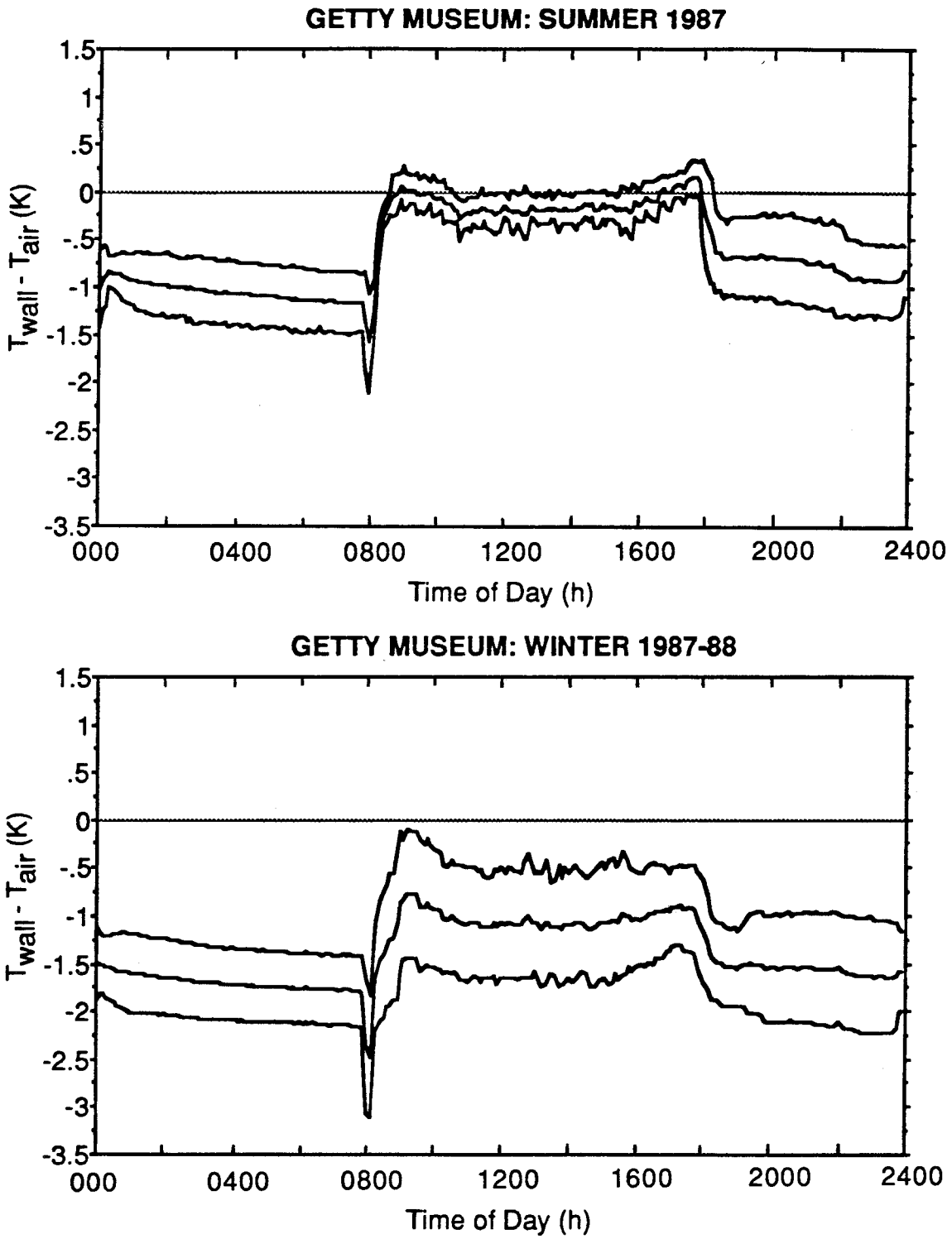

Figure 7.2 Results of long-term sampling of wall-air temperature difference at the five study sites. The three lines in each plot represent mean minus one standard deviation, the mean, and the mean plus one standard deviation of 11-12 temperature differences measured at intervals of approximately 6 days. The spikes in the wintertime traces at the Southwest Museum result from heating-system operation during one sampling day.

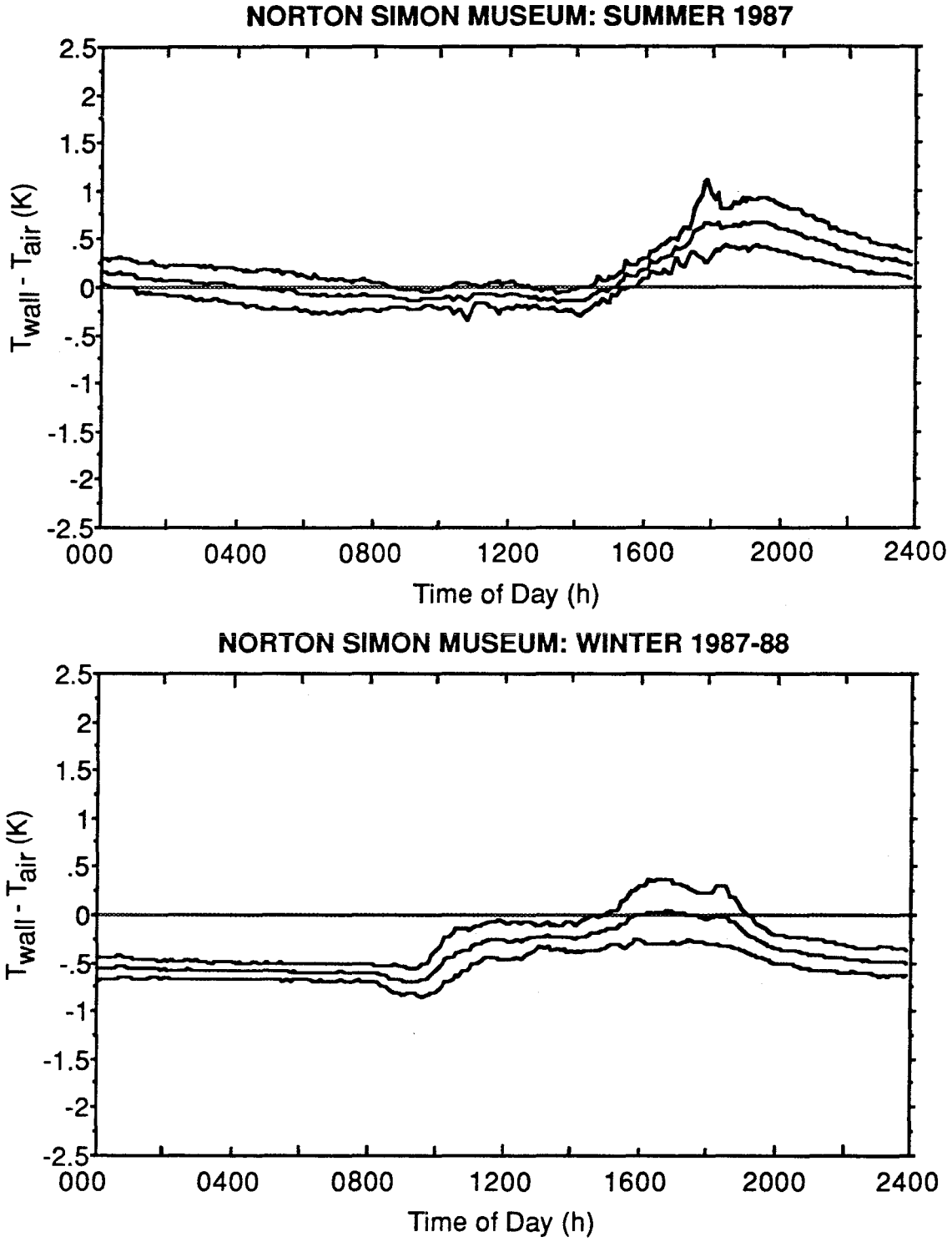

Figure 7.2 (cont.)

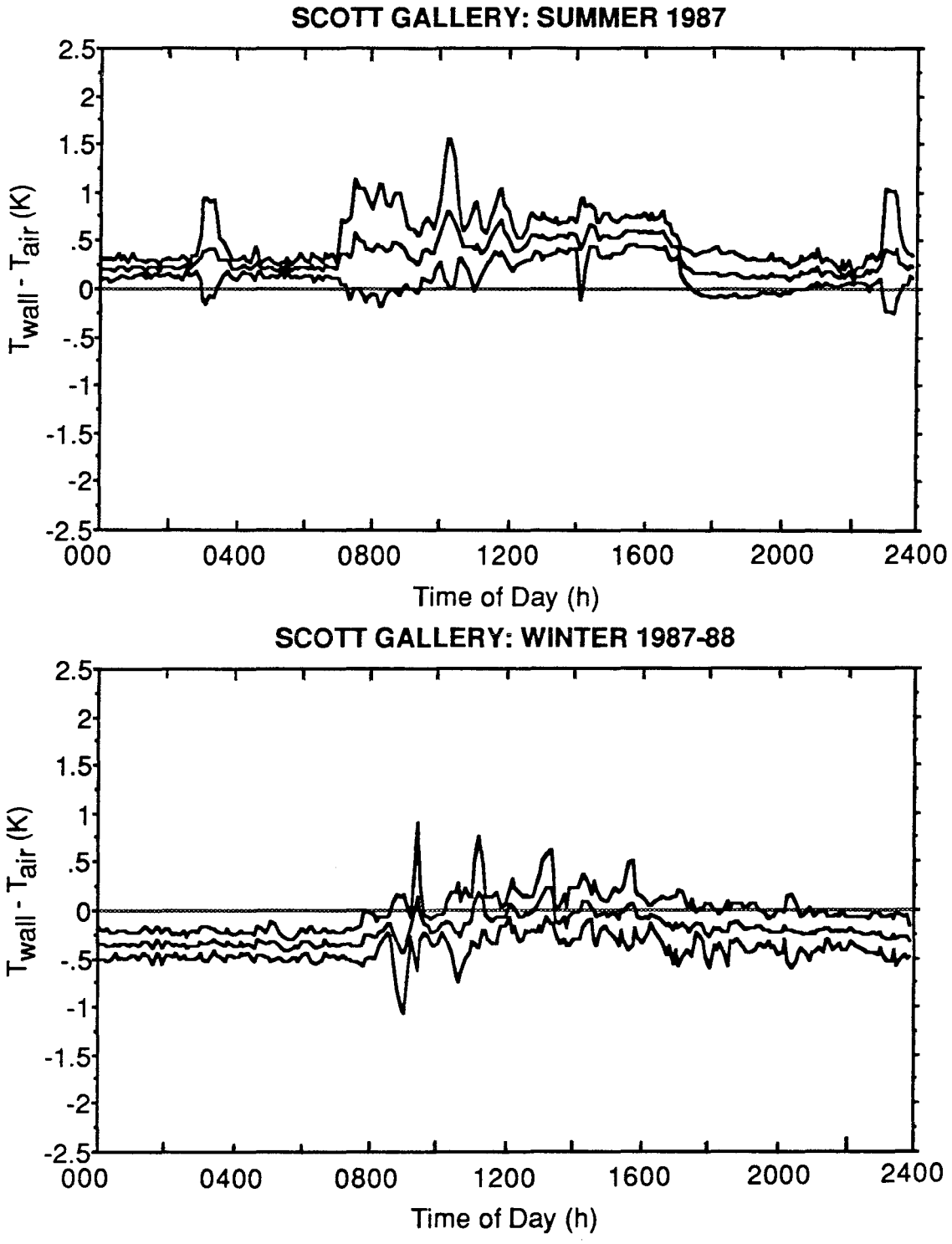

Figure 7.2 (cont.)

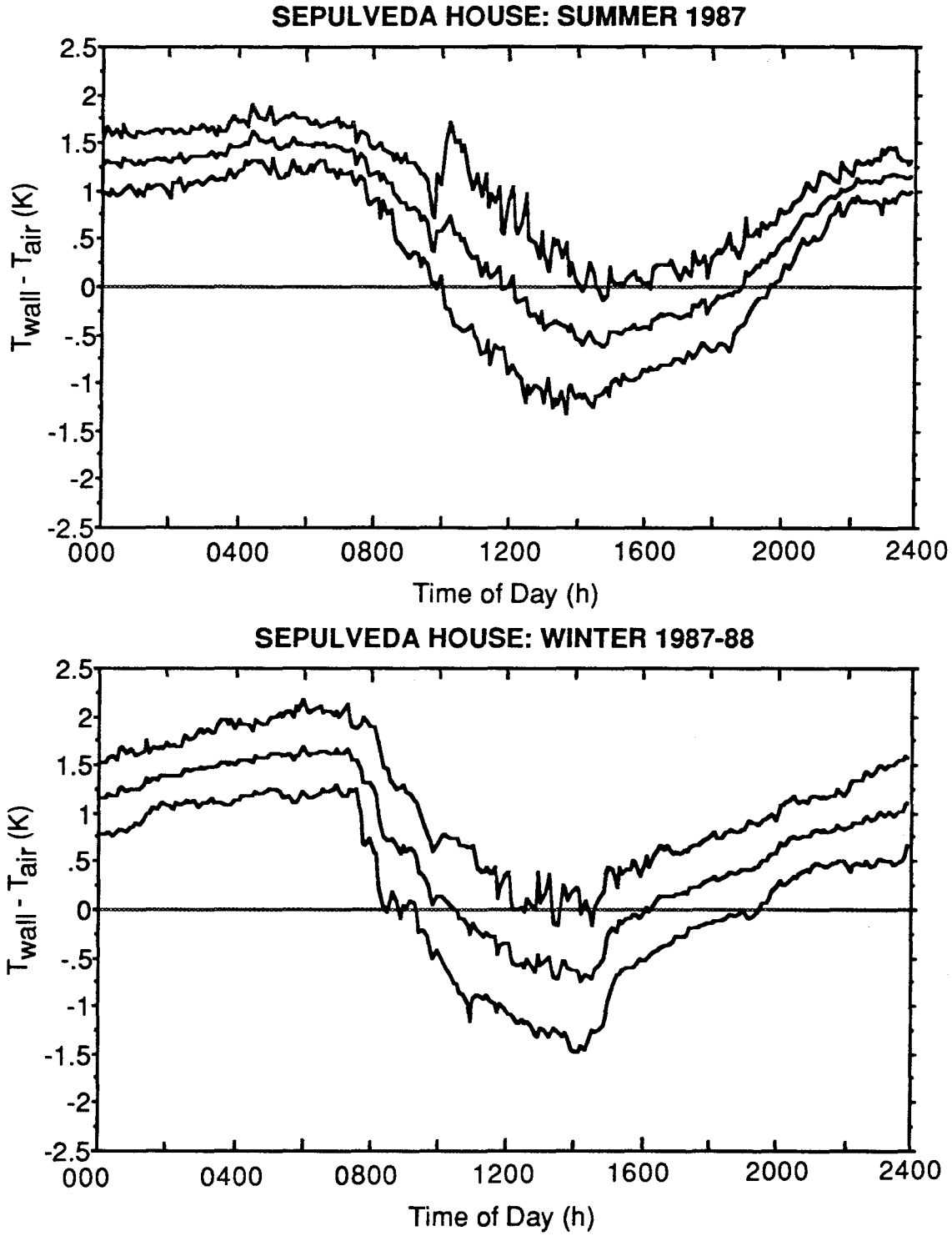

Figure 7.2 (cont.)

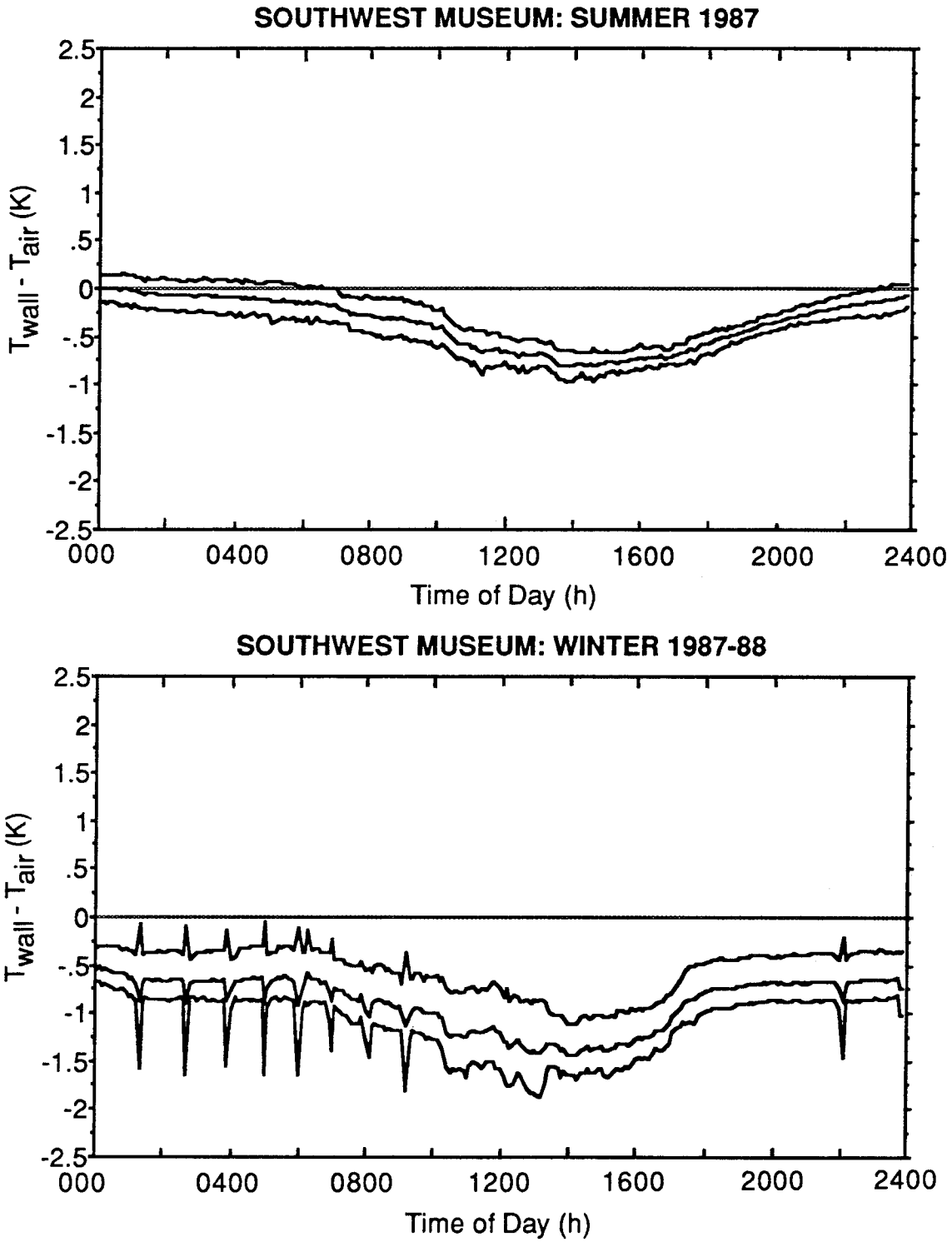

Figure 7.2 (cont.)

distance from the ceiling to the probe of approx. 2 m. For example, at a location of 1 cm away and 2 m from the leading edge of an isolated, vertical, isothermal flat plate, a temperature difference of 1.5 K would induce an air velocity of 17 cm s^{-1} (Schlichting, 1979). For an enclosure, assuming an adiabatic ceiling and floor, the predicted velocity for comparable conditions is reduced by about 50% relative to the isolated flat plate case (Schiller, 1984). The higher observed velocity might be a result of the coincident occurrence of other buoyancy-induced flow, due for example to a warm floor, a cool ceiling or a warm opposing wall, relative to the indoor air temperature.

Results for the Norton Simon Museum show relatively small fluctuations consistent with (1) a relatively high degree of thermal control and (2) a sampling location along an interior wall. A pronounced feature at this site is the increased value of $T_{wall} - T_{air}$ consistently observed in the late afternoon (see Figure 7.2). The near-wall velocity profile in Figure 7.1 shows substantially reduced air flow beginning at 2000 hours PDT that may be associated with the same cause. In the early afternoon, the air temperature in this area of the museum increases, probably because of solar heating of the roof and of the south and west-facing walls. During this time, the mechanical ventilation system is supplying air that is cooler than the room air in an attempt to maintain a set-point temperature in the vicinity of 21.7 °C. Air is supplied to the gallery at the ceiling level, so the introduction of cool air leads to buoyancy-induced mixing in addition to forced ventilation and consequently a moderately high near-wall air velocity. After sunset, the outer walls of the gallery cool, and the air temperature within the gallery falls below the set-point temperature. Warmer air is supplied to the room by the ventilation system again at ceiling level; this air is buoyant and is already at the maximum elevation within the building, and so convective mixing and the near-wall air velocity are reduced.

At the Scott Gallery no consistent diurnal pattern is observed in the wall-air temperature difference shown in Figure 7.2. However, pronounced short-term fluctuations in the air temperature are seen, reflecting underdamped control in the thermal

conditioning system (Figures 7.1 and 7.2). As seen in Figure 7.1, the sudden changes in air temperature appear with reduced magnitude and reversed sign in the temperature difference data. As the air is suddenly warmed, heat is transferred to the wall, but the increase in wall temperature lags so that a negative surface-air temperature difference is observed. When the air is suddenly cooled, the reverse process occurs. At the Scott Gallery, these sudden changes in air temperature are also reflected in the near-wall air velocity data, probably for the same reason as that discussed in the previous paragraph for the Norton Simon Museum. Whenever the air temperature at the Scott Gallery is suddenly rising, the air being discharged from the ventilation registers, which are located near the level of the ceiling, must be warmer than the air in the room. Being buoyant and already located at ceiling height, convective mixing of this warm air is suppressed, and the near-wall velocity is reduced. Conversely, when the air temperature is suddenly falling, the air being discharged must be cooler than the air in the room. Convective mixing is enhanced and the near-wall air velocity increases.

At the Sepulveda House, air temperature and near-wall velocity are dominated by the diurnal pattern in outdoor air temperature. The maximum air temperature and, therefore, the largest negative value of the surface-air temperature difference, occurs in early afternoon; the minimum air temperature and maximum positive value of the surface-air temperature difference are observed just before dawn. The near-wall air velocity on 5-6 August 1987 (Figure 7.1) is not correlated with $T_{wall} - T_{air}$ as it would be if the flow were due to natural convection driven by the surface-air temperature difference. However, during a subsequent monitoring period (30-31 March 1988), the near-wall velocity was consistent with expectations based on natural convection flow driven by the surface-air temperature difference except when the museum was open to the public (1000-1500 hours) (see Chapter 6, Figure 6.3).

At the Southwest Museum, the surface-air temperature difference is typically negative (Figure 7.2), indicating that the indoor air is chronically warmer than the inside

of the northwestern wall of the building. The California Room has an uninsulated roof exposed to the sun, which constitutes a significant heat load for the indoor air. Ventilation does not serve to dissipate this heat rapidly: the average rate of air-exchange in the room is 0.3 h^{-1}, as measured by the perfluorocarbon tracer technique (Dietz et al., 1986). Although the room has a cooling system, it appears to have inadequate capacity to overcome the summertime heat load: in Figure 7.1, for example, the indoor air temperature is seen to rise sharply during the afternoon hours to above 30 °C even though the cooling system would be operating during this time. The spikes observed in the wintertime profiles of T_{wall} - T_{air} at the Southwest Museum (Figure 7.2) appear to be associated with intermittent demand for heating coupled with slow transport of air from the discharge registers to the thermostat: the room air is heated by several degrees each time the heater is activated before the thermostat senses that sufficient heat has been supplied. The long-term temperature records show that heater operation occurred for an average of only 50 minutes per day during the autumn/winter study period, a direct result of the warm winter temperatures in Southern California.

The near-wall air velocity at the Southwest Museum appears to be dominated by turbulent air movement in the core of the room that is driven in turn by a combination of forced flow from the mechanical ventilation system and heat transfer at surfaces other than the interior panel on which the deposition plates and sensors were mounted. Referring to Figure 7.1, during the period 1400-1700 hours PDT, the near-wall air velocity is effectively zero. During this period, the indoor air temperature is steadily rising. This heat gain could result from one or two factors: (1) the discharge at a level near the ceiling of inadequately cooled warm air that is entrained by the local mechanical ventilation system from the highly ventilated core of the building and/or (2) direct heating of the roof by the sun. Stagnant flow conditions would result from the increase in temperature with height in the room. At approximately 1800 hours PDT, after the mechanical ventilation system is turned off and as the sun approaches the horizon, the

indoor air temperature no longer increases with time, and, within a few hours, begins to decrease. The roof cools by radiant heat transfer to the sky and convective heat transfer to outdoor air. In turn, the air near the ceiling begins to cool and an unstable temperature profile is established, inducing convective mixing within the room. After 1800 hours PDT, the near-wall air velocity is seen in Figure 7.1 to increase in a manner that corresponds approximately to the rate of cooling of indoor air with time.

7.6 Predicting the Mean Particle Deposition Velocity

The rate of deposition of particles onto a vertical surface depends on particle transport in the fluid mechanical boundary layer near the wall, which in turn varies according to details of near-surface air movement. If the air flow regime (forced laminar flow, natural convection flow, etc.) is known, particle deposition velocities can be related to the mean air velocity along the wall and the surface-air temperature difference, parameters that were measured during this study. Neither the data obtained in this study, nor previous field work inside buildings, constitute a basis for conclusively identifying the air flow regime that prevailed over all the surfaces that were investigated. However, calculations still can be performed for alternative flow regimes with velocities and temperature differences that are consistent with the data taken in this study.

For the present chapter, three model air flow conditions are considered: (1) forced laminar flow parallel to the wall (designated L); (2) laminar or turbulent natural convection induced by the temperature difference between the wall and the nearby air (designated NC); and (3) homogeneous turbulence induced by forced and/or convective air movement in the core of the room (designated T). Analyses of the these cases are presented in Chapter 4. The relevant equations are presented in Table 7.2.

For the case of forced laminar flow (case L), the freestream air velocity, u_∞, is required to compute the deposition velocity. The air velocity probe position at 1-cm from the wall was within the momentum boundary layer. The freestream air velocity was

Table 7.2. Equations for predicting particle deposition velocity, v_d, to vertical surfaces

deposition velocity [a,b]	conditions
forced laminar flow	
$v_d = D\left[\frac{u_\infty}{\nu L}\right]^{\frac{1}{2}} [\omega'(0)]_L$	$Re_L < (2\text{-}6) \times 10^5$
natural convection	
$v_d = [g \mid \Delta T \mid / 4\nu^2 T_\infty]^{1/4} \alpha^{1/3} D^{2/3} L^{-1/4} \{[\omega'(0)]_N / Le^{1/3}\}$	$Ra_H < 10^9$
v_d = maximum of $\left\{ [g \mid \Delta T \mid / 4\nu^2 T_\infty]^{1/4} \alpha^{1/3} D^{2/3} L^{-1/4} \{[\omega'(0)]_N / Le^{1/3}\} \right\}$	$10^9 < Ra_H < 10^{12}$
or $\left\{ v_t + \frac{D}{H}\left[0.825 + \frac{0.387\, Ra_H^{1/6}}{\left\{1 + (0.492/Sc)^{9/16}\right\}^{8/27}} \right]^2 \right\}$;	
where $v_t = -N_t\left(\frac{\nu}{H}\right)\left[0.825 + \frac{0.387\, Ra_H^{1/6}}{\left\{1 + (0.492/Pr)^{9/16}\right\}^{8/27}} \right]^2$	

Table 7.2. (Cont.)

	homogeneous turbulence in an enclosure	
$v_d = v_{CP} + v_t$		all
where	$v_t = - N_t \nu \frac{(K_e/\alpha)^{1/2}}{\tan^{-1}[\delta (K_e/\alpha)^{1/2}]}$	all; see note c
and	$v_{CP} = \frac{(D K_e)^{1/2}}{\tan^{-1}[\delta (K_e/D)^{1/2}]}$	see note c

[a] Nomenclature:

D	coefficient of Brownian diffusivity of particles ($m^2 s^{-1}$)
g	gravitational acceleration (9.8 m s^{-2})
H	height of room (m)
K	thermophoresis coefficient (-) [see footnote b]
K_e	turbulence intensity parameter (s^{-1})
L	distance from leading edge of wall to deposition plate (m)
Le	particle Lewis number, α/D (-)
N_t	thermophoresis parameter, $K\frac{\Delta T}{T_\infty}$ (-)
Pr	Prandtl number of the fluid, ν/α (-)
Ra_H	Rayleigh number, $\frac{g \beta \lvert\Delta T\rvert H^3}{\alpha\nu}$, where β is the coefficient of thermal expansion of air (-)

Table 7.2. (Cont.)

Re_L	Reynolds number, $\frac{u_\infty L}{\nu}$
Sc	particle Schmidt number, ν/D (-)
T_∞	air temperature outside of boundary layer (K)
u_∞	air velocity parallel to wall outside of boundary layer (m s^{-1})
v_{CP}	deposition velocity according to theory of Corner and Pendlebury (1951) (m s^{-1})
v_t	thermophoretic velocity of particles near surface (m s^{-1})

Greek Symbols

α	thermal diffusivity of air (m^2 s^{-1})
δ	boundary layer thickness for turbulent flow (m)
ΔT	temperature of surface minus temperature of air outside boundary layer (T_∞) (K)
ν	kinematic viscosity of air (m^2 s^{-1})
$[\omega'(0)]_L$	slope of normalized particle concentration at surface under laminar forced flow conditions (see Chapter 4) (-)
$[\omega'(0)]_N$	slope of normalized particle concentration at surface under laminar natural convection conds. (see Chapter 3) (-)

[b] The thermophoresis coefficient, K, which enters in the expression for N_t, was computed from the expression of Talbot et al. (1980), assuming that the thermal conductivity of the particle was equal to that of water.

[c] In these expressions, δ is the boundary layer thickness given approximately by $\delta \sim (1.2)\,(\nu/K_e)^{4/9}\, x_s^{1/9}$ where x_s is the length of the surface in the direction of flow, taken here as the geometric mean of the wall height and the wall width.

estimated from these data by iteration, knowing the characteristic length of the wall in the assumed direction of flow and using the boundary layer flow profile for an isolated flat plate (Schlichting, 1979).

Particle deposition induced by homogeneous turbulence in the core of an enclosure (Case T) may be computed by the method of Corner and Pendlebury (1951). In this case, the turbulence intensity parameter, K_e, is needed to compute the particle deposition velocity. Corner and Pendlebury estimated the value of K_e on the basis of the mean air velocity measured near the wall, as follows:

$$K_e = k_o^2 \frac{0.073}{\mu} \frac{\rho u^2}{2} \left(\frac{\mu}{\rho u x_s}\right)^{\frac{1}{5}} \qquad (7.1)$$

where k_o is von Kármán's constant, taken to be 0.4, μ is the dynamic viscosity of air, ρ is the air density, u is the mean air velocity, and x_s is the distance of the surface in the direction of the mean motion. This equation is based on a correlation for the turbulent drag on a flat plate in an infinite fluid moving parallel to the plate. For the data from our experiments, with x_s taken as the geometric mean of the width and height of the wall, equation 7.1 yields average values of the turbulence intensity parameter as shown in Table 7.3. Despite widely varied ventilation systems among the five sites, the mean turbulence intensity parameters estimated on this basis span a range of only a factor of five. The corresponding range of predicted deposition velocities for a given particle size is even smaller, since the deposition velocity to a vertical surface for the homogeneous turbulence flow regime varies as the square root of the turbulence intensity parameter (Table 7.2). The mean values of K_e in Table 7.3 are consistent with expectations for indoor rooms: all are well within the range of 0.1-10 s^{-1}, which was shown in Chapter 4 to yield deposition velocity predictions that approximately bound deposition velocity observations in actual rooms.

Table 7.3. Mean turbulence intensity parameter (K_e, estimated), near-wall air velocity (u, measured at 1 cm from wall) and wall-air temperature difference (ΔT) for the five study sites. [a]

			Summer		Winter	
Museum	$\overline{K_e}$ (s^{-1})	$\overline{u}$ ($m\ s^{-1}$)	$\overline{\Delta T}$ (K)	$\overline{\lvert \Delta T \rvert}$ (K)	$\overline{\Delta T}$ (K)	$\overline{\lvert \Delta T \rvert}$ (K)
Getty	1.9 (1.0-2.7)	0.19 (0.13-0.23)	-0.61	0.64	-1.4	1.4
Norton Simon	0.4 (0.16-1.3)	0.08 (0.05-0.17)	0.13	0.25	-0.40	0.43
Scott Gallery	1.7 (0.9-2.3)	0.18 (0.13-0.22)	0.34	0.34	-0.21	0.24
Sepulveda House	0.4 (0.2-0.8)	0.09 (0.06-0.12)	0.64	0.92	0.61	0.88
Southwest	0.5 (0.0-1.1)	0.08 (0.00-0.15)	-0.36	0.39	-0.89	0.89

[a] Numbers given in parentheses represent the range of hourly mean values;
$\overline{\Delta T} = \overline{(T_{wall} - T_{air})}$; and $\overline{\lvert \Delta T \rvert} = \overline{\lvert T_{wall} - T_{air} \rvert}$.

For comparison against experimental data, calculations of particle deposition velocity were carried out for each site and for each sampling season using up to three alternative air flow regimes, as detailed in Table 7.4. For each simulation, the time-averaged deposition velocity was computed for 31 particle diameters, k, in the range 0.01-10 μm using the following expression:

$$\overline{v_{d_k}} = \frac{\sum_{i=1}^{n} m_i \sum_{j=1}^{24} v_{d_k}(K_{e_j}, u_{\infty_j}, \Delta T_{i,j}, d_{p_k}, W)}{24 \sum_{i=1}^{n} m_i} \qquad (7.2)$$

where m_i is the 24-hour average aerosol mass concentration ("fine" for particles less than 2 μm in diameter and "coarse" for larger particles), and n is the number of sampling days, 11 for the summer period and 12 for the autumn/winter interval. The parameter v_{d_k} is the particle deposition velocity for particles of diameter d_{p_k} as given in Table 7.2. Evaluation of the deposition velocity may depend on several parameters: K_{e_j} and u_{∞_j} are the hourly average turbulence intensity and freestream velocity, respectively, for the corresponding time of day, $\Delta T_{i,j}$ is the surface-air temperature difference at hour j on day i, d_{p_k} is the particle diameter for particle size k, and W represents the dimensions of the wall. Equation 7.2 incorporates all of the available experimental data with as much detail as is justified. While data on $\Delta T_{i,j}$ are available hourly for each study day, values of K_{e_j} and u_{∞_j} as a function of time of day must be estimated from the results of the single day experiments depicted in Figure 7.1. The predictions would be more accurate if information were available on the variation of indoor aerosol concentration with time of day and on the variation of the turbulence intensity or freestream air velocity from day to day during the study period.

Table 7.4. Air flow regimes used in calculating particle deposition velocities. [a]

	Case A	Case B	Case C
Getty Museum	NC(00-08;18-24) T(08-18)	T	NC(00-08;18-24) L(08-18)
Norton Simon Museum	L	T	-
Scott Gallery	L	T	-
Sepulveda House	NC(00-10;15-24) T(10-15)	T	-
Southwest Museum	T	-	-

[a] T ⇒ homogeneous turbulence; NC ⇒ natural convection; L ⇒ forced laminar flow. Parentheses, where present, contain time of day (hours) over which indicated condition applies; otherwise, the condition holds at all times.

7.7 Comparing Modeling and Measurement Results

Figure 7.3 presents a comparison of particle deposition velocity predictions and measurements for each of the five study sites. A full discussion of the experimental data is provided elsewhere (Ligocki et al, 1988a); key points are summarized here. While the bulk sulfate deposition data are shown as a horizontal bar over the diameter range 0.3-1.0 μm, it is noteworthy that the Los Angeles outdoor sulfate aerosol size distribution typically peaks strongly within the diameter range 0.5-0.7 μm. The vertical bars for deposition velocities measured by single-particle analysis reflect estimates of the measurement uncertainty, incorporating factors such as the effect of substrate differences between air samples and deposition plates, and statistical variation due to the small numbers of particles detected. The particle concentrations within the Norton Simon Museum were very low. A statistically significant number of particles were detected on the mica plate for only two size ranges at this site, and the sulfate data are based on measurements near the detection limit.

Considering the predictions alone, the highest particle deposition velocities are obtained for the homogeneous turbulence air flow regime and the lowest values are obtained for the laminar, forced flow regime. For any particle size, the differences in deposition velocities among sites for a given flow regime are generally smaller than the differences that would occur for alternative flow regimes at a given site. This observation can be explained as follows. For a given flow regime, the deposition velocity varies as u_∞^n, with $n \leq 1$. The average near-wall air velocities for the five sites vary only over a narrow range—less than a factor of three. However, for a given near-wall mean velocity, particle transport to the surface is much more rapid—characteristically an order of

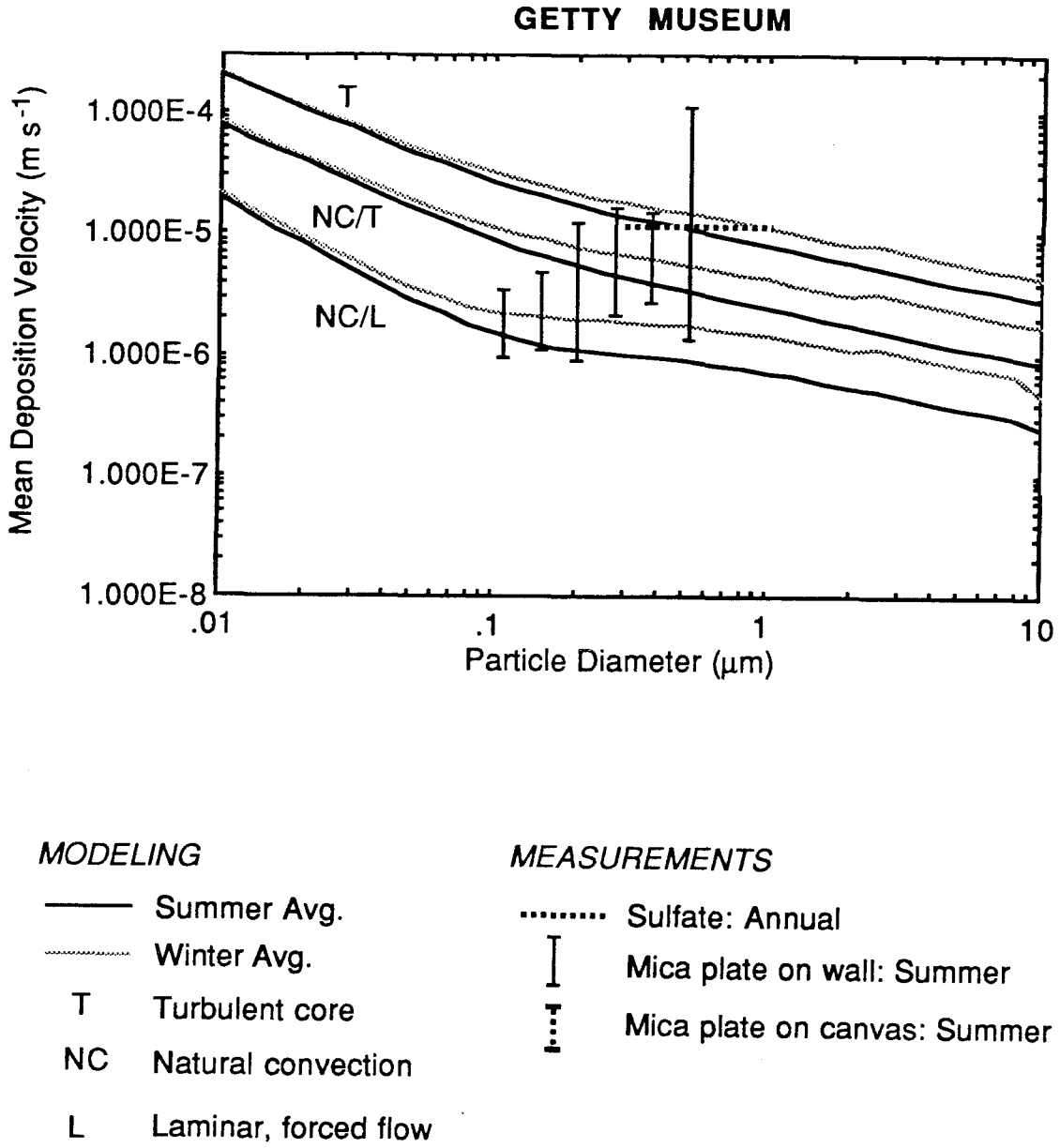

Figure 7.3 Comparison of predicted and measured particle deposition velocities vs. particle diameter for the five study sites. See Table 7.3 for definition of the air flow regimes studied. The experimental results from the mica plates are based on preliminary analyses. It is expected that the corresponding vertical bars will be smaller when the analyses are complete.

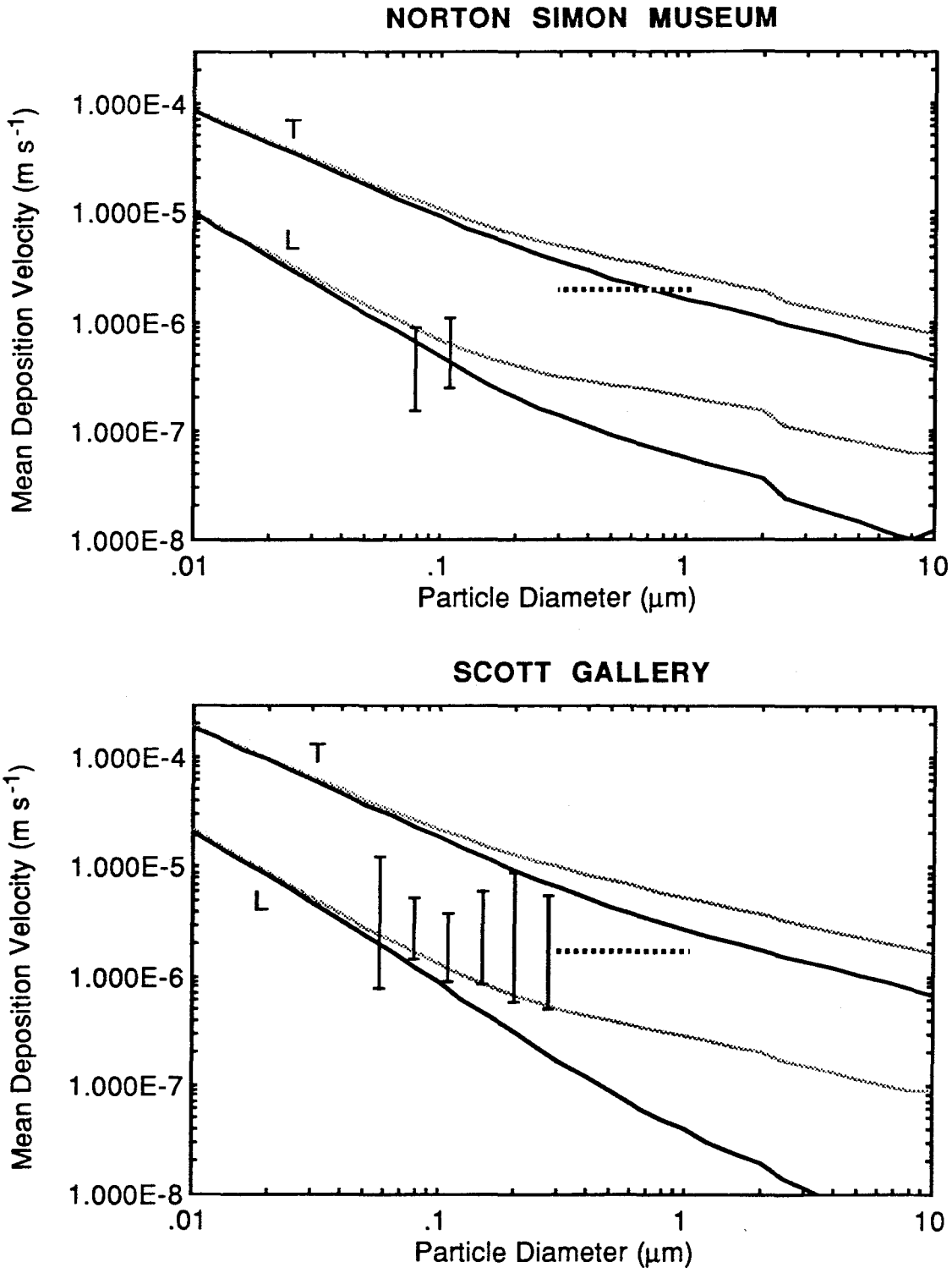

Figure 7.3 (cont.)

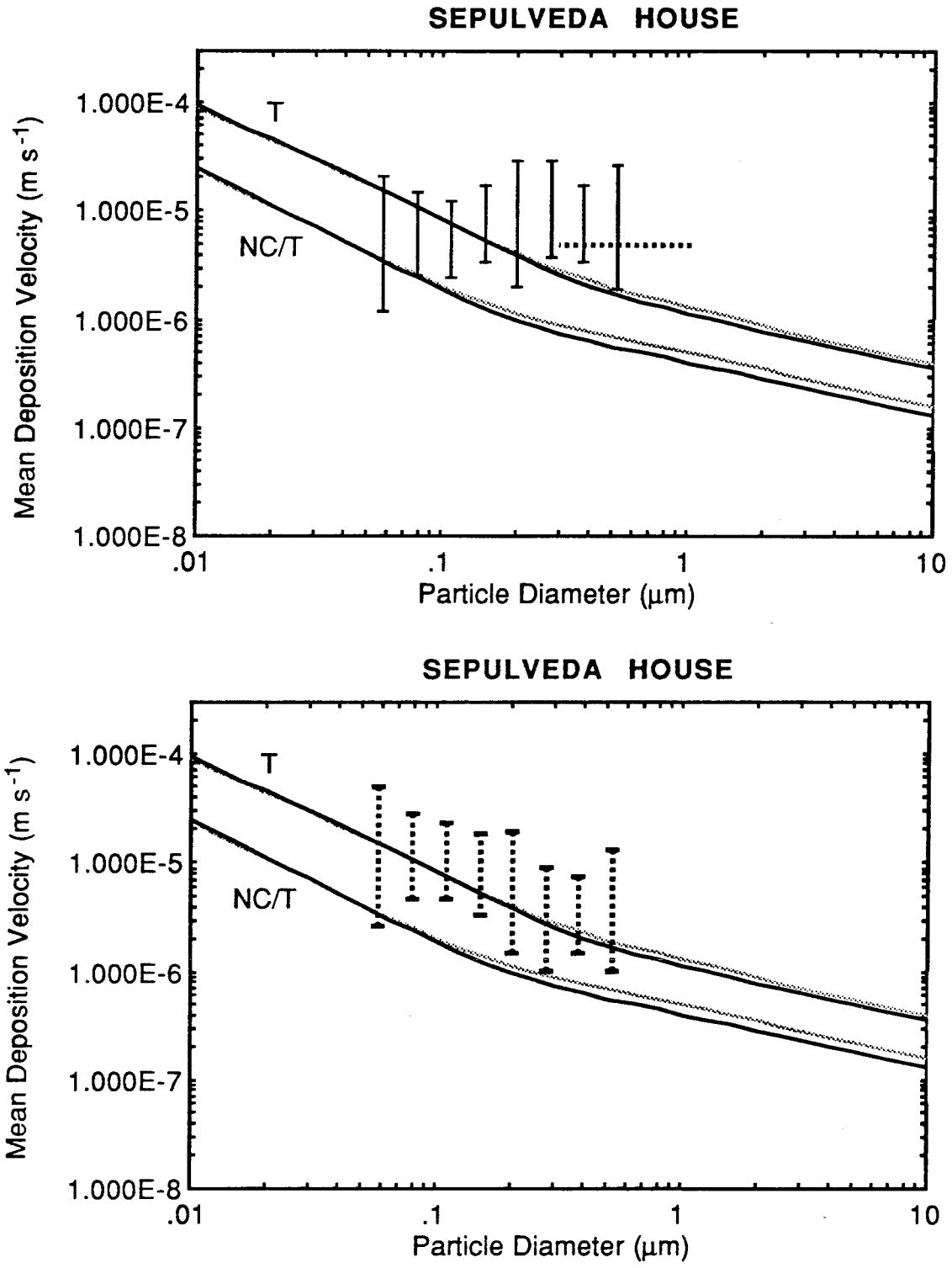

Figure 7.3 (cont.)

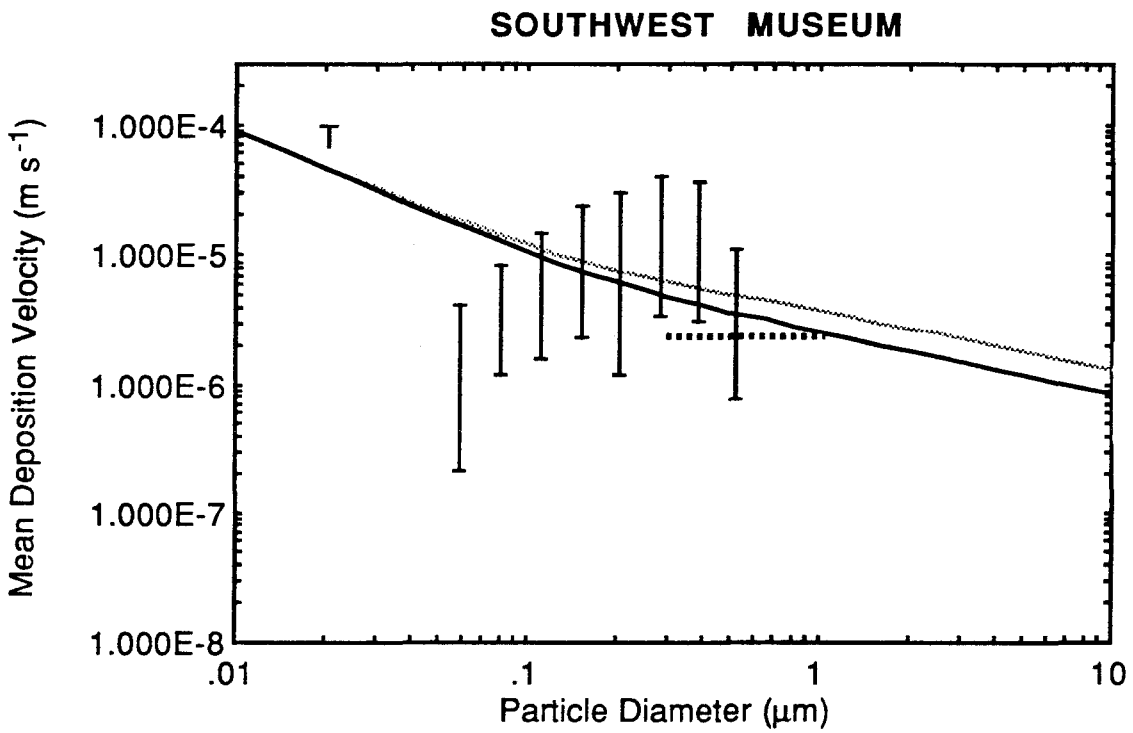

Figure 7.3 (cont.)

magnitude—for the homogeneous turbulence flow regime, due to the contribution of eddy diffusion, than for the laminar forced flow regime.

The differences between predictions for winter and summer arise from the thermophoretic effect. Seasonal differences are greatest at the Norton Simon Museum and at the Scott Gallery where the mean value of $T_{wall} - T_{air}$ changes sign from summer to winter.

The available information on the factors driving air flow and the corresponding comparison between measured and predicted particle deposition velocities may be combined to serve as a basis for deciding on the most likely flow regime for particle deposition onto the wall studied at each site. Our appraisal of the information produces the following results: Getty Museum—homogeneous turbulence from 0800-1800 hours and natural convection at other times; Norton Simon Museum—laminar forced flow; Scott Gallery—geometric mean of homogeneous turbulence and laminar forced flow; Sepulveda House—either homogeneous turbulence at all times or homogeneous turbulence during 1000-1500 hours daily with natural convection at other times; Southwest Museum—homogeneous turbulence. "Best-estimate" values of particle deposition velocity as a function of particle size, obtained from modeling predictions for these flow regimes, are presented for several particle sizes in Table 7.5. The range of deposition velocities among sites for a given particle size is approximately 15-30.

Further discussion is warranted of the comparison between measurement results and the predictions corresponding to the "best-estimate" values. At the Getty Museum and at the Southwest Museum, measurement results for the smallest two particle size ranges shown are lower than the predicted values. The measurement of particles in these size ranges may have larger uncertainty than reflected in the error bars. A large evaporative loss of very fine particles may occur during vapor deposition of carbon onto a sample in preparation for SEM analysis. If the losses are not constant from one sample to another, then the measured deposition velocity will be inaccurate in general. Since the

Table 7.5 Best estimate values of the annual-average particle deposition velocity ($\times 10^{-6}$ m s^{-1}) to the wall studied at each museum site. [a]

d_p (μm)	Southwest Museum	Getty Museum	Sepulveda House	Scott Gallery	Norton Simon Museum
0.05	20	17	4.1-18	10.1	1.3
0.1	11	10	2.0-8.4	4.7	0.6
0.2	7.0	6.6	1.1-3.9	2.3	0.3
0.5	4.3	4.4	0.6-1.8	1.2	0.2
1.0	3.1	3.3	0.5-1.2	0.8	0.1

[a] Obtained as the mean predicted deposition velocity for summer and winter periods, using the following flow regimes: Southwest Museum - T; Getty Museum - NC/T; Sepulveda House - range of values with lower limit corresponding to NC/T and upper limit corresponding to T; Scott Gallery - geometric mean of L and T; Norton Simon Museum - L. See Table 7.3 for definition of flow regimes.

measurement is based on the ratio of particles detected on only one deposition plate to those detected on several filter samples, the occurrence of a large error is more likely to yield too low a result than one that is too high.

At the Norton Simon Museum, the deposition velocity data based on single particle analysis agree well with predictions for forced laminar flow. This flow regime is consistent with the general flow conditions in that building: air is discharged into the galleries through perforated ceiling tiles and returned to the mechanical ventilation system at low velocity through the hallways. The measured deposition velocity for sulfates is higher than that resulting from single particle analysis, even though the sulfates are probably associated with larger particles that should have a smaller deposition velocity. Information about the size distribution of sulfates within this museum is lacking; furthermore, because of the low sulfate concentrations generally present in this museum, the sulfate deposition velocity is based on samples that are close to the detection limit.

At the Scott Gallery and at the Sepulveda House, the agreement between "best-estimate" predictions and measurements is very good. The agreement is excellent for the deposition plate mounted on a stretched canvas frame at the Sepulveda House.

There is a tendency throughout the data for the measured deposition velocities to exhibit less of a decrease with particle size than predicted for any of the flow regimes. As discussed above, the evaporative loss of the smallest particles studied during carbon coating could lead to a downward bias in the measurement results for small particle sizes at some sites. In addition, the finite thickness of the deposition plates could produce a higher average deposition velocity for large particles than predicted for a flat plate in forced laminar or natural convection flow. In the experiments, a characteristic thickness of the mica plate plus the layer of thermal joint compound was 0.25 mm. The momentum and thermal boundary layers would not be severely disturbed by the presence of the mica plate, since they have a characteristic dimension that is the order of a centimeter.

However, referring to Chapter 3, Table 3.2 for the case of natural convection flow, the thickness of the particle concentration boundary layer for particle diameters in the range 0.1-1 μm and temperature differences in the range -1 to 1 K are in the range 0.02-0.6 mm. Thus, as air flowing along the wall passes the mica plate, its presence creates a disruption of the particle concentration boundary layer. The net effect is to increase the deposition velocity, and because the boundary layer thickness decreases with increasing particle size, the increase in deposition velocity to the mica plate relative to the flat wall is greater for larger particle sizes.

7.8 Conclusion

Relative to previous studies, the work reported in this paper constitutes a stringent comparison of predicted and measured rates of particle deposition onto indoor surfaces. The emphasis has been on particles with diameters in the range 0.05-1 μm. These particles pose a significant soiling hazard for indoor surfaces, because most of the elemental carbon that is responsible for the blackness of the atmospheric aerosol (Cass, et al., 1984) is found in these sizes (Ouimette, 1981).

Deposition velocity predictions were based on long-term measurements of surface-air temperature differences, shorter-term measurements of near-wall air velocities, and idealized representations of the complex air flow fields. The predictions were compared against the deposition velocity measurements of Ligocki et al. (1988a) which were taken under conditions where low deposition velocities mandated many weeks for sample collection, and even then it was necessary to analyze individual particles using state-of-the-art measurement tools to obtain data on the size dependence of the deposition velocity. These constitute challenging conditions for obtaining accurate results from either approach. Consequently, the general concurrence of modeling and measurement results is encouraging. In those cases where the range of measured deposition velocity values overlaps the predictions for alternative air flow regimes, further work is required to

refine both the measurement and modeling methods. To this end, the deposition-velocity measurement technique based on single-particle analysis should be tested under controlled conditions that produce a deposition velocity that can be confirmed by other means. Further studies into the nature of near-wall air flow in buildings is also strongly recommended as a basis for improving numerical simulations of particle deposition. With the present work as a foundation, understanding the hazard posed to works of art due to the deposition of airborne particles can be greatly improved. With roughly an order of magnitude difference in predicted deposition rates, depending largely on the air flow regime next to a wall, deliberate control of temperature and air flow conditions within a room can be added to other methods, such as particle filtration, as a tool for effectively suppressing soiling rates in museums.

7.9 Acknowledgements

Financial support for this work was provided through a contract with the Getty Conservation Institute. Additional support was received through graduate scholarships from the Switzer Foundation and the Air Pollution Control Association, and through summer undergraduate research fellowships from Caltech. We thank Harvey Liu, Mike Jones, Theresa Fall, Lynn Salmon, and Paul Solomon for their assistance in obtaining the experimental data. The SEM analyses were carried out at the Air and Industrial Hygiene Laboratory of the California Department of Health Services, Berkeley, California. The active support and cooperation of the staffs of the five study sites is gratefully acknowledged.

7.10 References

Camuffo, D. (1983) Indoor dynamic climatology: Investigations on the interactions between walls and indoor environment, *Atmospheric Environment* **17**,1803-1809.

Cass, G. R., Conklin, M. H., Shah, J. J., Huntzicker, J. J., and Macias, E. S. (1984) Elemental carbon concentrations: Estimation of an historical data base, *Atmospheric Environment* **18**, 153-162.

Corner, J., and Pendlebury, E. D. (1951) The coagulation and deposition of a stirred aerosol, *Proceedings of the Physical Society (London)* **B64**, 645-654.

Dietz, R. N., Goodrich, R. W., Cote, E. A., and Wieser, R. F. (1986) Detailed description and performance of a passive perfluorocarbon tracer system for building ventilation and air exchange measurements, in *Measured Air Leakage of Buildings*, Trechsel, H. R., and Lagus, P. L., eds., report ASTM STP 904, American Society for Testing and Materials: Philadelphia, pp. 203-264.

Gadgil, A. J. (1980) *On Convective Heat Transfer in Building Energy Analysis*, Ph. D. Thesis, University of California, Berkeley, California.

Gray, H. A., Cass, G. R., Huntzicker, J. J., Heyerdahl, E. K., and Rau, J. A. (1986) Characteristics of atmospheric organic and elemental carbon particle concentrations in Los Angeles, *Environmental Science and Technology* **20**, 580-589.

Kurabuchi, T., and Kusuda, T. (1987) Numerical prediction for indoor air movement, *ASHRAE Journal* **29(12)**, 26-30.

Ligocki, M. P., Liu, H. I. H., Cass, G. R., and John, W. (1988a) Measurements of particle deposition rates inside Southern California museums, to be submitted to *Aerosol Science and Technology.*

Ligocki, M. P., Salmon, L. G., Fall, T., Jones, M. C., Nazaroff, W. W., and Cass, G. R. (1988b) Characteristics of airborne particles inside Southern California museums, California Institute of Technology: Pasadena (manuscript in preparation).

Ouimette, J. (1981) *Aerosol Chemical Species Contributions to the Extinction Coefficient*, Ph.D. Thesis, California Institute of Technology, Pasadena, California.

Schiller, G. E. (1984) *A Theoretical Convective-Transport Model of Indoor Radon Decay Products*, Ph.D. Thesis, University of California, Berkeley, California.

Schlichting, H. (1979) *Boundary-Layer Theory* (seventh edn). McGraw-Hill: New York, pp. 315-321.

Talbot, L., Cheng, R. K., Schefer, R. W., and Willis, D. R. (1980) Thermophoresis of particles in a heated boundary layer, *Journal of Fluid Mechanics* **101**, 737-758.

CHAPTER 8

PROTECTING MUSEUM COLLECTIONS FROM SOILING DUE TO THE DEPOSITION OF AIRBORNE PARTICLES

8.1 Abstract

Objects in Southern California museums may become perceptibly soiled within periods as short as a year due to the deposition of airborne particles onto their surfaces. Methods for reducing the soiling rate include reducing the building ventilation rate, increasing the effectiveness of particle filtration, reducing the particle deposition velocity onto surfaces of concern, placing objects within display cases or glass frames, managing a site to achieve low outdoor aerosol concentrations, and eliminating indoor particle sources. A mathematical model of indoor aerosol dynamics and experimental data collected at an historical museum in Southern California are combined to illustrate the potential effectiveness of these control techniques. According to model results, the soiling rate can be reduced by at least two orders of magnitude through practical application of these control measures. Combining improved filtration with either a reduced ventilation rate for the entire building or low-air-exchange display cases is a very effective approach to reducing the soiling hazard in museums.

Nazaroff, W. W., and Cass, G. R. (1988) Protecting museum collections from soiling due to the deposition of airborne particles, to be submitted to *Atmospheric Environment*.

8.2 Introduction

An object may become soiled due to the deposition of airborne particulate matter onto its surface. Deposited particles that contain elemental carbon (soot) or soil dust are of particular concern because they absorb light that would otherwise be reflected from the surface to an observer. If enough light-absorbing particles accumulate on an object, its visual qualities may become perceptibly degraded.

Among objects that are at risk, works of art may deserve the greatest attention. Often these objects are valued solely for their visual qualities. The works themselves are irreplaceable, and the value of some pieces is extraordinarily large. Even modest rates of deterioration may lead to unacceptable cumulative damage over the centuries.

There is an awareness among museum conservators of the potential damage that may be caused to art objects due to air pollutant exposure in museums (Thomson, 1978). Recommended limits on indoor concentrations of some species have been issued (Baer and Banks, 1985). To achieve an indoor environment in which these stringent air quality criteria are met requires an aggressive control strategy. However, detailed information on the available control options and their potential effectiveness is limited. Such information is essential to the deliberate engineering of control measures to reduce the rate of soiling.

The aim of this chapter is to explore the options that are available to museum conservators to reduce soiling rates within museums. As a tool for discussing the control opportunities, a simplified version of the mathematical model described in Chapter 5 is developed. In its parametric form, this model captures the essential factors that govern the rate of soiling due to particle deposition onto many surfaces in a variety of buildings. The potential effectiveness of several control options—reducing ventilation, improving filtration, and reducing particle deposition velocities—is assessed by computing their effect on the soiling rate of surfaces in a specific Southern California museum—the

Sepulveda House. For these calculations, the complete indoor aerosol model of Chapter 5 is applied, using data on outdoor aerosol concentrations and building parameters from the experiments discussed in Chapter 6. Assessment of other control options—using display cases, managing a site to achieve low outdoor aerosol concentrations, and limiting indoor aerosol sources—shall be obtained through additional modeling calculations and measurement results for this site. The results demonstrate that the rate of soiling of surfaces may be reduced by two to three orders of magnitude relative to uncontrolled conditions through the application of practical control measures.

The work in this chapter complements a recent examination of control options for protecting works of art from damage due to atmospheric ozone (Cass et al., 1988). However, because the chemical and physical properties of soiling particles are distinct from those of reactive gases, the control options are somewhat different in the two cases, and the effectiveness of a particular control measure may be quite different.

8.3 Factors Governing the Soiling Rate of Indoor Surfaces due to Particle Deposition

In Chapter 5, a detailed mathematical model was developed to predict the time-dependent chemical composition and size distribution of indoor aerosols. That model accounts in detail for the effects of emission, filtration, ventilation, coagulation and deposition. As was shown in Chapter 6, the model is capable of making accurate predictions of the aerosol characteristics in Southern California museums based on building parameters and data on outdoor aerosol properties. Predictions of the rate of particle deposition onto surfaces in museums were shown to be reasonably consistent with measurement results (Chapter 7). In the present chapter, that model is applied to evaluate the effectiveness of control measures aimed at reducing the soiling rate. However, to clarify the discussion of potential control options, and to provide a basis for rapidly obtaining a rough estimate of their efficacy, a simplified mathematical model of

the soiling of indoor surfaces also will be stated by distilling from the detailed modeling calculations the essential factors that govern the rate of soiling.

Several approximations are employed for this purpose. First, only two chemical components of the aerosol—elemental carbon and soil dust—shall be considered. Elemental carbon is directly associated with the blackness of the atmospheric aerosol (Cass et al., 1984) and so is a major concern as a soiling agent. Soil dust contributes much of the brown color seen in coarse aerosol samples and thus may lead to soiling. Elemental carbon is predominantly found among fine particles with a mass-median diameter in the vicinity of 0.1 μm (Ouimette, 1981). Airborne soil dust, by contrast, occurs primarily as coarse particles, larger than 2 μm in diameter. (See, e.g., Chapter 6, Table 6.3.) Because of its relatively large size, the dominant mechanism for soil dust deposition indoors is gravitational settling onto surfaces with an upward orientation; the soiling of vertical and downward-facing surfaces by soil dust is generally small. On the other hand, the gravitational settling velocity of particles with 0.1 μm diameter is smaller than typical deposition velocities for particles of this size due to convective diffusion and thermophoresis; as a result, surfaces with any orientation may be soiled by the deposition of elemental carbon particles.

With this representation of the aerosol, three further assumptions are made to establish the simplified model. First, coagulation is not considered. It was shown in Chapter 6 that for the combination of particle concentrations and residence times commonly found in museums, coagulation has a minor influence on the indoor aerosol. Second, a characteristic value of particle deposition velocity to museum surfaces shall be employed for each component and for each surface. One source of such values is the detailed modeling calculations applied to three Southern California museums (Chapter 6), which yields the following range of results: for elemental carbon to ceilings—$(0.04\text{-}14) \times 10^{-6}$ m s^{-1}; for elemental carbon to walls—$(0.7\text{-}15) \times 10^{-6}$ m s^{-1}; and for soil dust to upward surfaces—$(4.7\text{-}7) \times 10^{-3}$ m s^{-1}. Third, since soiling is a relatively long-term

hazard, temporal variations in the parameters that affect the indoor aerosol are ignored; instead, results are computed for steady-state conditions.

Given these assumptions, the simplified model is developed as follows. The building is represented as a single well-mixed chamber, as shown schematically in Figure 8.1. A balance on aerosol mass yields equation (8.1) that applies to any single component, k, of the aerosol, where a component consists of a particular chemical species (e.g., elemental carbon or soil dust) in a defined particle size range:

$$V\frac{dC_{i_k}}{dt} = C_{o_k} f_{oi} + C_{o_k} (1-\eta_{ox_k}) f_{ox} + C_i (1-\eta_{ii_k}) f_{ii}$$

$$+ S_k - C_{i_k} \sum_j A_j v_{d_{jk}} - C_{i_k} (f_{oi} + f_{ox} + f_{ii}) \qquad (8.1)$$

where C_{i_k} and C_{o_k} are the indoor and outdoor concentrations of component k, respectively; f_{oi}, f_{ox} and f_{ii} are the rates of air flow associated with infiltration, introduction of outdoor air through the mechanical ventilation system, and recirculation, respectively; η_{ox_k} and η_{ii_k} are the removal efficiencies for component k by filters in the supply and recirculating ventilation line, respectively; S_k is the emission rate of component k into the indoor volume; A_j is the area of the jth surface; and $v_{d_{jk}}$ is the deposition velocity of component k onto the jth surface. A form of this equation was first derived by Shair and Heitner (1974), who applied it to the relationship between indoor and outdoor ozone concentrations. In the present formulation, equation 8.1 could be used to account for the complete chemical composition and size distribution of the indoor aerosol if a sectional representation of the aerosol size distribution is used.

Although the aerosol components may be expressed in terms of number concentration, conventional measurement techniques determine the mass concentration of the components, and so C_{o_k} and C_{i_k} shall be considered on this basis.

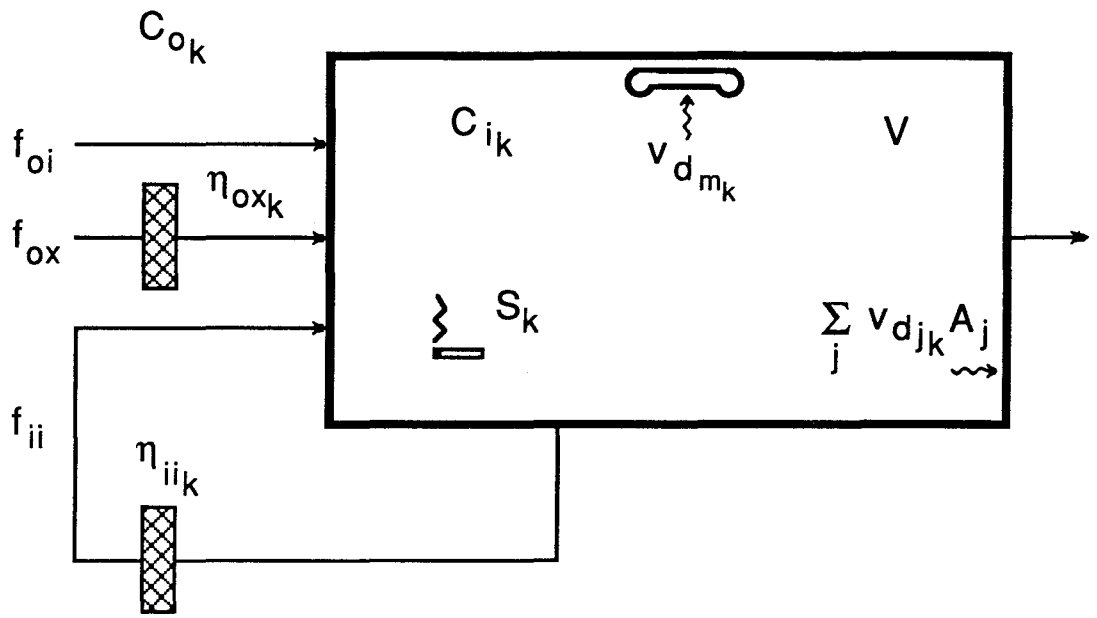

Figure 8.1 Schematic representation for a single-chamber mathematical model of the soiling rate.

If the time-varying parameters governing the indoor concentration of a soiling component (e.g., the air flow rates and the outdoor concentration) are not strongly correlated, then a good approximation to the long-term average concentration is given by the steady-state solution to equation 8.1:

$$C_{i_k} = C_{o_k} \frac{[f_{oi} + (1-\eta_{ox_k})\, f_{ox}] + \frac{S_k}{C_{o_k}}}{[\eta_{ii_k} f_{ii} + f_{oi} + f_{ox} + \sum_j A_j v_{d_{jk}}]} \tag{8.2}$$

The associated rate of mass accumulation per unit surface area onto a particular surface m, is given by

$$F_m = v_{d_{mk}} C_{i_k} \tag{8.3}$$

where $v_{d_{mk}}$ is the deposition velocity of particles of component k onto surface m. The rate of soiling is determined by the rate of effective area coverage of the surface. Studies have shown that a white surface is perceptibly darkened when 0.2% of its area is covered by either black dots that are too small to be seen individually (Carey, 1959) or by black particles (Hancock et al., 1976). The rate of effective area coverage of a surface due to particle deposition is related to the rate of mass accumulation by a conversion factor α. For spherical particles, $\alpha = 1.5\ (\rho\ d_p)^{-1}$, where ρ is the particle density and d_p is the particle diameter. For non-spherical particles, α has a higher value since these particles would tend to lie with their major axis oriented nearly parallel with the plane of the surface. However, for the purpose of evaluating the *relative* effectiveness of measures to control soiling it is reasonable to treat the particles as spheres. The rate of effective area coverage of surface m due to deposition of aerosol component k is then

$$\Psi_{m_k} = \frac{3}{2\rho\, d_p} v_{d m_k} C_{o_k} \frac{[f_{oi} + (1-\eta_{ox_k})\, f_{ox}] + \frac{S_k}{C_{o_k}}}{[\eta_{ii_k} f_{ii} + f_{oi} + f_{ox} + \sum_j A_j\, v_{d_{jk}}]} \qquad (8.4)$$

For the purposes of this chapter, a *characteristic time for soiling*, τ_s, associated with the accumulation of a soiling deposit will be taken as the time necessary to accumulate an effective surface area coverage of 0.2% by the particles of interest. It is recognized that the actual point at which soiling becomes perceptible may well depend on additional factors, such as the chemical composition and morphology of the particles and the optical properties of the real surface of interest. Since the light absorbing properties of elemental carbon differ from those of soil dust, the degree of surface coverage needed to produce perceptible soiling probably differs for the two components. The information needed to combine the accumulation of the two components into a single soiling rate is lacking, and so for now the control objective shall be to increase the value of τ_s associated with both soiling components k of the atmospheric aerosol for all surfaces of interest m to as great an extent as possible, where

$$\tau_{s_{m_k}} = \frac{0.002}{\Psi_{m_k}} \qquad (8.5)$$

In general, the use of the detailed mathematical model from Chapter 5 yields more accurate estimates than can be obtained from the simplified model developed in equations 8.1-8.5. However, in cases where a detailed computer-based model is unavailable, useful rough estimates of the effectiveness of some control measures may be obtained quickly by applying the simplified model.

8.4 Evaluating the Effectiveness of Measures to Control Soiling Inside Museums

In this section, methods for controlling soiling rates inside museums will be evaluated quantitatively using the indoor aerosol dynamics model of Chapter 5. That

model computes the total deposited mass of particles onto a given surface as a function of particle size and chemical composition, includes coagulation, and captures the full effect of the particle size distribution on deposition velocities and filtration efficiencies. As discussed in Chapter 6, the total rate of effective area coverage of a surface by a given aerosol component may be computed by summing the rates for that component over each size section. The characteristic time of soiling is then obtained as

$$\tau_{s_{m_k}} = 0.002\left[\sum_i \left(\frac{3}{2d_{p_i}}\right)\left(\frac{\Delta J_{i_{mk}}}{\rho}\right)\right]^{-1} \tag{8.6}$$

where i represents the particle size section, $\Delta J_{i_{mk}}$ is the rate of mass deposition of soiling component k in size section i onto surface m, and d_{p_i} is the particle diameter for section i, taken as the logarithmic mean for the section. In applying the model, characteristic soiling times are computed for the floor, the walls, and the ceiling. These results are indicative of soiling times for other exposed surfaces, such as those of art objects, with corresponding orientations.

A case study based on data taken at an historical museum in downtown Los Angeles will be presented for purposes of illustration. First, a retrofit of the building to add a conventional mechanical ventilation and particle filtration system will be analyzed. Then, further measures to control the rate of soiling of indoor surfaces will be considered.

8.4.1 Site Description and Baseline Soiling Conditions. The Sepulveda House is a two-story historic museum located on the grounds of El Pueblo de Los Angeles State Historic Park in downtown Los Angeles. The building has no mechanical ventilation or indoor climate control system. Air-exchange is provided by uncontrolled leakage through openings in the building shell. A large gap (~0.35 m^2 total area) around the perimeter of a carriage door downstairs, coupled with skylight vents in the upstairs ceiling, leads to a frequently strong buoyancy-driven flow through the building. The average (± one

standard deviation) of hourly air-exchange rates, measured by tracer-gas decay for a 24-hour period on 30-31 March 1988, is 3.6 (±1.4) h^{-1}.

Within a few city blocks of the downtown location of this museum are major aerosol sources, including the intersection of two major freeways, the main railroad station for Los Angeles, and numerous routes for diesel trucks and buses. The high concentrations of airborne particulate matter in outdoor air, in combination with the high air-exchange rate and lack of any particle filtration within the building, leads to high indoor particle concentrations, including the highest indoor elemental carbon and soil dust concentrations that we have observed from among the five museums that we have examined during this study (Ligocki et al., 1988). In turn, the rate of soiling of surfaces within this museum is large. Modeling calculations indicate that the deposition of elemental carbon particles onto walls would lead to perceptible soiling within a year (see Chapter 6). This prediction is confirmed by experimental measurements showing that the rate of color change of a white filter mounted on a wall within this site was sufficient to be perceptible within approximately 1.5 years (M. P. Ligocki, Caltech, personal communication, 1988). Soiling of upward-facing horizontal surfaces is even more rapid. Thus, the deposition of airborne particles constitutes a major soiling hazard for objects in this museum. Sepulveda House provides a challenging case against which the effectiveness of control options to reduce the soiling rate may be judged. This site is also very interesting as it may closely approximate the situation at many small, older, urban museums and churches in Europe and elsewhere.

For the purposes of this evaluation, detailed experimental results from the Sepulveda House on outdoor aerosol characteristics and factors governing particle deposition rates are used as input data to the indoor aerosol dynamics model. (See Chapter 6 for a discussion of these data.) The building parameters are changed for each case to reflect the successive adoption of control techniques (see Table 8.1). The characteristic soiling rate associated with each case is computed based on modeling

Table 8.1 Building conditions for modeling the effect of control measures at the Sepulveda House. [a]

Baseline Conditions

Case 1 No filtration or mechanical ventilation; mean infiltration rate: $f_{oi} = 1.2\ m^3\ s^{-1}$; deposition according to homogeneous turbulence 1000-1500 hours, mean turbulence intensity parameter: $K_e = 0.56\ s^{-1}$; deposition according to natural convection model 000-1000 and 1500-2400 hours, surface-air temperature difference as shown in Figure 6.3. See also Chapter 6.

Standard Mechanical Ventilation Retrofit

Case 2 Same as Case 1 with following exceptions: infiltration rate reduced: $f_{oi} = 0.06\ m^3\ s^{-1}$; mechanical ventilation added: $f_{ox} = 0.6\ m^3\ s^{-1}$ and $f_{ii} = 2\ m^3\ s^{-1}$; all air in mechanical ventilation system passed through filter with efficiency of 15-30% ($\eta_{ox} = \eta_{ii} = 0.15\text{-}0.3$), varying according to particle size as shown for Filter F_{B1} in Figure 6.2, Chapter 6.

Reduce Ventilation Rate

Case 3 Same as Case 2 with following exception: reduce mechanical ventilation make-up air flow rate to design occupancy while holding total flow rate constant: $f_{ox} = 0.167\ m^3\ s^{-1}$, $f_{ii} = 2.43\ m^3\ s^{-1}$, and $f_{oi} = 0.06\ m^3\ s^{-1}$.

Case 4 Same as Case 3 with following exception: eliminate mechanical ventilation make-up air flow when building is closed to public: $f_{ox} = 0.0$, $f_{ii} = 2.6\ m^3\ s^{-1}$, and $f_{oi} = 0.06\ m^3\ s^{-1}$ during 000-1000 and 1500-2400 hours.

Improve Filtration Effectiveness

Case 5 Same as Case 4 with following exception: improve filter efficiency: $\eta_{ox} =$ 0.99 for coarse particles ($d_p > 2\ \mu m$) and 0.88 for fine particles, and $\eta_{ii} = 0.95$ for coarse particles and 0.875 for fine particles.

Case 6 Same as Case 3 with following exceptions: improve filter efficiency: $\eta_{ox} =$ 0.99 for coarse particles ($d_p > 2\ \mu m$) and 0.88 for fine particles, and $\eta_{ii} = 0.95$ for coarse particles and 0.875 for fine particles; eliminate infiltration: $f_{oi} = 0.0$.

Reduce Particle Deposition Velocities

Case 7 Same as Case 6 with following exception: natural convection flow regime assumed to hold at all times for computing particle deposition rates with $T_{surface} - T_{air} = 1\ K$.

Table 8.1 (Cont.)

Case 8	Same as Case 6 with following exception: laminar forced flow regime assumed to hold at all times for computing particle deposition rates with free stream air flow rate and surface-air temperature differences corresponding to conditions at Norton Simon Museum, Case A, in Chapter 6.

[a] Basic building data: volume = 1200 m^3; floor area = 330 m^2; wall area = 1050 m^2. Air flows (f_{oi}, f_{ox}, and f_{ii}) and filtration efficiencies (η_{ox} and η_{ii}) are defined in the text and illustrated schematically in Figure 8.1.

calculations for a 24-hour period beginning on 30 March 1988 at 2100 hours PST, with input data provided on an hourly averaged basis. The 24-hour average outdoor aerosol size distribution and chemical composition is presented in Figure 8.2. For this day, the total mass concentration of elemental carbon associated with fine particles was 5.0 μg m^{-3}, essentially the same as the annual mean for this site (see Table 8.2). Most of the mass of elemental carbon particles is in the size range 0.05-0.2 μm. The total mass concentration of coarse particle soil dust on this day was 41 μg m^{-3}, three times larger than the annual mean value for this site. The characteristic times for soiling associated with soil dust, based on the 30-31 March 1988 data, are therefore larger than those that would result from annual-average conditions; assuming that the size distribution is unchanged, results for the annual mean conditions may be obtained by linear scaling. Information on the time dependence of the outdoor aerosol concentration may be found in Figure 8.3 and in Chapter 6, Figure 6.4.

For the baseline conditions, the rates of particle deposition onto indoor surfaces are computed as in Chapter 6: homogeneous turbulence in the core of the building is assumed to govern deposition rates during 1000-1500 hours, when the museum is open to the public, and natural convection flow adjacent to the surfaces is assumed to govern deposition rates at other times.

The indoor air quality model of Chapter 5 was run for base case uncontrolled conditions at the Sepulveda House, and the results are reported in Chapter 6 (see Figure 6.4 and Table 6.3). It was found that the characteristic soiling times are three days for the accumulation of a perceptible deposit of soil dust on upward facing surfaces, and 0.9 and 1.5 years, for the accumulation of a perceptible deposit of elemental carbon particles on walls and ceilings, respectively (see Chapter 6, Table 6.5, and Table 8.3).

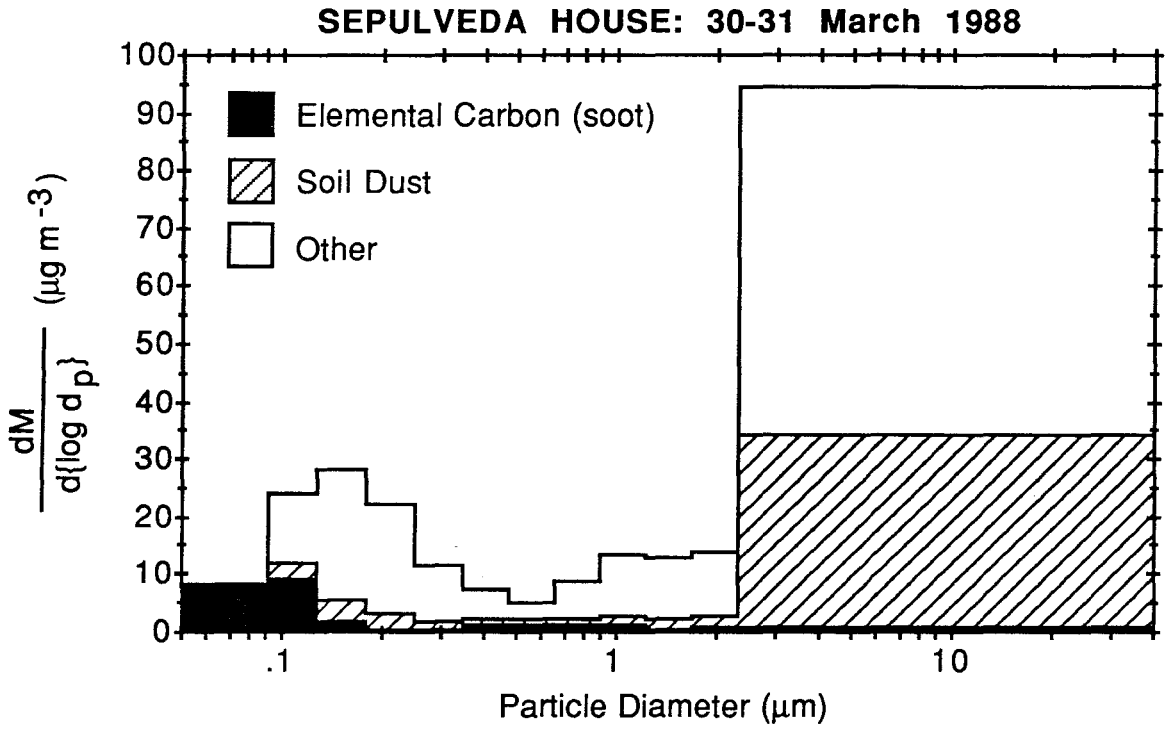

Figure 8.2 Average outdoor aerosol size distribution and chemical composition measured on the second floor balcony of the Sepulveda House in downtown Los Angeles. Measurements were conducted over a 24-hour period beginning on 30 March 1988 at 2100 PST.

Table 8.2. Mean outdoor concentrations ($\mu g\ m^{-3}$) of aerosol components measured at museum sites in Southern California

City	Museum	Fine elemental carbon			Coarse soil dust		
		Summer [a]	Winter [b]	Mean	Summer [c]	Winter [d]	Mean
Malibu	Getty Museum	0.3	1.3	0.8	5.8	5.9	5.9
Los Angeles [e]	Sepulveda House	2.6	7.3	4.9	15.0	9.8	12.4
Los Angeles [f]	Southwest Museum	1.5	3.3	2.4	17.2	22.0	19.6
Pasadena	Norton Simon Museum	1.5	3.3	2.4	12.3	12.5	12.4
San Marino	Scott Gallery	1.3	2.8	2.1	20.3	12.9	16.6

[a] Average of 10-11 24-hour samples collected at six-day intervals during 2 July - 31 August 1987.

[b] Average of 12 24-hour samples collected at approx. six-day intervals during 23 November 1987 - 28 January 1988.

[c] Average of 9-11 24-hour samples collected during 2 July - 31 August 1987.

[d] Average of 5-9 24-hour samples collected during 23 November 1987 - 28 January 1988.

[e] Located in the downtown area.

[f] Located in Highland Park, roughly 10 km north of downtown.

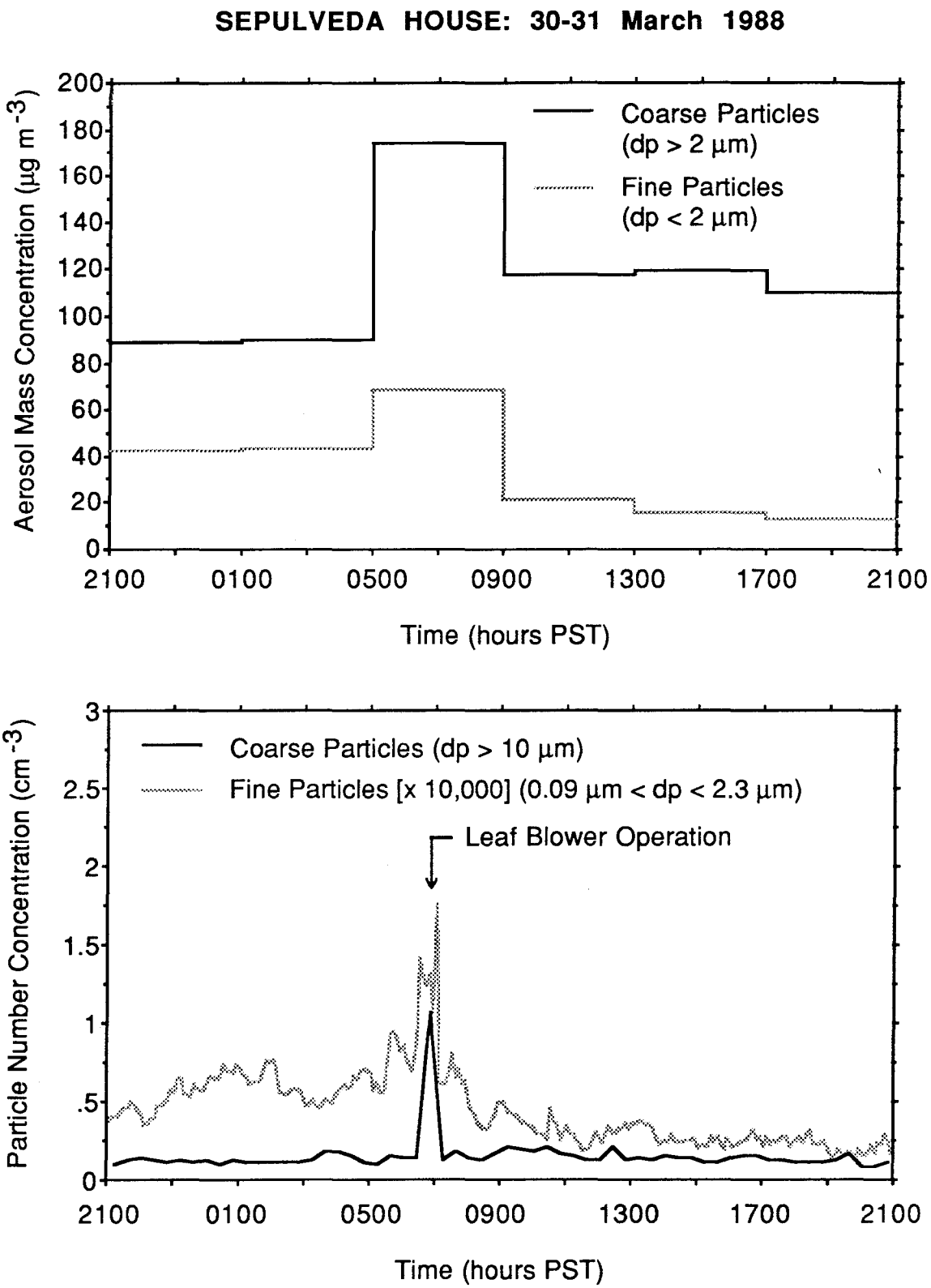

Figure 8.3 Outdoor aerosol mass concentration and particle number concentration vs. time at the Sepulveda House in downtown Los Angeles. Measurements were made on the second floor balcony.

Table 8.3 Predicted effect of control measures for reducing soiling rates at the Sepulveda House resulting from the deposition of soil dust (SD) and elemental carbon (EC) particles onto indoor surfaces.[a]

	Aerosol Conc. ($\mu g\ m^{-3}$)				Mass Deposition Rate ($\mu g\ m^{-2}\ day^{-1}$)						Characteristic Soiling Time (y)					
	Coarse		Fine		Floor		Walls		Ceiling		Floor		Walls		Ceiling	
Case	SD	EC	SD	EC	SD	EC	SD	EC	SD	EC	SD	EC	SD	EC	SD	EC
Outdoor	41.6	1.34	2.51	4.92												
1	14.4	0.49	2.47	4.92	8500	280	0.70	0.69	0.32	0.40	0.01	0.2	4.1	0.9	6.2	1.5
2	6.3	0.21	1.18	2.79	3600	118	0.32	0.41	0.15	0.24	0.02	0.3	7.8	1.4	12	2.4
3	2.71	0.093	0.62	1.59	1400	47	0.16	0.24	0.077	0.14	0.05	0.7	14.3	2.4	21	4.0
4	1.49	0.052	0.33	0.74	680	23	0.14	0.18	0.074	0.13	0.10	1.2	16.6	3.3	23	4.5
5	0.46	0.015	0.069	0.13	350	11	0.022	0.021	0.010	0.013	0.24	4.8	126	29	190	45
6	0.014	0.0007	0.022	0.043	9.9	0.41	0.003	0.006	0.002	0.003	7.4	34	490	100	740	170
7	0.016	0.0008	0.022	0.043	8.5	0.31	0.000	0.003	0.000	0.000	10	90	3100	220	---	---
8	0.016	0.0008	0.022	0.043	8.5	0.32	0.001	0.003	0.000	0.001	10	48	1650	180	---	930

[a] Outdoor aerosol properties and baseline data on building characteristics measured over 24-hour period beginning at 2100 hours PST on 30 March 1988.

8.4.2 Preliminary Renovation: Adding a Conventional Mechanical Ventilation and Particle Filtration System. To achieve reduced soiling rates for all surfaces within the building, the first step considered is the addition of a mechanical ventilation system with particle filtration. The parameters of this first system studied, summarized in Table 8.1 (Case 1), are taken to reflect the properties of a typical installation in a modern commercial building. To achieve the retrofit, the rate of uncontrolled leakage of air into the building must be reduced. Closing the skylight vents and the large perimeter gaps around the downstairs carriage doors would substantially reduce the effective leakage area of the building shell. Air flow through other leakage pathways also can be reduced. A conventional mechanical ventilation system would be designed to operate with the building at a slightly higher air pressure than outdoors, so that most of the air entering the building would pass through the mechanical ventilation system, rather than through the remaining leaks and openings in the building shell. However, some uncontrolled leakage into the building is likely to persist, for example, due to the opening of doors as visitors enter the museum.

For the baseline retrofit assumptions, the mechanical ventilation system provides 1.8 building volumes per hour of outdoor air, which constitutes 23% of the total air flow rate through the mechanical ventilation system, the remainder being recirculated from the building itself. The rate of uncontrolled air leakage into the building is taken to be 10% of the outdoor air supply rate of the mechanical ventilation system, or 0.18 building volumes per hour. All of the air handled by the mechanical ventilation system, both make-up and recirculated, passes through a fibrous mat filter with filtration efficiency characteristics corresponding to the filters presently used at a new museum in the Los Angeles area (Scott Gallery, Filter F_{B1}, see Chapter 6, Figure 6.2), i.e., 15-35% removal, depending on the particle size.

Model calculations show that the installation of such a mechanical ventilation and particle filtration system would lead to a moderate improvement in the characteristic soiling times (Table 8.3). The accumulation of either soil dust or elemental carbon particles onto upward-facing surfaces still would lead to perceptible soiling in a period of less than three months. Characteristic times for perceptible soiling of walls and ceiling due to deposition of elemental carbon particles would be extended to only 1.4 and 2.4 years, respectively.

Clearly, a conventional air conditioning system at this location would be insufficient to control the soiling problem. Measures that lead to more dramatic improvements in the characteristic times before soiling becomes apparent are discussed in the following subsections.

8.4.3 Evaluation of the Effectiveness of Further Control Measures

Examination of equation 8.4 reveals several control opportunities to reduce the rate of soiling, Ψ_{m_k}. These may be grouped into five categories: (1) reducing ventilation rates (making $f_{oi}+f_{ox}$ small); (2) improving particle filtration (making η_{ox_k} and/or η_{ii_k} large); (3) reducing the deposition velocity to the surface to be protected (making $v_{d_{m_k}}$ small); (4) limiting indoor aerosol sources (making S_k small); and (5) managing a site in a way that maintains lowered outdoor aerosol concentrations (making C_{o_k} small). An additional control option is (6) to use display cases or framing to reduce the rate of particle deposition onto the surfaces of an art object.

In this section, the effect of applying these control measures for the Sepulveda House case study is considered. The first three measures are applied as further measures to improve the soiling-control performance of the preliminary renovation discussed in Section 8.4.2. The last three measures are considered independently, without presuming the existence of a mechanical ventilation system for the building.

8.4.3.1 Reducing ventilation rates. In the absence of significant indoor emissions, the indoor concentration of airborne particles, and consequently the soiling rate, may be reduced by lowering the rate at which outdoor air enters the museum. The effect of reducing the outdoor air-exchange rate from the nominal value for the conventional mechanical ventilation system design stated in Section 8.4.2 thus will be examined. In adopting this control measure, it is necessary to ensure that adequate ventilation is provided for the occupants of the building. The recommended lower limit for the supply of outdoor air to a building is 8.5 $m^3\ h^{-1}\ person^{-1}$, based on the need to prevent CO_2 accumulation due to the building occupants (ASHRAE, 1985). In a system where the building is pressurized relative to outdoors, the flow rate of the mechanically induced outdoor air supply must exceed the mechanically induced exhaust flow rate, e.g., from restrooms. Furthermore, reducing the supply rate will reduce the degree to which the building operates at a higher air pressure than outside. To avoid concomitantly increasing the infiltration rate it may be necessary to reduce further the leakiness of the building shell.

The occupancy of a museum gallery may be highly variable. With many conventional mechanical ventilation systems, the rate of supply of outdoor air is fixed according to the size of the building to a level sufficient for the maximum expected occupancy. If, instead, the ventilation rate were varied according to the actual occupancy, the average ventilation rate would be much lower, and the rate of soiling could be considerably reduced. Outdoor air supply rates are generally controlled by the position of dampers at the inlet register. By equipping the inlet register with dampers that are easily adjusted, the ventilation rate could be changed in response to changing occupancy.

Model predictions of characteristic soiling times indicate the reduction in soiling rates that can be achieved by reducing outdoor air-exchange rates. Two cases will be examined, defined as Cases 3 and 4 in Table 8.1. For Case 3, the baseline retrofit mechanical ventilation system is retained, but the outdoor air make-up flow rate is

reduced to a constant lower level (f_{ox} = 0.167 m^3 s^{-1}). This flow rate corresponds to 8.5 m^3 h^{-1} $person^{-1}$ at a design occupancy of 20 persons per 1000 square feet of floor area. In Case 4, the reduced make-up flow rate stated for Case 3 is used during the hours when the museum is open to the public, but it is assumed that the intake dampers are closed at other times of the day. The mechanical ventilation system fans continue to operate, causing air recirculation through the particle filters. Table 8.3 indicates that these measures extend the characteristic soiling times to 0.05-0.1 y for soil dust settling on upward-facing surfaces and to a range of 2-5 years for elemental carbon deposition on the walls and ceiling.

Benefits beyond reduced soiling rates may be realized by implementing this control measure. Reducing the ventilation rate reduces operating costs by lowering the amount of energy required to control the indoor air temperature and relative humidity. An improvement in the stability of indoor air temperature and relative humidity may also be realized, which will reduce the mechanical stresses experienced by objects that would otherwise expand and contract as temperature and relative humidity fluctuate. Improved climate control therefore constitutes an important additional benefit toward preservation of the museum collection.

8.4.3.2 Improving particle filtration. Indoor particle concentrations may be reduced by improving the particle filters that are otherwise customarily specified for commercial air conditioning systems. The filters found in many conventional mechanical ventilation systems are designed primarily to protect the ventilation system components, rather than to provide a deliberately controlled level of air pollution in the indoor environment. The air filters commonly used in commercial buildings are generally efficient at removing very large particles from the air stream, but have only a modest single-pass efficiency (commonly 20-30%) for removing fine particles, such as those containing elemental carbon.

The efficiency of commercial air filters is commonly specified according to one or more of three rating tests. The "synthetic dust weight arrestance" rating refers to the effectiveness of a filter in removing suspended mass of a coarse artificial dust from an air stream (ASHRAE, 1976). The "atmospheric dust spot efficiency" rating refers to the effectiveness of a filter in reducing the opacity of atmospheric particulate matter (ASHRAE, 1976). The "DOP efficiency" rating refers to the effectiveness of the filter in removing from an air stream liquid droplets of dioctyl phthalate having an approximate median diameter of 0.3 μm (United States Department of Defense, 1956).

Fibrous air filters may be obtained with a wide range of rated particle removal efficiencies. A recent discussion of the efficiency of particle filters used in general ventilation applications (Rivers, 1988) indicates that the least effective filters commonly employed (home furnace, room air-conditioner) have an atmospheric dust spot efficiency of 20-25%. Rigid, pleated paper filters and pocket bag filters have an atmospheric dust spot efficiency of 60-95%. High efficiency particle (HEPA) filters with a 99.97% DOP efficiency rating also are available. An important consideration in selecting an air filter is its resistance to air flow, which generally increases with increasing filtration efficiency. The design choice involves balancing the goal of removing particles from the air against the additional equipment and operating cost of high filtration efficiency.

In addition to fibrous filters, an electrostatic precipitator may be used to remove particles from an air stream. These devices operate with much lower pressure drop than a fibrous filter; however, they may be a source of ozone (Sutton et al., 1976; Allen et al., 1978).

The effect on soiling rates of incorporating higher efficiency filters into the baseline retrofit mechanical ventilation system at the Sepulveda House (along with reduced outdoor air flow conditions) is considered in Cases 5 and 6 (see Table 8.1). The particle removal efficiencies adopted in this example—0.99 for coarse particle removal by the intake filter (η_{ox}), 0.95 for coarse particle removal by the filter in the recirculating

line (η_{ii}) and 0.875 for fine particle removal by both filters—represent the minimum dust weight arrestance and dust spot efficiency, respectively, recently specified in a draft ANSI standard for the storage of library and archival documents (ANSI, 1985; see also Baer and Banks, 1985, and Committee on Preservation of Historical Records, 1986). To achieve these overall efficiencies, a sequence of several filters of progressively higher efficiency is recommended (see ANSI, 1985). Results for Case 5 (Table 8.3) indicate that the characteristic soiling time associated with soil dust settling on upward surfaces is increased to 3 months, and that the soiling time associated with elemental carbon deposition on the walls and ceiling is extended to 30-45 y.

For high efficiency filtration to be effective, it is essential that the leakage of untreated air directly into the building be reduced to the greatest extent possible. This is demonstrated by comparing the results for Cases 5 and 6. The most signifant difference between these cases is that infiltration is entirely eliminated in Case 6. With this combination of high filter efficiency, no infiltration, and low rate of outdoor air supply, the characteristic times before soiling would become apparent are increased by more than two orders of magnitude relative to the base case assumptions (see Table 8.3).

In historical buildings and other sites that lack a mechanical ventilation system, air filtration may still be provided to reduce somewhat the rate of soiling due to fine particle deposition. Unducted console units designed to filter the air in a single room are commercially available. The more effective of these devices combine an efficient air filter with a fan, and are capable of removing 0.45 μm diameter particles from air at an effective rate (corresponding to the product $\eta_{ii}\, f_{ii}$) of 100-300 $m^3\, h^{-1}$ (Offermann et al., 1985). For a building lacking both mechanical ventilation and significant indoor sources of particles, the concentration of a component of the indoor aerosol may be estimated from a simplified form of equation 8.2:

$$C_{i_k} = C_{o_k} \frac{f_{oi}}{[\eta_{ii_k} f_{ii} + f_{oi} + \sum_j A_j v_{d_{jk}}]} \tag{8.7}$$

It is clear from this equation that the introduction of a recirculating filtration device will substantially reduce C_{i_k} only if the effective filtration rate, $\eta_{ii} f_{ii}$, is significantly greater than the sum of the ventilation rate, f_{oi}, and the total particle deposition rate, $\sum A_j v_{d_{jk}}$. This condition will seldom be met for coarse particles (because the coarse particle deposition rate is so high), but may be achieved for fine particles if the infiltration rate is low. Consider, for example, a room having plan dimensions of 8 m × 12 m, a ceiling height of 3 m, and an average infiltration rate of 0.3 h^{-1}, so that f_{oi} = 86 m^3 h^{-1}. Assume, for the purposes of illustration, that the particle deposition velocities are near the middle of the range corresponding to typical conditions in Southern California museums: 5×10^{-3} m s^{-1} for soil dust onto upward surfaces and 2×10^{-6} m s^{-1} for elemental carbon particles onto all surfaces. Then, $\sum A_j v_{d_{jk}}$ has a value of 2.3 m^3 h^{-1} for fine elemental carbon particles and 1700 m^3 h^{-1} for coarse soil dust particles. If a console filtration unit having $\eta_{ii} f_{ii}$ = 300 m^3 h^{-1} for both fine and coarse particles is introduced into the room, the concentration of fine particles will be reduced to 23% of the prior value, but the concentration of coarse particles only will be reduced to 86% of the value in the absence of the filtration unit. Thus, the soiling rate of vertical and downward-facing surfaces would be reduced by approximately a factor of four. This improvement is not large relative to the potential improvement of two orders of magnitude for a high efficiency, low outdoor-air exchange, ducted ventilation and filtration system. However, employing an unducted filtration unit at least provides some improvement in cases where finances will not permit a complete building retrofit.*

* A HEPA filter unit with $\eta_{ii} f_{ii}$ = 300 m^3 h^{-1} was commercially available for $400 in 1983; replacement filters cost $80; and the unit consumed less than 70 W of power (Offermann et al., 1985). The reader is cautioned that not all devices marketed as air cleaners are effective. Five of the 10 devices tested in the same study had effective cleaning rates ($\eta_{ii} f_{ii}$) in the range 0-12 m^3 h^{-1}, insignificantly low values for almost all applications. Furthermore, ion generators are particularly to be avoided in museum

8.4.3.3 Reducing particle deposition velocities. The soiling control measures just discussed act by reducing indoor particle concentrations. Soiling rates depend not only on ambient particle concentrations but also on the rate of particle transport to surfaces. That transport phenomenon is parameterized by the deposition velocity, which is calculated as the particle flux to the wall divided by the airborne concentration. Modeling calculations described in Chapter 7 indicated that, for a given particle size, the deposition velocity to the walls of five Southern California museums differed by as much as a factor of 30 among different sites. By controlling the factors that govern the deposition velocity, a substantial reduction in the soiling rate may be achieved without reducing the indoor particle concentration.

The soiling of vertical and downward-facing surfaces is predominantly due to the deposition of fine particles. The rate of deposition of these particles onto a surface is governed by the rate of particle migration across the thin concentration boundary layer adjacent to the surface (see Chapters 3 and 4). The particle flux to the surface varies with the gradient of the particle concentration at the wall, which increases as the particle concentration boundary layer becomes thinner. The deposition rate can be reduced by increasing the thickness of the concentration boundary layer or by reducing the migration velocity toward the surface. For a given distance downstream along a flat surface, the concentration boundary-layer thickness is relatively large if the near-surface air flow is laminar and if the air velocity is low; conversely, high velocities and turbulent flow conditions lead to a relatively smaller boundary-layer thickness. A simple means of limiting soiling rates that employs this principle is to avoid placing works of art near doors, windows, or mechanical ventilation registers, where local air velocities are likely to be higher than the average for the room as a whole. Likewise, the more precious works in a collection should not be placed on or near exterior walls, as heat transfer through

---

environments: these devices reduce airborne concentrations by electrically charging particles and causing them to deposit more rapidly onto indoor surfaces.

these walls can lead to large local flow velocities due to natural convection and, if the surface is cooler than the air, enhanced deposition due to thermophoresis (see Chapters 3 and 4). For example, particle deposition velocities at the Getty Museum were among the highest of the five sites studied (Chapter 7). An exterior, concrete wall that was generally cooler than the air in the room (Chapter 7, Figure 7.2) was investigated at this site. Even though the mechanical ventilation system operated less than 50% of the time, the mean near-wall air flow velocity (0.19 m s^{-1} at 1 cm from the wall) was the highest observed among the five sites. The high particle deposition velocities resulted from a combination of the large near-wall velocity and the relatively cool surface. In contrast, near-wall air velocities were lowest at the Norton Simon Museum (0.08 m s^{-1} at 1 cm from the wall) where an interior wall was investigated, and despite continuous operation of a forced-air mechanical ventilation system.

The design and operation of the mechanical ventilation system is a vital factor governing the near-wall air flow regime. In much conventional ventilation system design, air is discharged into a room at high velocity through small-area registers. From the standpoint of thermal control, this approach offers the benefit of good mixing. However, this approach also promotes particle deposition by producing relatively high turbulence intensities: for example, streaks of soot on building surfaces near a ventilation discharge register are a common sight. An alternative approach is low velocity air discharge from large area diffusers. To be effective for thermal control, the return air path for this approach must be at a different elevation; otherwise, the discharged air may not be distributed throughout the room, but instead follow the return-air path directly. Ideally, if the air supply diffusers are located at ceiling level, the entrance to the return air path would be near the floor. At the Norton Simon Museum, this approach is successfully employed by using perforated ceiling tiles to discharge air into the galleries, with the return air flowing back to the mechanical ventilation system through the hallways. At

this site, the particle deposition velocities onto walls were the lowest observed among the five museums studied.

To minimize near-wall air flows and to avoid enhancing deposition by thermophoresis, it is important that the building shell of a museum gallery is constructed to have low thermal conductivity. It is common in museums to find works of art, such as paintings, hanging from a display panel (for example, a sheet of plywood mounted to the wall with furring strips) or from a false wall. That the surface-air temperature difference is generally smaller for the display panel than for the wall itself is beneficial in reducing deposition velocities.

Further reductions in near-wall air velocity appear possible through the use of a "displacement" ventilation system. A full implementation of this technique might employ two sets of mechanical ventilation system registers, one each at floor and ceiling level, that can each be switched from discharging air into the gallery to returning air to the mechanical ventilation system. When the indoor thermostat calls for cooling, air would be discharged from the register at floor level and removed from the register at ceiling level. When the indoor thermostat calls for heating, the role of each register is reversed. This ventilation strategy promotes a stable thermal stratification of the air in the room, which suppresses turbulent mixing. The paired mechanical supply and exhaust provide for a slow upward or downward net air flow sufficient to prevent total air stagnation in the presence of this thermal stratification. In the ideal case, each parcel of air discharged into the room remains there for a constant period before being removed. This approach has attracted attention as a means of maximizing the effectiveness of ventilation (Sandberg, 1981; Skåret and Mathisen, 1982). From the perspective of preventing soiling, this approach minimizes the contribution of the mechanical ventilation system to the near-wall air velocity and also minimizes the turbulence due to buoyancy induced mixing in the core of the room. A hint of the effect of displacement flow on reducing near-wall air velocities can be seen in the case of the Norton Simon Museum during

periods when warm air is being discharged through the ceiling tiles and removed down the halls (Chapter 7, Figure 7.1, 2200-0800 hours, mean near-wall air velocity of 0.05 m s^{-1}). For a pure displacement flow, the net vertical velocity is flow rate of air through the mechanical ventilation system divided by the floor area of the building, which, for typical conditions, is order 0.01 m s^{-1}.

It is also possible to employ the thermophoretic effect deliberately to reduce the particle deposition rate. This control method can be viewed at two levels. First, situations where walls are chronically cooler than the room air (e.g., at the Getty Museum, see Chapter 7, Figure 7.2) can be avoided. This goal might be achieved by using better insulation in the building. Second, there may be cases where active use of thermophoresis to drive particles away from surfaces is possible by maintaining the surface of interest at a slightly higher temperature than the adjacent air. For example, this might be achieved in buildings located in warm climates by heat leakage through the exterior walls of the building combined with cooling of the indoor air. An indication of the effectiveness that this measure could provide is examined for a building the size of the Sepulveda House in Case 7 (Table 8.1). In that case a temperature difference of 1 K is postulated between the surfaces and the air, with the air cooler, and the natural convection flow regime is assumed to prevail at all times. Table 8.3 shows that these conditions—in combination with the previous controls of eliminating infiltration, using low mechanical ventilation supply rates, and employing particle filters with high efficiency—eliminate particle deposition onto the ceiling, and extend the characteristic soiling time due to elemental carbon particle deposition onto the walls from one century to more than two centuries.

An alternative technique for reducing particle deposition velocities that may be easier to achieve, especially in an existing structure, is to obtain laminar forced flow conditions coupled with small surface-air temperature differences by employing a forced flow system similar to that at the Norton Simon Museum. In modeling Case 8 (Table 8.1)

applied to the Sepulveda House, the air flow regime for computing deposition velocities is assumed to be forced laminar flow with the freestream air velocity and temperature difference as a function of time corresponding to conditions measured at the Norton Simon Museum on April 6-7, 1988. (See Chapter 6.) Table 8.3 shows that these conditions also lead to a significant improvement in characteristic soiling times for walls and ceiling, but that the improvement is not as large as for Case 7.

For coarse particles, which migrate primarily due to gravitational settling, one should simply avoid, to the extent possible, any upward orientation of the surface. A benefit might be realized by mounting paintings with an orientation that is slightly downward from vertical, as this practice would reduce the rate at which coarse particles settle onto the roughness elements of the surface.

8.4.3.4 Using display cases and framing. An alternative means of effectively providing local pollution control in the vicinity of an art object is through the use of display cases and framing behind glass. When analyzed in this context, a display case may be considered as a room within a room. Thus, to predict the effectiveness of a display case, one can apply equations 8.2-8.4, or the complete aerosol dynamics model of Chapter 5, regarding C_{o_k} as the component concentration within the *room*, and C_{i_k} as the component concentration inside the display case. Then, as with the control problem for the museum as a whole, the control options within a display case include reducing the rate of air exchange between the display case and the room, improving particle filtration within the display case, reducing the particle deposition velocity to objects within the display case, controlling the concentration within the room outside of the display case, and eliminating emissions inside the display case.

To consider the potential effectiveness of the use of display cases, additional data from the Sepulveda House will be considered. In recognition of the soiling problem at this site, one of its rooms—a bedroom furnished with historical artifacts—has been

retrofitted to be, in effect, a large display case. All identifiable air leakage paths were sealed. In the room's one doorway, a glass-walled alcove from the hallway into the room was constructed, entirely sealing the doorway. By standing in this alcove, visitors may examine the entire room, but, except for maintenance activities, no one enters.

To determine the effectiveness of this approach in reducing soiling, measurements of the size distribution and concentration of fine particles were made at two locations—one inside the enclosed bedroom, the other on a stairway landing in a central location in the building. A pair of optical particle counters (OPCs; Particle Measuring Systems, model ASASP-X) were used to make the measurements continuously for a day and a half during the spring of 1988. These instruments are capable of detecting particles over a nominal size range of 0.09-3 μm optical diameter and classifying them, according to the amount of light scattered in the forward direction, into 32 size channels (see Chapter 6). The air-exchange rate between the bedroom and its surroundings (outdoors plus the rest of the building) was measured throughout this period by the tracer-gas decay technique (ASHRAE, 1985), using sulfur hexafluoride as the tracer.

Figure 8.4 depicts results for a twenty-four hour segment of the monitoring period: the total volume concentration of fine particles detected by the OPCs as a function of time, and the 24-hour-average aerosol size distributions. By sealing the bedroom, the soiling hazard has been substantially reduced. For soot-sized particles of 0.1 μm diameter, the concentration in the bedroom is 32 % of the concentration in the core of the building. For particles of 2 μm diameter, the corresponding ratio is 8 %.

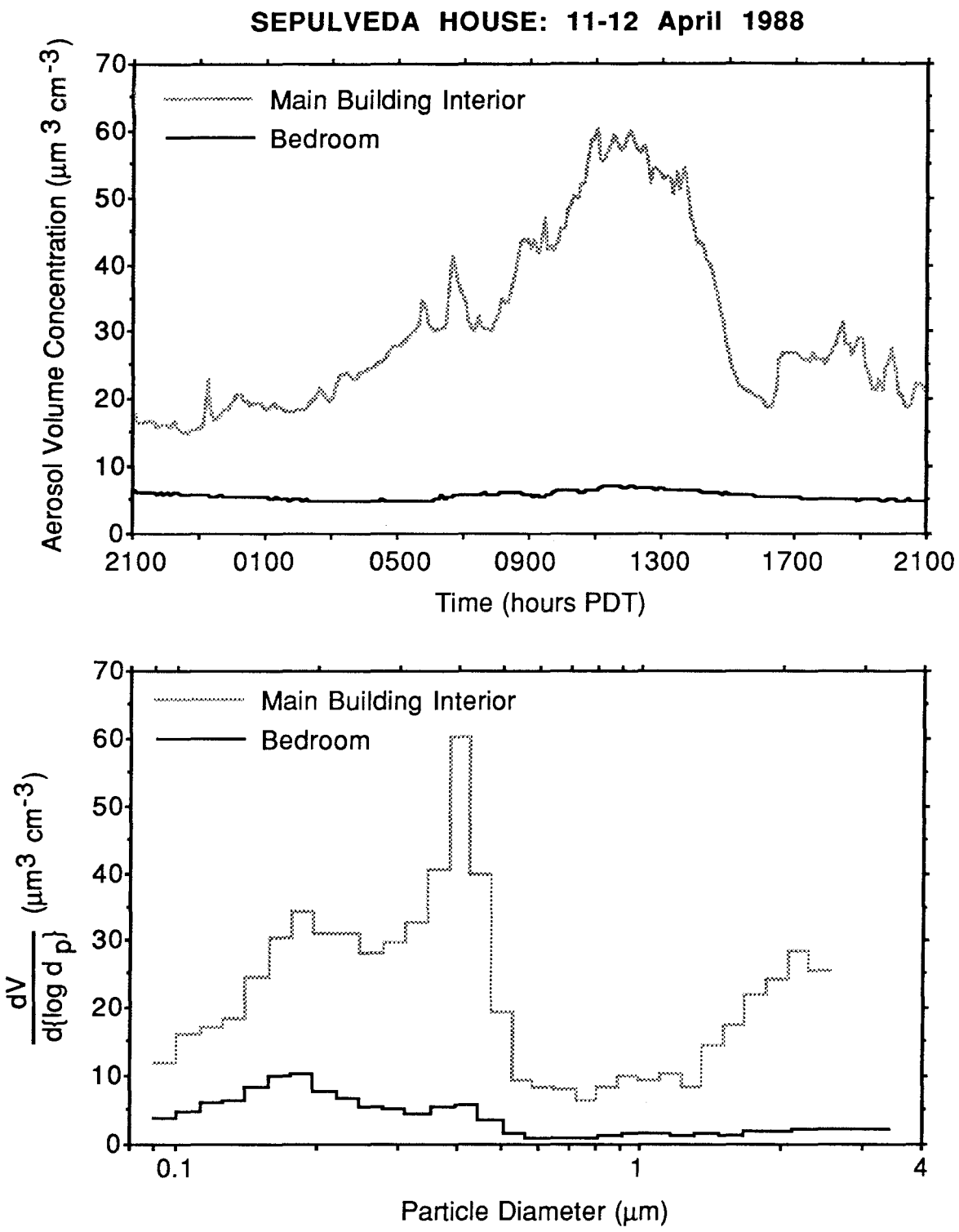

Figure 8.4 Volume concentration of fine particles (0.09-2.3 μm optical diameter) versus time and mean aerosol size distribution measured over a 24-hour sampling period, beginning at 2100 PDT on 11 April 1988, inside the Sepulveda House in downtown Los Angeles.

A substantial further reduction in the soiling rate could be achieved through the use of a local particle filtration unit in the room. The average rate of air leakage into this room is 4.3 $m^3\ h^{-1}$ (f_{oi}). Employing an air filter having an effective filtration rate of 300 $m^3\ h^{-1}$ ($\eta_{ii}\ f_{ii}$) would reduce the concentration of 0.1 μm particles by a factor in the range of 20-60 according to equation 8.7. The power consumption rate of an unducted filtration unit is generally less than 100 W (Offermann et al., 1985); however, some attention must be given to heat dissipation if such a unit is to be used in a small, tightly enclosed space. If heat dissipation or aesthetic considerations dictate that an unducted unit may not be used in a small, enclosed space, it is possible to achieve the same benefit by using a ducted, local recirculation and filtration system. Using this approach, the heat and noise generated by the fan can be separated from the items in the exhibit.

8.4.3.5 Site management to achieve low outdoor aerosol concentrations. Some consideration may be given in the planning of a new facility to the outdoor concentrations of soiling particles. Within the central portion of the Los Angeles air basin, the annual average concentrations of fine elemental carbon particles vary within a relatively narrow range (coefficient of variation among 10 sites monitored in 1982 was 0.2; Gray et al., 1986). However, measurements taken outside of five museums during the summer of 1987 and the winter of 1987-88 show that the mean concentration of fine elemental carbon particles in Malibu, located along the coast northwest of Los Angeles, was 0.8 μg m^{-3}, only 27% of the corresponding mean for the four sites centrally located in the air basin (see Table 8.2). A significant benefit in reducing the soiling rate may therefore be realized through careful site selection.

In designing new museum facilities and in considering control measures to reduce the soiling hazard at existing sites, care should be taken to minimize aerosol generating activities that are close to the location of the air-intake register through which outdoor air

is provided to the building. For example, in a new building, placing the intake register near a street should be avoided, because the soot and road dust concentrations there are relatively high. Areas near parking lots should be avoided because of particle generation by idling vehicles. The use of landscape maintenance equipment, such as leaf blowers, may also generate high concentrations of airborne particles, as illustrated with data collected at the Sepulveda House in Figure 8.3. In that case, a prominent peak is observed in the number concentration of very large particles due to the suspension of soil dust by a leaf blower; a large fraction of the total number of very large particles to which the building inlet was exposed in the 24-hour period studied is due to this brief (10-15 minute) episode of leaf-blower operation. A corresponding peak in the number of very fine particles also is observed at that time, probably due to the exhaust from the gasoline-powered leaf-blower engine. Preventing particles such as these from entering a museum can be largely achieved through careful planning.

8.4.3.6 Limiting sources of indoor aerosol. Many activities may result in the direct emission of particles into indoor air. Combustion processes that lead to the emission of elemental carbon indoors include the burning of candles (e.g., inside churches), the operation of motor vehicles in attached garages, fireplace combustion of wood, and the use of gas-fired cooking appliances in kitchens contained within the building.

Other activities that do not involve combustion may also generate particles that could contribute to the soiling hazard. Construction activities that involve abrasion or grinding will generate coarse airborne particles. Simply allowing people in a gallery will lead to some particle generation through the shedding of skin flakes, through tracking of soil dust into a building on clothes and shoes, and through abrasion of floors and clothing due to movement (e.g., Cooper, 1986). Cleaning activities within the museum, such as vacuum cleaning and floor polishing, may lead to resuspension or generation of airborne particles. With available information, it cannot be stated that these sources pose a

significant soiling hazard in museums. However, since the control cost for reducing or eliminating indoor particle generation by many activities is small (if not zero), it is advisable to adopt measures to control indoor particle generation as part of the overall strategy for controlling the indoor soiling hazard.

8.5 Conclusions

In this chapter, techniques have been examined for protecting works of art from soiling due to the deposition of airborne particulate matter. A simplified version of a detailed mathematical model for indoor aerosol processes was introduced to serve as a basis for discussion and identification of the control options (and to provide an easily obtained estimate of their effectiveness in cases where a more detailed computer-based model is unavailable). Six control techniques were identified: reducing the rate of supply of outdoor air to the building, improving particle filtration, reducing particle deposition velocities, using display cases or framing, managing a site to achieve low outdoor aerosol concentrations and eliminating indoor aerosol sources. Calculations based on the detailed model of indoor aerosol dynamics (Chapter 5) applied to the Sepulveda House show that, relative to the current uncontrolled conditions, characteristic soiling times could be increased by two to three orders of magnitude through a combination of adding a mechanical ventilation system, maintaining a low outdoor-air exchange rate, improving particle removal by filters and designing the building and mechanical ventilation system to achieve lower particle deposition velocities. In the uncontrolled case at the Sepulveda House, the characteristic time to accumulate a perceptible deposit of soiling particles on walls and ceilings is measured in years; with the application of aggressive, but achievable control measures, the characteristic times are measured in centuries (see Table 8.3). Furthermore, having a suite of control options from which to choose, more modest improvements can be obtained at a correspondingly lower cost. Through the use of

display cases and localized air filtration, it is possible to protect a portion of a collection without the expense of modifying an entire building.

The control measures discussed in this chapter are not only technically feasible, they also either involve no additional equipment purchase, or are based on commercially available products. Furthermore, many of the measures are at least economically practical, if not economically attractive. For example, as discussed in the Section 8.4.3.1, reducing the rate of supply of outdoor air to a building can not only reduce soiling rates, but actually lower operating costs by reducing the amount of energy required to control the indoor air temperature and relative humidity. At the Sepulveda House, the cost of remodeling the bedroom to create a large display case has been offset by the reduction in the cost of cleaning the exhibit (John Coghlan, El Pueblo de Los Angeles State Historic Park, personal communication).

Thus, a variety of techniques are available to control the rate of particle deposition onto surfaces. Many of these techniques have low associated costs; some may even yield savings. With sufficient information and careful planning, most museum collections can be protected from soiling due to the deposition of airborne particulate matter.

8.6 Acknowledgements

Financial support for this work was provided through a contract with the Getty Conservation Institute. Additional support was received through graduate scholarships from the Switzer Foundation and the Air Pollution Control Association. We gratefully acknowledge the cooperation and support rendered by John Coghlan, artifacts curator of El Pueblo de Los Angeles State Historic Park, during our monitoring program at the Sepulveda House.

8.7 References

Allen, R. J., Wadden, R. A., and Ross, E. D. (1978) Characterization of potential indoor sources of ozone, *American Industrial Hygiene Association Journal* **39**, 466-471.

ANSI (1985) *Practice for Storage of Paper-Based Library and Archival Documents*, American National Standards Institute Standard Z39.xx-1985, draft.

ASHRAE (1976) *Method of Testing Air-Cleaning Devices used in General Ventilation for Removing Particulate Matter*, ASHRAE Standard 52-76, American Society of Heating, Refrigeration, and Air-Conditioning Engineers: Atlanta.

ASHRAE (1985) *ASHRAE Handbook: 1985 Fundamentals*, American Society of Heating, Refrigeration, and Air-Conditioning Engineers: Atlanta, Chapter 22.

Baer, N. S., and Banks, P. N. (1985) Indoor air pollution: Effects on cultural and historic materials, *International Journal of Museum Management and Curatorship* **4**, 9-20.

Carey, W. F. (1959) Atmospheric deposits in Britain: A study of dinginess, *International Journal of Air Pollution* **2**, 1-26.

Cass, G. R., Conklin, M. H., Shah, J. J., Huntzicker, J. J., and Macias, E. S. (1984) Elemental carbon concentrations: Estimation of an historical data base, *Atmospheric Environment* **18**, 153-162.

Cass, G. R., Druzik, J. R., Grosjean, D., Nazaroff, W. W., Whitmore, P. M., and Wittman, C. L. (1988) *Protection of Works of Art from Photochemical Smog*, final report submitted to the Getty Conservation Institute, California Institute of Technology, Pasadena, California, Chapter 12.

Committee on Preservation of Historical Records (1986) *Preservation of Historical Records*, National Research Council, National Academy Press: Washington.

Cooper, D. W. (1986) Particulate contamination and microelectronics manufacturing: An introduction, *Aerosol Science and Technology* **5**, 287-299.

Gray, H. A., Cass, G. R., Huntzicker, J. J., Heyerdahl, E. K., and Rau, J. A. (1986) Characteristics of atmospheric organic and elemental carbon particle concentrations in Los Angeles, *Environmental Science and Technology* **20**, 580-589.

Hancock, R. P., Esmen, N. A., and Furber, C. P. (1976) Visual response to dustiness, *Journal of the Air Pollution Control Association* **26**, 54-57.

Ligocki, M. P., Salmon, L. G., Fall, T., Jones, M. C., Nazaroff, W. W., and Cass, G. R. (1988) Characteristics of airborne particles inside Southern California museums, California Institute of Technology: Pasadena (manuscript in preparation).

Offermann, F. J., Sextro, R. G., Fisk, W. J., Grimsrud, D. T., Nazaroff, W. W., Nero, A. V., Revzan, K. L., and Yater, J. (1985) Control of respirable particles in indoor air with portable air cleaners, *Atmospheric Environment* **19**, 1761-1771.

Ouimette, J. (1981) *Aerosol Chemical Species Contributions to the Extinction Coefficient*, Ph.D. Thesis, California Institute of Technology, Pasadena, California.

Rivers, R. D. (1988) Interpretation and use of air filter particle-size-efficiency data for general-ventilation applications, *ASHRAE Transactions* **94(2)**, in press.

Sandberg, M. (1981) What is ventilation efficiency? *Building and Environment* **16**, 123-135.

Shair, F. H., and Heitner, K. L. (1974) Theoretical model for relating indoor pollutant concentrations to those outside, *Environmental Science and Technology* **8**, 444-451.

Skåret, E., and Mathisen, H. M. (1982) Ventilation efficiency, *Environment International* **8**, 473-481.

Sutton, D. J., Nodolf, K. M., and Makino, K. K. (1976) Predicting ozone concentrations in residential structures, *ASHRAE Journal* **18(9)**, 21-26.

Thomson, G. (1978) *The Museum Environment,* Butterworths: London.

United States Department of Defense (1956) *Military Standard: Filter Units, Protective Clothing, Gas-Mask Components and Related Products: Performance-Test Methods*, MIL-STD-282, U. S. Government Printing Office: Washington.

CHAPTER 9

CONCLUSIONS

9.1 Summary of Results

A mathematical model for indoor air pollution has been described that links a flexible description of building and ventilation system structure to a mechanistically sound analysis of pollutant dynamics. The model tracks the evolution in time both of the indoor concentrations of gaseous pollutants in the photochemical smog system and of the chemical composition and size distribution of indoor aerosols. The model also predicts the magnitude of the sources and sinks of indoor pollutants, explicitly accounting for the effects of ventilation, filtration, deposition, direct indoor emission, homogeneous chemical reaction, and coagulation.

The problem of pollutant deposition onto indoor surfaces has been analyzed in detail. The results of these analyses have been incorporated into the indoor air quality model to permit simulation of certain indoor air quality problems such as the soiling of works of art. The analyses also may have application to other situations. For example, the demonstration that thermophoresis can effectively prevent particles from depositing onto a vertical heated surface from a natural convection flow could lead to changes in methods of manufacturing microelectronic circuits to reduce particle deposition rates and thereby increase yields.

The soiling of works of art in museums due to particle deposition was investigated. Field measurements were made in several Southern California museums of building characteristics and of indoor and outdoor aerosol size distribution and chemical composition. The experimental data were combined with model calculations to assess the soiling hazard and to evaluate control options. The results showed that surfaces in some museums in Southern California may become perceptibly soiled in short periods of time,

ranging from less than a year to a few decades in most cases. A variety of control methods—reducing outdoor-air exchange rates, improving particle filtration, reducing particle deposition velocities, using display cases, managing a site to achieve low outdoor aerosol concentrations, and eliminating indoor aerosol sources—were evaluated for their effect on reducing the rate of soiling within museums. Practical control techniques were found that can be used to reduce the rate of soiling by two or more orders of magnitude, thereby extending to centuries the time periods before noticeable soiling will occur. Investigations in museums also provided a basis for comparing modeling predictions with measurement results. The finding of generally good agreement establishes a basis for confidence in the accuracy of model predictions, and justifies further use of the model as a tool for studying indoor air quality.

9.2 Directions for Future Research

Many questions arose during the course of this research that were peripheral to the main objectives and therefore could not be pursued. Important issues that merit further study are described briefly in the following subsections.

9.2.1 Model Development. The mathematical model described in this thesis represents a significant advance in the ability to predict concentrations of indoor air pollutants for a wide range of circumstances. However, additional model development would expand the domain of problems that could be addressed. For example, simple calculations show that one might expect substantial gas-to-particle conversion in some indoor environments. Because of the considerable temperature sensitivity of the equilibrium dissociation constant for ammonium nitrate (Russell et al., 1983), the cooling of polluted outdoor air upon entry into an air-conditioned building could lead to conversion of gaseous NH_3 and HNO_3 to aerosol phase NH_4NO_3. In this case, accurate prediction of the indoor concentrations of the gas phase species or of the aerosol size distribution and chemical composition requires an accounting of the gas-to-particle conversion process. The model

described in this thesis can track the evolution of gas phase and aerosol phase species in a building. To treat gas-to-particle conversion processes would require only the addition of a module that accounts for the net loss and gain of the mass of individual species by this route.

As another example, the nucleation of fresh aerosol is clearly important indoors in connection with combustion sources, and the model treats such a process by accounting for direct indoor emissions. However, the model does not presently account for spatially distributed aerosol nucleation, which might also be important in some circumstances. Investigators are currently exploring whether distributed aerosol production may be promoted by the radioactive decay of ^{222}Rn and its decay products, often present in high concentrations indoors.

Another area of model development that might be usefully pursued is to relax the assumption of uniform mixing throughout each room. While this assumption did not interfere with obtaining accurate predictions in the present work, there clearly are problems in which the assumption of uniform mixing is not appropriate. An example is assessing the effectiveness of smoker segregation in reducing the exposure of nonsmokers to environmental tobacco smoke. One approach to relaxing the uniform mixing assumption is to use the atmospheric diffusion equation (Seinfeld, 1986) to describe the time-rate-of-change of pollutant concentrations as a function of location within a room. To solve the problem using this approach, one requires information on indoor air velocities and eddy diffusivities. The basis for describing indoor air motion is partially described in numerical codes for natural convection (Gadgil, 1980) and forced turbulent flow (Kurabuchi and Kusuda, 1987) in rooms. It appears, though, that considerable work is required to firmly establish an understanding and a predictive capability for air movement and pollutant dispersion indoors. The use of mixing concepts developed in chemical engineering (Brodkey, 1981; Nauman, 1981) may prove useful as an alternative

to applying the atmospheric diffusion equation, as might probability density function methods (Pope, 1985).

With respect to the deposition calculations, extensions can be made in several directions to the prediction methods developed in this thesis. One useful objective is to improve the capability for predicting the deposition rate of gaseous pollutants, such as ozone, that are lost at less than the mass-transport-limited rate. Prediction of particle deposition rates might be improved by accounting for the effects of surface roughness (e.g., Shimada et al., 1987) and electrostatic attraction (e.g., McMurry and Rader, 1985). More detailed understanding of near-surface air velocity and temperature profiles would permit further refinement of the deposition calculations.

9.2.2 Model Application. An important goal of the present research was to develop a model that could be applied usefully to a variety of indoor air quality problems. One such problem that was explored in this thesis is assessing and controlling the soiling hazard to works of art due to particle deposition. A few other applications that are of current interest are mentioned here.

The model can be used directly to address some important aspects of the problem of nonsmokers' exposure to environmental tobacco smoke, such as how exposure characteristics vary with frequency of smoking and with building ventilation conditions. For this problem, the present model represents an important advance over previously available tools in that it predicts the aerosol size distribution which is necessary to accurately relate dose to exposure.

Another application of the model concerns the health risk associated with exposure to radon decay products indoors. The total radiation dose and its distribution within the lung depend critically on the fractions of the decay product concentrations that are not attached to airborne particles, and on the size distribution of the attached fraction (James, 1984). Existing models of the dynamics of radon decay product behavior treat

the indoor aerosol size distribution as a static entity that must be known *a priori* (Knutson, 1988). As a result, certain problems, such as the influence of air filtration—removing both airborne particles and radon decay products—on dose to the lung, cannot be studied adequately with existing modeling tools. A module accounting for radon decay product dynamics could be added to the model described in this thesis to establish a means of addressing this and related issues.

Air pollution exposure studies are another area of current interest to which the indoor air quality model may be applied. In many current and recent studies, laboratory animals are exposed to mixtures of pollutants (e.g., Malanchuk, 1980; Kleinman et al., 1985). Since the pollutant concentrations in these cases are relatively high, processes such as homogeneous chemical reaction and coagulation are often important factors in determining the actual mix of pollutants to which the animals are exposed. The model described in this thesis could be usefully applied both to designing such experiments and to interpreting the results.

9.2.3 Museum Atmospheres and Protecting Works of Art from Air Pollution. The analyses in this thesis that concern museum air quality started with information on outdoor pollutant concentrations and building factors and ended with predictions of indoor pollutant concentrations, pollutant fluxes onto indoor surfaces, and rates of effective area coverage by soiling particles. For the deposition of gaseous pollutants, no explicit consideration was given to the damage that these pollutants cause. Recent studies have investigated the fading of artists' pigments from ozone and nitrogen dioxide exposures (Cass et al., 1988). Material-damage effects have been studied for other combinations of pollutants and materials (Graedel and McGill, 1986). However, much more work is needed to have comprehensive information for all of the potentially important combinations.

For the deposition of airborne particles, the problem of soiling associated with the elemental carbon and soil dust components of indoor aerosols was emphasized. Estimates of soiling rates could be refined with better information on the relationship between the accumulation of these components and the rate of optical degradation of surfaces. No explicit consideration was given to the potential for particle deposition to cause damage to surfaces through chemical reactions. It was noted in Chapter 6 that the mass flux to vertical and downward-facing surfaces may be much smaller for particles than for reactive gases such as ozone and nitric acid. However, large mass fluxes may result from gravitational settling of coarse particles onto upward-facing surfaces. Furthermore, as with the case of soiling, even slow rates of accumulation of chemically reactive particles may constitute a significant cumulative hazard to works of art over the long periods that they are to be preserved. Consequently, the potential for chemical damage caused to the surfaces of art objects from particle deposition should be investigated.

Several control measures for reducing the rate of soiling were discussed. Theoretical analyses show that control measures based on available technology can be very effective in reducing soiling, with two orders of magnitude improvement being an achievable goal. Experiments are needed to demonstrate that improvements of this scale can be accomplished.

9.3 References

Brodkey, R. S. (1981) Fundamentals of turbulent motion, mixing and kinetics, *Chemical Engineering Communications* **8**, 1-23.

Cass, G. R., Druzik, J. R., Grosjean, D., Nazaroff, W. W., Whitmore, P. M., and Wittman, C. L. (1988) *Protection of Works of Art from Photochemical Smog*, final report submitted to the Getty Conservation Institute, California Institute of Technology: Pasadena, California.

Gadgil, A. J. (1980) *On Convective Heat Transfer in Building Energy Analysis*, Ph. D. Thesis, University of California, Berkeley, California.

Graedel, T. E., and McGill, R. (1986) Degradation of materials in the atmosphere, *Environmental Science and Technology* **20**, 1093-1100.

James, A. C. (1984) Dosimetric approaches to risk assessment for indoor exposure to radon daughters, *Radiation Protection Dosimetry* **7**, 353-366.

Kleinman, M. T., Mautz, W. J., McClure, T. R., Mannix, R., and Phalen, R. F. (1985) *Comparative Effects of Acidic and Non-Acidic Multicomponent Atmospheres on the Lungs of Rats Exposed by Inhalation*, Paper 85-29.3, Air Pollution Control Association: Pittsburgh, Pennsylvania.

Knutson, E. O. (1988) Modeling indoor concentrations of radon's decay products, In *Radon and Its Decay Products in Indoor Air*, Nazaroff, W. W., Nero, A. V., Eds., Wiley: New York, Chapter 5.

Kurabuchi, T., and Kusuda, T. (1987) Numerical prediction for indoor air movement, *ASHRAE Journal* **29(12)**, 26-30.

McMurry, P. H., and Rader, D. J. (1985) Aerosol wall losses in electrically charged chambers, *Aerosol Science and Technology* **4**, 249-268.

Malanchuk, M. (1980) Exposure chamber atmospheres, sampling and analysis, In *Long-Term Effects of Air Pollutants: in Canine Species*, Stara, J. F., Dungworth, D. L., Orthoefer, J. G., and Tyler, W. S., Eds., Report EPA-600/8-80-014, U. S. Environmental Protection Agency, Environmental Criteria and Assessment Office: Cincinnati, Ohio.

Nauman, E. B. (1981) Residence time distributions and micromixing, *Chemical Engineering Communications* **8**, 53-131.

Pope, S. B. (1985) PDF methods for turbulent reactive flows, *Progress in Energy and Combustion Science* **11**, 119-192.

Russell, A. G., McRae, G. J., and Cass, G. R. (1983) Mathematical modeling of the formation and transport of ammonium nitrate aerosol, *Atmospheric Environment* **17**, 949-964.

Seinfeld, J. H. (1986) *Atmospheric Physics and Chemistry of Air Pollution*, Wiley: New York.

Shimada, M., Okuyama, K., Kousaka, Y., and Ohshima, K. (1987) Turbulent and Brownian diffusive deposition of aerosol particles onto a rough wall, *Journal of Chemical Engineering of Japan* **20**, 57-64.